Virus-based Nanoelectronic devices

By

Atul Mohan

A thesis submitted in accordance with the requirements for the degree of Ph.D.

The University of Leeds

Faculty of Biological Sciences

July 2019

कविं पुराणम् अनुशासितारम्
अणोर् अणीयांसम् अनुस्मरेद् यः ।
सर्वस्य धातारम् अचिन्त्यरूपम्
आदित्यवर्णं तमसः परस्तात् ॥

॥८.९॥

.
am anuśāsitāram
aṇor aṇīyāḿsam anusmared yaḥ
sarvasya dhātāram acintya-rūpam
āditya-varṇaḿ tamasaḥ parastāt

He who meditates on the omniscient, primordial, the controller, smaller than the atom yet the upholder of all whose form is inconceivable, resplendent like the sun and beyond the darkness (of ignorance).

Śrimad Bhagavad Gītā 8.9

Acknowledgements

I would like to express my sincere gratitude to my supervisors Prof. Peter Stockley for all his guidance, support and encouragement throughout this PhD and

Prof. Christoph Walti in the Dept. of Electrical Engineering for his advice.

In addition, I am indebted to:

Prof Giles Davies in the Dept. of Electrical Engineering, for his inputs during group meetings.

Dr. Vijay K. Parmar for his endless patience and support. His encouragement, guidance and the proof reading of the thesis were indispensable in completing this thesis.

Dr Joan Boyes for her intervention on my behalf with the administrative protocols of the University of Leeds without which this endeavour would not have reached fruition.

Dr. Simon White for his support and encouragement.

Dr. Nandan Kumar co-founder of HPT, India for his constant support and interactions.

Dr. Zulfiqar Hasan and Dr. Rajan Sharma for his guidance at the beginning of my PhD. Dr. Jamie Caryl, Dr. Gabriella Basnak and Dr. Pietro Taylor for showing me the ropes around the lab.

Dr. Steve Johnson, Dr. Michael Measures and Dr. Alex Walton for their help with virtual AFM and 4-probe electrical transport measurement.

The various people, past and present, that makes up the Prof. Stockley’s laboratory team. My apologies to anyone, I have omitted.

My final thanks are to my mother and my brothers, Arun Lal and Amit Lal. They have always stood by my side despite my many failures. I would like thank my wife, Dr. Kanika Prasad especially. I am lucky to have a partner, who is constant in her support during good times as well as bad. Finally, I thank my daughter, Sharvi for putting a smile on her dad’s face, whenever she wishes.

Dedicated to my dear mother and the memory of my dear late father

Abstract

Bacteriophages are useful templates for the fabrication of electronically useful nanostructures. These phage-based nanostructures can be self-assembled into simple nanoelectronics device using the molecular recognition properties displayed on their surface. The aim of this work was to use such phage-based nanostructures to form a self-assembling molecular transistor. Filamentous bacteriophage M13 and icosahedral bacteriophage MS2 were selected for the fabrication of the gold nanowires and nanoparticle encapsulated capsid respectively.

First a ~1 μm long gold nanowire was made by modifying the major coat protein, pVIII to express gold binding peptide on its surface. This phage bound to gold nanoparticles of various sizes. Then a dual functional phage was created by genetically modifying the minor coat protein gene, *gIII* of this gold binding phage to express biotin binding motif on pIII. Although, this phage bound to florescent tagged biotin, but the binding affinity was not strong enough to bind other biotin functionalized phage and form higher order structures. Physical and electrical characterization of these nanostructures were carried out. The gold nanowire was found to have an electrically insulating coat on their surface which could be burnt off after passing current through it at high voltage sweeps. The MS2 bacteriophage encapsulated gold nanoparticles of various sizes and their encapsulation efficiency was determined. The pores on the surface of the phage were used to modify the encapsulated nanoparticle.

AFM tip was moved using a virtual haptic to manipulate such virus-templated nanostructures on silica and mica surfaces in order to fabricate rapid prototypes of nanoelectronic device. Although, much progress was made towards the goal of a self-assembling transistor, the aspects devised within this study need to be combined.

Contents

Chapter 1: Introduction 1

1.0 Introduction.. 2

1.1 Current trends in nanotechnology 2

1.2 Bionanotechnology 4

1.3 Biomineralization 5

    1.3.1 Specific biomineralization of metals and semiconductors 6

    1.3.2 Non-specific biomineralization of metals and semiconductors............ 8

1.4 Virus-templated nanostructures...10

1.5 M13 bacteriophage 14

    1.5.1 The major coat protein pVIII 16

    1.5.2 The major coat protein pIII 18

    1.5.3 The life-cycle of the M13 bacteriophage 19

1.6 Phage display 22

    1.6.1 pVIII based phage display.. 22

    1.6.2 pIII based phage display... 24

    1.6.3 Biopanning 24

1.7 Use of M13 coat proteins in bionanotechnology 26

    1.7.1 pVIII used in nanotechnology applications 27

    1.7.2 pIII used in nanotechnology applications 29

1.8 MS2 bacteriophage.. 29

1.8.1 The life cycle of MS2 33

1.9 Synthetic viruses 33

1.10 Molecular transistor and bottom-up fabrication of nanoelectronic devices...... 34

1.11 Aim and Scope of the work in thesis 37

Chapter 2: Materials and methods 38

2.1 Materials 39

2.1.1 General reagents .... .39

2.1.2 Antibiotic solution 39

2.1.3 Media recipes 39

2.1.3.1 2xYT medium 40

2.1.3.2 Agarose top 40

2.1.3.3 Agar 40

2.1.4 Buffers and reagents 41

2.1.4.1 Phosphate buffered saline (PBS) 41

2.1.4.2 Tris-HCl buffer 41

2.1.4.3 20% (w/v) Polyethylene glycol (PEG) in 2.5 M NaCl solution ……….………………………………………………………42

2.1.4.4 Protein loading buffer (Stock concentration – 2x) (LaemmLi buffer)……………………………………………………42

2.1.4.5 Glycine running buffer (Stock concentration – 10x) 43

2.1.4.6 Coomassie blue staining solution 43

2.1.4.7 De-stain solution 43

2.1.4.8 λ buffer for linear sucrose gradients 44

2.1.5 Nucleic acid primers and sequencing 44

2.1.6 Enzymes 44

2.1.7 Bacterial strains 45

2.2 General Methods 45

2.2.1Protein and DNA gel electrophoresis 45

2.2.1.1 1% and 2% agarose gel electrophoresis 45

2.2.1.2 Native polyacrylamide gel electrophoresis (PAGE): 47

2.2.1.3 Tris-glycine SDS protein gel 47

2.2.2 Transmission electron microscopy (TEM) 48

2.2.3 Molecular biology techniques 48

2.2.3.1 Preparation of host *E. coli* ER 2738 48

2.2.3.2 Preparation of bacterial stocks for freezing 49

2.2.3.3 Polymerase chain reaction 49

2.2.4 Preparation of phage stock 50

2.2.4.1 Growth of phage and PEG precipitation 50

2.2.4.2 Caesium chloride purification 52

2.2.5 Competent cells preparation 52

2.2.6 Transformation of M13 KE DNA 53

2.2.7 Preparation of M13 phage stock and RF DNA 53

2.2.8 Phenol chloroform extraction of DNA 54

2.2.9 Ethanol precipitation of DNA 54

2.2.10 Ligation of DNA fragments 55

2.2.11 Determination of the phage concentration using spectrophotometry of phage particles (measured in virions/mL).......................................55

2.2.12 Phage titre (measured in pfu/mL)... 56

2.2.13 Site-directed mutagenesis to clone gold binding insert in *gVIII*…...57

2.2.14 Colony PCR... 60

2.2.15 Concentration of 5 nm gold nanoparticles without ligand exchange. 62

2.2.16 Goldenhanced nanowires ………………………………………… 62

2.2.17 Electroless deposited nanowires …………………………………... 63

2.2.18 Residual background reduction of the M13 gold nanowire on the SiO_2 surface……………………………………………………………64

2.2.19 Adsorption of M13 phage particles on the SiO_2 surface…………….64

2.2.20 AFM (Atomic Force Microscopy)…………………………………..64

2.2.21 Cleaning the SiO_2 surface using Piranha solution…………………..65

2.2.22 Patterning of electrodes on the nanowires…………………………..66

2.2.23 Conductivity measurement using the 4-probe Scanning Probe Microscope…………………………………………………………67

2.2.24 Annealing of the M13 phage-based gold nanowire in a vacuum oven……………………………………………………………....67

2.2.25 Scanning electron microscopy (SEM) of gold nanowires…………..68

2.2.26 Phosphine stabilisation and concentration of GNP………………….69

2.2.27 Invitrogen quantum dot used for encapsulation in a MS2 capsid…...69

2.2.28 Protocol for nanoparticle encapsulation in MS2 capsid…………….70

  2.2.28.1 Preparation of MS2 capsids for disassembly to get MS2 coat proteins…………………………………………………...70

2.2.28.2 Dissociation of MS2 capsids and purification of MS2 coat protein dimers…………..……………………………..………..71

2.2.28.3 TR RNA conjugation to gold nanoparticles and CdTe quantum dots ……………………………….…………71

2.2.28.4 Reassembly of gold nanoparticles encapsulated MS2 virus like particles…………………………………………...72

2.2.28.5 Sucrose density gradient for the purification of the MS2-GNP complex. ……..……………………………...72

2.2.28.6 Fractionation of the MS2-nanoparticle virus-like particle solution…………………………………………...74

2.2.29 Bacteriophage manipulation using a virtual AFM haptic…...75

Chapter 3: Construction of the gold-binding filamentous phage..............76

3.1 Introduction 77

3.1.1. Requirements for self-assembly of a molecular transistor 77

3.1.2 M13 as an ideal template for molecular transistor electrodes 78

3.1.3 Mutagenesis strategies for insertion in the pVIII gene 80

3.1.4 Aim of the work described within this chapter 81

3.2 Results and Discussions 83

3.2.1. Cloning of the gold-binding peptide motif in pVIII 83

3.2.2 Validation of mutant M13G phage ability to bind to gold particles …86

3.2.3 Physical characterization of the phage-GNP complexes 93

3.2.4 Cloning of biotin-binding DNA insert in the *gIII* of the M13G Phage…………………………………….…………………..93

3.2.5 Test to determine if M13GB phage binds to biotin............................ 95
3.3 Conclusion 97

Chapter 4: Fabrication of M13 phage-based gold nanowire……...............98

4.1 Introduction 99
4.1.1 Electroless deposition of gold 99
4.1.2 Annealing of nanostructures... 100
4.1.3 Aims of the work described in this chapter…………………………101
4.2 Results and Discussion……………………………………………..…………103
4.2.1 Fabrication of gold nanowires 103
4.2.2 Chemical and physical characterization of gold nanowires 108
4.2.3 Annealing of the gold nanowires 111
4.2.3 Characterization of the annealed gold nanowires 118
4.3 Conclusion 122

Chapter 5: Electrical characterization of gold nanowires………............... 124

5.1 Introduction 125
5.1.1 Nanowires on a biological template 125
5.1.2 Electrical characterization of nanowires 126
5.1.3 Aims of the work described within this Chapter 127
5.2 Results and discussion 129
5.2.1 Reduction of the background of unbound nanoparticles 129

5.2.2 Deposition of Goldenhanced nanowires on a silicon substrate 132

5.2.3 Deposition of hydroxylamine electroless deposited gold nanowires .137

5.2.4 Electrical characterization of the M13 nanowire 138

5.2.4.1 Conductivity measurement using the MPSTM 138

5.2.4.2 Patterning of contacts onto the gold nanowires using EBL.141

5.2.4.3 Electrical characterization of the gold nanowires ………...143

5.3 Conclusions 149

Chapter 6: MS2 phage encapsulated nanoparticle….................................... 151

6.1 Introduction 152

6.1.1. Phage capsid or protein shell encapsulated nanoparticle..................152

6.1.2 In-vitro assembly of a MS2 bacteriophage capsid 154

6.1.3 Higher order biological super structures 155

6.1.4 Aims of the work described in this chapter 156

6.2 Results and Discussion 157

6.2.1 Encapsulation of gold nanoparticles in the MS2 phage capsid 157

6.2.2 Encapsulation of GNPs, bigger than 5 nm 162

6.2.3 Encapsulation of quantum dots in the MS2 phage capsid 166

6.2.4 Deposition of gold on the nanoparticle inside the MS2 VLP 169

6.2.5 Higher order structure using virus like particles 173

6.3 Conclusions 176

Chapter 7: Nanomanipulation of virus templated nanostructures........ 177

7.1 Introduction 178

7.1.1 Bottom-up assembly by nanomanipulation 178

7.1.2 Atomic Force Microscope 179

7.1.3 Manipulation of nanostructures using an AFM tip............................181

7.1.4. Virtual haptic AFM………………………………………………..…182

7.1.5 Aims of the work described within this chapter 184

7.2 Results and Discussion……………………………………………………..185

7.2.1 Nanomanipulation of filamentous organic and inorganic structures .185

7.2.1.1 Manipulation of the M13 bacteriophage 185

7.2.1.2 Manipulation of the M13 phage-based gold nanowire 188

7.2.1.3 Manipulation of the gold nanowire using different AFM tips ……………………………….…………………………190

7.2.1.4. Manipulation of a gold nanowire on silica substrate submerged in water…….………………………………191

7.2.2 Manipulation of GNPs and sphere-like VLPs……………...……192

7.2.2.1 Manipulation of GNPs on silica surface…………………..193

7.2.2.2. Manipulation of MS2 phage particle…………………..…194

7.2.2.3. Manipulation of MS2-PEGNP complex……………….196

7.3 Conclusions 198

Chapter 8: General Conclusions and Future Works............................. 199

8.1 Conclusions from Chapter 3 200
8.2 Conclusions from Chapter 4 201
8.3 Conclusions from Chapter 5 202
8.4 Conclusions from Chapter 6 203
8.5 Conclusions from Chapter 7 205
8.6 Closing remarks 206

References 207

Appendix A 239

1.0 PCR primers and sequence gold-binding phage, M13G……………………...240
    1.1 Forward primer: Gold mut-1 DNA sequence…………………………240
    1.2 Reverse Primer: Gold mut-1 DNA sequence…………………………240
    1.3 Goldoligo2-S DNA sequence……………………………………………240
    1.4 Goldoligo2-AS DNA sequence………………………………………….240
    1.5 Peptide sequence of pVIII in M13KE……………………………….. 240
    1.6 Peptide sequence of pVIII in M13G…………………………………. 240
    1.7 Gene VIII sequence in M13KE…………………………..……………241
    1.8 Gene VIII sequence in M13G…………………………….………….. 241

Appendix B 242

1.0 Analytical ultracentrifugation run of 5 nm GNPs with M13G phage …….243

2.0 Analytical ultracentrifugation run of 2 nm GNPs with M13G phage …….244

Appendix C 245

1.0 PCR primers and sequences for Biotin-binding insert preparation…………………… 246

- 1.1 Biotin-For-Template DNA sequence………………………………. .246
- 1.2 Biotin-For-1 DNA sequence……………………………………… 246
- 1.3 Biotin-Rev-2 DNA sequence……………………………………… 246
- 1.4 Gene III Sequence DNA sequence…………………………………... 246
- 1.5 pIII peptide sequence……………………………………………… 247
- 1.6 Biotin-binding peptide Gene III Sequence……………………….…. 248

Appendix D 250

1.0 Mass Spectroscopy of 5’ thiol TR RNA …………………………………….. 251

2.0 Polyacrylamide gel electrophoresis of 5’ thiol TR RNA…………………………….. 251

3.0 Analytical HPLC run of 5’ thiol TR RNA……………………………………252

List of Figures

Chapter 1: Introduction 1

Figure 1.1 Examples of bio-mineralization found in nature. ….……………………...…….5

Figure 1.2 SEM and AFM image of a silver nanowire on a DNA scaffold………………....9

Figure 1.3 Examples of different morphology exhibited by viruses……………………..... 11

Figure 1.4 Digital reconstruction of six TMV subunits in a wild type virion…………….. 12

Figure 1.5 The structure of the M13 bacteriophage……………………………………….. 15

Figure 1.6 Structure of the major coat protein pVIII……………………...…………… 17

Figure 1.7 Structure of the minor coat protein pIII…………………………………...…… 19

Figure 1.8 Life-cycle of the M13 bacteriophage…………...……………………...…….21

Figure 1.9 Selection of ligand binding peptide using phage display……………………….25

Figure 1.10 Liquid crystalline property of M13 used for device fabrication………………..28

Figure 1.11 Structure of the MS2 phage…………………………………………...……30

Figure 1.12 Genetic Map of MS2 bactriophage……………………………………………31

Figure 1.13 Structure of MS2 phage coat protein dimers…………………………………..32

Figure 1.14 A diagram showing the basic layout of the molecular transistor …...……….. 35

Figure 1.15 Schematic of the fabrication of the proposed self-assembling molecular transistor……….……………………………………………………………...36

Chapter 2: Materials and Methods...38

Figure 2.1 DNA and protein ladders used for gel electrophoresis…………………….……..46

Figure 2.2 A typical absorption spectrum of the M13 phage solution obtained by PEG/NaCl precipitation……………………………………………………………………… ..56

Figure 2.3 The primers used for the insertion of gold binding peptide gene in the major coat protein, pVIII of the M13KE bacteriophage using site directed mutagenesis to create (A) *Hpa I* site and (B) by creating *Pst I* and *BamH* I site……..……… 58

Figure 2.4 Sequencing primers for pIII and pVIII on the M13KE sequence……………….61

Figure 2.5 Electroless deposition of gold on the gold nanoparticles using the Goldenhance kit from Nanoprobes………….. ….…………….…………………………... 63

Figure 2.6 The 4-probe Scanning Probe Microscope used for the electrical characterization of the M13 gold nanowire……….……………………………………………67

Figure 2.7 The high temperature vacuum tube oven used for the annealing of the M13 gold nanowire…………………………………………………………………….68

Figure 2.8 The quantum dot from Invitrogen…….………………...………………………70

Figure 2.9 (A) Sucrose density gradient station and fractionators from Biocomp. (B) shows the close up of a section showing the tube holder, the trumpet and the piston. (C) shows the components supplied with the Biocomp gradient station and used to create linear sucrose gradients. Images taken from the Biocomp gradient station manual………………………………………………………..……..73

Chapter 3: Construction of the Gold-Binding Filamentous Phage..............76

Figure 3.1 Insertion of the gold-binding DNA sequence in the pVIII gene of the M13 phage using *Hpa I* restriction site. …........…………………………………………... 83

Figure 3.2. Insertion of the gold-binding motif in gene VIII of the M13 phage……….… 85

Figure 3.3. Mixture of phage and 5 nm GNPs after 16 hours of incubation at 4°C………. 87

Figure 3.4. TEM images of the phage mixed with 5 nm GNPs…..…..……………….… 88

Figure 3.5 EDX analysis of (A) the M13G phage-nanoparticle complex on a copper TEM grid, and (B) Wild-type phage on a copper TEM grid…….…………………….. 90

Figure 3.6 TEM image of: (A) the M13G phage mixed with 2 nm GNPs on which further gold was electroless deposited. (B) Magnified section of the phage-NPs array. (C) EDX analysis of the phage-NPs array………..…..……………………….. 91

Figure 3.7 TEM images of the phage-GNPs complex at high phage concentration (5 x 10^{13} pfu/mL)…………………………..…………………………………...….. 92

Figure 3.8 Insertion of biotin-binding motif in gene III of the M13G phage………..…… 94

Figure 3.9 Validation of biotin-binding capability of M13GB phage…………………..…… 96

Chapter 4: Fabrication of M13 Phage-Based Gold Nanowire……..........98

Figure 4.1. Schematic showing the electroless deposition of gold ions on the GNPs in the solution to get bigger GNPs…………..……………………………………..…100

Figure 4.2. Fabrication of gold nanowires by two electroless deposition procedures…….104

Figure 4.3. Transmission electron micrographs of the reaction time evolution of the Goldenhance-EM reaction on a p-GNP complex…………..……..…………106

Figure 4.4. Techniques to reduce the background of free GNPs during Goldenhance reaction………………..…………………………………………………….107

Figure 4.5. HRTEM micrographs of: (A) a non-annealed M13G phage-based gold nanowire. (B) selected area from A, showing crystal lattices upon further magnification …………..…………………………………………….……108

Figure 4.6. EDX of a non-annealed M13G phage-based gold nanowire………………….109

Figure 4.7. SAED of the non-annealed M13G phage-based gold nanowire…...…………110

Figure 4.8. Effects of thermal annealing of M13G phage-based based gold nanowires..………………………………………………………………….112

Figure 4.9. TEM images of the thermal annealing of M13G phage-based gold nanowires at different temperatures…….…………….……………………………………….114

Figure 4.10. Graph showing the effect of thermal annealing of the M13G phage-based gold nanowire..…………………………………………………………….……..116

Figure 4.11. HRTEM micrographs of: (A) a M13G phage-based gold nanowire before annealing, (B) a M13G phage-based gold nanowire annealed at 250°C, (C) Magnification of selected area from B………...………………………….......119

Figure 4.12. EDX spectrum of an annealed M13G phage-based gold nanowire………….120

Figure 4.13. SAED of the M13G phage-based gold nanowire annealed at 250°C………..120

Chapter 5: Electrical Characterization of gold nanowires……….............. 127

Figure 5.1. SEM image of the M13G phage-based gold nanowire suspension…………..131

Figure 5.2. A) TEM image of the dialyzed phage-based gold nanowires. (B) SEM image of the gold nanowires on a SiO_2 surface ……………………………………...133

Figure 5.3: SEM images of M13G phage-based gold nanowires after 2 hours of dialysis on different surfaces …………………..……………………………….………135

Figure 5.4: SEM image of the electroless deposited M13G phage-based gold nanowires deposited on a Piranha cleansed SiO_2 surface……………………………….…...137

Figure 5.5. (A) Length dependent non-linear conductivity characteristics of the nonannealed M13 phage-based gold nanowires. (B) Controls showing the I-V characteristics of the tip-to-tip interaction and of the Si3N4 substrate………………………….139

Figure 5.6: The steps in nanowire contacts fabrication using EBL……………………….142

Figure 5.6: Conductivity measurement of the non-annealed gold nanowire………….…. 144

Figure 5.7: Conductivity measurements on an annealed gold nanowire……………..…...145

Figure 5.8: AFM image of the controls patterned with the gold contacts using EBL…….146

Figure 5.9: Conductivity measurements of the annealed gold nanowire………………….148

Figure 5.10: Comparison of the conductivity of the gold nanowire with other published results..………………………………………………………………...149

Chapter 6: Nanoparticle Encapsulated MS2 Capsid.................................... 151

Figure 6.1. Schematic showing the mechanism of assembly of nanoparticles encapsulation in a MS2 virus-like particle.……………………………………………………..157

Figure 6.2. TEM image of MS2 phage coat proteins mixed with: (A) reassembly buffer, (B) TR RNA, (C) citrate coated GNPs, (D) phosphine coated GNPs, (E) 5 nm GNPs bound to TR RNA, (F) 5nm GNPs and TR RNA not bound to each other…...159

Figure 6.3. (A) TEM images of different MS2-PEGNPs formed during the encapsulation of 5 nm GNPs (B) Graph showing the probability distribution of the four different MS2 GNP VLPs populations after the assembly reaction. (C) Schematic showing a possible explanation of the encapsulation of up to four 5 nm GNPs inside a MS2 phage capsid ……………………………………...161

Figure 6.4. TEM images of MS2-PEGNPs encapsulating…………………………...163

Figure 6.5. A) shows the TEM image of MS2-PEGNPs encapsulating a 10 nm GNP and their (B) probability distribution during the encapsulation. (C) shows the TEM images of two different kinds of MS2-PEGNPs formed during encapsulation of a 10 nm GNP and their (D) size and probability distributions. (E) shows the TEM images of MS2-PEGNPs incorporating a 15 nm GNP and a 20 nm GNP and their (F) size and probability distributions. …………………….……..165

Figure 6.6. A) shows the TEM images of the empty capsid and the quantum dot encapsulating VLP. The individual TEM images were selected (indicated by the red circle) from the widefield TEM image. The sample was stained with 2% (w/v) uranyl acetate. Scale bars equal 60 nm. (B) shows the Probability distribution and (C) shows the size distribution of the VLPs formed during the encapsulation of the quantum dot in a MS2 phage capsid…………….167

Figure 6.7. Graph showing the incorporation efficiency of nanoparticles (GNPs and QDs) inside a MS2 phage capsid against their size……….……………………..168

Figure 6.8. TEM image of GoldenhanceTM reaction on MS2-PEGNPs encapsulating 5 nm GNP…………….……………………………………………………..170

Figure 6.9 A) MS2-PEGNPs solution encapsulating a 10 nm GNP after electroless gold deposition at varying concentration of gold ions. (B) TEM images of the MS2-PEGNPs after the gold deposition ………..……..………………………171

Figure 6.10. A) Schematic showing the pores on the surface of the MS2 phage capsid (taken from Stockley, 2007). TEM image of the VLPs after electroless gold deposition reaction on MS2-PEGNPs (B) for an empty capsid, (C) at the start of the reaction, (D) after 5 minutes, (E) after 10 minutes and (F) after 3 hours. Scale bars equal 60 nm. (G) Graph showing the size of the GNPs against time for the gold deposition reaction……………………………………………….………172

Figure 6.11. A) Denaturing polyacrylamide gel electrophoresis of biotin-labelled MS2 phage capsid. (B) Western blot of the biotin-labelled MS2 phage capsid. (C) TEM image of the biotin-labelled MS2 phage capsid mixed with the M13GB phage……………………………………………………………….…………174

Chapter 7: Nanomanipulation of Virus Templated Nanostructures........ 177

Figure 7.1. AFM imaging using a cantilever tip…………………………………….....180

Figure 7.2. The virtual haptic atomic force microscope…………………………………..183

Figure 7.3. Manipulation of the M13 bacteriophage using an AFM tip…………………...186

Figure 7.4. AFM image of a non-annealed M13 phage-based gold nanowire……………188

Figure 7.5. AFM image of the annealed M13 phage-based gold nanowire………………189

Figure 7.6. AFM image of an annealed M13 phage-based gold nanowire using a ‘soft’ AFM tip ……………………………………..……………………………………190

Figure 7.7. AFM image of the M13G phage-based gold nanowire……………………….191

Figure 7.8. Manipulation of 10 nm GNPs using an AFM tip on a SiO_2 surface………….193

Figure 7.9. Manipulation of the MS2 bacteriophage capsid on a silica substrate……..…195

Figure 7.10. Manipulation of the MS2-PEGNPs on a silica substrate …………………196

List of Tables

Chapter 1: Introduction 1

Table 1.1- List of M13 genes, encoded proteins and their functions. Both proteins I and XI are encoded by gene I. ……………………………………..……………….14

Table 1.2 List of peptides identified using the phage display technique for binding affinity to some electronically useful materials…………….……………………………..27

Chapter 4: Fabrication of M13 Phage-Based Gold Nanowire……….........98

Table 4.1 Comparison of lattice '*d*' spacing of the polycrystalline non-annealed M13G phage-based gold nanowire with crystalline *fcc* gold………..………………….111

Table 4.2 Comparison of lattice '*d*' spacing of the thermally annealed M13G phage-based gold nanowire with the Au_2O_3…………………………………………….....121

Abbreviations

AFM	Atomic Force Microscopy
CPMV	Cowpea Mosaic Virus
EBL	Electron Beam Lithography
GNP	Gold Nanoparticles
HEPES	4-(2-hydroxyethyl)-1-piperazineethanesulfonic acid
HPLC	High-performance liquid chromatography
IC	Integrated circuit
IG	Intergenic
IPTG	Isopropyl b-D-l-thiogalactopyranoside
MWCO	Molecular weight cut-off
NEB	New England Biolabs
PCR	Polymerase Chain Reaction
PEG	Polyethylene glycol
PMMA	Poly(methyl methacrylate)
PS	Packaging signal
RF DNA	Replicative Form Deoxyribonucleic acid
QD	Quantum dot
TEOS	Tetraethoxysilane
TMV	Tobacco Mosaic Virus
TEM	Transmission Electron Microscope
VLP	Virus Like Particle
MS2-PEGNP	MS2 Phage Encapsulated Gold Nanoparticle
VEN	Virus Encapsulated Nanoparticle

Chapter 1

Introduction

1.0 Introduction

James Clerk Maxwell first proposed the idea of manoeuvring individual molecules using a device called ‘Maxwell’s demons’ in 1867 (Knott, 1911). However, he used them to explain his theory on the Second Law of Thermodynamics, rather than a method for device fabrication on a nanoscale. It was not until 1959, when the physicist Richard Feynman first came up with the idea of nanoscale device fabrication by “manipulation and control of atoms and molecules on the small scale” in his famous lecture entitled ‘*There is plenty of room at the bottom’* (Feynman, 1960). He argued that such a technology, later called Nanotechnology, was possible within the realms of physics and the natural laws. A few years later, physicists Jack Kilby and Robert Noyce separately filed patents for a novel way of making miniaturized electronic circuits called Integrated Circuits (IC); consisting mainly of semiconductor materials (Noyce, 1961; Kilby, 1964; Kilby, 1966). The introduction of IC revolutionized the electronics industry and forms the basis of a majority of the electronic devices today.

1.1 Current trends in Nanotechnology

In 1965, Intel’s co-founder, Gordon Moore, made the famous prediction that the number of transistors in an IC would double approximately every 24 months. This prediction called the Moore’s Law, has held true for the past four decades, resulting in miniaturization of electronics devices coupled with an improvement in their performance and decline in manufacturing cost (Moore, 1965). This trend has been the driving force behind the tremendous growth of the electronics industry during this period. However, it is predicted that this trend will increasingly face major technological and economic constraints in the future before reaching the physical limits of the device functioning at such a small scale. Optical lithography is the most widely used technique for fabricating current semiconductor based electronic devices. The wavelength of the light used for patterning features on the silicon dioxide surface during lithography determines their size. The ability to reduce the wavelength of the light used for lithography has been the major reason behind the success of Moore’s Law until now. However, it is agreed that any further reduction in the wavelength would not only require major technological and engineering challenges to be overcome, but also necessitate the use of new materials to achieve similar electrical characteristics of the device (Khan *et al.,* 2018).

Alternatives to photon-based lithography are Electron Beam Lithography (EBL) and X-ray Proximity Lithography. EBL is used to create features of 10 nm or less using a highly focused beam of electrons (Altissimo, 2010). However, the current EBL systems are based on a scan based write process using a single electron beam, making the process too slow to be used in high throughput nano-fabrication technologies (Tseng *et al.*, 2003). Other techniques using the Scanning Tunneling Microscope (STM) and the Atomic Force Microscope (AFM) have been used for manipulating atoms and molecules on the surface at precise locations (Tseng *et al.*, 2005). However, both these techniques are too slow to be used for the mass production of electronic devices in the foreseeable future.

In all the techniques discussed above, the electronic devices were fabricated using ‘top-down’ approaches by adding and removing material on a silicon wafer in order to obtain micro or nanoscale structures to make the device. An alternative approach is self-assembly from the ‘bottom-up’ whereby higher order structures are assembled from nanostructures.

1.2 Bionanotechnology

Self-assembly is observed throughout nature to form the structural and functional components of the biological entity. Motor proteins are molecular motors that can move along the cytoplasm of cells by converting chemical energy into mechanical energy (Schliwa, 2003). They are the driving force behind most of the active transport of proteins and vesicles within cells. The muscle protein myosin moves on actin filaments and is responsible for the contraction of the muscle fibers in animals. Kinesin and dyneins transport cargo inside the cell and use microtubules as tracks. The conformational change in the globular motor domain is the mechanism behind the movement observed in all three motor proteins.

Ribosome is another molecular machine, found in all living cells and is responsible for biological protein synthesis as per the instructions coded in the messenger RNA. It is a protein and a RNA complex comprising of two major components (Ramakrishnan, 2002). The smaller subunit is the site of mRNA binding and decoding while the larger subunit is where the amino acids join to form a polypeptide chain. These complex biological machines self-assemble in ambient conditions using the biomolecules produced by the genetic code. The fact that this process is reproducible and can be programmed by changing the genetic code makes them attractive for nanotechnology applications.

Nature also makes a vast variety of structural components using the same principles of self-assembly and molecular recognition and can have contrasting mechanical properties such as wood, membrane, skin etc. Although, most of these structures are carbon-based nature is also capable of forming inorganic structural motifs.

1.3 Biomineralization

Biomineralization is the process by which organisms build inorganic structures in and around their bodies as protective shells (skull, abalone shell), weapons (teeth) and sensors (magnetotactic bacteria) (Blakemore, 1975). The early evidence of biomineralization was observed in prokaryotes and stromatolites from about 3500 million years ago in the form of fossils (Awramik, 1992). With the evolution of biomineralization, many multicellular organisms began to produce mineralized skeletal structures, 540 million years ago (Sigel *et al.*, 2008).

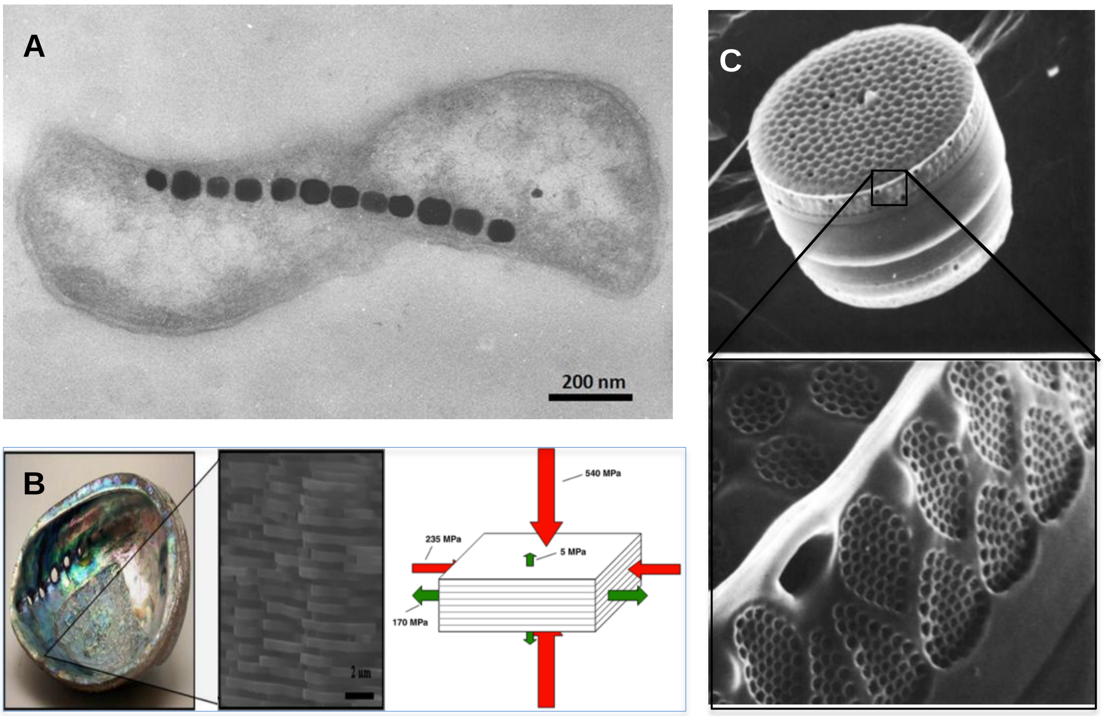

Figure 1.1. **Examples of bio-mineralization found in nature**. (**A)** shows the TEM image of biomineralized iron nanoparticles in magnetotactic bacteria (taken from Chen, 2010). (**B)** shows an abalone shell (left) and the magnified SEM image of a section of the shell (middle). Compressive and tensile strength of the shell under different loading directions is shown on the right (taken from Chen, 2008). **(C)** shows the SEM image of a diatom showing a two-valve construction of the cell wall (top) and the magnified image at the bottom shows the intricate structures of the valves (taken from Robinson, 1987).

Today members of all five kingdoms of life, exhibit biomineralization in some form. Magnetotactic bacteria produce single-domain magnetite (Fe_3O_4) nanoparticles about 35-120 nm (Figure 1.1 **A**). The linear arrangement of these magnetic nanoparticles acts as a motile compass needle and allows the organisms to orient themselves within the Earth's geomagnetic field and swim across water to oxygen-poor sediments (Chen, 2010). Mollusks build their shells out of calcium carbonate by depositing two distinct polymorphs of calcium carbonate, calcite and aragonite in separate layers (Figure 1.1 **B**). The compressive strength when loading is applied perpendicular to the shell is greater than that applied parallel to the shell. Vast strength anisotropy is also observed perpendicular to the shell (5 MPa vs. 540 MPa). This indicates that the minerals in each of these layers are deposited in a specific orientation, size and shape. This imparts the mollusk shell strength and superior mechanical properties not seen in naturally occurring minerals of $CaCO_3$ (Chen, 2008). Single cell diatoms biomineralize silica to form a siliceous cell wall which is comprised of two siliceous valves along with an organic component (Figure 1.3 **C**). Silicon is transported to the cell as silicic acid wherefrom insoluble silicon is formed from soluble precursors (Robinson, 1987).

1.3.1 Specific biomineralization of metals and semiconductors

It has been established that proteins act as nucleators, growth modifiers or scaffolds for mineral formation in almost all the observed biomineralization processes (Wang, 2013). In principle, these proteins can be used for material synthesis *in vitro* by controlled biomineralization. But only a limited variety of materials undergo biomineralization in nature such as calcium, iron, silica etc. Most of these materials do not have the desirable electrical properties for the fabrication of electronic devices. Biomineralization of electronically useful materials such as GaAs, CdSe etc. has not yet been observed in nature. Hence, most of the naturally occurring proteins used for the biomineralization process are not of much use in electronic device fabrication. But they can be imbued with electronic properties by nucleation and growth of inorganic material on their surface using the principles of biomineralization observed in nature.

The exact mechanism of specific binding of polypeptides to a metal is not yet fully understood; hence rational design of such metal-binding peptides has not yet been reported. Lu (1997; 2001) outlines strategies and challenges of rationally designing metal binding sites into native protein. However, peptides, which bind to electronically useful metals or semiconductors, can be selected empirically from a large library of peptides using various peptide display technologies (Sarikaya *et al.,* 2003). Brown (1997) displayed a pool of a repeating polypeptide on the surface of the *E.coli* to identify peptide sequences with binding affinity and specificity for iron oxide. The same technique was used later to identify gold and chromium binding polypeptides (Brown *et al.,* 2000). This showed that small peptide motifs could be identified from a large library that binds specifically to inorganic surfaces.

Angela Belcher's research group used phage display to screen for peptides with binding affinity to various semiconductor surfaces (Flynn, 2003). Whaley (2000) identified GaAs, Si and InP binding peptides. Remarkably, these peptides when displayed on the viral surface protein bound specifically to a crystal composition and even to a specific crystal face. Peptides selected for (100) GaAs did not display any binding affinity for (111)B GaAs. Such highly specific AlGaS binding peptides were also reported by Goede *et al.* (2004).

1.3.2 Non-specific biomineralization of metals and semiconductors

Most of the inorganic nano or microstructures formed in nature by the process of biomineralization is due to specific recognition and binding of polypeptides to inorganic surfaces. However, polypeptides can also bind non-specifically to inorganic surfaces because of favorable charge interactions and other mechanisms. Non-specific mineralization on biological templates has been used to create electronic nanostructures. Four glutamic acid (E4) or three glutamic acid plus one glycine (E3G) or three glutamic acid plus one glutamine (E3Q) residues were displayed on the N-terminus of the major coat protein of the M13 phage by Rosant *et al.* (2012) and Oh *et al.* (2014) to precipitate Co_3O_4 on the phage surface. The same E4 motif was used by Dang (2011) to precipitate TiO_2 on the phage surface. Nuraje (2012) used the E4 peptide to mineralize bimetallic oxides nanomaterials with perovskite structures, particularly strontium titanate ($SrTiO_3$) and bismuth ferrite ($BiFeO_3$) on the phage surface. Lee (2009) made $FePO_4$ nanowires using the same E4 display. The negatively charged carboxyl group in the glutamic acid provides an ionic environment, which favours non-specific interactions with most cations in the solution.

The nucleotide bases and the backbone of the DNA molecule can be used for non-specific nucleation and growth of metal deposits. The negatively charged phosphate group can bind to cationic metal ions forming metal clusters in the presence of a suitable reducing reagent (Braun, 1997). Park (2005) used three double helical DNA bundles connected by immobile crossover junctions to produce silver nanowires using a similar strategy (Figure 1.2 **A**). Braun used λ-DNA as a template to fabricate silver nanowires by depositing silver on the DNA strands using this method (Figure 1.2 **B**).

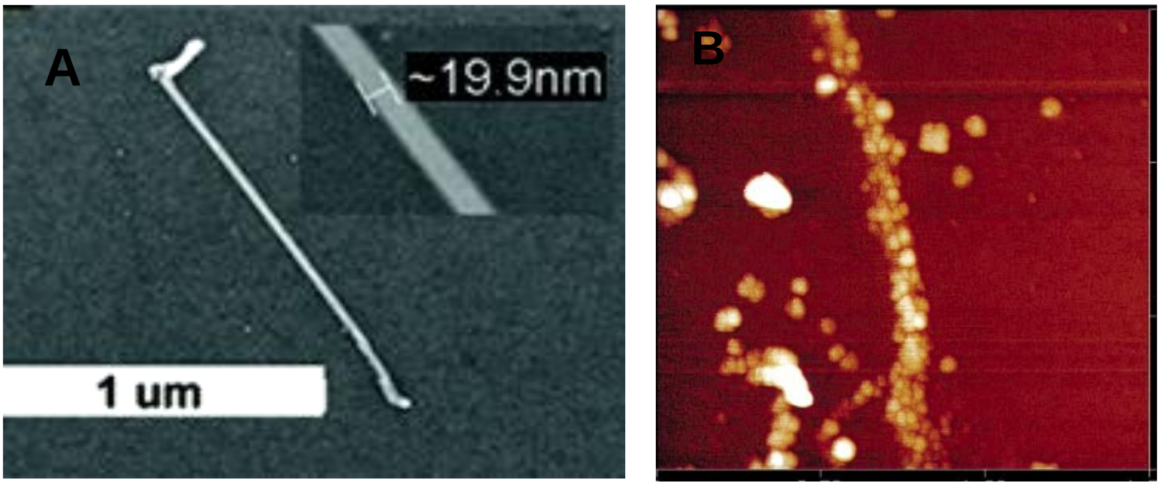

Fig 1.2. **(A)** SEM image of a silver nanowire (taken from Park, 2005) and **(B)** AFM image of a silver nanowire on a DNA scaffold. (Taken from Braun, 1998).

Torimoto (1999) used the phosphate backbone of the DNA to assemble an array of CdS semiconducting nanoparticles along the length of the DNA molecule. Yan (2003) used the DNA as a scaffold to create an array of proteins, which was metallized to form silver nanowires.

McMillan (2002) reported the assembly of ordered gold and CdSe-ZnS nanoparticles on engineered chaperonin protein templates. Peptide templated nanowires have also been fabricated using prions from *Saccharomyces cerevisiae,* which were genetically modified to display cysteine residues on their surface (Scheibel, 2003). The gold nanoparticles were covalently attached to these cysteine residues. More gold was electroless deposited on the gold nanoparticles to fabricate 100 nm wide continuous nanowires. The major limitations of such non-specific metallization of the biological template to create nanostructures are that they cannot be selectively mineralized with different materials. They also have a very limited number of sites for programmable self-assembly into higher order structures. These limitations pose several challenges in the self-assembly of such nanostructures into useful devices and limits their application in nanoelectronics. Viruses as scaffolds can display multiple peptides on their surface for material specific mineralization and complex assembly.

1.4 Virus-templated nanostructures

Viruses come in many shapes and sizes as shown in Figure 1.3. Many viruses maintain their structural integrity over a wide range of pH values and at temperatures as high as 60^{o}C (Gelderblom, 1996). They can often be purified in gram quantities using common microbiological techniques. This is a good yield for nanotechnology applications. Viral genome, made up of either DNA or RNA, is protected in a protein shell encoded by the viral genome and utilizes the host cell's machinery to replicate. Viral genomes can be engineered to modify the surface of viral particles by displaying multiple foreign peptides on the virion surface (Smith, 1985). These peptides can be used to bind inorganic surfaces and/or for further self-assembly. Their small sizes and programmable surfaces make viruses as useful scaffolds in bionanoelectronics. Further, different shapes of virus can be exploited to form various structural and functional components of a self-assembled nanaoelectronic device (Nam, 2006). The viral coat protein can also be chemically modified to bind to inorganic surfaces (Culver, 2015). Recently, viruses have attracted huge interest as scaffolds for fabricating nanoscale inorganic structures (Lomonossoff, 2011; Koudelka, 2015). However, the use of viruses as a scaffold is not a new concept. It was used in the first half of 20th century to develop the technique of negative stain for use in TEM (Horne, 1979). In one of the early attempts, the Tobacco Mosaic Virus (TMV) was used for depositing metal or semiconductors on the virion surface (Shenton, 1999). Bromley (2008) made gold nanowires using TMV as a scaffold.

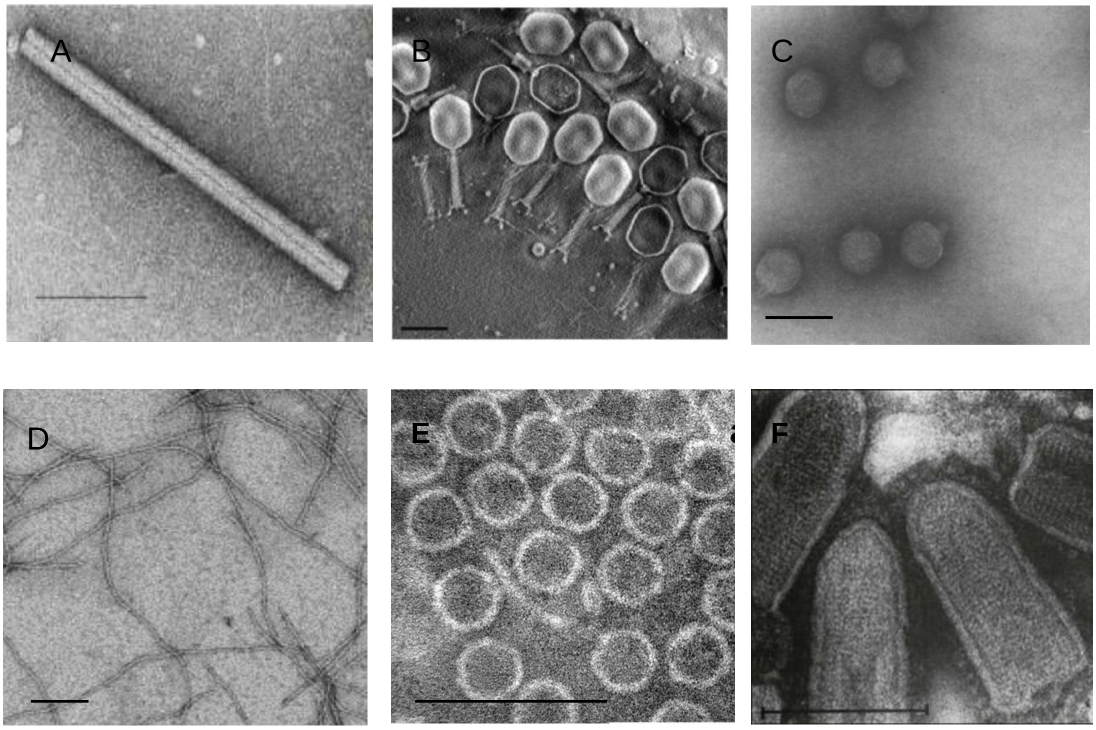

Fig 1.3. Examples of different morphology exhibited by viruses. All images are from the Transmission Electron Micrograph. **(A)** shows the helical rod-like particle of a tobacco mosaic virus (taken from Klug, 1999); **(B)** shows the lamp-shaped bacteriophage T4, with tail and fibers (taken from Danev, 2010); **(C)** shows the T7 bacteriophage with aa shorter tail (taken from Serwer, 1977); **(D)** shows the filamentous Fd bacteriophage (taken from Wang, 2006); **(E)** shows the icosahedral wild type MS2 bacteriophage (taken from Nguyen, 2011); **(F)** shows the bullet-shaped virions of the vesicular stomatitis Indiana virus (taken from Murphy, 1999). Scale bar equals 100 nm.

Because of its rod-like shape, TMV was mostly used as a scaffold to make nanowires. TMV is made of 2130 identical coat proteins, arranged in a helical pattern around a single strand of RNA to form a 300 nm long and 18 nm wide tubular structure with a 4 nm-wide inner channel. Shenton *et al.* (1999) reduced $CdCl_2$ and $Pb(NO_3)_2$ in solution with H_2S gas to get CdS and PbS nanotubes. A similar strategy was used for silica and iron oxide mineralization on the TMV surface. The biomineralization here was non-specific and can be attributed to favorable charge interactions between amino acids displayed on the TMV virion surface and metal ions or semiconductor. Negatively charged glutamate and aspartate groups are found on the surface of TMV as shown in the Figure 1.4 **(A)** and 1.4 **(B)** respectively. Positively charged metal ions binding to glutamate and aspartate residues on the virion surface explain the mineralization of CdS, PbS and iron oxide.

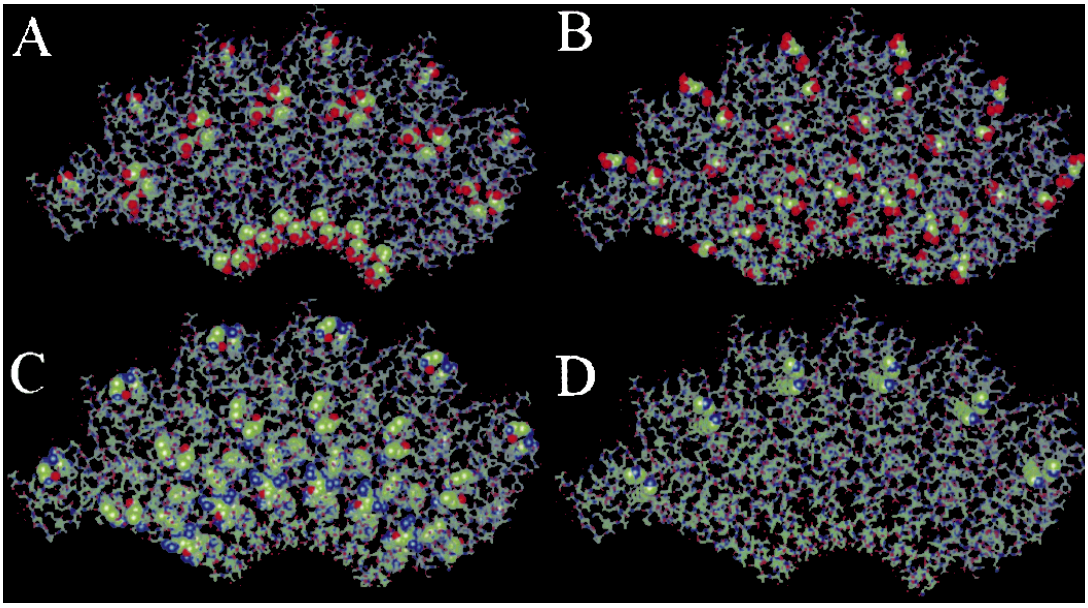

Fig 1.4 - Digital reconstruction of six TMV subunits in a wild type virion, viewed parallel to the helical axis (taken from Shenton, 1999). Amino acids of interest are highlighted using space-filling model. Red spheres correspond to negatively charged carboxyl group, while blue corresponds to positively charged amine group. The inner channel and the outer surface correspond to the bottom and top sections of each image respectively. **(A)** shows that although glutamic acid is displayed on the outer surface of virion, but the inner channel also has a high density of glutamic acid. **(B)** shows aspartic acid displayed on the virion surface. **(C)** shows the inner channel of TMV has a high density of arginine. **(D)** shows that lysine is displayed near the outer virion surface.

However, the protein surface becomes positively charged below the isoelectric point because of the presence of arginine and lysine residues on the virion surface as shown in the Figure 1.4 **(C)** and 1.4 **(D)**. As silica was mineralized from tetraethoxysilane (TEOS) in an acidic solution, strong charge interactions between the positively charged TMV particles and anionic silicate formed by the hydrolysis of TEOS caused silica to mineralize. Lee *et al.* (2005) inserted 2 cysteine residues on the outer TMV coat protein surface. As the sulfur in cysteine has a strong affinity for gold, gold nanoparticles bound to the engineered virion particles to form a gold cluster. Chemical reduction of gold in a gold salt solution resulted in the formation of gold nanowires. Wnek (2012) displayed six C-terminal histidine residues on the TMV coat protein which bound to gold nanoparticles. Further gold was electroless deposited to form a gold nanowire.

Viral surface modification has also been reported for icosahederal viruses using chemical or genetic approaches. Wang (2002) applied a chemical strategy to display biotin and fluorescein molecules on the surface of the Cowpea Mosaic Virus (CPMV) coat protein. Wang (2002) also genetically modified the CPMV coat protein to display sulfhydryl groups which bound to monomaleimido-Nanogold nanoparticles. Surface modification of CPMV was done to mineralize cobalt (Aljabali, 2011; Jaafar, 2014), FePt (Aljabali, 2010; Sachin, 2009), iron oxide (Aljabali, 2010), gold (Aljabali, 2011), nickel (Aljabali, 2010) and silica (Steinmetz, 2009).

However, the mineralization in these cases were the result of non-specific deposition of metal on the virus surface. This non-specific mineralization can limit the ability of the various coat proteins on viral surfaces to be selectively mineralized or for use in self-assembly. Alternatively, the surface coat protein of a virus can be modified to display peptides, which selectively bind to inorganic materials. As most of the viruses have more than one kind of coat protein on their surface, the different coat proteins can be genetically or chemically modified to selectively bind to inorganic or organic motifs to synthesize inorganic nanostructures. The same approach of chemical and genetic modification of virus surfaces can be used for self-assembly of virus-based nanostructures into higher order structures (Nam, 2004).

1.5 M13 bacteriophage

Filamentous phage M13 has received a lot attention in the field of virus-based nanotechnology for the fabrication of non-electric components and devices (Rakonjac, 2011). M13 is a member of the Ff (F-pilus specific) class of filamentous bacteriophages which includes phage fd and f1 (Marvin, 1963). The name Ff implies that it infects *E.coli* via a male-specific structure called the F Pilus. The three phages in the family possess 98.5% genomic identity and produce nearly identical interchangeable proteins. Hence, the replication of the viral genome is similar in all three and they share the same life-cycle processes (Clackson, 2004). The M13 genome consists of eleven closely packed genes (Table 1.1) followed by a non-coding intergenic (IG) region. This IG region also contains a 32-bp hairpin shaped packaging signal (PS) used for the encapsulation of phage DNA.

Table 1.1- List of M13 genes, encoded proteins and their functions. Both proteins I and XI are encoded by gene I. (van Wezenbeek, 1980; Russel, 1991)

Gene	**Protein name**	**Size** (amino acid)	**Size** (kDa)	**Function**
I	I	348	39.6	Assembly
	XI	108	12.4	Assembly
II	II	410	46.2	Replication
III	III	427	44.7	Capsid
IV	IV	426	45.9	Assembly/extrusion
V	V	87	9.7	Replication
VI	VI	112	12.4	Capsid
VII	VII	33	3.6	Capsid
VIII	VIII	73	7.6	Capsid
IX	IX	32	3.7	Capsid
X	X	110	12.7	Replication

The IG region also contains a signal for the initiation of DNA synthesis and termination of RNA synthesis (Dotto, 1983; Schaller, 1969; Webster, 1981). M13 phage is 6.5 nm wide but its length is determined by the size of the genome it packs. The wild-type phage has 7222 nucleotides and is approximately 900 nm long (Figure 1.5 **A**). Although, the M13 genome encodes eleven different proteins, only five coat proteins (pIII, pVI, pVII, pVIII and pIX) are used to encapsulate the ssDNA in the viral particle (Figure 1.5 **B** and **C**) (Clackson, 2004). The proteins pII, pV and pX are required for phage DNA replication while the remaining proteins pI, pIV and pXI are necessary for the assembly and secretion reactions (Rapoza, 1995; Rasched, 1986). The genome is encapsulated in a flexible capsid of approximately 2700 copies of the major coat protein, pVIII, arranged in a helical array.

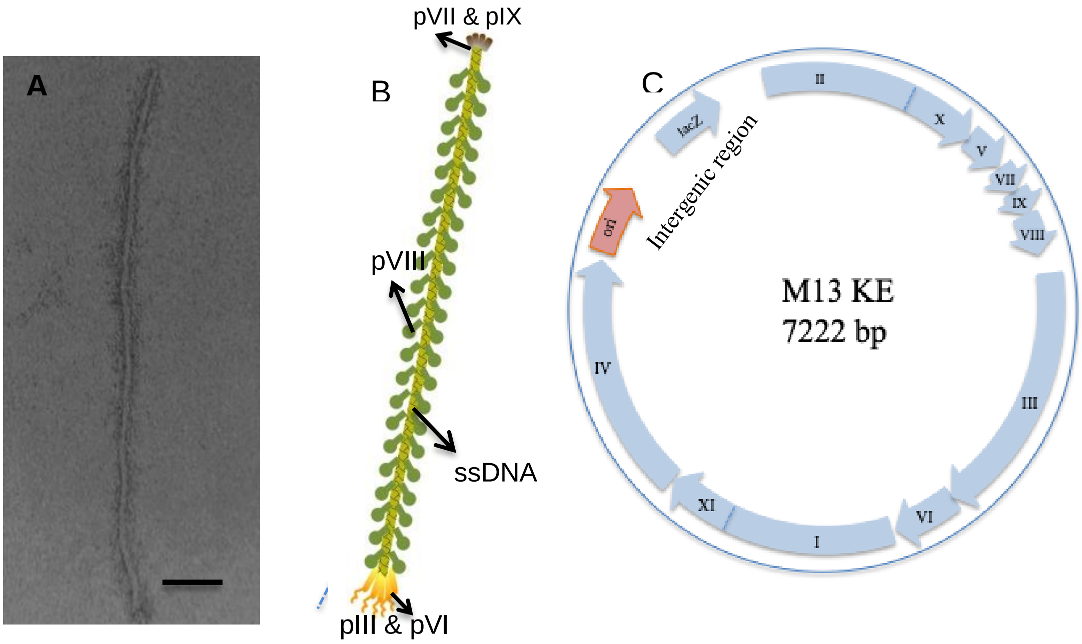

Fig 1.5. The structure of the M13 bacteriophage. (A) shows the transmission electron micrograph of the M13KE phage negatively stained with 2% (w/v) uranyl acetate. Scale bar is 100 nm. **(B)** shows a schematic of various M13 phage surface coat proteins. The major coat protein pVIII surrounds the ssDNA. **(C)** shows a schematic M13KE genome (Dotto, 1984; Zygiel, 2017).

The minor coat proteins, pIII, pVI, pVII and pIX, cap the two ends of the virion. The two ends can be distinguished under TEM, as one end appears blunt compared to the other pointed end (Figure 1.5 **A**). However, it is not always easy to differentiate (Dogic, 2006). One end of the phage is capped with five copies of minor coat proteins pIII and pVI, while the other end has five copies of proteins pIX and pVII. The M13 series of vectors contains a *lac* sequence, which is expressed as an α-complementing fragment of the β-galactosidase in the infected cells. On induction with IPTG, ß-galactosidase hydrolyzes the X-GAL to produce a characteristic blue staining of the phage plaque. This is used in the "blue-white" colour screening of mutants.

1.5.1 The major coat protein pVIII

The protein shell that surrounds the M13 ssDNA core is made up of 2700 copies of the major coat protein, pVIII. pVIII is synthesized as a 73 amino acid precursor which binds to the inner surface of the plasma membrane and is subsequently translocated across the plasma membrane as a loop structure in the presence of a transmembrane potential (Sidhu, 2001). pVIII is processed by the leader peptidase to yield a 50-residue transmembrane protein. The mature pVIII is a α- helical protein further arranged in a helical pattern, such that the α-helix of the protein is roughly parallel to the long axis of the virus (Figure 1.6 **A** and **B**) (Sidhu, 2001). The mature pVIII consists of 20 N-terminus residues, which reside in the periplasm, followed by a 19-residue hydrophobic transmembrane domain and an 11-residue long C-terminus cytoplasmic domain (Figure 1.6 **C**). The positively charged C-terminus in the cytoplasm interacts with the negatively charged phosphate backbone of the ssDNA during the phage assembly.

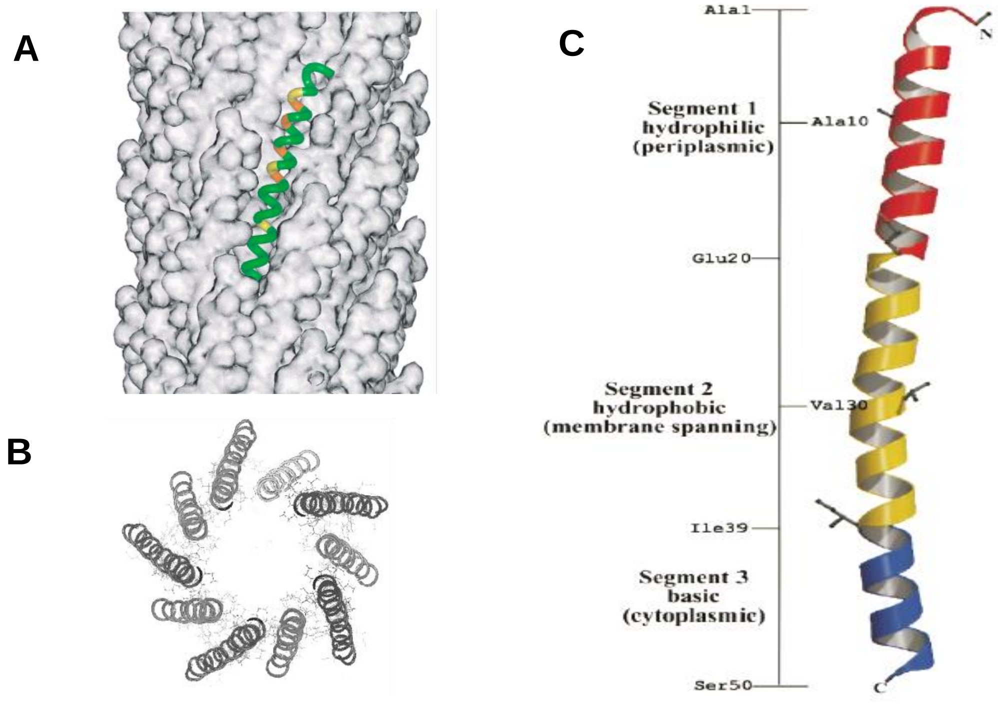

Figure 1.6. Structure of the major coat protein pVIII. (A) shows a side view of a computer-generated model showing the helical arrangement of pVIII on a M13 phage. **(B)** shows the top view of the model. **(C)** shows the three segments of the α-helical coat protein, pVIII. The N-terminus segment 1 (red - residues 1–20) forms the phage outer surface. Segment 2 (yellow - residues 21–39) is the hydrophobic core interacting with the adjacent pVIII. Segment 3 (blue - residues 40–50) interacts with the negatively charged DNA (taken from Sidhu, 2001).

The central hydrophobic domain of the adjacent pVIII provides additional stability and is necessary for the successful phage assembly. Phage particles fall apart in the presence of chloroform even though they do not contain any lipids. This further suggested that the phage particle is held together by hydrophobic forces (Roth, 2002). During the successive turns of the helix, the pVIII subunit interlocks with the subunit in the turn below and is tilted at an angle of 20^o to the long axis of the virus. They can be visualized as overlapping one another like the scales on a fish. The pitch, μ (pVIII subunits per complete helix turn) was found to be 4.5 while p (axial rise per subunit) was 1.5 nm (McDonnell, 1993).

1.5.2 The minor coat protein pIII

The minor coat protein, pIII, is synthesized as a precursor and processed to form a mature coat protein. The mature pIII consists of 406 residues, forming three domains separated by glycine rich repeats (Figure 1.7 **A** and **B**) (Van Wezenbeek, 1979). While the other coat proteins are mostly hydrophobic, pIII has a large hydrophilic domain (Beck, 1978). pIII can be divided into three main domains: N1, N2 and C-terminal (Figure 1.7 **B**) (Kremser, 1994; Stengele, 1990). The three domains are separated by glycine rich linker sequences, which have no defined conformation. The domains N1 and N2 near the N-terminus consist primarily of β strands with one short alpha helix in each domain (Lubowski, 1998). Crystallography and NMR spectroscopy show that the N1 and N2 domains interact to form a N1-N2 complex (Figure 1.8) (Holliger *et al.*, 1999; Lubowski, 1998). The exposed residues in this complex interact to form a central channel between the two domains, which probably acts as the binding site for the F-pilus (Lubowski, 1998; Chatellier, 1999).

The phage infection begins when the N2 domain binds to the *E.coli* F-pilus via residues located on the outer rim of N2 (Deng, 2002), causing it to retract into the *E.coli* cell (Deng, 1999). N2 undergoes a conformational change, which releases N1 from the N1-N2 complex freeing it to interact with the bacterial co-receptor protein TolA. The N1 domain binds to TolA, forming a complex with two other transmembrane proteins, TolQ and TolR (Webster, 1991). This results in the depolymerisation of the virus capsid, allowing the viral DNA to enter the host bacteria (Riechmann, 1997). Although, the domains N1 and N2 are exposed to the solution, the large C-terminal domain, C1 is buried within the phage particle.

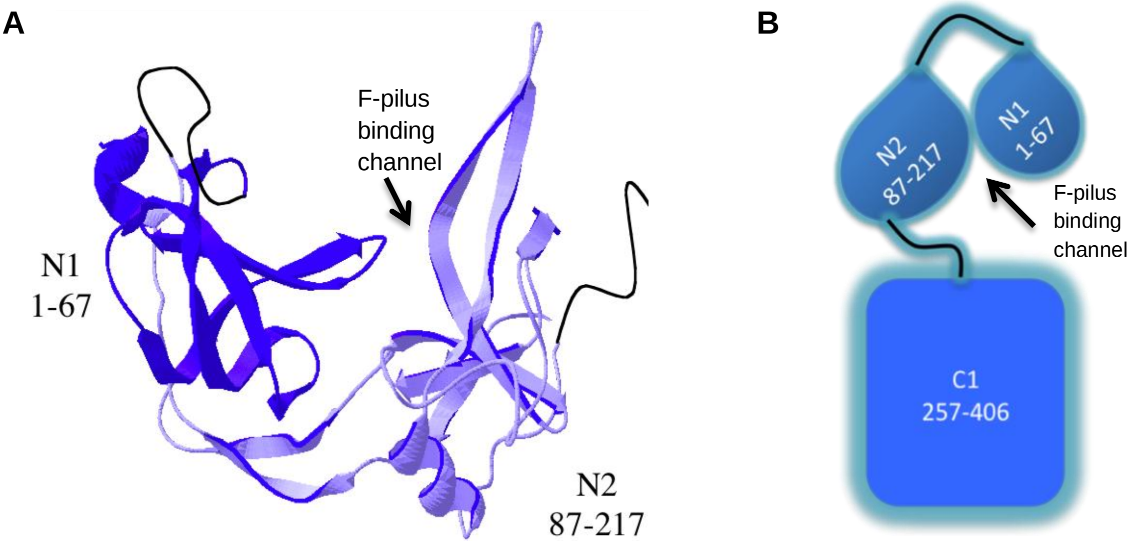

Fig 1.7. **Structure of the minor coat protein pIII. (A)** shows the domain structure of the minor coat protein, pIII near the N-terminus region, PDB code: Ig3p (Lubowski, 1998). **(B)** shows a schematic of the three main domains of pIII. The number in each domain indicates the position of amino acid residues forming the domains in the sequence. The domains are linked by repeats of natural glycine rich sequences GGGS and EGGGS indicated by the black lines joining the domains.

C1 interacts with the other minor coat protein, pVI and also plays a crucial role in the release of the phage from the cell (Rakonjac, 1999). A peptide can be inserted at the N-terminus region on the N1 domain, adjacent to the signal peptide cleavage site. M13KE genome has many restriction sites in the N-terminus region of pIII, which can be used for gene insertion (Messing, 1991).

1.5.3 The life-cycle of the M13 bacteriophage

M13 is not a lytic phage. Instead progeny phages are released continuously from infected cells as they grow and divide. Upon infection it slows down the host’s growth and forms turbid plaques on bacterial lawns. It is one of the most productive phages in nature, producing titers of up to 10^{13} pfu per mL of culture. Indeed Grieco (2009) used computer-controlled bioreactors to increase the yield by 10 times. During infection the minor coat protein, pIII binds to the *E.coli* surface protein, making way for the entry of ssDNA entry into cytoplasm (Figure 1.8). The single-stranded bacteriophage genome is converted into a double stranded circular form, called the replicative form (RF). The RF DNA then replicates and forms the template for the transcription of viral genes and progeny ssDNA. RF DNA can be extracted from *E.coli* cells like a normal plasmid DNA. Hence, the M13 phage was used as a common vector in the recombinant DNA research (Blum, 1989).

The protein, pV forms a dimer which binds to the ssDNA (Salstrom, 1971) to form a rod like structure (Gray, 1989) with a DNA hairpin packaging signal (PS) at one end. Proteins pI, pIV and pXI form a channel complex called the viral pore, along which the M13 particles pass through (Marciano, 2001). Protein, pIV assembles into a cylindrical structure within the outer cell membrane (Russel, 1991). It contains a gated channel (Marciano, 2001) running through the centre with a diameter of 8 nm (Linderoth, 1997). 5-6 copies each of pI and pXI form a complex that spans the inner membrane. After the ssDNA passes through this pore, the end is “capped” by the binding of pIII and pVI to complete the phage (Rakjonac, 1999). When the concentrations of pIII and pVI are not high enough within the *E.coli*, the phage remains tethered to the pore and more ssDNA is packaged behind it. This results in phage particles longer than the wild-type (Rakjonac, 1998). Upto 5% of such longer phage particles can be found in a phage population (Salivar, 1967). Although, the length of the phage can be manipulated by varying the size of the genome, the replication efficiency declines with increase in the genome size.

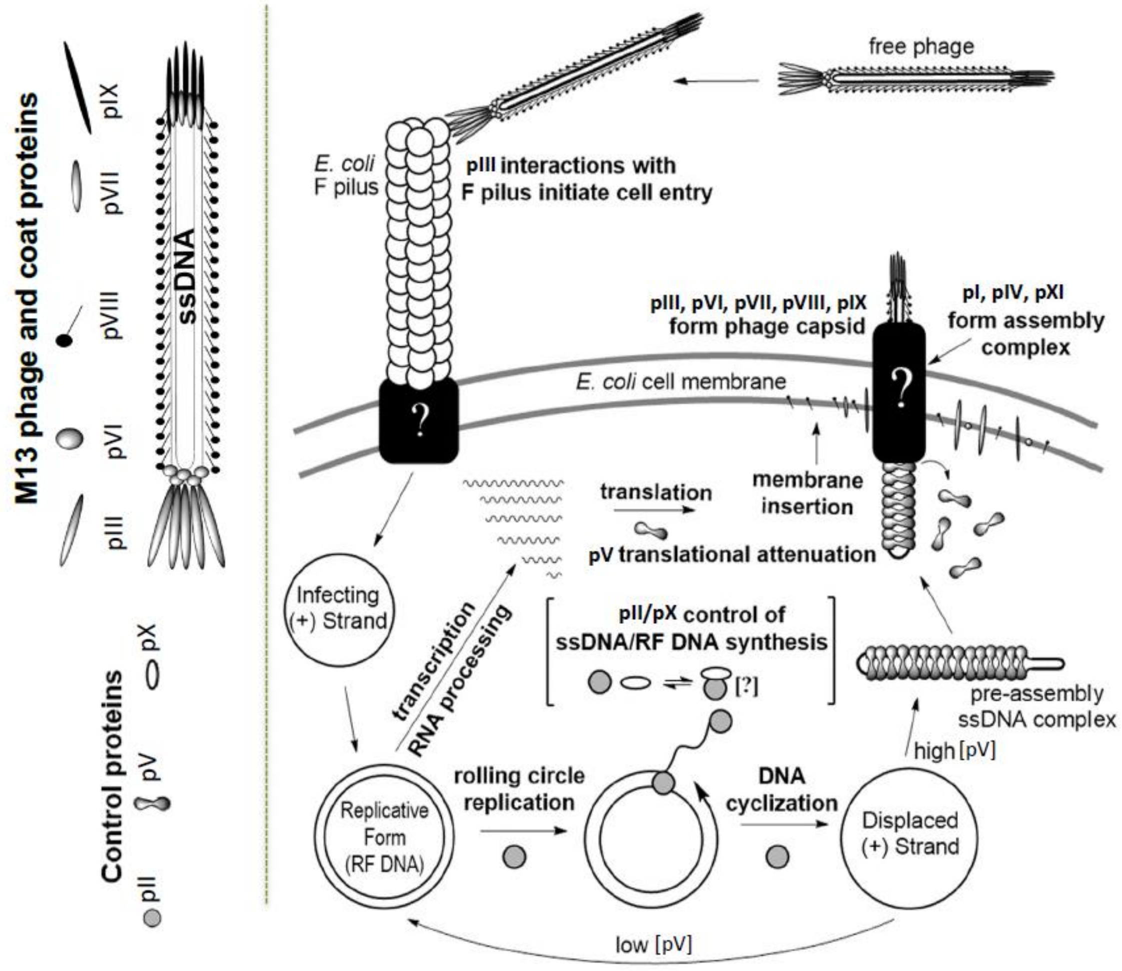

Fig 1.8. Life-cycle of the M13 bacteriophage. The image on the top left shows a schematic of the M13 phage, depicting the arrangement of coat proteins around the ssDNA genome. The image on the bottom left depicts the labels used in the scheme for the control proteins associated with the assembly and replication processes. The image on the right shows a schematic representation of the M13 bacteriophage life cycle from cell infection to release of the progeny phage. The question marks indicate the molecular interactions that are not well understood at this point (taken from Smeal, 2017).

Viruses with genome 50% longer than wild type are not easy to isolate because of their low titre.

1.6 Phage Display

Phage display is a strategy to display foreign peptides/polypeptides on the surface of bacteriophage coat proteins. This technique was first described by George P. Smith in 1985 and has been one of the primary drivers behind the advances made in the field of bionanotechnology ever since (Smith, 1985; Thota, 2017; Wu, 2016). A foreign gene is spliced into one of the coat protein genes, thereby fusing a foreign peptide to the endogenous amino acids of the coat protein to make a hybrid “fusion” protein. Thus, a decorated virus with distinct heterofunctional peptides expressed on a viral capsid is produced. M13 tolerates small insertions in the major and minor coat proteins without the loss of host infectivity. Hence, all five coat proteins can be engineered to display peptides (Gao, 1999; Hufton, 1999; McCafferty, 1990). However, pVIII and pIII are preferred for phage display (Smith, 1997; Webster, 1996). The pIII phage display can tolerate relatively large inserts, which is not observed for other coat proteins (Krebber *et al.*, 1997). Peptide inserts in pVIII can be displayed abundantly over the phage surface with up to 2700 copies of insert displayed per phage.

1.6.1 pVIII based phage display

The N-terminus of pVIII is exposed to the surface of the virion, which makes it appropriate for peptide insertion. The N-terminus region of pVIII varies slightly in closely related F-specific phages Ff (M13, fl, fd), IFI, IKe. This further suggests that pVIII tolerates insertions and mutations in this region (Marvin, 1994). However, not all insertions or mutations are equally welcome, and they can often disturb the processing of pVIII or phage assembly. Ilychiev et al. (1992) have shown that an insert, which encodes peptides similar to the amino residues on a neighboring locus in pVIII, is more likely to form viable phage particles. Insertions encoding amino acid residues differing substantially from the surface region of pVIII can disturb pVIII processing and subsequent phage assembly. Reduction in phage titre with respect to the wild-type, showed that insertion lowered the infectivity and yield of the phage particles (Chung, 2014).

The disturbance in the processing of pVIII upon insertion of peptides allowed Ilychiev to postulate that, sequences remote from the recognition site of the *E.coli* signal peptidase, also affect the processing specificity of pVIII. Weiss *et al.* (2000) incorporated artificial coat proteins in the M13 phage using a simple design based on pVIII segment properties mentioned in the Figure 1.6 (C). The C-terminus of these artificial coat proteins tolerate peptide insert unlike the natural pVIII coat protein, which works well with the N-terminus display only. Interestingly, this protein lacked any significant homology with any known protein. Thus, it was suggested that the peptide fusions do not need to be a variant of the coat protein but can be selected and evolved as per need. Such proteins can be used in a phagemid system, where artificial proteins can be incorporated along with the wild type to display peptides at C-terminus (Weiss, 2000).

Only short peptides sequences (6-8 residues long) can be displayed on each copy of pVIII due to size restrictions of the pIV-channel during assembly. Large peptide inserts in pVIII results in a non-viable phage. Larger polypeptide fragments have been displayed on pVIII using a helper phage in a phagemid system whereby the phage particle contains both the wild type and engineered pVIII proteins (Kang, 1991; McCafferty, 1990).

1.6.2 pIII based phage display

The fundamental design of a phage library has the DNA sequence encoding the peptide insert cloned into the coat protein gene of the phage DNA. This allows every copy of the coat protein to carry the peptide insert resulting in a ‘polyvalent’ display. To display a peptide insert on pIII, a DNA sequence corresponding to the peptide is inserted between the start of gene III and the signal sequence (Clackson, 2004). However, a polyvalent display is not always possible as large inserts affect the infectivity of the phage (Smith, 1988). This limitation can be overcome by using a phagemid system by cloning the peptide-encoding DNA into a bacterial plasmid that contains the *gene III* and the M13 origin of replication. However, when this plasmid is inserted into the *E.coli*, no phage particles are formed as only the modified pIII is produced by the plasmid. The phagemid and modified pIII coat proteins are “rescued” by superinfection with a helper phage that contains a defective viral origin of replication.

Thus, two kinds of pIII proteins are produced; a wild-type pIII by the helper phage and a recombinant pIII by the phagemid. As the origin of replication is defective in the helper phage, the phage produced primarily contains the phagemid DNA. The resultant phage particles produced have mostly wild-type pIII with less than one copy of the recombinant pIII protein on average (Carcamo, 1998). The pIII phage display libraries often have a short linker sequence (Gly-Gly-Gly-Ser) between the displayed peptide and pIII.

1.6.1 Biopanning

Biopanning is an *in vitro* affinity selection technique for selecting polypeptides with binding affinity to a ligand using combinatorial peptide libraries having a large number of clones (~ 10^9 - 10^{12}) each displaying a unique peptide (Clackson, 2004). The common selection method to identify the clones with the binding affinity to the presented ligand is shown in Figure 1.9.

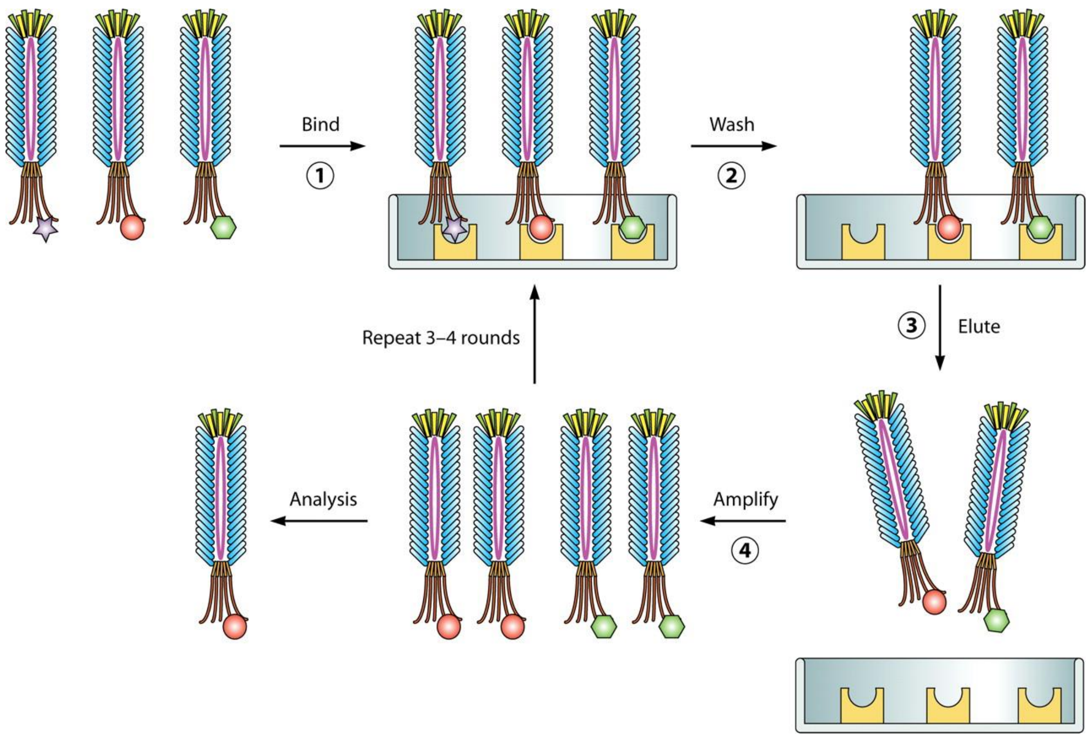

Fig 1.9. **Selection of ligand binding peptide using phage display**. Step 1 -The phage library is exposed *in vitro* to the immobilised target or surface. The phage particles with affinity for the target bind to the ligand. Step 2 - The unbound phage is washed off with a pH neutral buffer containing a small amount of a non-ionic detergent such as Tween. Step 3- In order to collect the phage bound to the immobilized ligand, it is first separated from the target by washing it with an acidic buffer to break the phage-ligand bond. Step 4- Upon infecting the *E.coli* strain with the eluted phage, their numbers amplify. These selected phages are purified and the process above is repeated 3-4 times with a more stringent elution buffer each time in order to isolate the clones with higher affinity. The DNA of the clones after the final round of selection is sequenced (taken from Huang, 2012).

However, there are some limitations to this selection method such as the chance of inherent bias in the selection of certain sequences (Bassindale, 2007). The bias may arise if the clones with high binding affinity to the target inhibit the infection or production of that phage particle. Such clones would progressively lose in the amplification step. Similarly, the low pH elution buffer used to disrupt the peptide-target interactions, may be more effective against highly basic peptides and are released more readily compared to the acidic or neutral peptides. Naik *et al* (2004) used a novel PCR based biopanning method to identify clones with stronger binding affinity to the ligand, which ironically, might not be identified using the traditional bio-panning due to their very strong binding affinity. After washing the target with the glycine-HCl buffer they heated the target to 95^{o}C for 10 minutes in water. The phage particles, bound too strongly to the target to be eluted by the glycine-HCl buffer, disassembled at high temperature and thus releasing their ssDNA genome. This ssDNA was used as a template for PCR using primers flanking the foreign insert on gene III to amplify the displayed peptide DNA sequence.

1.7 Use of M13 coat proteins in bionanotechnology

M13 is not just used for phage display but is also a useful scaffold for electronic nanostructures. This high aspect ratio of the bacteriophage makes them ideal for use as a scaffold for templated nanowires by modifying the major coat protein, pVIII (Huang, 2005). Phage display has been used to select peptide sequences against a number of electronically useful materials, some which are described in Table 1.2. These peptides often showed binding not just to the material but also to the specific crystal face of the material against which the selection was done (Goede, 2004). Peptides with affinity for different materials can be displayed on different phage coat proteins for the fabrication and assembly of nanoelectronic devices using biological scaffolds (Nam, 2004).

Table 1.2 List of peptides identified using the phage display technique for binding affinity to some electronically useful materials.

Materials	**Peptide Sequence**	**Library used**	**Reference**
Gold	VSGSSPDS	pVIII	Huang, 2005
Platinum	CDRTSTWRC	pIII	Sarikaya, 2003
Silver	CAYSSGAPPMPPFC	pIII	Naik, 2002
Palladium	CSVTQNKYC	pIII	Sarikaya, 2003
Gallium Arsenide	AQNPSDNNTHTH	pIII	Whaley, 2000
Cadmium Sulfide	CTYSRLHLC	pIII	Flynn, 2003
Zinc Sulfide	CNNPMHQNC	pIII	Flynn, 2003
Silicon oxide	TVVQTYSMVTRA	pIII	Eteshola, 2005
Titanium Oxide	ATWVSPY	pIII	Liu, 2010
Zinc Oxide	EAHVMHKVAPRPGGGSC	pIII	Umetsu, 2005
Carbon Nanotubes	HGHPYQHLLRVL	pIII	Lee, 2009
Chlorine doped polypyrrole	THRTSLDYFVI	pIII	Sanghvi, 2005

1.7.1 pVIII used in nanotechnology applications

pVIII libraries have been used to identify peptides with binding affinity to inorganic surfaces such as cobalt oxide (Nam, 2006), gold (Huang, 2005), cobalt-platinum (Lee, 2009), cadmium sulfide and zinc sulfide (Flynn, 2003). The filamentous phage arranges itself in liquid crystalline order at high concentration (Dogic, 2006; Welsh, 1996). Engineered phage particles with binding affinity to electronically active materials can thus be arranged in liquid crystalline order, which can then be used to arrange nanoparticles in liquid crystalline order. Nam *et al.* (2006) reported the fabrication of lithium ion battery electrodes using such an engineered M13 phage, genetically modified to bind to multiple inorganic surfaces (cobalt oxide and gold) (Figures 1.10 **A**, **B** and **C)**. Similarly, Chen et al. (2013) used an engineered M13 phage to fabricate a three-dimensional scaffold capable of improving both electron collection and light harvesting in dye-sensitized solar cells (Figures 1.10 **D** and **E**). Cung et al. (2013) reported fabrication of piezoelectric nanowires and devices using lead zirconate titanate (PZT) binding peptides displayed on a M13 bacteriophage. Zhang et al. (2018) fabricated virus template zinc sulfide nanofibers to be used as anodes for sodium-ion batteries. Dorval et al. (2015) fabricated a thin film solar cell using a nanoporous and continuous M13 phage bacteriophage-templated titania network. Blaik (2016) reported the design of a glucose oxidase electrode of a biofuel cell, bound covalently to GNPs that are assembled onto a genetically engineered M13 bacteriophage.

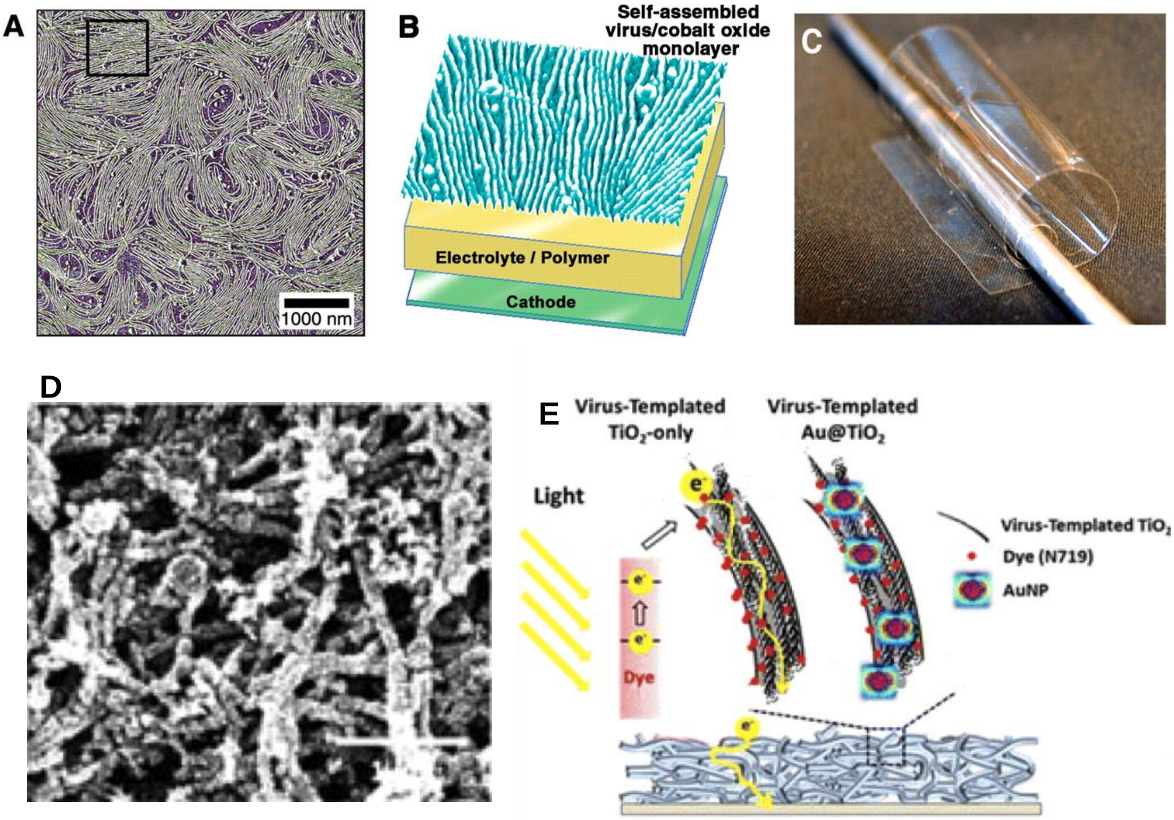

Fig 1.10 Liquid crystalline property of M13 used for device fabrication. (A) shows the AFM image of the ordering of M13 at high concentration **(B)** shows a scheme for fabricating a lithium ion battery electrode. **(C)** shows the fabricated lithium ion battery electrode as a free-standing film made from a M13 bacteriophage engineered to bind to Co_3O_4 (taken from Nam *et al.* (2006)). **(D)** shows the SEM image of the dye-sensitized solar cell electrode made using a M13 bacteriophage coated with TiO_2. **(E)** shows the structural scheme and mechanism of a dye-sensitized solar cell using M13 templated TiO_2 (taken from Chen *et al.* (2013)).

1.7.2 pIII used in nanotechnology applications.

Although, there are only five copies of pIII in a M13 phage compared to 2700 copies of pVIII, it offers the advantage of an ability to tolerate larger inserts in contrast to pVIII (Smith, 1997). Phage display using pIII has often been used to select peptides with higher affinity to a target than was observed using pVIII display (de Wilt, 2002; Speck 2011; Vrielink, 2010). However, this is not always the case as has been reported by Knez et al. (2013). Huang *et al.* (2005) made a higher order self-assembly of M13 phage particles, where two or more M13 phage particles bound to a streptavidin coated gold nanoparticle by modifying the pIII protein to bind to streptavidin. Nam *et al.* (2005) used pIII and pIX display on the same phage to create a ring-like structure. A streptavidin binding motif was displayed on pIII while a hexa histidine tag was inserted on pIX. The phage was added to a solution containing streptavidin conjugated to a nickel-nitrilotriacetic acid complex (Ni-NTA) by a linker molecule. The protein pIII bound to streptavidin while pIX bound to nickel in the Ni-NTA complex to form a ring-like structure.

1.8 Bacteriophage MS2

There are about forty RNA bacteriophages classified in the Leviviridae family, with closely related genomes (Gelderblom, 1996). They can be further classified in different groups based on their genomic similarity, serological cross-reactivity and physical properties (Witherall, 1991; Fiers, 1976). The single stranded RNA (ssRNA) bacteriophages are among the simplest and smallest known viruses. Hence, they have been used as a convenient model system to study virus structure and assembly (Koning, 2016; Rolfsson, 2016). The MS2 bacteriophage is a *T*=3 icosahederal ssRNA bacteriophage approximately 26 nm in diameter (Figure 1.11 **a** and **b)**. Its genome size is 3569 bases and has a molecular weight of 1.2 megadaltons.

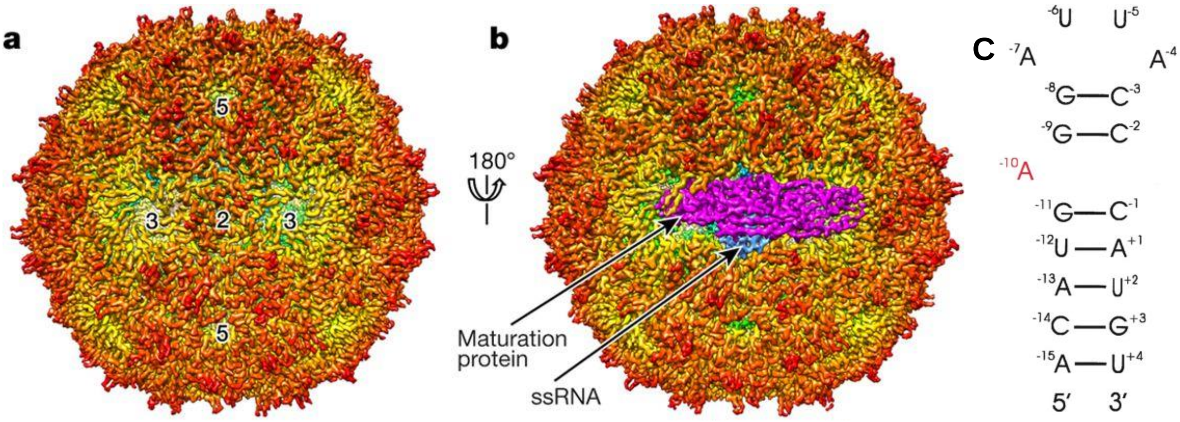

Fig 1.11. Structure of the MS2 phage. A cryoEM density map of MS2 phage at a resolution of 3.6A^{o} showing **(a)** the front view and **(b)** back view along an icosahedral two-fold symmetry axis as denoted by numeral 2. Some of the three-fold and five-fold axes are also indicated by numerals 3 and 5 respectively. The maturation protein is highlighted in magenta and the ssRNA genome inside the capsid is highlighted in blue. PDB entry 5TC1 (taken from Dai *et al.* 2017). **(c)** shows the 19 bases long TR RNA stem loop (Horn, 2006).

The MS2 bacteriophage has been used as a model to study protein-RNA interactions (Stockley *et al.*, 1995), virus structure (Valegard *et al.*, 1994), assembly (Twarock *et al.*, 2018) and their applications (Wu *et al.*, 2005). Most ssRNA viruses encode high-affinity coat protein binding sites in their RNA sequences that are considered to be virus assembly initiation sites. They have a defined secondary structure, which is specifically recognized by the viral coat proteins. 19- nucleotide long translational repressor (TR) stem loop is perhaps the most studied of all in the MS2 genome (Figure 1.11 **c**). It acts as a translational operator for the replicase cistron. *In vitro* assembly of the MS2 capsid can be triggered by the addition of a TR stem loop to the coat protein dimers in solution (Wu, 1988). Although, the TR operator is not compulsory for the assembly of the MS2 capsid. The capsid assembly can be initiated by many non-specific RNA stem loops (Stockley *et al.*, 2016). The capsid can also assemble in the absence of any RNA at high concentrations of coat protein dimers (Rohrmann, 1970).

The coat protein of the MS2 capsid also tolerates foreign peptide inserts (up to 24 amino acids) in the loop that protrudes from the capsid surface, while retaining the capsid ability to assemble *in-vitro* (Mastico, 1993). The genome within the capsid is tightly packed as two concentric icosahederal shells of RNA (Toropova, 2008). The inside of the capsid is hydrophilic and interacts with the RNA via hydrogen bonding.

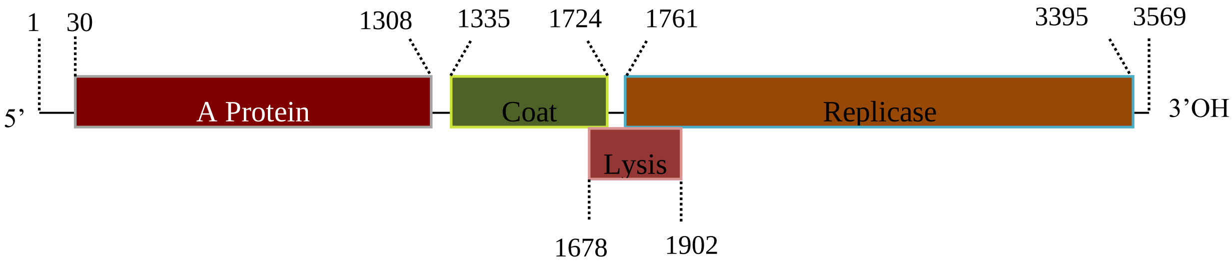

Fig 1.12. Genetic Map of MS2 bactriophage. (Kastelein et al., 1982, Fiers et al., 1976)

Thus, the MS2 genome encodes four different proteins (Figure 1.12), only two are incorporated in the MS2 capsid. The mature phage contains 180 copies of coat protein (MW - 13.7 kDa) and one copy of a maturation protein (MW - 43 kDa). The other two proteins are a replicase subunit and a lysis protein, which is produced late in the infection to facilitate the release of the virus from the host cell. MS2 coat proteins form non-covalent dimers that can be isolated by dissociating the capsid in mild acidic conditions. Small pores of 16 Å diameter exists at the five-fold and three-fold axes, which can be used to soak small molecules into the empty MS2 capsid without dissociating the capsid shell. RNA binds sequence-specifically to the coat protein dimer causing an allosteric conformational switch, as was shown by NMR studies (Stockley *et al.*, 2007). Two different coat protein dimers can be formed from the same coat protein because of the different conformation of the F-G loop (Figure 1.13). In the A/B dimer one F-G loop is extended while the other is bent back, while for the C/C dimer both the loops are extended. There are 60 units of A/B dimer while 30 units of C/C dimer in a capsid (Valegard, 1994).

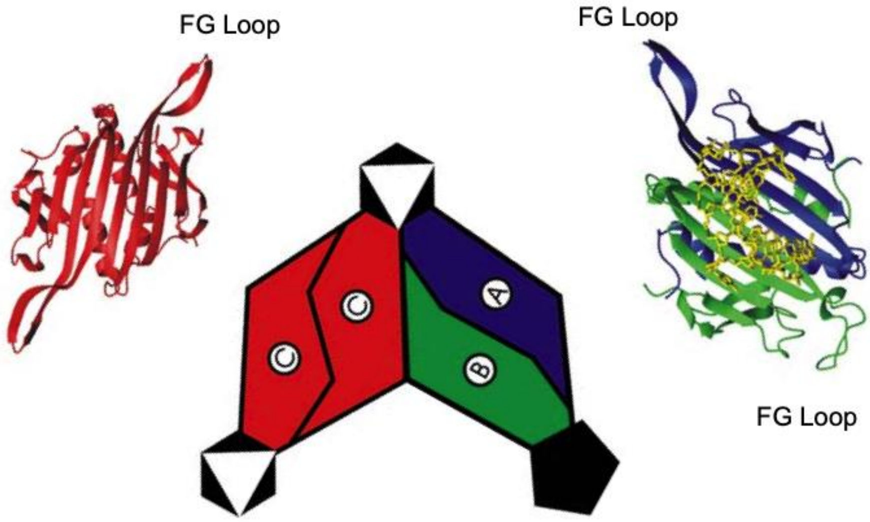

Figure 1.13. Structure of MS2 phage coat protein dimers. The ribbon model on the left corresponds to the structure of the CC dimer (red) while the ribbon model on the right (blue/green) show the structure of the A/B dimer bound to TR RNA. The diagram in the middle depicts their relationship within the capsid whereby the black and white symbols show the distribution of the symmetry axis on the phage surface. (taken from Stockley *et al.*, 2007)

The Tullman-Ercek group reported a point mutation in the MS2 coat protein that changed the MS2 VLP icosahedral supramolecular structure from a T = 3 capsid of 27 nm diameter to a T = 1 capsid of approximately 17 nm diameter consisting of 12 pentamers (Asensio, 2016). However, the reason behind this mutation was not based on a rational design. They recently developed a fitness landscape model to predict ways in which systematic point mutations can alter the resulting self-assembly competency (Hartman, 2018).

1.8.1 The life-cycle of MS2

The MS2 phage infects the *E.coli* by binding to the bacterial *F pilus* via the maturation protein. The maturation protein and the phage genomic RNA then enters the cell through the central channel of the pilus. The exact mechanism of this transfer is not understood completely. The MS2 coat protein exists mainly as dimers in solution and recognizes an RNA hairpin (TR operator) at the start of the replicase gene (van Duin, 2006). It binds to the TR stem loop and shuts off the replicase gene early in the infection cycle, and thus acts as a translational repressor of the replicase gene. A high concentration of replicase is poisonous to the host. The lysis protein gene is initiated by ribosomes only when they complete the translation of the coat protein gene. The binding of the maturation protein to the MS2 RNA most likely initiates the formation of the virion. The lysis protein forms pores in the bacterial cell wall, causing a loss of membrane potential and subsequent breakdown of the cell wall. Upon accumulation of the lysis protein bacterial lysis occurs with the release of newly formed virions (van Duin, 2006).

1.9 Synthetic viruses

Recently synthetic strategies to construct viral capsid-like structures by mimicking the self- assembly of viral capsids have gained a lot attention. β-sheet-forming peptides, coiled-coil-forming peptides and trigonal peptide conjugates were designed to construct synthetic virus-like structures. Edwardson (2018) designed a de novo protein cage and loaded siRNA in it for cellular uptake and subsequent release to induce the RNAi to knock down the gene expression. Noble (2016) reported the *de novo* fabrication of the smallest artificial virus-like structure, 12 nm in diameter, using self-complementary helical coiled-coil subunits which self-pair by hydrophobic interface and have three interfacial facets.

Sasaki (2017) mutated four residues on the enzyme lumazine synthase from the bacterium *Aquifex aeolicus* (AaLS) to negatively charged glutamates. The resulting engineered protein self-assembled into a virus-like capsid and encapsulated proteins with complementary positive charge. However, such encapsulation was via complementary electrostatic interactions and was not sequence selective. To overcome this the Hilvert group reengineered AaLs to make a synthetic capsid that selectively encapsulated its own full-length RNA genome *in vivo* (Terasaka, 2018).

1.10 Molecular transistor and bottom-up fabrication of nanoelectronic devices

A transistor is the one of the basic building blocks of all electronic devices. It regulates the flow of current or voltage and acts as a switch or gate for electronic signals. A basic transistor switch has two states: on and off, which corresponds to binary 1 and 0 in computer programming. A basic scheme of a molecular transistor is described in Figure 1.14. It has three metal electrodes (source, drain and gate) surrounding an island of metal or semiconductor nanoparticle. The gate electrode voltage controls the flow of electrons from the source to the drain as changing it can alter the energy state of the island. Thus, an electron from the source can "hop" to the island by applying a suitable voltage across the gate electrode. The electron can be made to "hop" again from the island to the drain by changing the gate potential.

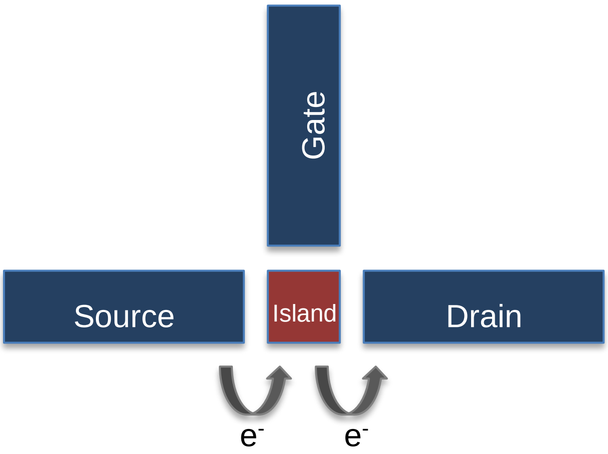

Figure 1.14. A diagram showing the basic layout of the molecular transistor. Altering the gate electrode voltage can regulate the flow of electrons from the source to the drain.

Fabrication of a molecular transistor using quantum dots, carbon nanotubes and nanowire junctions has been reported (Hayakawa, 2017; Kouwenhoven, 1997; Postma, 2001; Mirza, 2017). However, self-assembly of such a molecular transistor using molecular recognition with potential for further assembly into devices has not yet been reported. Such self-assembled devices are likely to have nanowires, quantum dots and quantum wells as their components. Such components have been developed using various techniques *viz.* chemical and biological templating (Flynn, 2003; Chen, 2006)). However, the assembly of these components into useful devices has met with little success. The nanowires and quantum dots produced using lithography or chemical methods do not carry the rich chemical information as found in biological structures and hence their self-assembly has not been widely reported yet.

The work described in this thesis focuses on genetically programming the M13 bacteriophage to bind to gold nanoparticles and self-assemble around a MS2 bacteriophage encapsulating nanoparticle, which should act as the island of the molecular transistor as shown in Figure 1.15. Further gold can be deposited on the M13 scaffold to make gold electrodes.

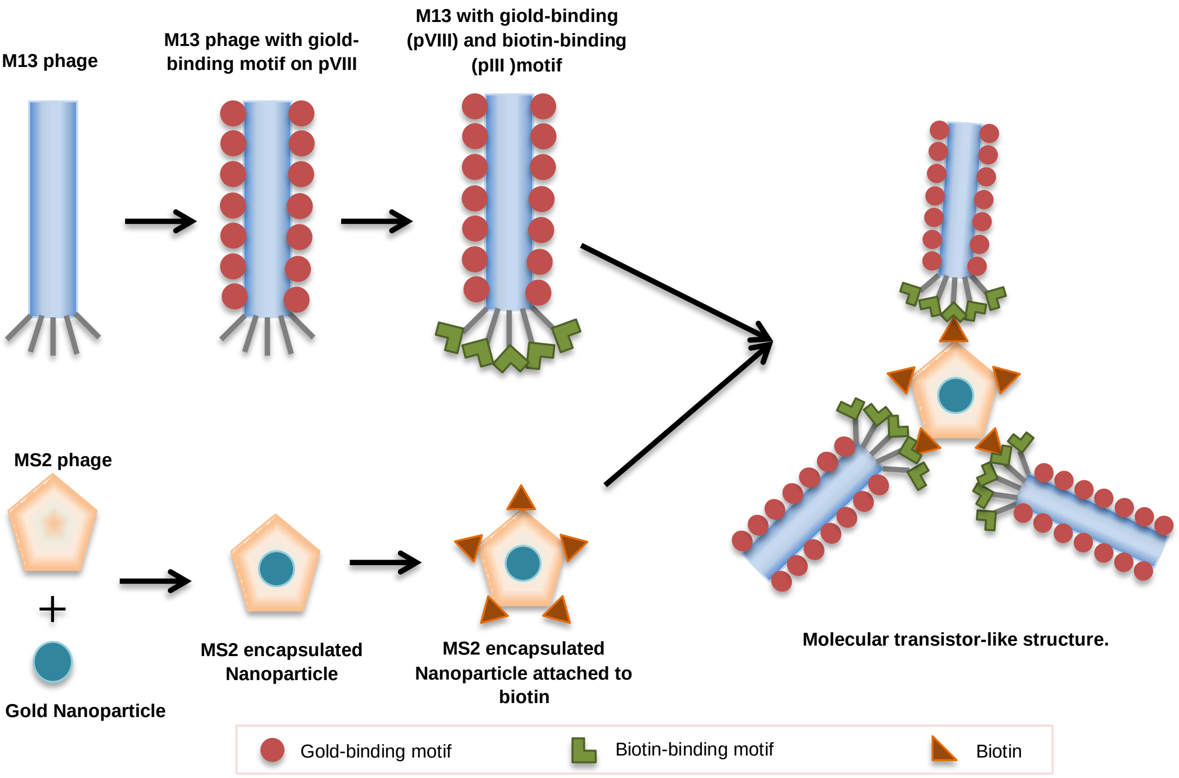

Figure 1.15. **Schematic of the fabrication of the proposed self-assembling molecular transistor**. The scheme shows the steps in the fabrication of a molecular transistor-like structure using a bacteriophage template.

The coat protein encapsulating the nanoparticle in a MS2 bacteriophage can be ‘burnt off’ to form the ‘tunneling gap’ between the electrodes and the island in the molecular transistor.

1.11 Aim and scope of the work in this thesis

The ultimate goal of the research done in this thesis was to fabricate a self-assembled molecular transistor-like structure from virus-templated nanostructures. Filamentous bacteriophage M13 was selected as the template for the fabrication of gold nanowires. Icosahederal MS2 bacteriophage was selected as the scaffold to form the island of the molecular transistor. The work described in Chapter 3 looks at the creation of a M13 bacteriophage with gold-binding peptides displayed on its major coat protein, pVIII and biotin-binding peptide on its minor coat protein, pIII. The work described in Chapter 4 looks at the synthesis of gold nanowires using an engineered phage and its physical characterization before and after annealing the nanowire at high temperatures. Chapter 5 describes the electrical characterization of the phage-templated gold nanowires. While the work described in Chapter 6 looks into the encapsulation of the gold nanoparticle inside a MS2 phage. Further chemistry on the gold nanoparticles using the pores on a MS2 surface is also discussed. Finally, Chapter 7 looks into a different top down approach of fabricating nano electronic devices by manipulating the phage templated nanostructures using an Atomic Force Microscope tip.

Chapter 2

Materials and methods

2.1 Materials

2.1.1 General reagents

The chemicals used for preparing media and gels for the molecular biology research were purchased from Sigma-Aldrich (St. Louis, MO, U.S.A.) unless stated otherwise. The DNA and RNA primers were purchased from MWG-Biotech (Ebersberg, Germany). The gold nanoparticles were purchased from Ted Pella (California, U.S.A) unless stated otherwise.

2.1.2 Antibiotic solution

The antibiotic solutions were made at 1000x stock concentration and filtered through a 0.2 micron filter and stored at -20^{o}C.

Kanamycin B sulfate: Stock concentration - 50 mg/mL in distilled water. Working concentration: 50 µg/mL. It inhibits translocation and elicits miscoding by binding to the 70S ribosomal subunit.

Tetracycline hydrochloride: Stock concentration - 10 mg/mL in 70% (v/v) ethanol. Working concentration: 10 µg/mL. It works by preventing the binding of aminoacyl-tRNA to the 30S subunit, thus inhibiting protein synthesis.

2.1.3 Media recipes

All media recipes are stated for a total volume of 1 litre unless is dictated otherwise.

2.1.3.1 2xYT medium

The following ingredients were added to 900 mL of distilled water:

- 16 g tryptone,
- 10 g yeast extract and
- 5 g NaCl.

The ingredients were dissolved. The pH was adjusted to 7.4 with 5 M NaOH. Distilled water was added to adjust the final volume to 1 litre. The medium was then autoclaved.

2.1.3.2 Agarose top

The following ingredients were added to 900 mL of distilled water:

- 10 g tryptone,
- 5 g yeast extract,
- 5 g NaCl,
- 1 g $MgCl_2.6H_2O$ (magnesium chloride hexahydrate) and
- 7 g agarose.

The ingredients were dissolved. The pH was adjusted to 7.4 with 5 M NaOH. Distilled water was added until the volume was 1 L. The medium was autoclaved after dispensing the mixture in 100 mL bottles to get 70 mL aliquot.

2.1.3.3 Agar

The following ingredients were added to 900 mL of distilled water:

- 16 g tryptone,
- 10 g yeast extract,

- 5 g NaCl and
- 15 g agar.

The ingredients were mixed until the powder had dissolved. The pH was adjusted to 7.4 with 5 N NaOH. Distilled water was added to adjust the final volume to 1 litre. The medium was then autoclaved. Agar was then allowed to cool to approximately 50°C before the antibiotic was added.

2.1.4 Buffers and reagents

2.1.4.1 Phosphate buffered saline (PBS)

PBS tablets (Dulbecco A) were obtained from Oxoid, part of Thermo Fisher Scientific (Cat. No. BR0014G). One tablet was used per 100 mL of distilled water.

Typical formula for 1 litre of PBS buffer is:

- 8 g NaCl,
- 0.2 g potassium chloride,
- 1.15 g di-sodium hydrogen phosphate and
- 0.2 g potassium dihydrogen phosphate.

PBS solution made using these tablets had pH 7.4. The buffer was finally autoclaved.

2.1.4.2 Tris-HCl buffer

To 900 mL of distilled water the following were added:

- 20 mL Trizma-HCl (Catalogue No. T3253) and

- 29.22 g NaCl.

The final volume was adjusted to 1 L with distilled water and the buffer was sterilised by passing the solution thorough 0.2 µm filter.

2.1.4.3 20% (w/v) polyethylene glycol (PEG) in 2.5 M NaCl solution

To 1 L of distilled water following were added:

- 200 g PEG (Sigma-Aldrich, Catalogue No. P5413) and
- 146.1 g NaCl.

The solution was then autoclaved and allowed to cool. To prevent the formation of separate layers, the PEG/NaCl solution must be mixed every 10 minutes or so while it is cooling down. A white cloudy solution was formed, but eventually it cooled to a point where the solution suddenly becomes clear upon mixing.

2.1.4.4 Protein loading buffer (Stock concentration – 2x) (LaemmLi buffer)

To make 5 mL of the protein loading buffer the following were added:

- 0.625 µL 1 M Tris-HCl, pH 6.8 (0.125 M),
- 2 mL of 10% SDS (Final conc. - 4%),
- 1 mL glycerol (Final conc. - 20%),
- 0.5 mL 2-mercaptoethanol and
- 1 mg bromophenol blue.

Distilled water was added to adjust the final volume to 5 mL and the solution was stored at 4^{o}C.

2.1.4.5 Glycine running buffer (Stock concentration – 10x)

To 1 L of distilled water the following were added:

- 10 g sodium dodecyl sulfate (SDS),
- 30.3 g Tris-base and
- 144.1 g glycine.

Distilled water was added to adjust the final volume to 1 L and the solution was stored at room temperature. 100 mL of 10x glycine buffer was added to 900 mL of distilled water to make the 1x glycine running buffer.

2.1.4.6 Coomassie blue staining solution

To 1 L of distilled water the following were added:

- 2.5 g Coomassie brilliant blue R-250 (Cat. No. B8647),
- 450 mL methanol and
- 100 mL acetic acid.

Distilled water was added to make the final volume to 1 L and the solution was stored at room temperature.

2.1.4.7 De-stain solution

To 1 L of distilled water the following were added:

- 450 mL methanol and
- 100 mL acetic acid.

Distilled water was added to adjust the final volume to 1 L and the solution was then stored at room temperature.

2.1.4.8 λ buffer for linear sucrose gradients (stock concentration – 10x)

To 1 L of distilled water the following were added:

- 24.5 g HEPES (4-(2-hydroxyethyl)-1-piperazineethanesulfonic acid) and
- 58.44 g NaCl

After the powder was dissolved, distilled water was added to make the final volume to 1 L and the solution was then sterilised by passing it thorough a 0.2 µm filter.

For linear sucrose density gradients: 25 mL of the 10x λ buffer was added to 1 mL of 0.25 M EDTA (ethylenediaminetetraacetic acid) and made up to 250 mL with distilled water. The final concentrations of the 1x λ buffer were as follows: 100 mM HEPES, 1 M NaCl and 1.25 mM EDTA.

2.1.5 Nucleic acid primers and sequencing

All primers were obtained by High Purity Salt Free purification and were sourced from MWG-Biotech (Ebersberg, Germany). DNA sequencing was carried by the Sequencing Service at Dundee University, U. K. or GATC Biotech Ltd (Cambridge, U.K.).

2.1.6 Enzymes

All restriction enzymes, DNA polymerase and Shrimp Alkaline Phosphatase were purchased from New England Biolabs (Hitchin, U.K.).

2.1.7 Bacterial strains

All of the bacterial strains described below have F-pilus expression linked to the tetracycline resistance. In the presence of tetracycline, it results in a high expression of F-pili, which is needed for M13 infection.

E.coli K12 ER2738 was obtained from New England Biolabs, (Hitchin, U.K.)

XL1-Blue supercompetent cells was obtained from Stratagene (La Jolla, Calafornia, U.S.A.)

2.2 General Methods

2.2.1 Protein and DNA gel electrophoresis

2.2.1.1 1% and 2% agarose gel electrophoresis

Gel Preparation**:** 0.5 g (1%) or 1 g (2%) agarose was mixed with 50 mL of 1x TBS buffer and the solution was heated in a microwave oven for 15 seconds or until all the agarose had melted. The molten agarose was allowed to cool to approximately 60^{o}C. Ethidium bromide (10 mg/ml) was then added to the molten agarose in the ratio of 0.05 µl/mL of the total gel volume. The gel was then poured in a tank with a comb to act as wells and was allowed to set.

Gel Electrophoresis – 5-20 µL of the sample was thoroughly mixed with 1-3 µL of 6x gel loading buffer and loaded into the well along with a suitable DNA or protein ladder (Figure 2.1). The gels were run using a Consort E832 power pack in a 1x TBS buffer at 100 V for approximately an hour or until the loading dye had migrated to 4/5th of the distance of the gel.

Gel Visualization – The gel was washed with distilled water and pat-dried with clean paper tissue. It was then placed under UV or fluorescent light to visualize the bands. An image of the gel was taken using the Syngene Documentation System (Cambridge, UK) gel documentation system.

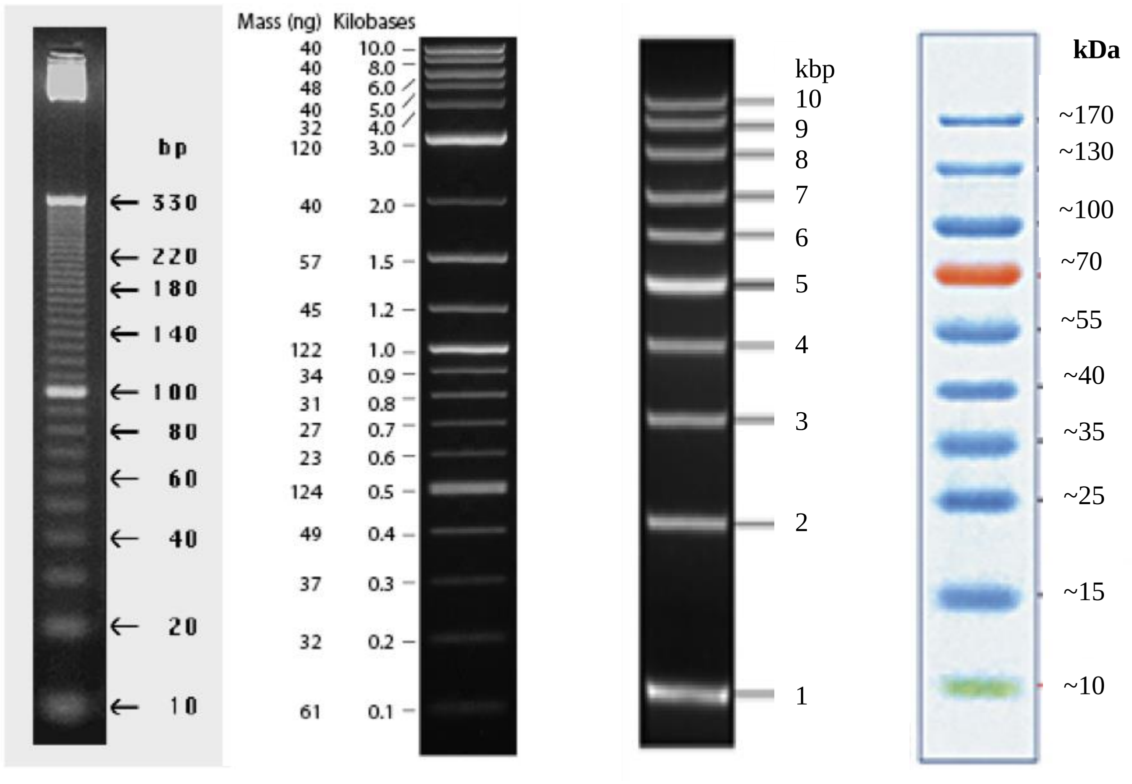

(A) **(B)** **(C)** **(D)**

Fig 2.1 DNA and protein ladders used for gel electrophoresis. All images were taken from the respective product brochure. **(A)** shows a 10 bp ladder (taken from Invitrogen), run on a 4 % low melting point agarose gel in Tris-acetate (pH 7.6). **(B)** shows a 2-log ladder (taken from New England Biolabs), run on a 1% (w/v) agarose gel in TBE buffer. 1 µL of the ladder in the well equals 1 µg of the total DNA. **(C)** 1 Kb DNA ladder (taken from New England Biolabs), run on a 0.6% (w/v) agarose gel. **(D)** PageRuler™ pre-stained protein ladder (taken from Fermentas), run on a 4-20% (w/v) Tris-glycine SDS-PAGE gel.

2.2.1.2 Native polyacrylamide gel electrophoresis (PAGE):

8% (w/v) polyacrylamide gel was prepared according to the following recipe

- 8 mL 30% w/v acrylamide (Severn Biotech, Kidderminster, U.K.),
- 3 mL 10 x TBE (Tris-borate-EDTA) (MP Biomedicals, Stretton, U.K.),
- 18.7 mL ddH_2O,
- 300µL of 10% w/v APS (ammonium persulfate) and
- 30µL TEMED (tetramethylethylenediamine).

It was used in the analysis of DNA fragments smaller than 200 bp. The samples were thoroughly mixed with a 6x gel loading buffer and loaded into separate wells. A 10 bp DNA ladder (Invitrogen, Cat. No. 10821-015, Figure 2.1 **A**, 10 - 330 bp) was typically used as a size marker. The gel was run using a Consort E832 power pack in a 1x TBE buffer at 8 watts for 40 minutes or until the dye moved along 2/3rd of the length of the gel. The gel was stained with ethidium bromide (1 g/mL) for viewing under UV light.

2.2.1.3 Tris-glycine SDS protein gel

Protein gels were run under denaturing condition using a 10-20% (w/v) Tris-HCl gradient gel with a 4% (w/v) stacking gel, obtained from Biorad laboratories (Catalogue No. 345-0042). These gels were used to run protein samples in a 1x glycine running buffer under denaturing conditions. The PageRuler™ prestained protein ladder from Fermentas (St. Leon-Rot Germany, Cat. No. SM0671, Figure 2.1 **D**) was used to determine the sample size. Criterion cell system (Biorad laboratories, Cat. No. 165-6001) and a Consort E832 power pack was used for the electrophoresis run. The gel was submerged in the Coomassie blue staining solution and rocked overnight. The gel was subsequently covered in a de-stain solution and rocked overnight, until the bands could be visualised.

2.2.2 Transmission electron microscopy (TEM)

400 mesh ultra-thin carbon-coated copper grids or carbon coated formvar supported copper grids from Agar Scientific (Essex, U.K.). 5 µL of the sample was dropped directly over the charged copper grid and allowed to stay for 1 minute. The excess sample was then removed carefully with a filter paper. The sample was stained with 10 µL of 2% (w/v) uranyl acetate (pH 4.0) solution, if necessary. Again, the excess stain was removed using a filter paper. The Philips CM10 (Philips Electronics UK Ltd, Guildford, U.K.) or the Jeol 1200EX (Jeol Inc, Tokyo, Japan) TEM was used to visualise the samples at 80 keV.

For high resolution TEM (HRTEM) a Philips CM200 Field Emission Gun TEM operating at 197 kV was used. The HRTEM was fitted with a Gatan GIF200 imaging filter and an Oxford instruments UTW EDX detector. ISIS software was used for image visualisation and analysis.

2.2.3 Molecular biology techniques

2.2.3.1 Preparation of the host *E. coli* ER 2738

E. coli strain, ER2378 was obtained from New England Biolabs (Hitchin, U.K.). It was streaked on a LB-Tet plate and grown overnight at 37^{o}C. 5 mL of fresh LB media with Tetracycline (10 µg/mL) was inoculated with a single colony of the *E. coli* picked using a sterile toothpick. The culture was incubated at 37^{o}C in an incubator at 225 rpm for 6 hours. The culture plate and the liquid culture in media were preserved at 4^{0}C for further use.

2.2.3.2 Preparation of bacterial stocks for freezing

900 µL of the overnight *E.coli* culture (section 2.2.3.1) was mixed with 100 µL of 0.2 µm filtered 80% (v/v) glycerol in a 1.5 mL tube. The tubes were then flash frozen in liquid nitrogen and stored in a -80ºC freezer.

2.2.3.3 Polymerase chain reaction

Taq DNA polymerase (Invitrogen, Cat. No. 18038-026) was used to carry out the Polymerase Chain Reaction (PCR) in a 10x buffer and 50 mM $MgCl_2$ solution, provided by the manufacturer. The composition of the 10x buffer was 200 mM Tris-HCl, pH 8.4 and 500 mM KCl.

Primers were obtained from MWG-Biotech (Ebersberg, Germany) and were centrifuged in a tabletop centrifuge (1-15K, Sigma, Osterode am Harz, Germany) for 5 minutes at maximum speed to get the lyophilised DNA at the bottom of the tube. Primers were re-suspended in a suitable volume of EB buffer (10 mM Tris-Cl, pH 8.5) or distilled water (as instructed by the primer supplier) to obtain a primer concentration of 100 nmol/mL. The 10 mM dNTP mixture, containing 10 mM of dATP, dCTP, dGTP and dTTP was created from a 100 mM dNTP set (Invitrogen, Catalogue Number-10297-018). The composition of a typical PCR reaction is described below.

- 2 µL10x Invitrogen buffer (200 mM Tris-HCl pH 8.4, 500 mM KCl),
- 0.6 µL Invitrogen 50 mM $MgCl_2$ solution,
- 0.2 µL of 100 nmol/mL primer 1
- 0.2 µL of 100 nmol/mL primer 2,
- 0.4 µL 10 mM dNTP mixture (final concentration 200 µM),

- 2 µL 0.1 pmole/µLtemplate (final concentration 1 nM),
- 0.2 µL *Taq* polymerase (1-2 unit) and
- 14.4 µL distilled water to make the final volume to 20 µL.

In control PCR tubes, 2 µL of ddH_2O was used instead of template. The PCR tubes were placed in a thermocycler (Peltier Thermal Cycler PTC-200, Global Medical Instrumentation Inc., Minneapolis, MN, U.S.A., Cat. No. BC-MJPC200) and the following temperature cycle was used.

Step 1 - 95^{o}C for 30 seconds,

Step 2 - 95^{o}C for 30 seconds,

Step 3 - Annealing for 1 minute at x^{o}C (the annealing temperature depends on the melting temperature, T_m of the primers).

Step 4 - 72^{o}C for *y* minutes (1 minute per kb of DNA).

Step 5 - Repeat 24 times, the step 2 to step 4.

Step 6 - The final step was 68^{o}C for 10 minutes.

Unless stated otherwise, the annealing temperature was 55^{o}C and the extension time was 1 minute.

2.2.4 Preparation of phage stock

2.2.4.1 Growth of phage and PEG precipitation

A phage plaque was picked from an agar plate using a sterile toothpick and was used to inoculate 1 mL of LB media containing tetracycline, in a 50 mL tube. 10 µL of the overnight *E.coli* ER 2738 culture (section 2.2.3.1) was also added to the tube. This culture was incubated at 37°C for approximately 4.5 hours while shaking at 220 rpm in an orbital shaker. The growth culture was transferred to a 1.5 mL tube and the tube was centrifuged at 10000 rpm (9167 x g) in a table top centrifuge (1-15K, Sigma, Osterode am Harz, Germany) for 10 minutes at 4°C. The pellet containing the cell was discarded but the supernatant containing the phage particles was transferred to another clean 1.5 mL tube using a sterile pipette. In a 500 mL conical flask, 400 µL of the supernatant was added to 100 mL of LB media containing tetracycline. 1 mL of an overnight *E.coli* ER2738 growth culture was also added. The culture was then incubated in an incubator at 37°C, shaking at 220 rpm for approximately 4.5 hours in an orbital shaker. The culture was then transferred to a 250 mL autoclaved centrifugation tube (Nalgene, Rochester NY USA, Catalogue No. 3120-0250). The tubes were centrifuged in a Sorvall RC-5B ultracentrifuge (Thermo Fisher Scientific Inc, Waltham, MA, USA) at 10000 rpm (8000 x g) using JA-14 rotor (Beckman Coulter, Part No. 339247) for 10 minutes at 4°C. 40 mL of the supernatant was transferred to several fresh 50 mL centrifuge tubes (Nalgene, Rochester NY USA) using a pipette and the pellet was discarded.

In order to precipitate the phage particles PEG/NaCl (20% (w/v) PEG / 2.5 M NaCl) solution was used. 7 mL of PEG/NaCl or 1/6th the volume of the supernatant was added to the 50 mL tube and left overnight at 4°C. The tube was placed in rotor while taking precaution not to shake the tube. The tube was centrifuged at 10,000 rpm (6500 x g) for 10 minutes at 4°C. The supernatant was discarded, and the pellet was re-suspended in 1 mL of the PBS buffer (section 2.1.4.1) and transferred to a 1.5 mL tube. 165 µL or 1/6th volume of PEG/NaCl (20% (w/v) PEG / 2.5 M NaCl) was added and the solution was left overnight at 4°C. The tube was centrifuged down at 10,000 rpm for 10 minutes in a table top centrifuge (GenFuge 24D, Progen Scientific London UK, Cat. No. C-2400) as before and the supernatant was removed. The pellet was re-suspended in 1 mL of the

PBS buffer (pH 7.4) and the tube was centrifuged at 10,000 rpm (9200 x g) for 10 minutes at 4°C in a table top centrifuge to remove any insoluble matter. The supernatant, containing the purified phage, was transferred to a clean 1.5 mL tube and stored at 4°C. Concentration of the phage stock was determined using spectrophotometry or phage titre as described in section 2.2.11 and section 2.2.12 respectively.

2.2.4.2 Caesium chloride purification

A method developed by Prof. George Smith at the University of Missouri was used for this purification step. 4.83 g of 98% pure CsCl (Cat. No. C4036-250G) was added to a 50 mL glass beaker. The balance with the glass beaker containing the CsCl was then set to zero. The PEG purified phage (from section 2.2.4.1) was added to the beaker along with distilled water to the final weight of 10.75 g. To dissolve the CsCl, the beaker was swirled gently, and the mixture was subsequently poured into a 12 mL open-top polyclear tube (Seton Scientific, Los Gatos CA USA, Cat. No. 7031). The tube was placed in a SW 32 Ti open bucket rotor (Beckman Coulter, Brea CA USA, Part No. 369650) and centrifuged at 30,000 rpm for 48 hours in an Optima L-80 XP centrifuge (Beckman Coulter, Part No. 392051). This tube was then placed in a gradient fractionator (Biocomp instruments, Frederiction NB Canada, Cat. No. 152-002) to identify the phage band, which appears as a milky band about a quarter way down the tube. A gradient fractionator was used for the phage fractionation.

2.2.5 Competent cells preparation.

A single colony from the culture plate of the *E.coli* ER2378 was used to inoculate 10 mL of LB media containing tetracycline. The culture was grown until the optical density at 600 nm was in the range 0.55 - 0.65. The cells were harvested by centrifugation at

1500 rpm for 10 minutes at 4°C in a Sorvall RC-5B ultracentrifuge (Thermo Fisher Scientific Inc, Waltham, MA, USA). The pellet was re-suspended in 2 mL or 1/5th volume of culture in ice-cold 50 mM $CaCl_2$. It was left on the ice for another 20 minutes. The cells were harvested as before in an ultracentrifuge at 1500 rpm at 4°C and re-suspended in 1/10th volume of ice-cold 50 mM $CaCl_2$. It was left on the ice again for 1 hour. The cells were dispensed in 5 aliquots of 200 µL. The cells were kept on ice at 4°C and used the same day or within 3 days at the most.

2.2.6 Transformation of M13 KE DNA

A maximum of 100 ng of the phage RF DNA was added to 200 µL of competent cells and the mixture was incubated on ice for 40 minutes. The cells were then heat shocked at 42°C for 2 minutes and returned to ice for 2 minutes. Four volumes (800 µl) of LB media were added and the mixture was left to stand in a 37°C incubator for 60 minutes to allow the regeneration of normal cell permeability. 100 µL of the competent cell culture, 100 µL of host *E. coli* grown to OD 5-6.5 and 20 µL of IPTG-XGAL solution was added to 3 mL of agarose top kept at 48°C in water bath. The mixture was vortexed for 5 seconds and immediately transferred to LB-Tet plates. The *E. coli* lawn and competent cells were plated without adding any phage DNA as negative controls. The plates were incubated overnight at 37°C. Blue plaques of phage were observed on the lawn of *E. coli* cells on respective plates.

2.2.7 Preparation of M13 phage stock and RF DNA

The M13 phage particles were added to the host *E.coli* in the growth media. The M13 infected *E.coli* culture was centrifuged at 2500 rpm and the supernatant containing phage particles was stored at 4°C for further use. The phage RF DNA was obtained from the cell pellet using Qiagen Miniprep kit by alkaline cell lyses. The RF DNA was adsorbed by the silica gel and eluted using Tris buffer or distilled water.

2.2.8 Phenol Chloroform extraction of DNA

The DNA solution was first diluted to 100 µL - 200 µL with distilled water in a 1.5 mL tube, if the sample volume was less than 100 µL. It is because the extraction is difficult with smaller volumes. The sample can always be concentrated after the final step of ethanol precipitation. Two volumes of phenol solution (Sigma-Aldrich, Cat. No. P4557) was added to the DNA solution and vortexed for 1 minute before being centrifuged at 20,000 rpm for 1 minute in a table-top centrifuge. Two phases were formed with the DNA residing in the top phase. DNA in this phase was aspirated with a pipette, while avoiding any transfer of protein at the phase interface and was placed in a 1.5 mL tube.

Two volumes of chloroform were added to the aspirated DNA and vortexed for 1 minute at 20,000 rpm in a table top centrifuge. Two phases were formed and the top phase containing the DNA was aspirated with a pipette into a fresh 1.5 mL tube. The chloroform step was then repeated again to remove any traces of phenol.

2.2.9 Ethanol precipitation of DNA

2 volumes of 100% (v/v) ethanol and 0.1 volume of 3M sodium acetate was added to one volume of DNA. The mixture was incubated on ice for 10 minutes and centrifuged subsequently at 14000 rpm at 4ºC for 20 minutes. The supernatant was discarded and the pellet was resuspended in 70% ethanol (v/v) in order to remove the residual salt. The sample was then centrifuged at 14000 rpm at 4ºC for 20 minutes. The supernatant was discarded and the pellet was vacuum dried by centrifuging the sample at low speed in

GeneVac EZ-2^{plus} (GeneVac, Ipswich, Suffolk, U.K.), to remove the trace ethanol. The pellet was suspended in 30 µL of the Tris buffer or distilled water as per requirement.

2.2.10 Ligation of DNA fragments

100 ng of restricted and gel-purified M13KE phage DNA was mixed with the insertion gene (in a ratio of 1:1, 1:2 and 1:5 equivalents) and 1 µL (3 Units) of T4 DNA ligase (Promega, Cat. No. M1801). 1 µL of 10x buffer (provided with the ligase enzyme) was added. The final volume was then made up to 10 µL with distilled water. The ligation reaction was then incubated for 3 hours at room temperature. 1 µL, 3 µL and 6 µL of the ligated DNA was then transformed into chemically competent *E.coli* cells as described in the section 2.2.6.

2.2.11 Determination of the virions concentration using spectrophotometry of phage particles (measured in virions/mL)

The phage concentration can be described as either the number of viroins/mL or the number of plaque forming units (pfu) per mL. Day and Wiseman (1978) defined virions/mL in their work using the absorption properties of the filamentous phage. 2 µL of the phage stock was diluted in ddH_2O to make the final volume of 10 µL. The absorbance of the phage stock was measured at 269 nm and 320 nm using a Nanodrop 3300 spectrophotometer (Wilmington, Delaware, U.S.A.). Using the following equation given by Day (1978), the number of phage particles in a solution was calculated:

$$\text{Virions/mL} = \frac{(A_{269} - A_{320}) \text{ x } 6 \text{ x } 10^{16}}{\text{Number of bases/virion}}$$

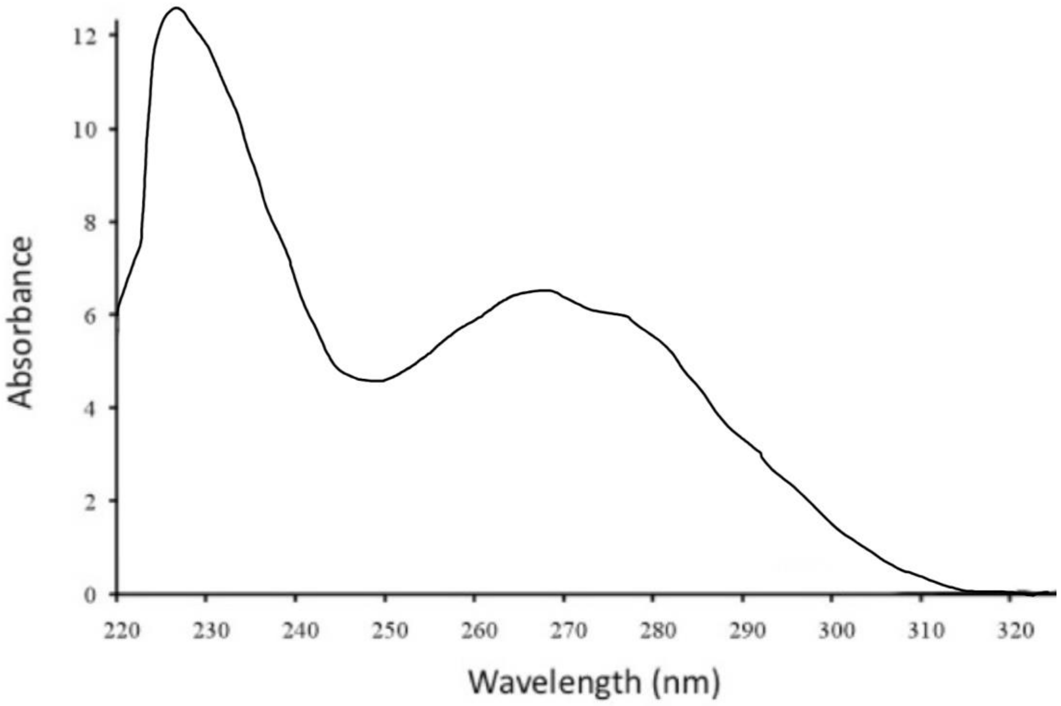

Figure 2.2 A typical absorption spectrum of the M13 phage solution obtained by PEG/NaCl precipitation.

As the filamentous phage has 6 times more protein than DNA, a broad peak was seen in the absorption spectrum between 260 and 280 nm (Day, 1978). The absorbance value at 269 nm corresponds to the maxima of this peak (Figure 2.2). The value at 320 nm was used to correct for the light scattering arising from the phage particle and other contaminants.

2.2.12 Phage titre (measured in pfu/mL)

The phage concentration is also measured as plaque-forming units (pfu) which corresponds to the number of infective phage particles within a solution and thus the number of phage particles with intact pIII protein. Spectrophotometric measurement in virions/mL does not differentiate between infective and non-infective particles. Typically, the pfu/mL value is 10 times lower than the virions/mL value.

Sterile tubes containing 3 mL of melted top agarose were equilibrated at 47^{o}C in a water bath. The M13 phage stock was tenfold serially diluted in water by mixing 10 µL of the phage stock with 90 µL of distilled water. The dilution was mixed vigorously before the next serial dilution to ensure even mixing of the phage. Once the estimated concentration 10^6 - 10^{10} phage/mL was achieved, 10 µL of the dilution was added to 20 µL of IPTG/XGAL solution and 100 µL of *E.coli* culture grown overnight to an optical density value between 5 and 6.5. The mixture was vortexed for 2 seconds and immediately poured on to LB Agar plates containing tetracycline. The plate was swirled gently to ensure an even distribution of agarose top over the agar. The plates were incubated overnight at 37^{o}C.

Blue phage plaques were observed on the plates the next day. A plate with the number of plaques over or near 100 was picked and the number of plaques was then counted. Multiplying this number with the dilution factor gives the number of plaque forming units (pfu) in 10 µL of the stock solution. Multiplying this final number with 100 gives pfu/mL.

2.2.13 Site-directed mutagenesis to clone gold binding insert in g-VIII.

To prevent primer-dimer formation, Wang *et al.* (1999), reported a 2-stage PCR protocol for long insertions and deletions using QuikChange™ site-directed mutagenesis (Agilent Technologies, Stockport, Cheshire, U.K., Cat. No. 200519). In this method, the two primers are used in two different site directed mutagenesis reactions before being mixed together to complete the reaction. Thus, separate single-primers are PCR amplified, before the actual PCR amplification, to generate mutated single-stranded copies of the plasmid. The same protocol was used for inserting the gold binding insert in the major coat protein, pVIII of the M13KE bacteriophage.

Primers are designed in the same way as for the site directed mutagenesis, whereby primers overlap the template DNA both before and after the DNA sequence to be inserted by 20 bp. The primers used for the mutagenesis, with underlined gold sequence are shown in Figure 2.3. Primers were ordered from MWG-biotech with High Purity Salt Free (HPSF) purification.

A Gold Binding insert by ligating the DNA using Hpa I site in mutant M13.

Forward 5’ – GATCATGTTAGGTACCTTTCTATTCTCACTCTG -3’
Reverse 5’–GTATCTGATAACGGCCGAGCCGCCGCCCGGAAC– 3’

B

Forward Primer –

5’...GTTCCGATGCTGTCTTTCGCTGCAGTATCTGGTTCTTCTCCG
GACTCGGATCCCGCAAAAGCGGCC …3’

Reverse Primer –

5’ ...GGCCGCTTTTGCGGGATCCGAGTCCGGAGAAGAACCAGA
TACTGCAGCGAAAGACAGCATCGGAAC-3’

Fig 2.3 – The primers used for the insertion of gold binding peptide gene in the major coat protein, pVIII of the M13KE bacteriophage using site directed mutagenesis to create (A) *Hpa I* site and (B) by creating *Pst I* and *BamH I* site.

For a single insertional PCR reaction, two separate PCR reactions in total volume of 250 µL were used. Each contained the following:

5 µL 10x buffer (given with QuikChange® Site-directed mutagenesis kit)

1 µL dNTP solution (given with QuikChange® Site-directed mutagenesis kit)

1 µL of template DNA (50 to 200 ng of plasmid or RF DNA)

1 µL of 10 pmol/µLprimer (Forward or Reverse primer in separate PCR tube)

42 µLof distilled water.

The two reactions differ only by the primer used. The two tubes were mixed on ice and 0.4 µL (1 unit) of *pfu* polymerase (provided with QuikChange® Site-directed mutagenesis kit) was then added to each tube. The two reactions were then placed into a thermocycler (Peltier Thermal Cycler PTC-200) and the following cycle was used:

Step 1: 95^{o}C for 30 seconds,

Step 2: 95^{o}C for 30 seconds,

Step 3: 55^{o}C for 60 seconds,

Step 4: 68^{o}C for X minutes (1 minute per kb of DNA),

Step 5: Repeat 10 times, the step 2 to step 4,

Step 6: 68^{o}C for 10 minutes.

An extension time of 8 minutes was used, unless stated otherwise.

The newly generated ‘hybrid’ plasmid had one wild-type and one newly synthesized mutant strand. The two hybrid plasmids are mixed with primers for PCR amplification again. 25 µL of each reaction was taken and mixed together in a single PCR tube and 0.4 µL of *pfu* polymerase was added. The PCR tube was then placed back into the thermocycler and the same programme used but the number of cycles in step 5 was increased to 18. In this case, the annealing of the mutagenesis primers to the mutated template strand was more efficient, as against the wild type template strand. Since the mutated template strands is perfectly complementary to the respective primers, they compete equally well to prevent primer-dimer formation.

1 µL (10 units) of *dpn I* enzyme (provided with the QuikChange® Site-directed mutagenesis kit) was subsequently added to the PCR reaction and incubated for 3 hours at 37^{o}C. The enzyme *dpn I* digests only methylated DNA and therefore it should only digest the template DNA. 1 µL of the *dpn I* digested PCR reaction was then transformed into chemically Competent *E.coli* cells as described in sections 2.2.5 and 2.2.6. The transformed cells were then plated on agar plates and viral plaques were picked for screening the correct mutant phage.

2.2.14 Colony PCR

Colony PCR was used to identify the success of the ligation or the site-directed mutagenesis reaction. In this method, viral plaques from the transformation of the ligation or mutagenesis reactions were picked from the agar plates using a sterile toothpick. The toothpick was used to inoculate 200 µL of the LB media in a 1.5 mL tube and the tube was tapped three times on the bench after inoculation for mixing the plaque in the media. The tube was incubated for 1 hour at 37^{o}C with shaking at 220 rpm. Primers designed to amplify either *gene III* or *gene VIII* of the M13KE bacteriophage is shown in Figure 2.4 along with their position on the sequence of M13KE.

The sequencing primers used for the colony PCR were as follows:

cPCR-g3-for: - CACCTCGAAGCAAGCTGATAAAC

cPCR-g3-rev: - GACAACCCT CATAGTTAGCGTAACG

cPCR-g8-for: - GCTATGCCT TCGTAG TGGCATTACG

cPCR-g8-rev: - AACGCAGCTTGCTTTCGAGGTG

1201 CAAAGATGAG TGTTTTAGTG TATTCTTTTG CCTCTTTCGT TTTAGGTTGG
cPCR-g8-for →
1251 *TGCCTTCGTA GTGGCATTAC* GTATTTTACC CGTTTAATGG AAACTTCCTC

1301 **ATG**AAAAAGT CTTTAGTCCT CAAAGCCTCT GTAGCCGTTG CTACCCTCGT
Pst I **Bam HI**
1351 TCCGATGCTG TCTTTCG**CTG CAG**AGGGTGA **GGATCC**CGCA AAAGCGGCCT

1401 TTAACTCCCT GCAAGCCTCA GCGACCGAAT ATATCGGTTA TGCGTGGGCG

1451 ATGGTTGTTG TCATTGTCGG CGCAACTATC GGTATCAAGC TGTTTAAGAA
← *cPCR-g8-rev*
1501 ATT*CACCTCG AAAGCAAGC**T GA**TAAAC*CGA TACAATTAAA GGCTCCTTTT
cPCR-g3-for →
1551 GGAGCCTTTT TTTTGGAGAT TTTCAAC**GTG** AAAAAATTAT TATTCGCAAT
Acc 65 I **Eag I**
1601 TCCTTTAGT**G GTACC**TTTCT ATTCTCACT**C GGCCG**AAACT GTTGAAAGTT

1651 GTTTAGCAAA ATCCCATACA GAAAATTCAT TTACTAACGT CTGGAAAGAC
← *cPCR-g3-rev*
1701 GACAAAACTT TAGAT*CGTTA CGCTAACTAT GAGGG*CTGTC TGTGGAATGC

Figure 2.4 Sequencing primers for pIII and pVIII on the M13KE sequence. The *Pst I* and *Bam HI* restriction sites in *gVIII* (From 1301-1522) and the *Acc65* I and *Eag I* sites in *gIII* (From 1578-2852) are used to identify the inserts. The size of the *gIII* PCR product is 237 bp and *gVIII* PCR product is 279 bp. Sequence of the M13KE bacteriophage was available from New England Biolabs product catalogue.

The following PCR reaction was set-up

- 2 µL of the 1 hour culture above was used as the template,
- 1 unit of the *Taq* DNA polymerase (Invitrogen, Cat. No. 18038-026),
- 2 µL of the 10 x buffer (provided with the polymerase),
- 2 µL of the 1.5 mM $MgCl_2$ (provided with the polymerase),
- 0.5 mM dNTPs (Invitrogen) and
- 1 pmol/µL of the relevant primers to make the final volume of 20 µl.

The PCR tube was placed in a thermocycler (Peltier thermal cycler PTC-200) and the cycle employed in section 2.2.3.3 was used, whereby the tube was heated to 95°C for 30 seconds, followed by 24 cycles of: 95°C for 30 seconds, 55°C for 1 minute, and 72°C for 1 minute. The final elongation step was 68°C for 10 minutes. The PCR reaction was also set-up for a wild type M13KE plaque, grown for 1 hour as described above and ddH_2O as a negative control. The PCR products were run on a 10% (w/v) polyacrylamide gel (section 2.2.1.2) after digesting them with the respective restriction enzymes.

2.2.15 Concentration of 5 nm gold nanoparticles without ligand exchange

To increase the concentration of the gold nanoparticles colloidal suspension, 500 µL of the 5 nm gold nanoparticles (Ted Pella Inc., California, USA) having a concentration of 5.0×10^{13} gold nanoparticles/mL was centrifuged at 1000 rpm in a vacuum at room temperature. The volume of the sample was reduced to 250 µL after 2 hours. The concentration of the gold nanoparticles in the suspension was measured using spectrophotometer by measuring its absorbance at 520 nm. No visible precipitate was observed even after 5 days of storage at 4°C suggesting that the concentrated gold nanoparticles were stable and did not form any aggregates on their own. Although, clusters of 2-5 gold nanoparticles were often seen under TEM, this was not observed for the gold nanoparticles sourced from the supplier, Ted Pella.

2.2.16 Goldenhanced nanowires

Gold can also be deposited on the linear array of gold nanoparticles on a M13 bacteriophage using the Goldenhance EM toolkit (Nanoprobes Inc., NY, USA).

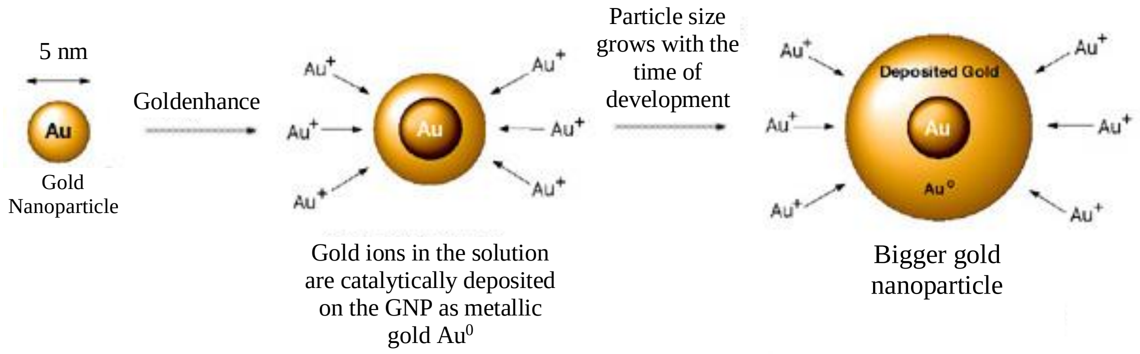

Fig 2.5 Electroless deposition of gold on the gold nanoparticles using the Goldenhance kit from Nanoprobes. Image adapted from Goldenehance product catalogue.

2 µL of 1 x 10^{11} virions/mL of gold binding phage were added to 20 µL of 5nm gold nanoparticles (Ted Pella Inc., California, USA) and incubated for 10 minutes. Goldenhance solutions A and B were added in the ratio of 1:2 and incubated for 2 minutes. 8 µL of Goldenhance solution C was then added; so that the final reaction mixture volume was 60 µL. M13 nanowires were obtained after 5 minutes of the Goldenhance reaction and deposited on a regular carbon coated copper TEM grid.

2.2.17 Electroless deposited nanowires

40 µL of 1 x 10^{11} virions/mL of gold-binding phage, M13G was added to 10 µL of 5 nm Gold nanoparticles (Ted Pella Inc., California, USA) and incubated for 10 minutes. 80 µL of 2 nm Gold nanoparticles (Ted Pella, California, USA) was then added to the solution and further incubated for 2 minutes. 40 µL of 6 mM HAuCl4 (chloroauric acid/ gold (III) chloride solution in 2.9 M HCl: Cat. No. 484385 from Sigma-Aldrich) was then added and the solution was vortexed for 5 seconds. 10 µL of 5 mM hydroxylamine (NH_2OH) was then added immediately afterwards while gently mixing the solution by shaking the tube.

2.2.18 Residual background reduction of the M13 gold nanowire on the SiO_2 surface

Gold nanowires on the M13 bacteriophage template made by either electroless deposition of gold using hydroxylamine (NH_2OH) or by using the Goldenhance toolkit left residual solids on the SiO_2 surface after drying the nanowire suspension. Hence, the nanowire suspension was dialysed using a 50,000 Molecular weight cut-off (MWCO) dialysis membrane (Spectrum Laboratory) in 5 L of distilled water for 5-6 hours with two changes of the buffer. The resulting nanowire suspension in water was used for electrical and physical characterisation within 2-3 hours.

2.2.19 Adsorption of M13 phage particles on the SiO_2 or SiN surface

10 µL of 5 X 10^{10} M13 phage particles in ddH_20 were deposited on a piranha cleaned SiO_2 chip or a SiN wafer for 30 minutes in a humidity chamber. Distilled water was sprayed on the surface from an angle using a squeeze bottle nozzle to wash off any unbound phage. The surface was then dried using a gentle flow of nitrogen gas, keeping the angle of the jet same as for the water wash, until the surface was dried. The same angle for the water wash and nitrogen drying step ensured that the phage particles were aligned in the same direction. Samples were viewed via AFM.

2.2.20 AFM (Atomic Force Microscopy)

Veeco Dimension 3100 AFM was used for imaging using the AFM tip in tapping mode. For scanning M13 or MS2 phage particles, low tip amplitude was used so that the tip tapped on the phage as lightly as possible. To get the optimum amplitude, the amplitude was reduced until the tip lost contact with the surface and then the amplitude was increased gradually until the tip regained contact. Tapping the phage particles harder with AFM tip compromised the structural integrity of the phage particles.

2.2.21 Cleaning the SiO_2 or SiN surface using Piranha solution

A thorough cleaning of the surface was needed before it could be used for patterning electrical circuits onto it. The piranha solution works very well in laboratory for this purpose for silicon-based surfaces. It is very corrosive and hence all piranha cleaning was carried out in a fume hood, while wearing the necessary face mask, gloves, goggles and apron to protect the body and clothes from accidental spills. Ceramic tweezers were used for handling the silicon chips in and out of the piranha solution, as any other tweezer material would corrode.

The piranha solution was prepared by adding 21 mL of 95-97% sulfuric acid (Cat. No. 30743) and 9 mL of 35 % fresh hydrogen peroxide (Cat. No. 349887) in a 100 mL beaker. Upon mixing, the beaker became too hot to the touch and fumes could be seen coming out of the solution. SiO_2 chips, approximately 1 cm^2 in area, were prepared from a single sheet of SiO_2 (Compart Technology Ltd, Peterborough, U. K.). SiO_2 chips were placed into the freshly prepared piranha solution for 10 minutes. The side of the SiO_2 chip to be used for electrical patterning and placing the sample should be facing up such that bubbles are formed on the surface. If no bubbles are formed, then the hydrogen peroxide used is likely to be inactive and another fresh hydrogen peroxide solution should be used. Using ceramic tweezers, the SiO_2 chips were then transferred to 50 mL of ddH_2O in a 100 mL beaker and sonicated (Fisherbrand FB11020) for 5 minutes. While the SiO_2 chips were being sonicated, the piranha solution was poured away in a waste jar and the beaker was washed thoroughly with ddH_2O and dried with a nitrogen spray gun. The beaker was then filled with 30 mL of 100% isopropanol (Fisher Scientific, Cat. No. P/7500/PC17) and the SiO_2 chips were transferred into it and sonicated again for 5 minutes. The chips were then removed from the isopropanol and dried using a pressurised nitrogen nozzle. The clean SiO_2 chips were placed in a humid chamber and sealed with parafilm® (Alphalaboratories, Cat. No. WS5000-10) and aged overnight at room temperature before further use.

2.2.22 Patterning of electrodes on the nanowires

Dialysed nanowires were deposited on the SiO_2 substrate with pre-fabricated gold alignment marks (kindly fabricated by Dr Steve Johnson). Cleaning and preparation of the surface to fabricate such a 2 x 2 cm SiO_2 chip with piranha solution is described in section 2.2.21. The nanowires were then annealed at 250°C under vacuum as described in section 2.2.24. A 300 nm thick layer of polymethyl methacrylate (PMMA, molecular weight - 950) was spin coated on the SiO_2 surface at 5000 rpm for 30 s. A 4% (w/v) PMMA solution in Anisole was used as the resist mask. It was then baked overnight at 170°C. A Raith 50 electron gun (Raith, Dortmund, Germany) was used to pattern 10 x 10 µm cross-hairs. The SiO_2 surface was incubated in 3:1 volumetric solution of methyl isobutyl ketone, (MIBK) in isopropyl alcohol for 70 seconds to dissolve the irradiated PMMA. An electron beam evaporator (Univex 350, Germany) was then used to deposit a 100-150 nm thick layer of gold onto the SiO_2 layer. Finally, 100% (v/v) acetone was used to lift off the PMMA covered with gold by incubating the SiO_2 surface overnight. An AFM image was taken after depositing the gold nanowire. The gold deposition process was then repeated using the AFM image to align the Raith 50 EBL machine to get the desired gold electrode pattern connected to the ends of the gold nanowire.

2.2.23 Conductivity measurement using the 4-probe Scanning Probe Microscope

The 4-probe SPM (Omicron Nanotechnology GmbH, Taunusstein, Germany) in Figure 2.6 was used for the electrical conductivity measurement of the M13 phage-based gold nanowires. Liquid helium flow cryostat was used to get the nanowires on the grid to come in equilibrium with the liquid helium temperature, for low temperature conductivity measurement.

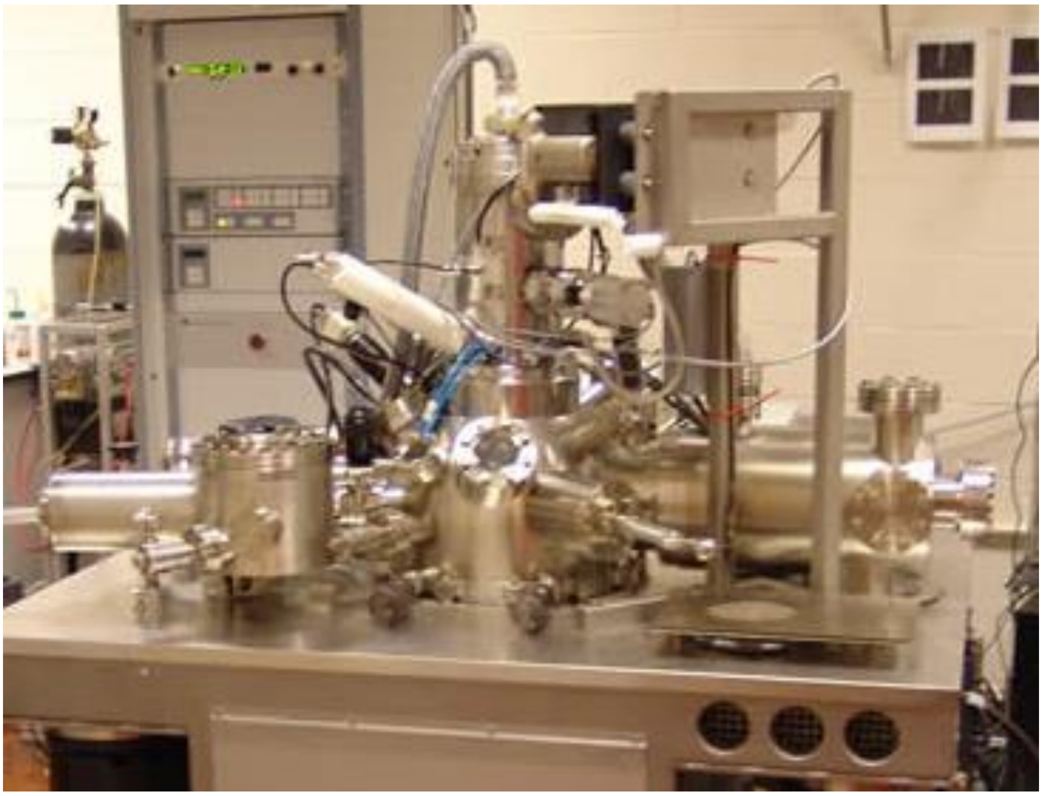

Fig 2.6 The 4-probe Scanning Probe Microscope used for the electrical characterisation of the M13 gold nanowire.

2.2.24 Annealing of the M13 phage-based gold nanowire in a vacuum oven

A drop of the M13 gold nanowire suspension was placed on a formvar coated 300 mesh copper TEM grid (Agar Scientific, Essex, U.K.). The drop was dried using filter paper and then the copper grid was placed inside the glass tube of the vacuum oven. The glass tube was vacuum-sealed, and the rotary pump was turned on. Once the pressure inside the tube reached 10^{-3} psi. The oven (Lenton Furnaces, Hope Valley, UK) was turned on. The heating element of the oven was turned on and the temperature allowed to reach the set temperature. The tube was then inserted inside the oven for a fixed duration for the nanowire annealing.

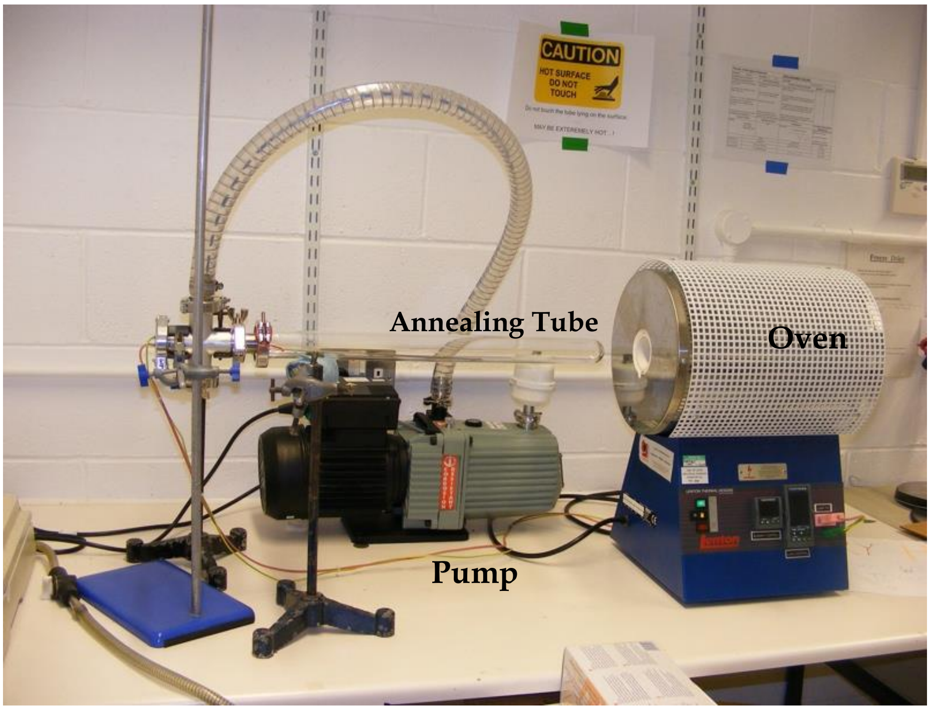

Fig 2.7 The high temperature vacuum tube oven used for the annealing of the M13 gold nanowire.

2.2.25 Scanning electron microscopy (SEM) of gold nanowires

A drop of M13 phage templated gold nanowire suspension dialysed in deionised water was deposited on a clean SiO_2 surface. The samples were then examined using a LEO 1530 Gemini field emission gun SEM with Oxford Instruments INCA 350 energy-dispersive X-ray (EDX) spectroscopy system. EDX helps determine the elemental composition of a sample within an SEM.

2.2.26 Phosphine stabilisation and concentration of GNP

2 mg phosphine (4,4′-(phenylphosphinidene) bis (benzenesulfonic acid), dipotassium salt hydrate) (Sigma-Aldrich, St. Louis, MO, U.S.A.) was added to 10 mL of citrate stabilised 5nm gold nanoparticles from Ted Pella in a 15 mL tube. The solution was gently mixed for 10 hrs at room temperature on an orbital shaker at low speed. Solid NaCl was added to the final concentration of 2-3 M with occasional gentle mixing, until the solution turned from a deep burgundy to a lighter purple colour. The solution was centrifuged for 30 min at 500xg at room temperature to pellet the gold nanoparticles. The supernatant was discarded, and the particles resuspended in 1 mL of 0.5 mM phosphine in 1.5 mL tube. 0.5 mL methanol was added to this tube to precipitate the gold nanoparticles. The tube was centrifuged again for 30 min at 500x g at room temperature in a table top microcentrifuge.

Again, the supernatant was discarded, and the nanoparticles were resuspended in 1 mL of 0.5 mM phosphine. If the gold nanoparticles were to be used for electrophoresis 110 mL of 5 x TBE buffer was added to this solution to get the gold nanoparticles in a final buffer concentration of 0.5 x TBE.

2.2.27 Invitrogen quantum dot used for encapsulation in a MS2 capsid.

Streptavidin functionalised CdTe quantum dots with emission maximum at 565 nm were obtained from Invitrogen (Paisley, UK). Biotin functionalised TR RNA was used to obtain the nanoparticle-TR RNA conjugate for the assembly reaction. Though the actual semiconductor core of the quantum dot is 5 nm in diameter, it is encapsulated in a ZnS and a polymer shell. Streptavidin binds to the polymer shell using a linker molecule. Thus, effectively the size of the quantum dot is 15-20 nm.

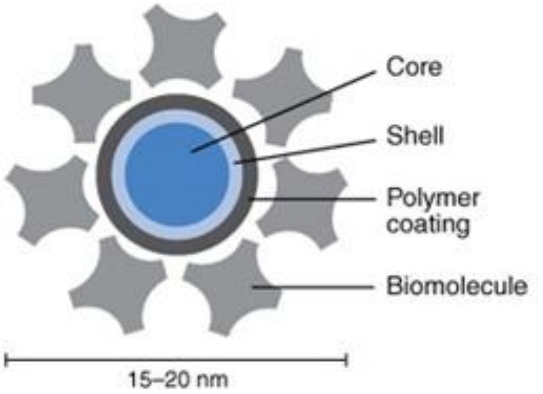

Fig 2.8 The Qdot quantum dot from Invitrogen. The diagram was taken from the Invitrogen catalogue and shows the main structural elements of the quantum dot and is drawn to scale relative to one another.

2.2.28 Protocol for nanoparticle encapsulation in MS2 capsid

2.2.28.1 Preparation of MS2 capsids for disassembly to get MS2 coat proteins

A stock of recombinant MS2 capsids stored in 80% saturated ammonium sulfate at 4°C was obtained from Dr. Gabriella Basnak in our research group. 6 mL of the stock MS2 solution was taken and transferred to three different 2 mL tubes and centrifuged down at 13,000 rpm for 15 minutes in a table top centrifuge. The supernatant was discarded, and the pellet was resuspended in a minimal volume of 40mM ammonium acetate buffer. The suspension was then placed into a dialysis cassette (Spectrum Laboratories) of 5,000 MWCO and dialysed against 40 mM ammonium acetate buffer (pH = 6.8), at 4°C overnight with two changes of buffer. After dialysis 10 µL volume of the suspension was diluted to a final volume of 1 mL in 40 mM ammonium acetate buffer. The absorbance of the resultant solution was measured at 260 nm and 280 nm. The concentration of the solution was measured using the absorption coefficient of the MS2 coat protein dimer.

2.2.28.2 Dissociation of MS2 capsids and purification of MS2 coat protein dimers

0.33 mL of the MS2 capsid dialysed against 40 mM ammonium acetate (section 2.2.28.1) was taken and 0.66 mL of glacial acetic acid (CH_3COOH) was added to it in a 1.5 mL tube. The 1:2 (v/v) solution was left on ice for 1-2 hours to dissociate the MS2 capsids into coat protein dimers. The suspension was then centrifuged down at 20,000 rpm in a table top micro-centrifuge at 4°C for 20 minutes. Meanwhile a size-exclusion NAP-10 column (GE Healthcare and Life Sciences, USA) packed with Sephadex G-25 was washed with 3-5 column volume (5mL) of 20 mM CH_3COOH at 4°C. The dissociated coat protein on ice was loaded onto the column and then the coat protein was washed with 20 mM CH_3COOH in 0.5 mL fractions. The coat protein was eluted with the first 1.5 mL elute. Cold temperature was kept throughout by first equilibrating everything at 4°C and by working in a 4°C cold room throughout. 5 µL of the elute was diluted to 1 mL and the absorbance was measured at 280 nm to calculate the concentration of the MS2 coat protein dimers, which is likely to have been between 40-100 µM.

2.2.28.3 TR RNA conjugation to gold nanoparticles and CdTe quantum dots

5’ thiol functionalised TR RNA of the MS2 bacteriophage was synthesised in an RNA synthesiser. The thiol group was attached to the 5’ end of the RNA using the six-carbon linker molecule. The trityl-protecting group attached to the sulfur was removed using a silver nitrate solution and treated with DTT. The RNA was finally purified using high performance liquid chromatography.

The citrate stabilized 5 nm GNP (Ted Pella Inc., California, USA) was ligand exchanged, concentrated and stabilized with phosphine as described in section 2.6.1. To 1 molar equivalent of the phosphine stabilised gold nanoparticles (concentration of approximately 600 nM), 0.9 molar equivalent of thiol functionalised TR RNA was mixed and left overnight at 4°C to bind to the gold nanoparticles.

For conjugation to the streptavidin coated quantum dot to TR RNA, 1 molar equivalent of biotin-functionalized TR RNA solution was mixed with 1 molar equivalent of quantum dot in solution. The solution was placed on an orbital shaker at a low speed (<1 Hz) and incubated for 16 hr at 4°C for the TR RNA to bind to the quantum dots.

2.2.28.4 Reassembly of gold nanoparticles encapsulated MS2 virus like particles

The reassembly reaction was set up on ice for 1-3 h as follows:

8 µL	Reassembly buffer (20 mM TA/0.4 mM MgOAc, when neutral condition
2 µL	TR RNA conjugated gold nanoparticles (0.5 µM final concentration)
4 µL	dissociated coat protein dimer, CP2 (1 µM final concentration)
6 µL	distilled water

2.2.28.5 Sucrose density gradient for the purification of the MS2-GNP complex.

171 g of sucrose was weighed and a stock of 2 M (68.4%) ultrapure sucrose (USB corporation, Cleveland, OH, USA, Cat. No. 21938) with total volume of 250 mL was prepared in 1x λ buffer. The solution was mixed overnight at 4°C with a magnetic stirrer to dissolve the sucrose. The stock 2 M sucrose solution can be stored for a long duration at 4°C. However, it must be used within few hours upon dilution.

A gradient station (Biocomp, Cat. No. 153-002), was used to create linear sucrose gradients in open-top polyclear tubes (Seton scientific). Two solutions of different concentration (30% and 50% solutions) were used to make a 30 – 50% gradient, using the 2 M sucrose stock solution and λ buffer. The 30% sucrose solution was first poured into the tubes until the meniscus was just above the line marked by a permanent marker pen with the aid of a marker block (Figure 2.9 **C**). The 50% sucrose solution was then filled in a 20 mL disposable syringe. A long metal needle attached to the syringe was gently inserted into the bottom of the tube and the 50% sucrose solution was slowly pushed into the tube, thus displacing the lower concentration sucrose already in the tube above the marked line.

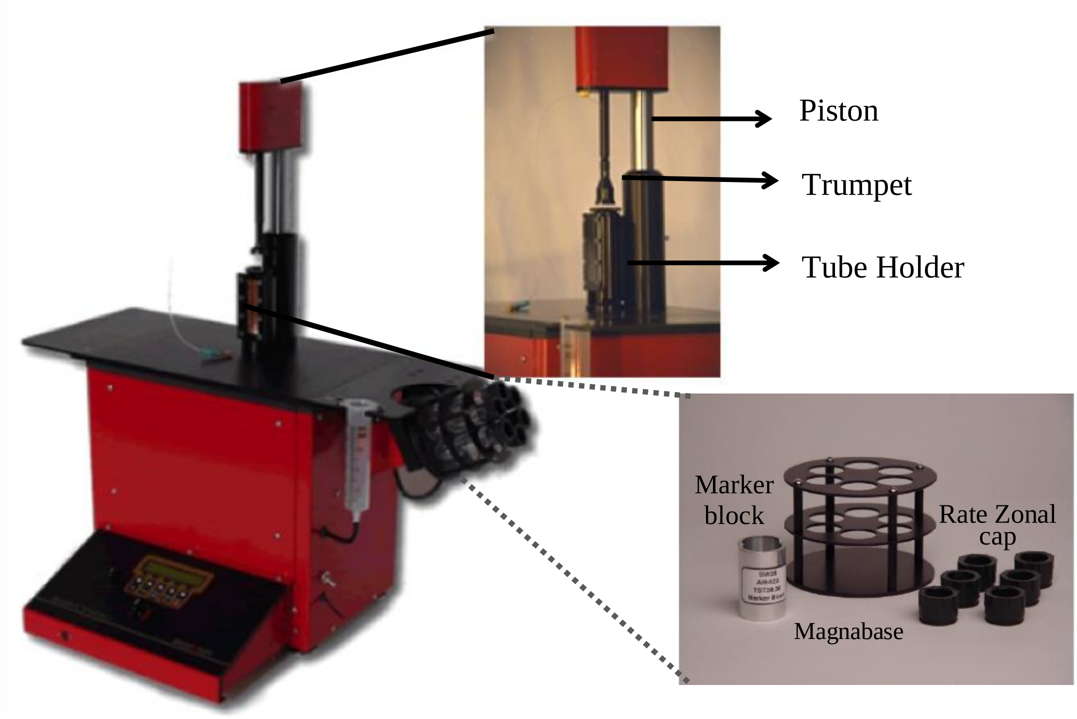

Fig 2.9 (A) Sucrose density gradient station and fractionators from Biocomp. **(B)** shows the close up of a section showing the tube holder, the trumpet and the piston. **(C)** shows the components supplied with the Biocomp gradient station and used to create linear sucrose gradients. Images taken from the Biocomp gradient station manual.

Thus, the higher concentration 50% sucrose solution, was below the lower concentration (i.e. 30%) sucrose solution. The rate zonal caps shown in Figure 2.9 (C) were used to close the tubes and the tubes were left for 30 minutes at 4°C. The Biocomp gradient station has many readymade programmes to create linear sucrose gradients with different tubes and sucrose concentrations. The tubes were placed in the supplied Magnabase shown in Figure 2.9 (C) and the pre-set programme was run to create the desired linear sucrose gradient. The tubes were then stored at 4°C for 1 hour, to allow the sucrose to settle.

The volume of the MS2-nanoparticle virus-like particle solution to be loaded onto the sucrose gradient was determined and an equivalent volume of sucrose was taken out after the caps were gently removed from the tubes. The MS2-nanoparticle virus-like particle solution was loaded on top of the gradient carefully without disturbing the gradient. After balancing the tubes with water, the tubes were loaded onto a SW 32 Ti open bucket rotor (Beckman Coulter, Brea CA USA, Part No. 369650). The tubes were centrifuged at 18,500 rpm overnight (typically 17 hours) using an Optima L-80 XP (Beckman Coulter, Part No. 392051). The MS2-nanoparticle virus-like particle solution were fractionated using a gradient fractionator (Biocomp instruments, Frederiction NB Canada, Cat. No. 152-002) as described in section 2.2.28.6.

2.2.28.6 Fractionation of the MS2-nanoparticle virus-like particle solution

A gradient fractionator (Biocomp instruments) as shown in Figure 2.9 (A) was used to fractionate the MS2-nanoparticle virus-like particle solution in open-top polyclear tubes (Seton Scientific), after ultracentrifugation. Absorbance was measured at 280 nm and 520 nm while the samples were fractionated continuously at a speed of 0.3 mm/second. The gradient fractionator was provided with a specialized trumpet (Figure 2.9 B) that is attached to a piston (Figure 2.9 B). This trumpet provides a better sample resolution compared to needle fractionation. The tube was placed in the tube holder (Figure 2.9 B), which was aligned under the trumpet. The trumpet formed an air-tight seal within the tube when the piston pushes it down into the tube. The solution in the tube was forced upwards though the trumpet and into the connected tubing (Figure 2.9 **A** and **B**). The solution in the tubing then passed through a UV detector (Pharmacia UV-M II, GE Healthcare, Cat. No. 18-1001-10) where the absorbance was measured. The absorbance reading was acquired by a DI-158U USB data acquisition device (DataQ instruments, Akron OH USA) connected to a computer. Finally, the liquid in the tubing was collected in tubes outside in different fractions.

2.2.29 Bacteriophage manipulation using a virtual AFM haptic

The M13 gold nanowires or MS2 bacteriophages in suspension were placed on a freshly cleaved mica surface from Agar Ltd or on a piranha cleaned SiO_2 surface. The stub containing the sample was then placed in the sample holder. The AFM tip was then brought to the surface and a random scan was done in tapping mode with a low amplitude.

2.2.30 Electron Beam Lithography (EBL)

EBL was used to transfer the patterned circuit onto the semiconductor substrate. A 300 nm thick layer of poly methyl methacrylate, PMMA was used as the resist mask on which a scanning electron beam was used to pattern a circuit. The patterned region exposed to the electron beam was selectively removed using a solvent. Gold was then evaporated and deposited onto the exposed substrate using an electron beam evaporator (Oerlikon, Pfaffikon, Switzerland). The rest of the gold covered PMMA was then removed using a solvent, leaving the desired circuit pattern on the substrate.

Chapter 3

Construction of the gold-binding filamentous phage

3.1 Introduction

3.1.1 Requirements for self-assembly of a molecular transistor

The basic structure of a molecular transistor is described in Figure 1.14 in Chapter 1. It consists of four components *viz.* three metal electrodes (source, drain and gate) surrounding a conducting island. The size of the gap between the source and the island or between the island and the drain determines it performance (Carlsson, 1999). Even a small variation in this tunnelling gap can make the device function unpredictably. Biological templates such as proteins, viruses and other biomolecules have a well-defined size with very little variation. The biological self-assembling systems interact at a molecular level on the principle of molecular recognition and hence have precise control over the interaction interface dimension at a nanometer level. This makes biological structures very attractive templates for self-assembling device fabrication as the gap between two components can be controlled using appropriately chosen or designed biomolecules.

The energy needed for an electron to tunnel from the source to the island or from the island to the drain depends on the size of the island. For the molecular transistor to operate at room temperature, the size of the island should be 1–3 nm (Weis, 2005; Likharev, 1999). Although, transistors with island size up to 10 nm have been fabricated, they work at temperatures well below the room temperature (Wang, 2007). The nanoscale size of the island and its gap with other electrodes imply that at least one dimension of the electrodes making the transistor must be comparable to the size of the island, as geometrical constraints will prevent device fabrication otherwise. The electrodes also need to be patterned with contact electrodes using Electron Beam

Lithography (EBL) for electrical characterisation of the transistor. The Raith 50 Electron Beam Lithography machine (Raith, Dortmund, Germany) used for this work could reliably pattern features at the desired location on the substrate with the resolution of 80 nm as per the manufacturer's specification. This means that the electrodes of the self-assembling molecular transistor prototype must have a high aspect ratio with one of the dimensions in the range of tens of nm.

3.1.2 M13 phage as an ideal template for molecular transistor electrodes

Various biological structures with filamentous or rod-like shapes were considered to act as a template for the electrode nanowire. The filamentous phage M13 stood out because various coat proteins could be engineered on the same phage to achieve multifunctionality that can further be used in device fabrication and self-assembly. The M13 bacteriophage has been studied extensively, creating a vast library of structural and functional data and associated protocols. Hence, M13 bacteriophage was selected over other viruses, to act as a template for the fabrication of molecular transistor electrodes.

The electrode needs to be conducting in nature and hence the M13 phage needs to be coated with a conducting material to fabricate the nanowires. Metal-binding peptides can be selected empirically from a large pool of peptide sequence variants using a phage display library or another combinatorial selection library (Table 1.2 in chapter 1). Peptides have been selected against materials, which are useful for electronic device purposes, but are not found naturally in biomineralized forms (Sarikaya, 2003; Whaley, 2000). Biological structures displaying these peptides on their surfaces can be used as templates to create nanowires and other nanostructures (Mao, 2004; Macmillan, 2002;

Yan, 2003). The M13 phage has been used as a template to create nanowires of zinc sulfide, cobalt oxide and iron-platinum (Mao, 2004).

Ligand-stabilized gold nanoparticles have been extensively used in nanoelectronics research because of their chemical stability, size-dependent physical and electrical properties as well as the ease of surface functionalization (Daniel, 2004; Homberger, 2010). Hence, they were selected as the material of choice to coat the M13 phage in order to create nanowire electrodes for a molecular transistor. The M13 bacteriophage can be genetically modified to bind to gold nanoparticles by displaying a gold-binding peptide on each copy of the major coat protein, pVIII. A few gold-binding peptides have been identified using a combinatorial peptide display library (Sarikaya, 2003; Sarikaya 2004; Brown, 2004). M13 tolerates peptide inserts up to eight amino acids long near the N-terminus of pVIII (Petrenko, 1996). Most of these gold binding peptide sequences were too long to be tolerated for insertion in pVIII. The shortest among these was an eight amino acid long gold-binding peptide sequence (Val-Ser-Gly-Ser-Ser-Pro-Asp-Ser) identified by Hunag *et al.* (2005) using a combinatorial peptide display library and thin gold films as a target substrate. Hydroxyl rich sequences have previously been reported to have an affinity for gold (Sarikaya, 2003; Brown, 1997). This gold-binding sequence was selected for the purpose of creating nanowires by displaying it on the major coat protein, pVIII. Also, the peptide sequence displayed specific binding to gold unlike non-specific binding to metal of peptide sequences such as Glu-Glu-Glu-Glu (E4) or His-His-His-His-His-His (H6) (Nam, 2006; Khalil, 2007; Moon, 2015).

Three of the mutant gold-binding phage particles thus created need to bind to a phage encapsulated nanoparticle, which will be the island of the molecular transistor as shown in the schematic in Figure 1.15. The minor coat protein of this gold-binding phage can be used for self-assembly into a molecular transistor-like structure. The minor coat protein, pIII can be modified to bind to the MS2 coat protein or chemical epitopes on the MS2 phage surface. The MS2 phage coat protein can be labelled with biotin with relative ease using the biotin-NHS ester (Parameswaran, 1990). Saggio *et al.* (1993) reported the selection of a 21 amino acid long biotin-binding peptide (AEGEFCSWAPPFKASCGDPAK). This peptide was selected from a constrained phage display library on phagemid pVIII. This peptide was selected for display on the minor coat protein, pIII of the gold-binding M13 phage in order to bind to biotin functionalised MS2 phage capsids with nanoparticles inside the capsid.

After the dual functional M13 phage binds to the biotin-labelled nanoparticle encapsulating MS2 phage particle, the higher structure can be purified from the suspension for further characterization. The M13 phage can then be coated in gold to create gold nanowire electrodes, thus creating a molecular transistor-like structure. Creation of such a dual functional M13 phage, which binds to gold using the pVIII protein and to a biotin-labelled nanoparticle-encapsulated MS2 capsid using the pIII protein was one of the aims of the work described in this thesis.

3.1.3 Mutagenesis strategies for insertion in the pVIII gene

Mao *et al.* (2004) reported the fabrication of a M13 phage templated ZnS and CdS nanowire. The ZnS-binding peptide (CNNPMHQNC) and CdS-binding peptide (SLTPLTTSHLRS) were identified using a phage display library. The peptides were inserted between amino acids 3 and 4 of the major coat protein, pVIII. A four amino acid long flexible linker sequence, Gly-Gly-Gly-Ser was also added before each peptide insert. The peptide inserts were thus 13 to 16 amino acid residues long. However, Iannolo *et al.* (1995) reported that the biggest peptides that can be displayed on every copy of pVIII were 6-8 amino acids long. Larger peptides as reported by Mao (2004) above were displayed on pVIII using a phagemid-based system, where mutant pVIII with insert were interspersed with the wild-type pVIII in the virus particle (Sidhu, 2001). Large inserts in pVIII prevent the packing of the phage particles because of the size restriction of the pIV channel through which the phage has to pass during phage extrusion. Malik *et al.* (1996) reported a cloning method whereby a unique *HpaI* restriction site was created between the codons that code for the residues three and four of the mature pVIII protein. This restriction site can be used for the cloning of foreign inserts in the pVIII gene or *gVIII*.

Petrenko *et al.* (1996) reported another strategy whereby two restriction sites *Pst I* and *BamH I* were introduced near the N-terminus of pVIII. The codons encoding for the residues 2–4 of the mature pVIII protein was removed when the resultant RF DNA of the phage was restricted with both the enzymes. Random inserts were ligated to display foreign peptides on all the copies of pVIII without any apparent effect on the phage assembly or infectivity. The phage particles produced by this method also did not show any marked bias towards a specific amino acid composition during the construction of the phage display library (Petrenko, 1996; Kehoe, 2005). Mutagenesis strategies as illustrated by both Malik (1996) and Petrenko (1996) were considered in order to clone the gold-binding sequence in the pVIII gene.

3.1.4 Aims of the work described within this Chapter

The aims were as follows:

1. The primary objective was to genetically engineer the M13 bacteriophage to display a gold-binding peptide on its major coat protein, pVIII.

2. To investigate the binding of the gold nanoparticles to this mutant gold-binding bacteriophage and physically characterise the resultant phage-nanoparticle complex.

3. To genetically engineer the gold-binding mutant M13 phage to display a biotin-binding peptide on its minor coat protein, pIII.

3.2 Results and Discussions

3.2.1. Cloning of the gold-binding peptide motif in pVIII

The Stratagene QuikChange™ site-directed mutagenesis kit (Agilent Technologies, Cheshire, U.K.) was used to create the *Hpa I* restriction site between the codons that code for residues three and four of the mature pVIII protein in WT M13 (Figure 3.1 **A**, **B**)

A

WT DNA -	5’-.... GCT GCT GAG G**G**T **G**AC GAT CCC GCA ... - 3’
Mutant DNA –	5’-.... GCT GCT GAG <u>GTT AAC</u> GAT CCC GCA ... - 3’
	Hpa I

	1	2	3	4	5	6	7
Mature WT pVIII	Ala	Glu	**Gly**	**Asp**	Asp	Pro	Ala
Mature mutant pVIII	Ala	Glu	**Val**	**Asn**	Asp	Pro	Ala

Position from N terminal

Gold-binding motif, **VSGSSPDS** to be inserted here

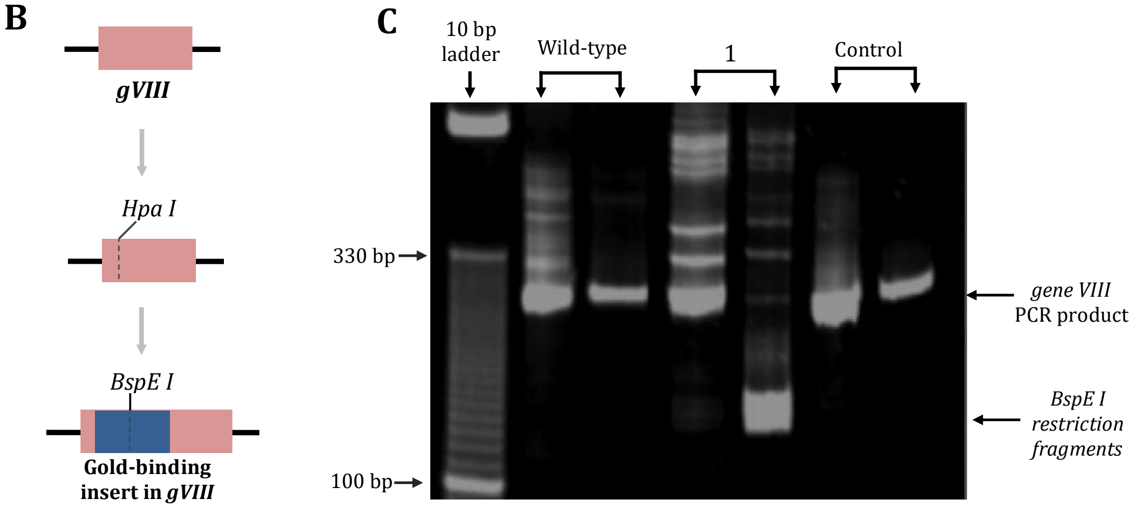

Fig 3.1 Insertion of the gold-binding DNA sequence in the *pVIII gene* of the M13 phage using *Hpa I* restriction site. (A) Nucleotide and amino acid sequences corresponding to the beginning of the mature form of pVIII in WT M13 (in black) and target mutant M13 (in red). The nucleotides highlighted in bold were substituted in order to create the *Hpa I* restriction site. The corresponding amino acid change can be seen in bold. **(B)** A schematic showing the cloning of the gold-binding gene sequence in *gVIII*. **(C)** A 10% (v/v) polyacrylamide gel showing the products of a PCR using the primers flanking *gVIII*. Each lane pair contains the PCR product on the left and its subsequent restriction with enzyme *BspE I* on the right. Enzyme *BspE I* did not cut the fragment obtained from the PCR done of WT M13, whereas it digested the PCR product obtained from the PCR done on the ligation reaction of the gold-binding motif in *gVIII* (lane 1). The control lane had no insert in the ligation reaction mix.

The oligonucleotides for the gold-binding peptide DNA to be used for the ligation and the oligonucleotides for the mutagenesis of *pVIII gene* to create the *Hpa I* site were obtained from MWG-Biotech (Ebersberg, Germany). After the ligation of the gold-binding motif into the mutant *gVIII*, the ligation reaction mix was transformed into *E.coli*. However, no plaques with the gold-binding insert were seen indicating that no viable phage progeny were produced from the ligated DNA. The success of the ligation reaction was confirmed using a simple test. The gold-binding peptide DNA sequence comprised a unique restriction site *BspE I* (Figure 3.1 **B**). Hence a region of *gene VIII* was PCR amplified using two flanking PCR primers and subsequently digested with *BspE I* (Figure 3.1 **C**). There are definite restriction fragments in lane 1, which are absent in wild-type and negative control. This clearly suggests that ligation was successful, but the mutant pVIII, displaying the gold-binding peptide resulted in unviable phage progenies.

Such issues with the pVIII phage display are not uncommon. Iannalo *et al.* (1995) reported that in the case of a long insert in pVIII, even if the phage assembly takes place, the titre of the mutant phage might be too low to be detected as plaques on a culture plate. Also, Malik *et al.* (1997) reported that in case of certain peptide insert sequences; the processing of the pVIII pro-coat protein by the leader peptidase enzyme is slowed down or even prevented at the inner membrane of the host, *E. Coli*; thus, stopping the production of mature pVIII. It has been reported that inserts only six amino acids long or less can be reliably inserted in each copy of pVIII (Malik, 1996; Malik, 1997; Petrenko, 1996, Kehoe, 2005). As it became obvious that the cloning using *Hpa I* restriction site was untenable, an alternative strategy was considered for inserting the gold-binding peptide into pVIII. Petrenko *et al.* (1996) inserted *Pst I* and *Bam HI* sites in to the *gene VIII* while creating the pVIII phage display library. The gold-binding motif was cloned in the *gene VIII* after cleaving the phage DNA with these two restriction enzymes (Figure 3.2 **A**; 3.2 **B**).

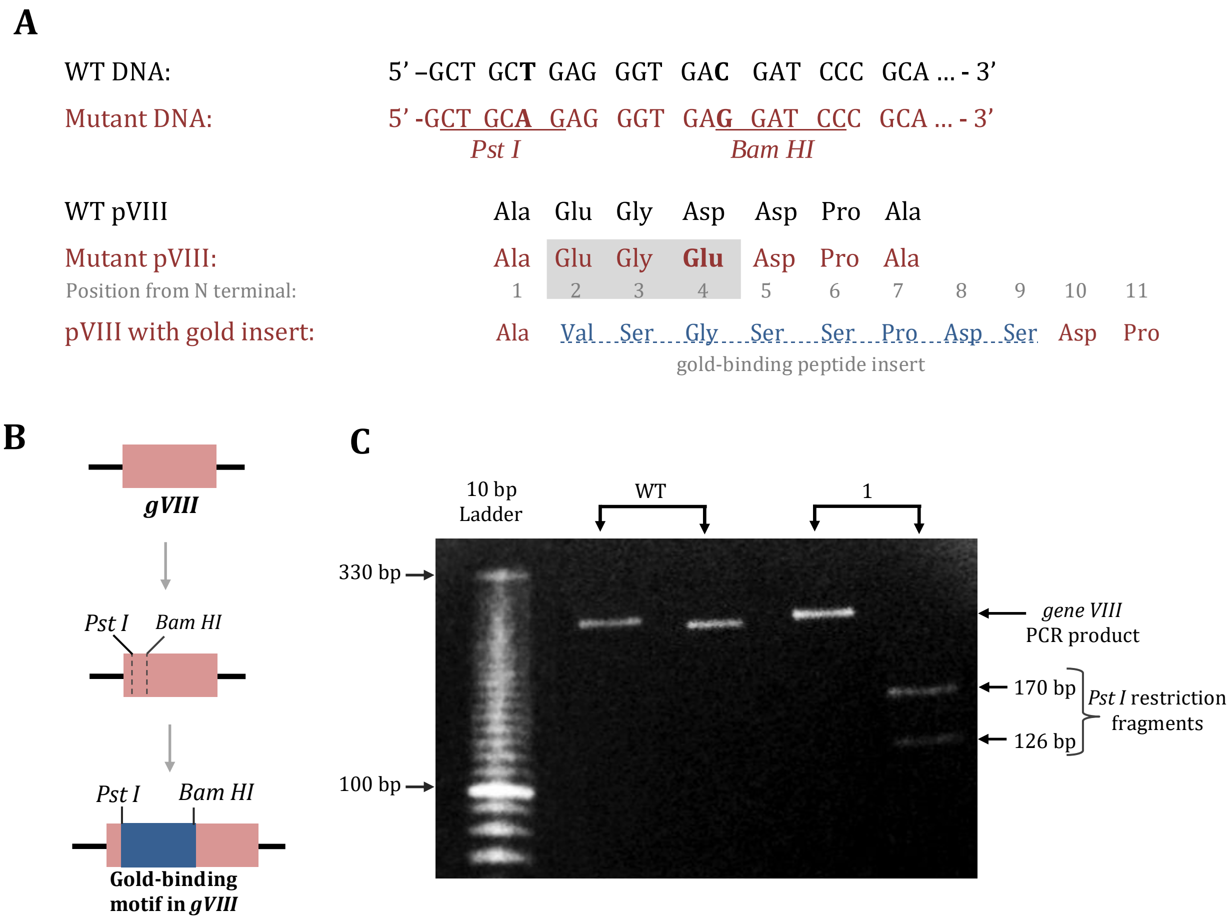

Fig 3.2. Insertion of the gold-binding motif in *gene VIII* of the M13 phage. (A) shows the nucleotide and amino acid sequences corresponding to the beginning of the mature form of pVIII in the WT M13 (in black) and the target mutant M13 (in red). The nucleotides highlighted in bold were substituted to create the *Pst I* and *Bam HI* restriction sites. The corresponding amino acid changes can be seen in bold. After cloning, the gold-binding peptide insert (in blue) replaced the amino acid residues at positions 2-4 (highlighted in grey). **(B)** shows a schematic showing the cloning of the gold-binding gene sequence in *gVIII*. **(C)** shows a 10% (v/v) polyacrylamide gel of the colony PCR fragments of an amplified region of *gVIII* from wild-type M13 and from a transformant of the site directed mutagenesis reaction. The PCR fragment on the right in each lane pair was cut by enzyme *Pst I*. *Pst I* digested the PCR fragment from the cloned transformant (lane 1) indicating successful cloning of gold-binding motif in pVIII.

However, it resulted in the removal of the codons encoding for residues 2-4 of the mature pVIII protein (Figure 3.2 **A**). The removal of the three amino acids after cloning meant that the net increase in the size of pVIII was five amino acids, even when an eight amino acid long peptide was inserted in pVIII. This was well within the insertion range of six amino acids as recommended by Petrenko (1996). Site directed mutagenesis using an insertion PCR technique of Wang *et al.* (1999) was used for cloning the gold-binding sequence in *gVIII*. To prevent the formation of primer-dimers, Wang *et al.* used a two-step PCR protocol for long insertions and deletions during site-directed mutagenesis. The gold-binding gene has a *Pst I* restriction site, not present in wild-type M13 DNA, which allowed for a simple screening of the phage with successful insertion of the gold-binding DNA sequence (Figure 3.2 **C**). Products from colony PCR using primers flanking *gene VIII* was loaded before and after restriction with enzyme *Pst I*. Two bands can be seen in lane 1 from PCR done on one of the transformants of the site directed mutagenesis reaction indicating successful insertion, while wild-type phage PCR product was left uncut. Sequencing of the mutant phage DNA further confirmed the presence of gold-binding DNA insert at the desired location (Appendix A). Since the titer of the mutant phage, henceforth called M13G phage, was comparable to that of the wild-type M13 phage, it can be concluded that the processing of pVIII had no apparent negative effect resulting from the addition of the foreign peptide to pVIII.

3.2.2 Validation of mutant M13G phage ability to bind to gold particles

The simple protocol used by Hunag *et al.*, (2005) was used to validate the ability of the M13G phage to bind to gold nanoparticles (GNPs). 10 µL of the M13G phage solution (2 x 10^{12} pfu/mL) was mixed with 100 µl of 5 nm GNP solution (5.0 x 10^{13} particles/mL) (Ted Pella Inc., California, USA). No visible precipitate was observed after incubating the mixture at room temperature for up to 2 hours. However, precipitation was observed overnight at room temperature as well as at 4^{o}C (Figure 3.3 **B**). No precipitates were observed with the wild-type M13 phage (Figure 3.3 A) or gold nanoparticles on their own (Figure 3.3 C). A precipitate was also observed with 5 nm GNPs purchased from Sigma-Aldrich (St. Louis, U.S.A.).

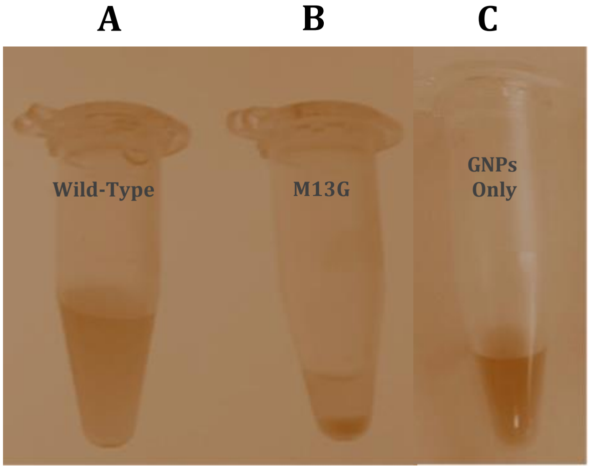

Fig 3.3. Mixture of phage and 5 nm GNPs after 16 hours of incubation at 4^{o}C. (A) Wild-type M13 phage mixed with GNPs. **(B)** Mutant M13G phage mixed with GNPs (**C**) Negative control of just the GNPs without any phage.

Although, precipitate was observed after a long duration only, the M13G phage bound to the GNPs as soon as they were added to the solution. A sample taken immediately after mixing the M13G phage with 5 nm GNPs, showed an array of GNPs along the phage surface under TEM (Figure 3.4 **A**). The length of this structure was ~1 µm, which is consistent with the length of the wild-type M13. No such ordered arrangement of GNPs was observed for the wild-type phage (Figure 3.4 **B**). A negatively stained sample of the wild-type phage with GNPs again showed that GNPs do not bind to the wild-type phage (Figure 3.4 **C**). Two pVIII subunits are only 1.5 nm apart in the phage particle and since the GNPs are 5 nm in diameter, it is physically impossible for each copy of pVIII to bind to a GNP. The average number of 5 nm GNPs bound to a M13G phage (sample size, n =

23) was 139 NPs (standard deviation, s = 14.95). There are around 2700 copies of the pVIII proteins (Clackson, 2004), with displayed gold-binding motif. Thus for 19 copies of pVIII one GNP is available, when mixed in the ratio of 1:1 of pVIII to GNP. As GNPs were in excess in the solution, expectedly, a 10-fold dilute phage solution, with pVIII to GNP ratio of 1:10, did not improve the GNPs coverage of the phage (data not shown).

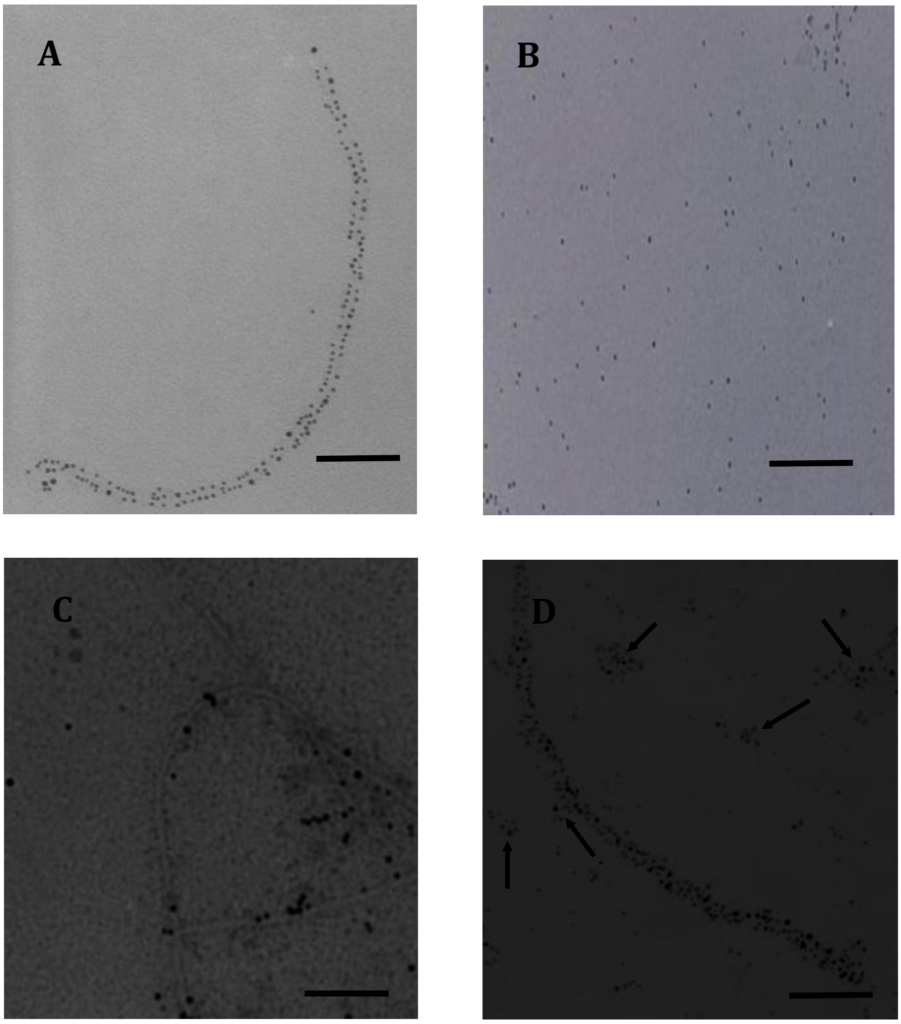

Fig 3.4. TEM images of the phage mixed with 5nm GNPs. **(A)** M13G phage mixed with GNPs **(B)** Wild-type M13 phage mixed with GNPs; **(C)** Wild-type M13 mixed with GNPs and then stained with 2% (w/v) uranyl acetate; **(D)** M13G mixed with 2x concentrated GNPs. Scale bar in the micrographs equal 100 nm.

Although, doubling the concentration of GNPs did increase the coverage of GNPs on the phage (sample size, n = 8) to 165 (standard deviation, s = 13.7), which could be because of the binding of the clusters of 3-9 GNPs to the phage (Figure 3.4 **D**; GNPs clusters are highlighted with arrows), which were formed after GNPs were concentrated (section 2.2.15).

The M13G phage also bound to 10 nm and 15 nm GNPs (Ted Pella, California, USA) (data not shown). However, no binding was observed in the case of 2 nm GNPs (Ted Pella, California, USA) and 1.4 nm GNPs (Nanoprobes Inc., NY, USA). The size-dependent binding of GNPs to the M13G phage is not unexpected. The gold-binding peptide displayed on the M13G was selected against a bulk gold surface by Huang et *al.* (2005). GNPs above the size of 3nm have predominantly a fcc crystal structure, similar to that of bulk gold (Petkov, 2005). Also, Goede *et al*. (2004) have shown that metal-binding peptides selected using phage display often bind specifically to the particular crystal surface they were selected against. Hence, the M13G phage binds to 5 nm – 15 nm GNPs, which have a well-defined atomic arrangement resembling the fcc structure occurring in bulk gold, but not to the 1.4 nm GNPs, which have been shown to exhibit amorphous-like or noncrystallographic structure (Petkov, 2005; Mottet *et al.*, 1997).

This presence of gold was further confirmed using the energy-dispersive X-ray spectroscopy (EDX) technique (Figure 3.5). EDX helps determine the elemental composition of a sample. EDX is often combined with TEM or SEM systems, such that EDX analysis can be performed while imaging the samples. The phage-nanoparticle complex was analyzed using a Philips CM200 Field Emission Gun Transmission Electron Microscope. EDX analysis of the M13G phage-GNPs complex shows clear peaks for gold, which are absent in the case of the wild-type phage and thus further supporting the hypothesis that gold was bound to the M13G phage (Figure 3.5 **A**, 3.5 **B**). The use of formvar supported copper TEM grids for sample preparation explains the copper, carbon and oxygen peak in the spectra.

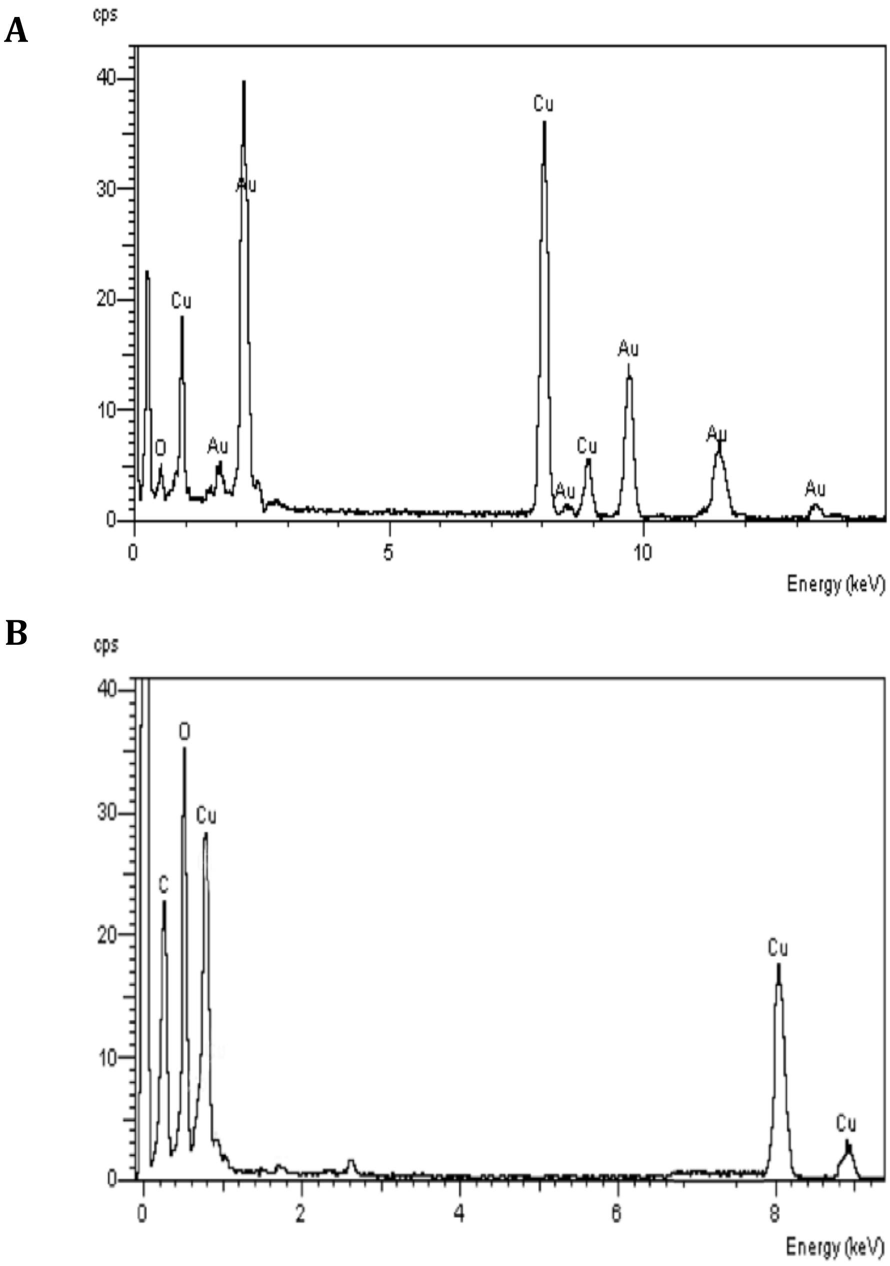

Fig 3.5 EDX analysis of (A) the M13G phage-nanoparticle complex on a copper TEM grid, and **(B)** Wild-type phage on a copper TEM grid.

Though 2 nm GNPs did not bind to the M13G phage, it was envisaged, a controlled increase in the size of 2 nm GNP can lead it to bind to the M13G phage. Hence a solution of the M13G phage and 2 nm GNPs were treated with 5 mM chloroauric acid

($HAuCl_4$) and further reduced with 50 mM sodium borohydride ($NaBH_4$) to electroless deposit gold on the GNPs. When the sample was viewed under TEM, a diffuse nanowire-like structure was seen which was the same length as the M13 phage (Figure 3.6 **A**). Indeed, a closer look at this structure complex showed tiny NPs bound to the phage (Figure 3.6 **B**). The presence of gold in the phage-NP complex was confirmed using EDX analysis (Figure 3.6 **C**). It is postulated that increasing the size of 2 nm GNPs via electroless deposition brought local structural ordering of the atoms in the GNP some of which then showed fcc-type structures. The gold-binding peptide on the M13G phage bound to these GNPs presenting fcc-type surfaces. The diffuse nature of the GNPs when viewed under TEM, indicates a polycrystalline nature of the GNPs (Zhou *et al.*, 2012).

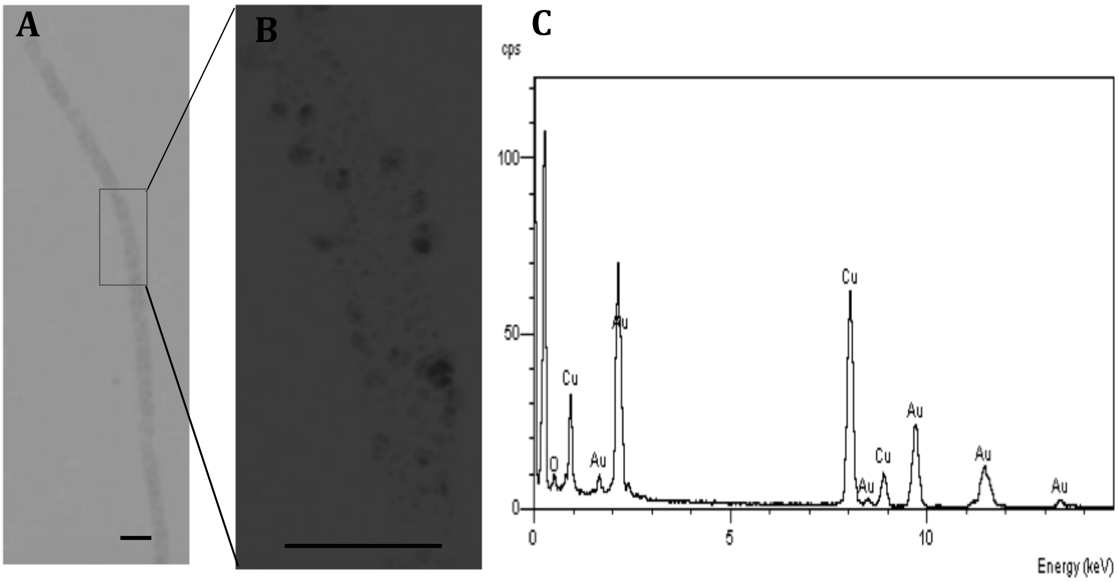

Fig 3.6 TEM image of: (**A**) the M13G phage mixed with 2nm GNPs on which further gold was electroless deposited. **(B)** Magnified section of the phage-NPs array. **(C)** EDX analysis of the phage-NPs array. Scale bars in the micrograph equal 50 nm.

The precipitate formed after incubating the phage-nanoparticle suspension overnight (Figure 3.3 **B**) suggested the aggregation of the phage-GNPs complex. However, the precipitate was formed in less than 4 hours when the concentrated phage (5×10^{13} pfu/mL) was mixed with the GNPs (Figure 3.7 **A** inset).

The filamentous M13 phage has been known to form ordered structures at high concentrations (Lee, 2002). However, no ordering was seen in the precipitate in Figure 3.7 **A**. A precipitate was also observed when an equivalent amount of M13G phage-GNP suspension was centrifuged at 13000 rpm for 10 minutes in a microcentrifuge (Figure 3.7 **B** inset). An ordering of the M13G phage-GNPs complex along its long axis was observed (Figure 3.7 **B)**. Such ordering is seen above a certain concentration only, which was likely achieved in the precipitate after centrifuging. The precipitate in Figure 3.7**A** could not reach the concentration required for ordering and formed random aggregates. The ordering was irreversible, as resuspending the precipitate did not result in a non-aggregated phage-GNP solution. This maybe because a GNP binds to two or more adjacent phage particles, as the phage particles align themselves along the long axis. This ordering can be useful for electronic device fabrication. Nam *et al.* (2006) used this liquid crystalline ordering of the M13 phage to fabricate electrodes for a lithium ion battery.

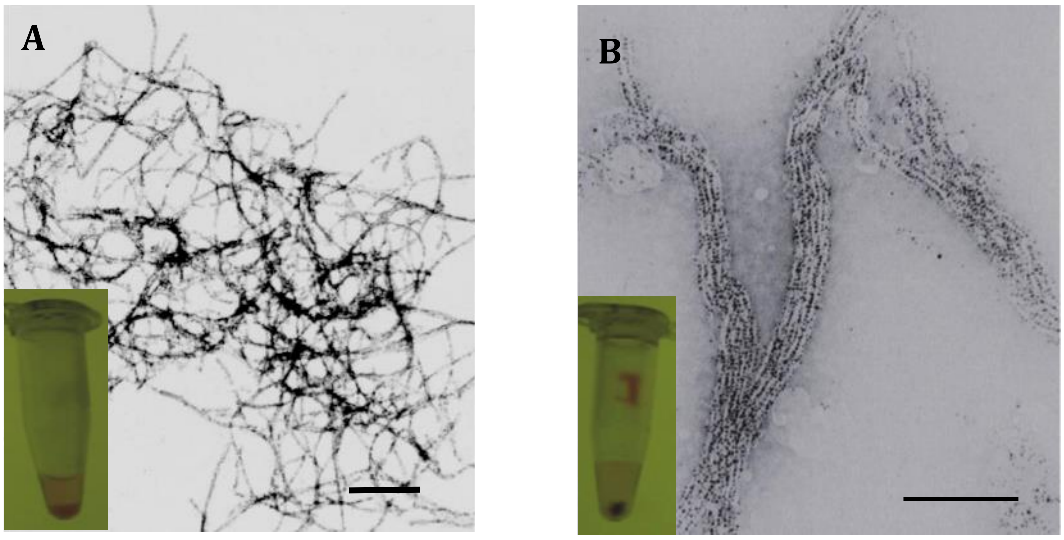

Fig 3.7 TEM images of the phage-GNPs complex at high phage concentration (5 x 10^{13} pfu/mL) (A) Phage-GNP complex precipitate (in inset) after 4 hours of incubation. **(B)** Phage-GNP complex precipitate (in inset) after centrifugation at 13,000 rpm. Sample was stained with 2% (w/v) uranyl acetate. Scale bars equal 1 μm.

3.2.3 Physical characterisation of the phage-GNP complexes

The structural integrity of the M13G phage-GNP complex in solution was found to be stable upto 70°C for 5 minutes. At temperatures above 70°C the phage particle dissociated (data not shown here). 5 nm GNPs, the M13G phage and the phage-GNP complex in solution were analyzed using an analytical ultracentrifuge to investigate their hydrodynamic property and further determine their sedimentation coefficients. The sedimentation coefficients of the gold nanoparticles and the phage-GNPs complex was found to be very close to each other and distributed over a wide range. Hence, centrifugation was not used to separate the gold-labelled phage particles from the free NPs in solution. The result of the analytical ultracentrifugation run is shown in Appendix B.

3.2.4 Cloning of biotin-binding DNA insert in the *gIII* of the M13G Phage

The schematic for creating a biotin and gold-binding phage, M13GB from M13G phage is shown in Figure 3.8. The peptide and the gene sequence of the minor coat protein, pIII after cloning the biotin-binding insert in *gIII* is shown in Figure 3.8 (**A**). The biotin-binding peptide AEGEFCSWAPPFKASCGDPAK is 21 amino acids long. The corresponding DNA insert 5'-G GTA CCT TTC TAT TCT CAC TCT GCT GAA GGT GAA TTC TGC TCT TGG GCT CCG CCG TTC AAA GCT TCT TGC GGT GAC CCG GCT AAA TCG GCC G-3' was generated using PCR from smaller primers. The three primers used for making the biotin-binding DNA insert are described in Appendix C. The gel in Figure 3.8 (**C**) shows the successful generation of the biotin-binding primer using PCR. The size of the insert was 100 bp.

A

V P F Y S H S A E G E F C S W A P P F K A S C G D P A K R P

5`- G GTA CCT TTC TAT TCT CAC TCT GCT GAA GGT GAA TTC TGC TCT TGG GCT CCG CCG TTC AAA GCT TCT TGC GGT GAC CCG GCT AAA **TCG GCC G**

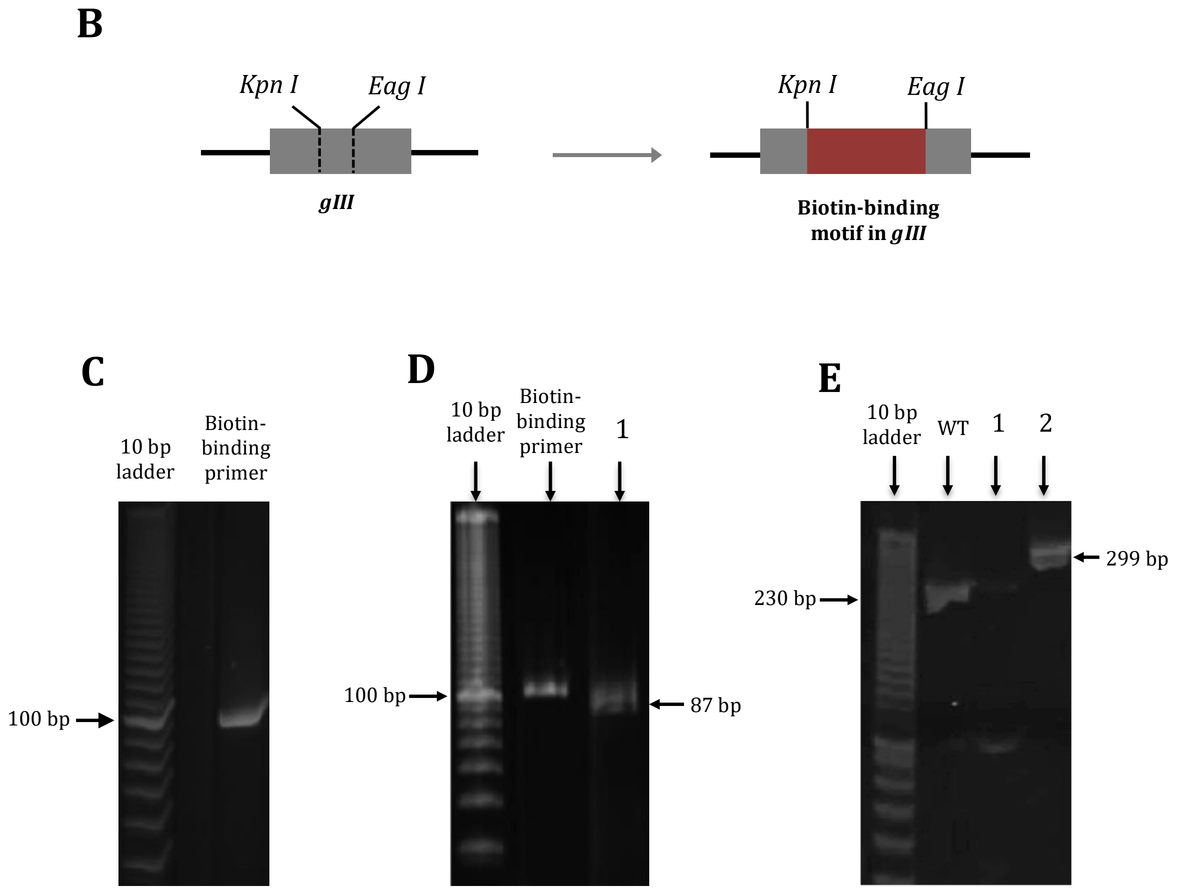

Fig 3.8 Insertion of biotin-binding motif in *gene III* of the M13G phage. (A) shows the amino acid and nucleotide sequence corresponding to the beginning of the mature form of pIII in the M13GB phage. The biotin-binding amino acid and nucleotide sequence is highlighted in red. **(B)** shows a schematic showing the cloning of the biotin-binding gene sequence in *gIII*. The restriction sites *Kpn I* and *Eag I*, near the N-terminus of *gIII* were used for cloning. **(C)** shows a 10% (v/v) polyacrylamide gel of the biotin-binding DNA insert obtained using PCR. **(D)** shows a 10% (v/v) polyacrylamide gel of the digestion of the biotin-binding insert by the restriction enzymes *Kpn I* and *Eag I*, indicating success of the PCR for insert preparation. **(E)** shows a 10% (v/v) polyacrylamide gel of the PCR fragments of an amplified region of *gIII* from an M13GH colony, indicating successful cloning of the biotin-binding motif in pIII.

The biotin-binding DNA insert was to be cloned using restriction sites *Kpn I* and *Eag I* near the N-terminus of the *gIII*. The restriction digest of the insert (Figure 3.8 **D**) shows the presence of the restriction sites *Kpn I* and *Eag I* in the biotin-binding insert prepared using PCR. The digested insert in lane 1 was smaller in size (87 bp) than the undigested insert. The digested insert was gel purified and added to the ligation reaction mix along with the template M13G RF DNA. The transformants from the ligation reaction mix were picked to validate the cloning of biotin-binding motif using PCR (Figure 3.9 **E**). The primers used for the PCR and the region of *gIII* amplified during PCR is described in section 2.2.14. The PCR product from the wild-type phage has no insert and is subsequently smaller in size at 230 bases. The negative control with water is loaded in lane 1. Lane 2 contains the PCR product of the transformant from the ligation mix at 299 bases. This shows that the biotin-binding peptide was inserted successfully in the minor coat protein of the M13G bacteriophage. The success of cloning was further corroborated by the sequencing of the *gIII* of M13GB phage as shown in Appendix C.

3.2.5 Test to determine if M13GB phage binds to biotin

500 µL of 1 x 10^{12} virions/mL of biotin-binding phage, M13GB was mixed with excess of biotin fluorescein (Pierce Biotechnology, Rockford, IL, USA). After incubating the mixture for 30 minutes, the mixture was passed through 100 kDa membrane. The retentate from membrane was suspended in TBS buffer (pH 7.9) while the filtrate was collected in a separate tube. The retentate and the flow-through were viewed under UV light (Figure 3.9 **A**). While the retentate from M13GB was found to fluoresce under the UV light, the wild-type M13KE phage retentate did not. The flow through from both the M13GB and M13KE phage fluoresced under UV as expected.

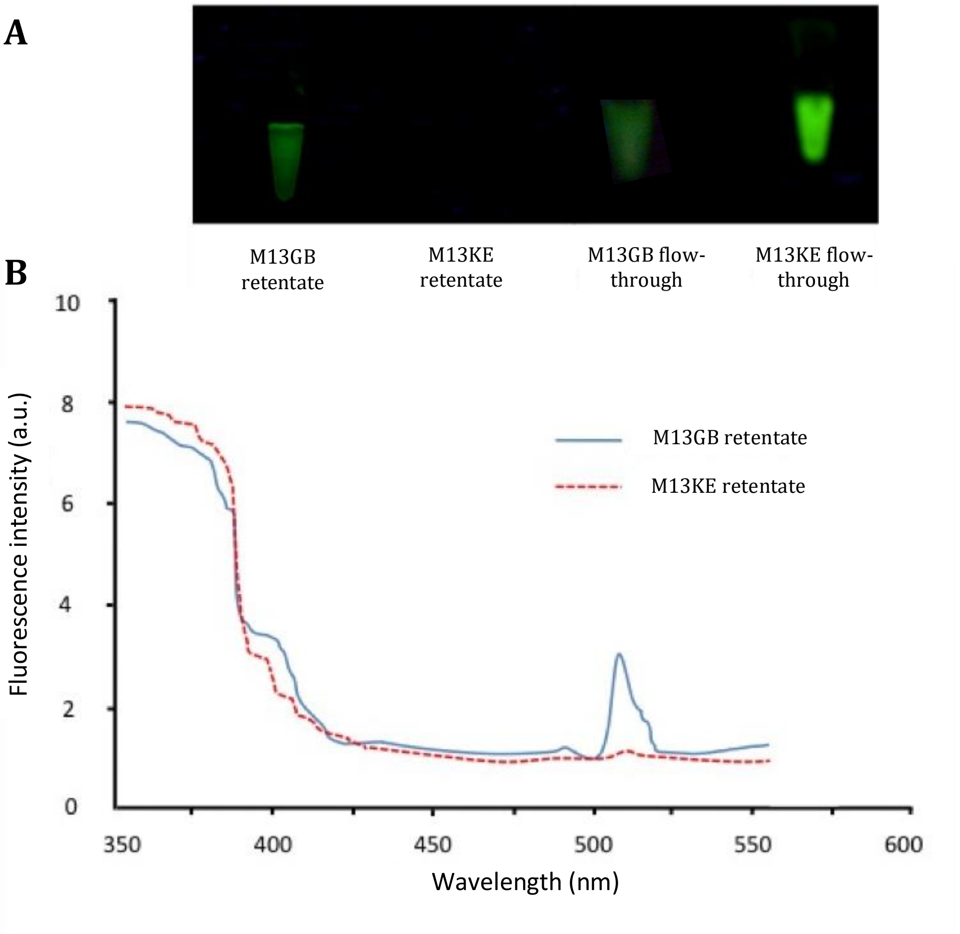

Fig 3.9 Validation of biotin-binding capability of M13GB phage. (A) Retentate and flow-through from M13GB and M13KE phage mixed with excess fluorescein biotin viewed under UV light, after they were passed through 100 kDa membrane. **(B)** Emission spectra of M13GB and M13KE phage retentate.

The M13GB retentate showed an emission peak at 518 nm while the M13KE retentate did not (Figure 3.9 **B**). This suggests that the biotin fluorescein binds to the biotin-binding motif on the pIII of the M13GB phage and not to the pIII on the wild-type M13. This dual-functional phage was later used in the attempt to fabricate the molecular transistor like structure.

3.3 Conclusions

An eight amino acid long gold-binding peptide (Huang, 2005) was successfully displayed on each copy of the major coat protein, pVIII of the M13KE bacteriophage by deletion-insertion cloning. The insertion of the gold-binding sequence was done with the simultaneous deletion of a three amino acid at the N-terminus of pVIII protein. Insertion of the gold-binding sequence in the *gVIII* without any deletion, failed to produce any viable phage, as the insert was too big to be inserted in all the copies of the major coat protein, pVIII.

The phage was shown to bind to GNPs of different sizes. But the phage did not bind to 1.4 nm or 2 nm GNPs. This was likely because of the high specificity of the metal-binding peptide selected using phage display library to bind only to the crystal structure of the metal surface against which these peptides were selected (Goede *et. al.,* 2004). But as the size of the 2 nm GNPs grew during the gold deposition reaction, the M13G phage bound to these GNPs. This was possibly because of the change in the crystal structure of 2 nm GNPs as they grew in size.

A 21 amino acid long biotin-binding peptide was also added near the N-terminus of the minor coat protein, pIII of this gold binding M13G bacteriophage. The mutant phage M13GB was shown to bind to biotin-functionalized fluorescein molecules. The wild-type M13KE phage showed no such binding affinity to biotin molecules. For the self-assembly of a molecular transistor, binding of the M13GB phage to biotin-functionalized MS2 phage capsid needs to be explored, which is discussed in Chapter 6.

Chapter 4

Fabrication of M13G phage-based gold nanowire

4.1 Introduction

4.1.1 Electroless deposition of gold

The gold nanoparticles bound to the outer coat proteins of the genetically modified M13G bacteriophage form a phage-nanoparticle complex (p-GNP). The GNPs on the p-GNP complex have significant gaps between them and more gold needs to be deposited on them to reduce the gap between the NPs and form a nanowire-like structure. Depositing gold on such a nanowire scaffold using conventional electroplating techniques would require the scaffold to act as the cathode during the electrodeposition reaction (Wilkinson, 1986; Green, 2007). By displaying cathode-binding peptides on the minor coat protein, pIII, it is possible to immobilize such a scaffold on the cathode surface (Vodnik *et. al.*, 2011; Ploss *et. al.*, 2014). Similarly, the pVII display using the phagemid system can be used to immobilize the p-GNP scaffold on the cathode surface (Løset, 2011). The dielectric protein used to immobilize the p-GNP complex and the gaps between the GNPs on the p-GNP complex are likely to prevent the p-GNP scaffold from becoming a 'true' cathode. However, such limitations can be overcome with a careful design of the cathode surface (Lee *et. al.*, 2013; Lee *et. al.*, 2017).

An alternative method would be electroless deposition of gold on the p-GNP scaffold to fabricate gold nanowires. In this process the scaffold is immersed in a solution containing gold ions. A chemical reducing agent is employed as an 'electron donor' to deposit the gold ions in the solution onto the gold nanoparticles in their zero-valence state (metallic gold). The gold deposited on the scaffold acts as a catalyst for further deposition of the gold ions in the solution (Ali, 1984). The schematic of such a process is shown in Figure 4.1. The resultant gold nanoparticles are bigger in size than the original gold nanoparticles.

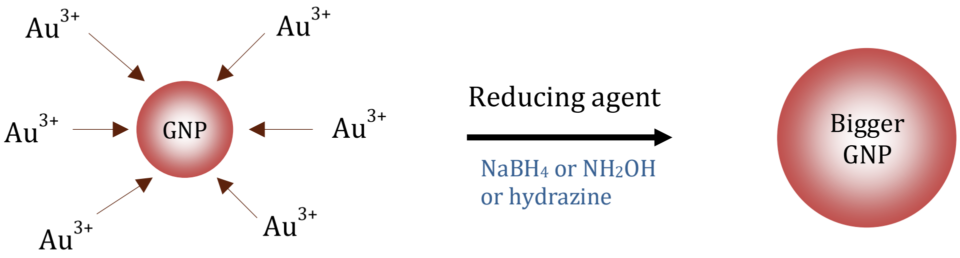

Fig 4.1. Schematic showing the electroless deposition of gold ions on the GNPs in the solution to get bigger GNPs.

Gold ions, Au^{3+} in chloroauric acid ($HAuCl_4$) in conjunction with different reducing agents are commonly used for depositing gold on a gold nanoparticle template (Her *et. al.*, 2017). Sodium borohydride ($NaBH_4$) is a widely used reducing agent for such electroless deposition reactions. However, $NaBH_4$ is a strong reducing agent and offers little control over the extent of the reaction (Narayanan, 2004; McBride, 1971). Hydroxylamine (NH_2OH) is a milder reducing agent and has also been used in such gold deposition reactions. It permits a better control of the gold deposition reaction by adjusting the reducing agent concentration, and/or the addition of reaction inhibitors such as acetic acid (Ali, 1984; Dettke, 1981).

4.1.2 Annealing of nanostructures

Grain boundaries, crystal structure and surface contamination can greatly affect the electrical and mechanical properties of these nanostructures (Xue, 2006; Wang, 2017; Wu, 2005; Langley, 2014). Thermal annealing of the deposited metal is often employed during the fabrication of the electronic devices to improve their characteristics (Kim, 2013; Lagrange, 2015). It involves heating the material to its crystallization temperature, followed by cooling. The resultant material's property is markedly different, and the structure is more homogenous. Mani *et. al.* (2006) reported a decrease in the resistivity of electroless deposited nickel nanowires than non-annealed wires upon annealing in a non-oxidizing environment. The decrease in resistance was attributed to bead coalescence and grain-boundary attrition. This happens by the diffusion of the atoms in the solid material, driving it towards an equilibrium state. The heat accelerates the rate of diffusion by providing the energy to break bonds. This process promotes grain growth with grain boundary reduction resulting in improved electrical characteristics of the nanostructure.

High temperature annealing process has also been used to remove the ligands covering the GNPs and the photoresist master grating during lithography based electronic device fabrication (Zhang *et. al.*, 2011). Zhang *et. al.*, (2006) showed that at high temperatures, molten gold from GNPs tends to spread on the surface of the substrate.

4.1.3 Aims of the work described in this Chapter

The objectives were as follows:

1. To fabricate gold nanowires from the M13G-NP complex using electroless deposition techniques.

2. To create continuous metal nanowire-like structures from the resultant gold nanowires by annealing at high temperatures under a vacuum.

3. To investigate the physical and chemical characteristics of the gold nanowires using High Resolution Transmission Electron Microscope (HRTEM), X-ray Diffraction (XRD) and Energy-dispersive X-ray spectroscopy (EDX) analysis.

4.2 Results and Discussion

4.2.1 Fabrication of gold nanowires

The gold-binding phage, M13G was mixed with 5 nm GNPs in solution to obtain a solution of the phage-gold nanoparticle complex (p-GNP) (Figure 4.2 **A** and **B**). This complex was added to 6 mM $HAuCl_4$ followed by the addition of 5 mM NH_2OH to the reaction mix (Section 2.2.17). Gold nanowires on M13 phage scaffold were obtained by the reduction of Au^{3+} ions in $HAuCl_4$ on to the GNPs bound to the phage (Figure 4.2 **C**). An AFM image of the nanowire is shown in Figure 4.2 (**D**). The increase in the thickness of the p-GNP complex to 40 nm is further evidence of the successful deposition of gold on the GNPs in p-GNP complex (Figure 4.2 **E**). The electroless deposition reaction would continue to deposit gold on the existing gold surface until either the gold ions or the reducing agent is exhausted. Therefore, in principle the nanoparticles should keep increasing in size, resulting in a thicker nanowire. However, it was observed that the gold nanowires clumped together after 60 minutes, followed by precipitation over 3-4 hours. The likely reason for this is the absence of a stabilizing agent in the electroless deposition reaction mix (Her *et. al.,* 2017).

Goldenhance^{TM}-EM formulation from Nanoprobes (New York, USA) is a commercially available reagent for electroless deposition of gold ions on GNPs. The manufacturer does not provide the details of the reagents in the Goldenhance kit. The kit contains four solutions (A-D), which are mixed in equal amounts. It uses a monovalent gold salt solution along with a reducing agent and a stabilizing agent in a near neutral buffer solution for the gold deposition reaction. In order to create a gold nanowire, the p-GNP solution was mixed with Goldenhance^{TM}-EM reagents. The nanoparticles grew in size to form phage templated gold nanowires (Figure 4.2 **F**).

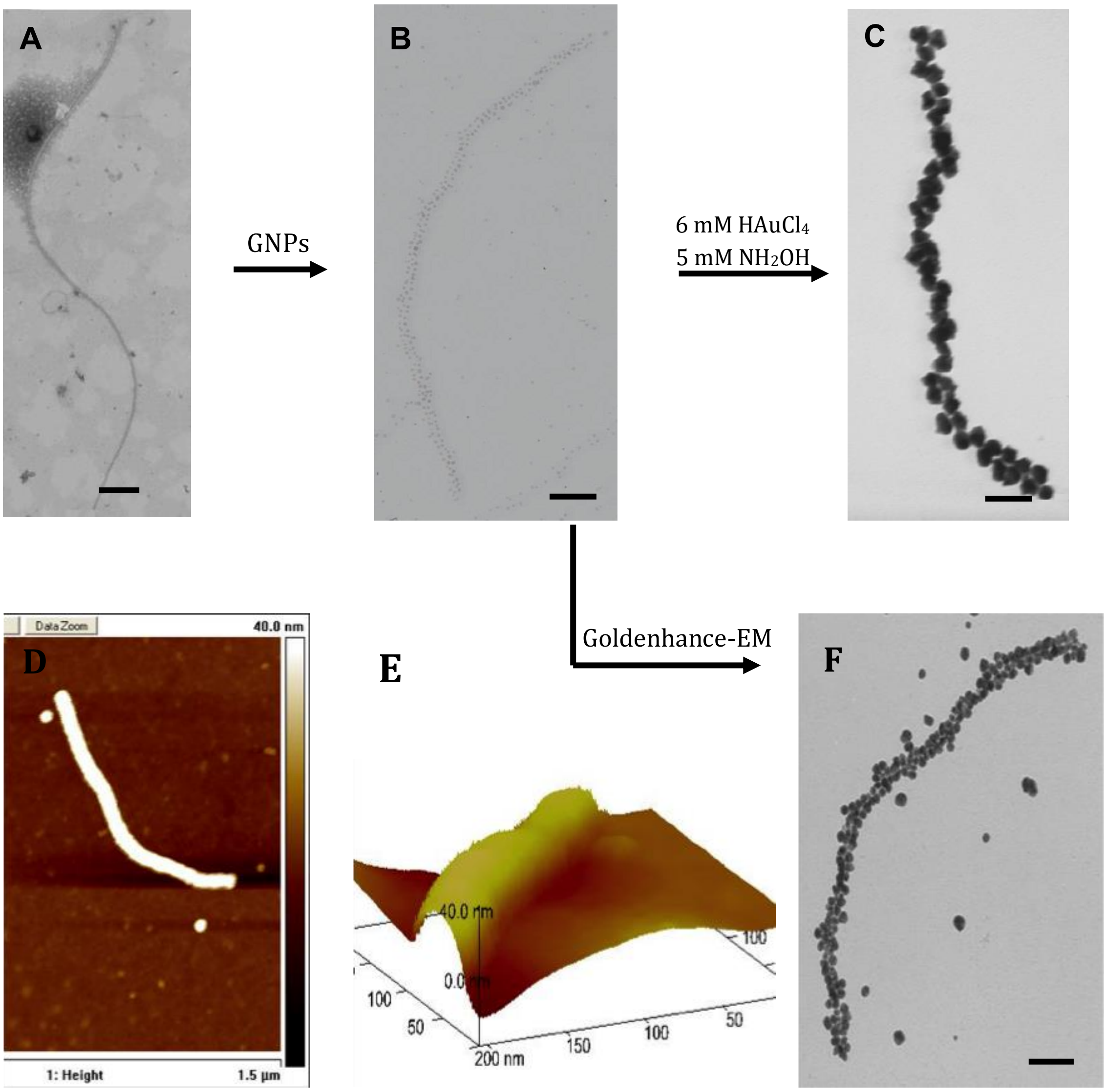

Fig 4.2. Fabrication of gold nanowires by two electroless deposition procedures. TEM image of **(A)** the M13G bacteriophage **(B)** the p-GNP complex using 5 nm GNPs (C) a gold nanowire obtained after gold was deposited on the p-GNP complex by reducing Au^{3+} ions in 6mM $HAuCl_4$ on GNP bound to the M13G phage using 5 mM NH_2OH **(D)** AFM image of the phage-based gold nanowire **(E)** the z profile of the gold nanowire showing the nanowire was about 40 nm in diameter **(F)** the TEM image of the gold nanowire obtained using Goldenhance-EM kit from p-GNP complex after 5 minutes of growth. Scale bars in micrographs equal 50 nm.

Figure 4.3 shows the time evolution of the electroless gold deposition reaction on a p-GNP complex using Goldenhance kit. The gold nanowires obtained after 5 minutes of the Goldenhance reaction had gaps between the GNPs bound to the M13G phage and the nanowire were not continuous along its length (Figure 4.3 **A**). After 10 minutes, the number of gaps and the gap length reduced with time (Figure 4.3 **B**). After 15 and 60 minutes of Goldenhance reaction, the GNPs seemed to fuse as they grew in size and the nanowires looked continuous when viewed under TEM (Figure 4.3 **C** and **D**). However, the TEM image is a 2D projection of a 3D object at nanoscale. Hence, electrical conductivity measurement of the gold nanowires would help determine, if the GNPs fused into each other as the Goldenhance reaction progressed to give a continuous nanowire. The electrical characterization of the nanowire is discussed in Chapter 5.

The GNPs unbound to the M13G phage also grew in size to form a background of free unbound GNPs. Although, the gold surface (Au^0) acts as a catalyst in the electroless deposition reaction, Au^{3+} can also reduce to Au^0 without a gold surface (Her *et. al.*, 2017; Ali, 1984). The ‘seeds’ thus formed also add to the population of background GNPs. This background of free GNPs was observed at all stages of the reaction (Figure 4.3). However, after 60 minutes, the size of background GNPs was considerably bigger than the size of phage-bound GNPs (Figure 4.3 **D**). This may be because of Ostwald ripening whereby small seed GNPs dissolve and re-deposit on the surfaces of larger GNPs (Bastus, 2011; Hansen, 2013). Restricted access of Au^{3+} ions between two adjacent GNPs on the phage surface can also inhibit growth of phage bound GNPs as opposed to the free GNPs in the solution. More study is needed to determine the mechanism. Many big GNPs in the background would be undesirable for further device fabrication using self-assembly. Hence, techniques to reduce the background of free GNPs were explored for this purpose.

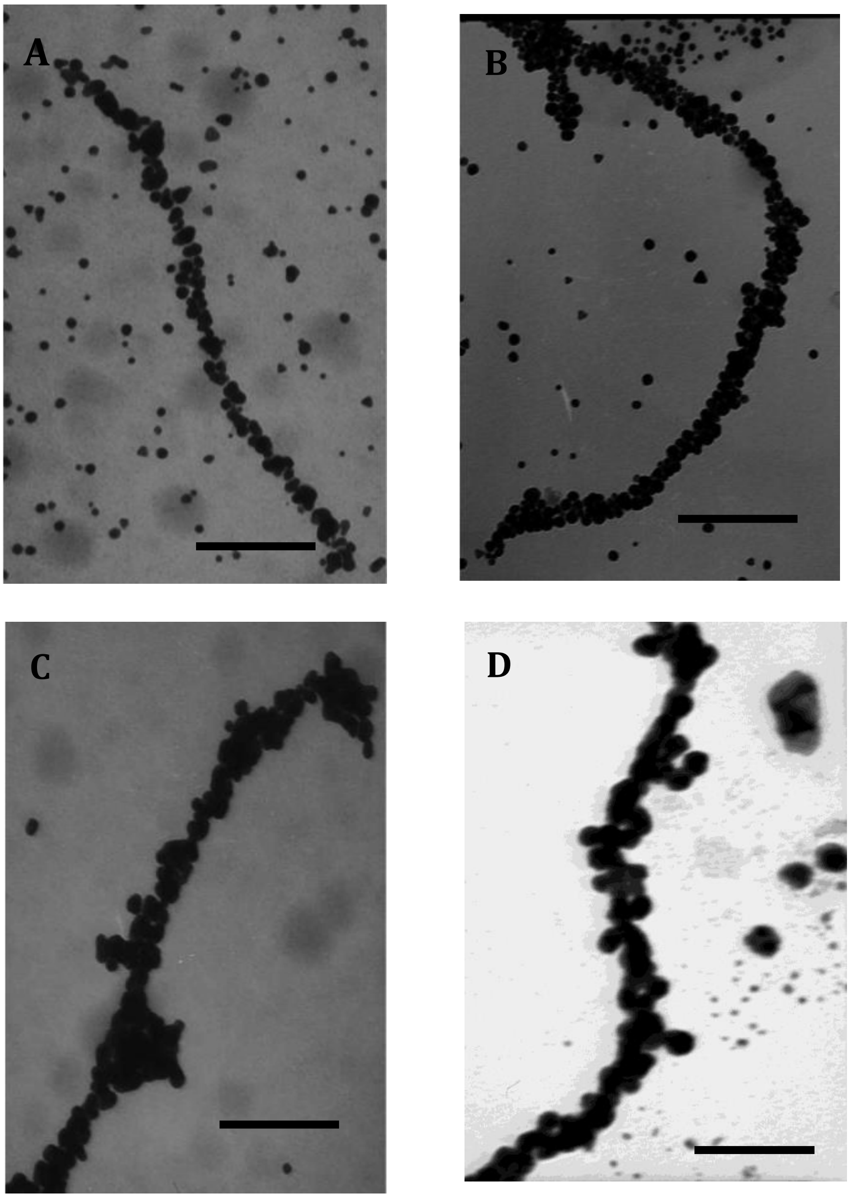

Fig 4.3. Transmission electron micrographs of the reaction time evolution of the Goldenhance-EM reaction on a p-GNP complex after **(A)** 5 minutes, **(B)** 10 minutes, **(C)** 15 minutes and **(D)** 60 minutes of reaction. Scale bars in micrographs equal 150 nm.

The high ionic strength of the reaction mixture had been reported to reduce the background, possibly by shortening the range of ionic interactions in the solution (Hayat, 1989). Hydrophobic interactions in the solution may increase the background debris by facilitating the deposition of any pre-formed gold clusters from the solution. Detergents like Tween-20 limit such interactions (Hayat, 1989). To test this 0.5 M NaCl along with

0.05 % (v/v) Tween-20 was added to the phosphate wash buffer. Although a reduction in the background gold particles was observed (Figure 4.4 **B**), it was not significant compared to regular Goldenhance reaction (Figure 4.4 **A**). Sodium thiosulfate reportedly arrests any free gold ions in solution, stopping the reaction and thus reducing the background (Danscher, 1981). However, it was found that after treating the grid with a 0.1 M sodium thiosulfate solution after the final wash step, the reduction in the background was not that significant (Figure 4.4 **C**). Autometallographic reactions like Goldenhance-EM proceed slowly at low pH (Takizawa, 1994). Solution B in the kit is a gold stabilizing agent, which controls the reactivity of the gold ions in the solution. Therefore, the amount of solution B was increased incrementally while keeping the other components the same. A significant reduction in the background was observed (Figure 4.4 **D**). However, the reaction time for the GNPs bound to the phage to fuse into each other also increased. Five parts of the activator solution B and one part of the enhancer solution A was used for the Goldenhance reaction. The final wash buffer was made of 0.05 M sodium phosphate with 0.1 M sodium chloride at pH 5.5.

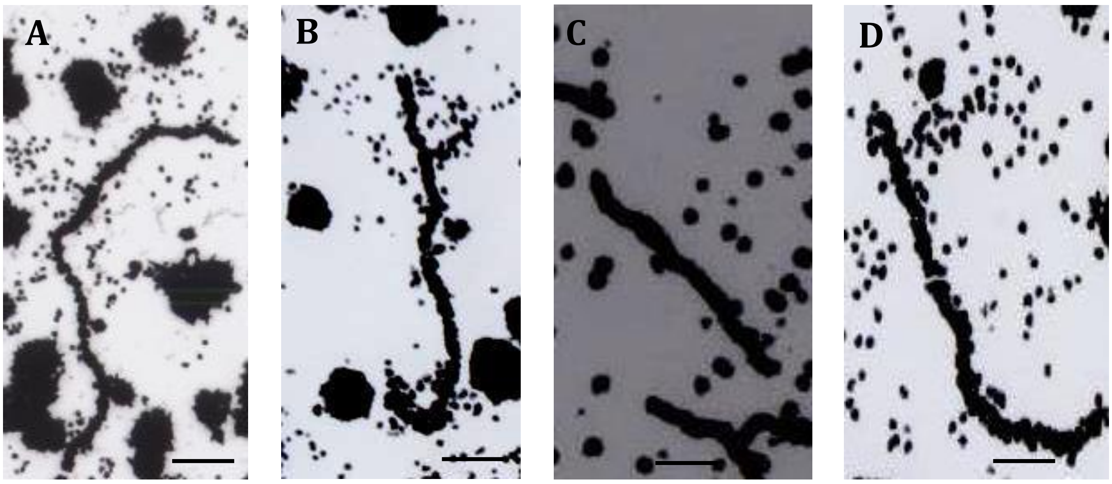

Fig 4.4. Techniques to reduce the background of free GNPs during Goldenhance reaction. TEM images of the Goldenhance reaction on p-GNP complex after 60 minutes with: **(A)** regular buffer **(B)** 0.5 M NaCl and 0.05 % (v/v) Tween-20 **(C)** 0.1 M sodium thiosulfate **(D)** 0.05 M Na_3PO_4 and 0.1 M NaCl, pH 5.5. Scale bars equal 150 nm.

4.2.2 Chemical and physical characterization of gold nanowires

The background of free GNPs in case of, M13G phage-based gold nanowires fabricated by electroless deposition of gold using 6 mM $HAuCl_4$ was less than that of Goldenhance reaction for shorter reaction time of up to 5 minutes (Figure 4.2 **C** and **F**). Hence, nanowires fabricated using this technique were selected for further characterization. These electroless deposited M13G phage-based nanowires were investigated using a Philips CM200 field emission gun transmission electron microscope. The HRTEM image in Figure 4.5 (**A**) confirms the deposition of a gold layer on the GNPs bound to the phage. Upon closer examination of the nanowire, the crystal fringes of the gold could be seen, confirming polycrystalline nature of the gold nanowire (Figure 4.5 **B**).

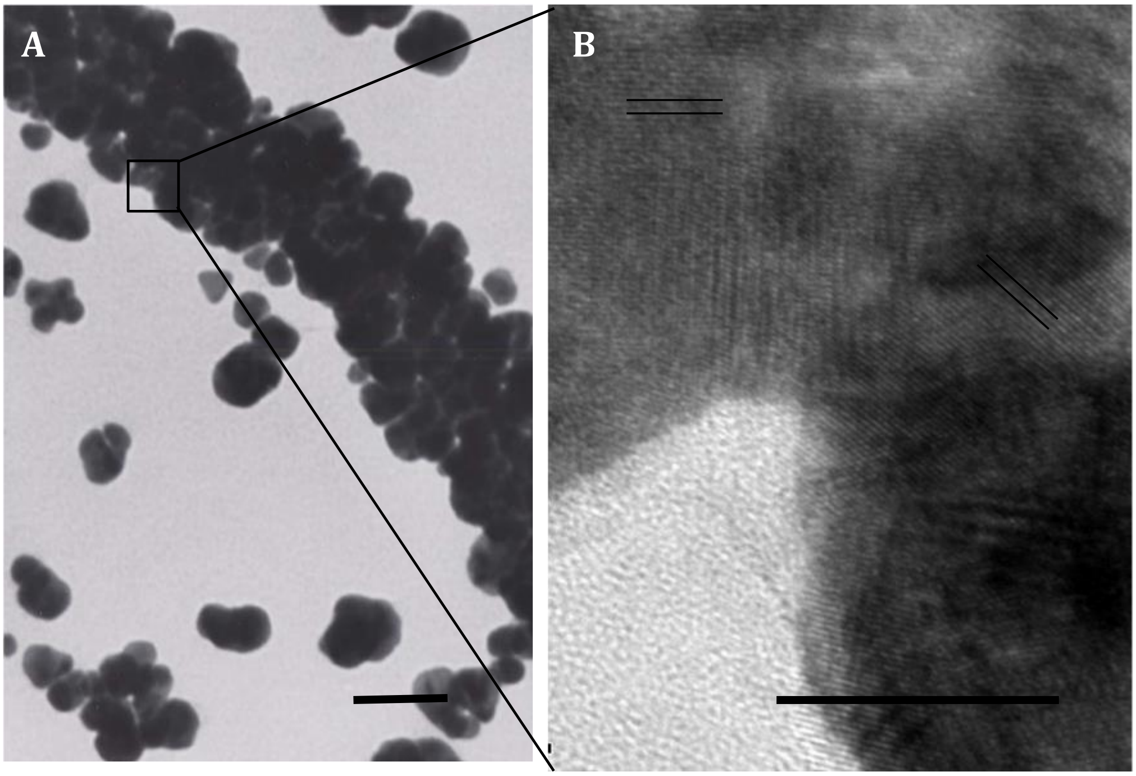

Fig 4.5. HRTEM micrographs of: **(A)** a non-annealed M13G phage-based gold nanowire. Scale bar equals 50 nm. **(B)** selected area from **A**, showing crystal lattices upon further magnification. The different orientation of the crystal fringes, as outlined by the two sets of two parallel lines, confirmed the polycrystalline nature of gold in phage-based gold nanowires. Scale bar equals 5 nm.

EDX spectroscopy was used for the chemical characterization of the non-annealed M13G phage-based gold nanowires. The EDX spectrum from a selected area (Figure 4.6 **A**) containing a M13G phage-based gold nanowire, revealed several peaks corresponding to gold (Figure 4.6 **B**). This confirmed the presence of gold in the nanowire. The peaks corresponding to copper can be explained from proximity of the gold nanowire in focus to the copper TEM grid.

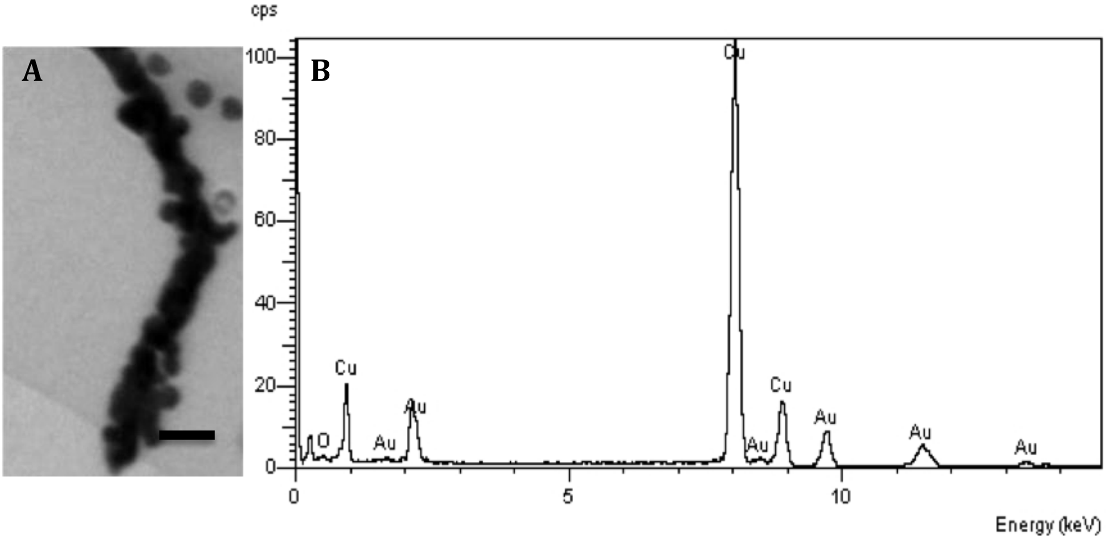

Fig 4.6. EDX of a non-annealed M13G phage-based gold nanowire. (A) Area of the gold nanowire selected for EDX investigation, unstained. **(B)** EDX spectrum of the non-annealed M13G phage-based gold nanowire. The different Au peaks are X-rays generated as electrons return to the inner shell of the gold atom, thus generating distinct energy signature. Scale bar equals 50 nm.

The crystal structure of the gold in the M13G phage-based gold nanowire was examined using SAED. This crystallographic technique is often coupled with HRTEM whereby a beam of electrons is focused on an object. The atoms in the crystalline object act as a diffraction grating for the electrons. Some of the electrons diffract at a particular angle depending upon the crystal structure of the sample, whilst other electrons pass through the sample without any deflection. The resultant diffraction pattern is a series of spots, whereby each spot corresponds to a diffracting plane (Champness, 2001). The M13G phage-based gold nanowire was investigated using SAED (Figure 4.7).

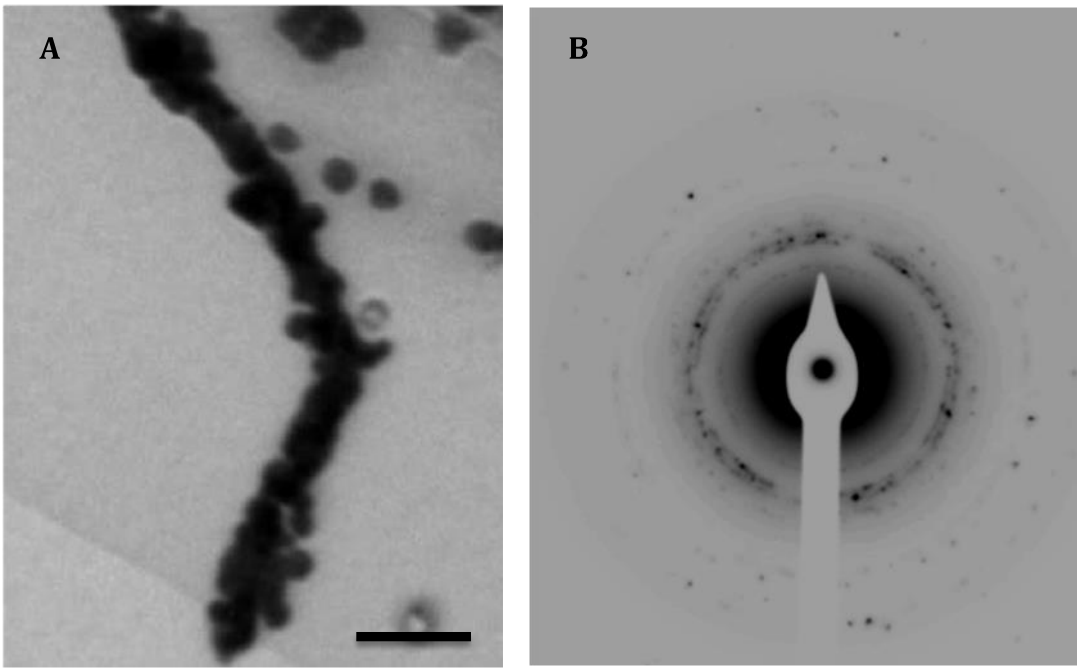

Fig 4.7 SAED of the non-annealed M13G phage-based gold nanowire. (A) The area selected for SAED investigation, unstained **(B)** The electron diffraction pattern obtained from the non-annealed M13G phage-based gold nanowire. Scale bar equals 100 nm.

The interplanar *d*-spacing of the crystal lattice can be determined by analyzing the diffraction data. Bragg's Law underlines the relationship between the interplanar *d*-spacing and wavelength λ of the electron beam. Angle of incidence and deflection of the electron beam was used to determine the interplanar *d*-spacing, using the simplified version of the Bragg's law.

$$d = \lambda l/\mathrm{R}$$

where, d is the interplanar spacing, λ the wavelength of the electron beam, l being the distance over which the diffraction pattern is projected, and R is the radius of the rings formed in the diffraction pattern. λl is also known as the camera constant, which is 23A^{o} for the machine used in the study.

From the diffraction pattern of the gold nanowire (Figure 4.7 **B**), eight rings were identified. The radius of the individual ring was measured to calculate the interplanar *d*-spacing as shown in Table 4.1. These spacing values were then compared with the data for face centred cubic (fcc*)* gold in the Joint Committee on Powder Diffraction Standards database (JCPDS), reference code 00-004-0784. The gold crystals in the M13G phage-based gold nanowire correspond to the fcc crystal structure of gold as shown in Table 4.1.

Table 4.1 Comparison of lattice ‘d’ spacing of the polycrystalline non-annealed M13G phage-based gold nanowire with crystalline fcc gold**.**

NON-ANNEALED GOLD NANOWIRE			**JCPDS for fcc gold**	
Ring No.	R (mm)	d (A°)	Ring No.	d (A°)
1	9.9	2.323	1	2.355
2	11.4	2.018	2	2.039
3	16.3	1.411	3	1.442
4	18.9	1.217	4	1.230
5	19.9	1.156	5	1.177
6	22.7	1.013	6	1.020
7	25	0.92	7	0.936
8	Ring undetected	Ring undetected	8	0.912
9	28.1	0.82	9	0.832

4.2.3 Annealing of the gold nanowires

One of the objectives of this study was to investigate the suitability of nanostructures based on virus scaffolds for fabricating electronic devices. Such devices would work best if the individual components such as nanowires have a predictable electrical behaviour. M13G phage-based gold nanowires fabricated above have minute gaps between the GNPs bound to the phage. The gaps in the nanowires are likely to make nanowires show non-linear conducting behaviour.

The M13G phage-based gold nanowires made using 6 mM $HAuCl_4$ and 5 mM NH_2OH was used. The nanowires were deposited on a carbon-coated formvar supported TEM copper grid and placed in a horizontal tube furnace (Lenton, Hope Valley, UK) under a vacuum of 10^{-3} mbar. The nanowires were annealed for an hour at the desired temperature in a non-oxidizing environment (vacuum). The nanowires were then gradually cooled back to room temperature in about 3 hours. The nanowire was heated gradually to reach the set point in all the cases. Precise control of the temperature of the nanowire sample was maintained using a thermocouple probe placed near the nanowire sample in the horizontal tube furnace which had an error of ± 1°C. The objective of the annealing study was to find the temperature at which the gaps in the nanowire were minimized as GNPs bound to phage fuse together at high temperature. In order to find the optimum annealing temperature of the M13G phage-based gold nanowire, the difference between the annealing temperatures was kept large initially to narrow down the temperature range. Nanowire samples from the same batch were annealed at 200°C, 300°C and 400°C in vacuum (Figure 4.8).

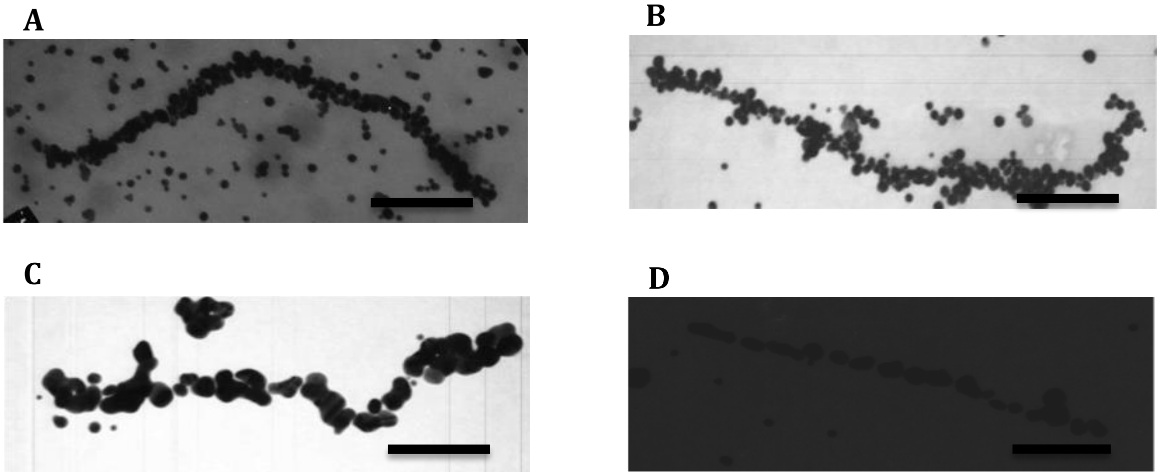

Fig 4.8. **The effects of thermal annealing of M13G phage-based gold nanowires.** TEM micrograph of **(A)** a non-annealed nanowire. TEM micrograph of nanowires annealed at **(B)** 200°C, **(C)** 300°C and **(D)** 400°C for an hour. Scale bars equal 200 nm.

The nanowires annealed at 200°C looked like non-annealed nanowires under TEM, as GNPs did not seem to fuse at this temperature (Figure 4.8 **A** and **B**). Surface diffusion of gold atoms was observed at 300°C, as the gold nanoparticles bound to the phage fused together as ‘beads’ (Figure 4.8 **C**). At 400°C, this process accelerated, and greater nanoparticles-to-bead transformation was observed (Figure 4.8 **D**). However, the resultant nanowires had bigger gaps between the adjacent fused GNPs. While annealing an 80 nm thick gold film, Porath *et al.* (1994) reported that the surface diffusion of gold atoms was the active mechanism at annealing temperatures of 300°C and below. However, the annealing temperature at which GNPs on a nanowire fused to form beads, with significant gaps between them, also depends on the thickness of the nanowire. Zhang *et. al.,* (2011) reported that 100 nm thick gold nanowires tend to break into segments when the annealing temperature is greater than 450°C. However, the bulk gold has reportedly a considerably higher annealing temperature at around 700°C in contrast to the annealing temperature observed for gold nanoparticles or nanomaterials (Fischer-Bühner, 2005). This may be because the nanoparticles have higher total surface area to volume ratio when compared to bulk gold material. Hence, for the atoms on the surface of a GNP its energetically favourable to diffuse at lower temperatures when compared to the atoms on the surface of bulk gold.

Therefore, in further annealing experiments, the annealing temperatures were kept between 200°C – 300°C in order to find the optimal temperature for the annealing of the M13G phage-based gold nanowires. The nanowires were annealed as before at temperatures: 210°C, 220°C, 230°C, 240°C, 250°C, 260°C, 270°C, 280°C and 290°C. The sample size of the study was ten nanowires for each annealing temperature. The nanowires were viewed under TEM before and after annealing (Figure 4.9).

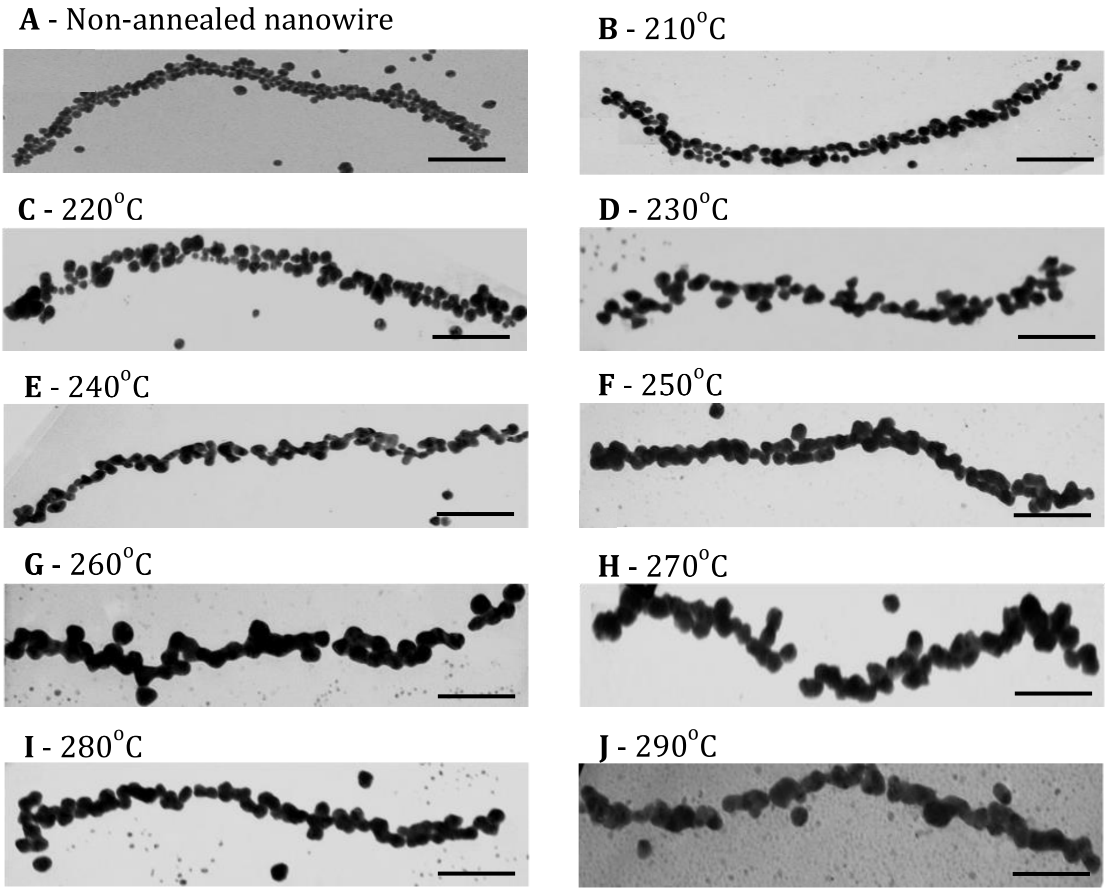

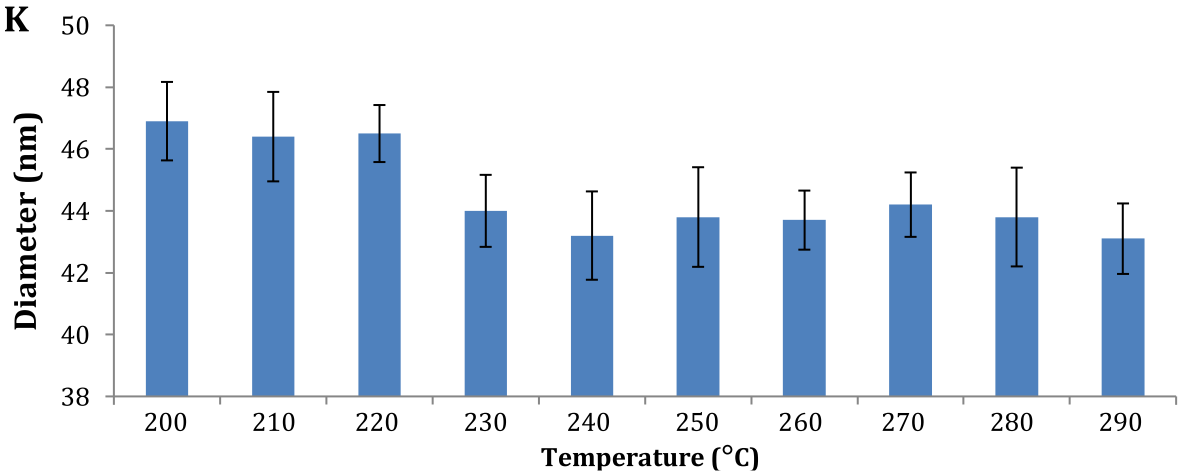

Fig 4.9. TEM images of the thermal annealing of M13G phage-based gold nanowires at different temperatures for an hour: **(A)** Non-annealed nanowire **(B)** 210°C **(C)** 220°C **(D)** 230°C **(E)** 240°C **(F)** 250°C **(G)** 260°C **(H)** 270°C **(I)** 280°C **(J)** 290°C. **(K)** Annealed nanowire diameter distribution. Data are means +/- SE (n=10). Scale bars in micrographs equal 150 nm.

The nanowires annealed at 210°C and 220°C was not very different from the non-annealed nanowires when viewed under TEM, as GNPs did not seem to fuse (Figure 4.9 **A, B** and **C**). The diameter of the nanowire also did not change for 210°C and 220°C (Figure 4.9 **K**). For temperatures below 220°C, no significant change was observed for the number of gaps in each nanowire and the length of the continuous section of the nanowire (Figure 4.10). For annealing temperature of 230°C a small decrease in the nanowire diameter and the number of gaps in a nanowire was observed (Figure 4.9 **K** and Figure 4.10 **A**). Annealing of the nanowires whereby nanoparticles fuse together to form a continuous nanowire was observed at temperatures above 230°C (Figure 4.9 **E, F, G, H, I** and **J**). The diameter of the nanowire also reduced from 47 nm in a non-annealed nanowire to 44 nm in nanowires annealed at temperatures above 230°C (Figure 4.9 **K**). A trend was observed, whereby, the gaps in the nanowire decreased to less than three and the length of the continuous section of the nanowire also increased to more than 400 nm at temperatures above 230°C (Figure 4.10).

Between 250°C and 270°C, the least number of gaps in a nanowire were observed. Also, longest sections of continuous nanowire were observed for annealing between this temperature range (Figure 4.10). At temperatures above 280°C the number of gaps in the nanowire starts increasing again as the GNPs fused to form bigger ‘beads’. At 250°C, the length of the continuous section of the nanowire was maximum and the number of gaps per nanowire reduced to 1.4 gaps per nanowire. This temperature was used for further annealing of the M13G phage-based gold nanowires. The TEM micrographs being a two-dimensional projection of the nanowires cannot reveal the gaps between two apparently overlapping nanoparticles, perpendicular to the incident electron beam. The error arising from this limitation of the imaging technique can give unpredictable results during electrical characterization of the nanowire as will be discussed in Chapter 5.

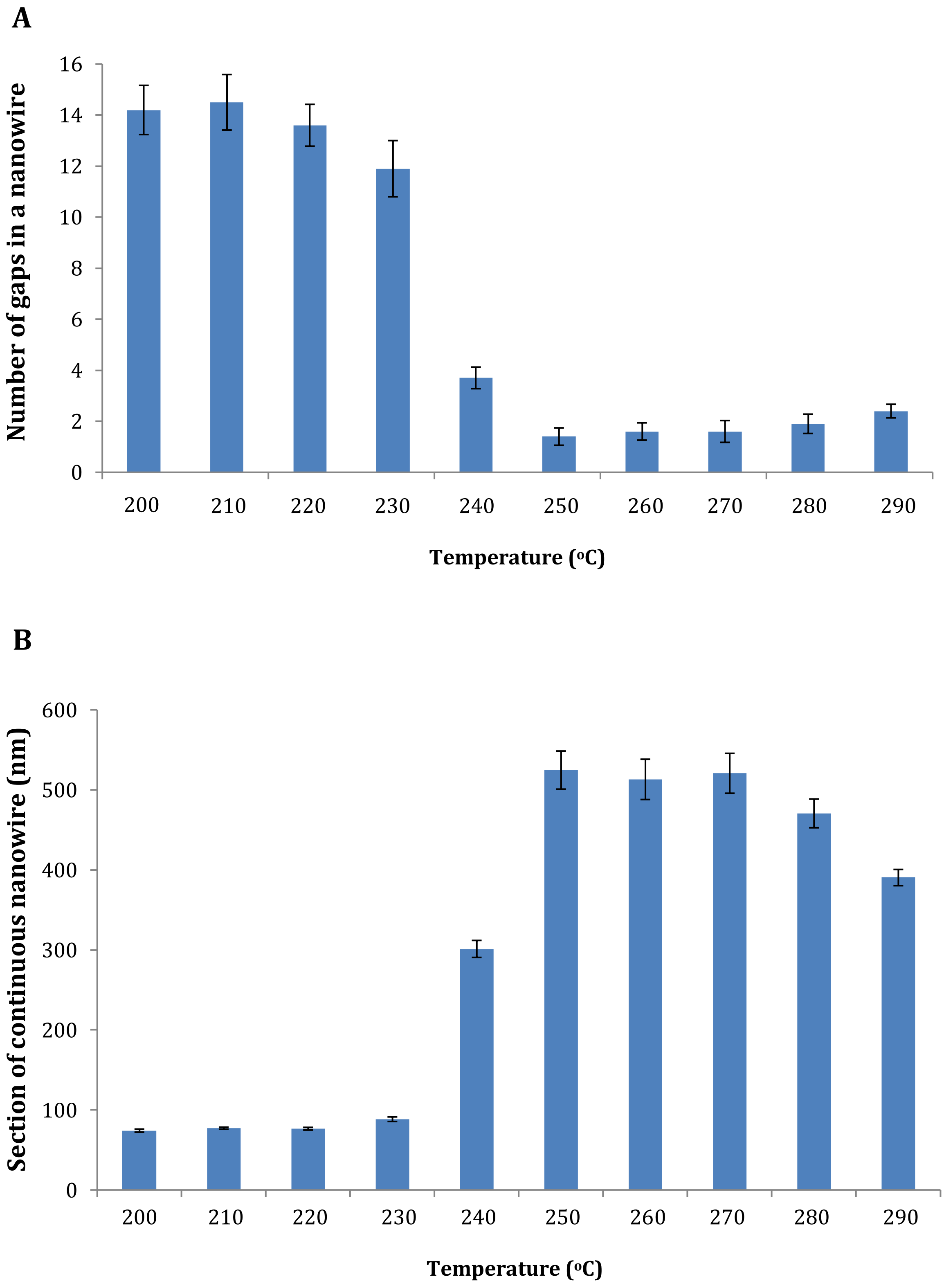

Fig 4.10. Graph showing the effect of thermal annealing of the M13G phage-based gold nanowire. (A) Number of gaps in nanowires annealed at different temperatures. **(B)** Lengths of the continuous nanowires at different annealing temperatures. Data are means +/- SE (n=10).

The effect of the annealing time at an annealing temperature on the number of gaps in the nanowire and the length of the continuous section of the nanowire was also investigated. The effect of time needed to subsequently cool the annealed nanowire was also investigated. Instead of heating the nanowire slowly to the desired temperature set point, as described above, the gold nanowires were annealed for either 1 minute or 1 hour at the desired temperature by inserting in a preheated oven, the glass tube containing the nanowire on a TEM grid. The nanowires were then subjected to rapid cooling by taking out the vacuum tube from the oven. A draught of air was introduced in the tube to cool the nanowire quickly by shutting off the vacuum pump. The nanowires were annealed at 200°C, 225°C, 250°C and 300°C. The nanowires thus annealed followed a trend similar to the one described above, whereby the number of gaps in each nanowire reduced around 250°C with a subsequent increase in the length of the continuous section of the nanowire (data not shown here). In another study, the nanowires were cooled at slower rate post-annealing by keeping the nanowires in the vacuum oven, while the heating element of the oven was turned off. However, the annealing the results in this case was also not significantly different from the one described in Figure 4.10.

The annealing experiment at different temperatures was also done for the M13G phage-based gold nanowires made using the Goldenhance method. However, again no significant difference in the annealing result was observed when compared to the nanowire made from electroless deposition of gold using 6 mM $HAuCl_4$ and 5 mM NH_2OH.

4.2.4 Characterization of the annealed gold nanowires

The M13G phage-based gold nanowires fabricated by electroless deposition of gold using 6 mM $HAuCl_4$ and 5 mM NH_2OH were annealed at $250^{o}C$ under vacuum for an hour. The nanowires were investigated further using HRTEM, EDX spectroscopy and SAED as described previously in Section 4.2.2. The nanowires annealed at $250^{o}C$ were examined using Philips CM200 FEG TEM.

HRTEM image of the annealed gold nanowire showed that post-annealing GNPs fused together to form a smoother nanowire (Figure 4.11 **A** and **B**). Upon further magnification of a section of the nanowire, crystal fringes in the gold crystals can be seen (Figure 4.11 **C**). The different orientation of these crystal fringes Figure 4.11 (**C**), similar to the case of non-annealed nanowires, confirmed the polycrystalline nature of the wire. Thus, the annealing of the nanowires promoted the growth of larger grains but did not affect their polycrystalline nature.

Further, the annealing of the nanowire at high temperature led to the removal of the bacteriophage template, resulting in a thinner gold nanowire. The M13 phage outline can be observed at the center of the non-annealed nanowire as indicated by an arrow in Figure 4.11 (**A**). The bacteriophage is not visible at the core of the nanowire after the annealing of the nanowire, even when viewed under TEM after staining with 2% (w/v) uranyl acetate solution.

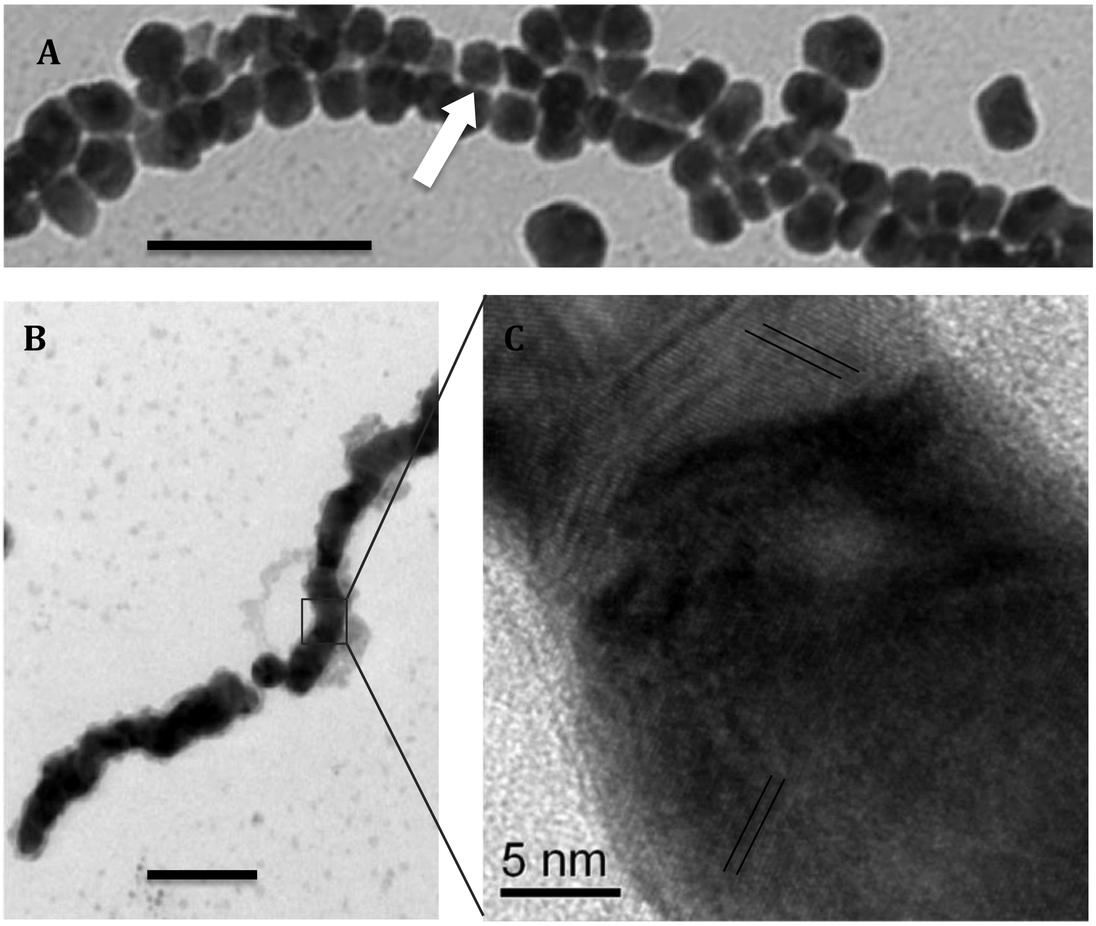

Fig 4.11. HRTEM micrographs of: **(A)** a M13G phage-based gold nanowire before annealing, **(B)** a M13G phage-based gold nanowire annealed at 250°C, **(C)** Magnification of selected area from **B**. The different orientation of the crystal fringes, as outlined by the two sets of two parallel lines, confirmed the polycrystalline nature of the annealed nanowire. Scale bar equals 100 nm unless stated otherwise.

Chemical characterization of the annealed gold nanowires was done using EDX spectroscopy (Figure 4.12). The EDX spectrum from a selected area (Figure 4.12 **A**) containing an annealed M13G phage-based gold nanowire, revealed several peaks corresponding to gold (Figure 4.12 **B**). This confirmed the presence of gold in the nanowire. The peaks corresponding to copper can be explained from the copper TEM grid used for depositing the gold nanowires.

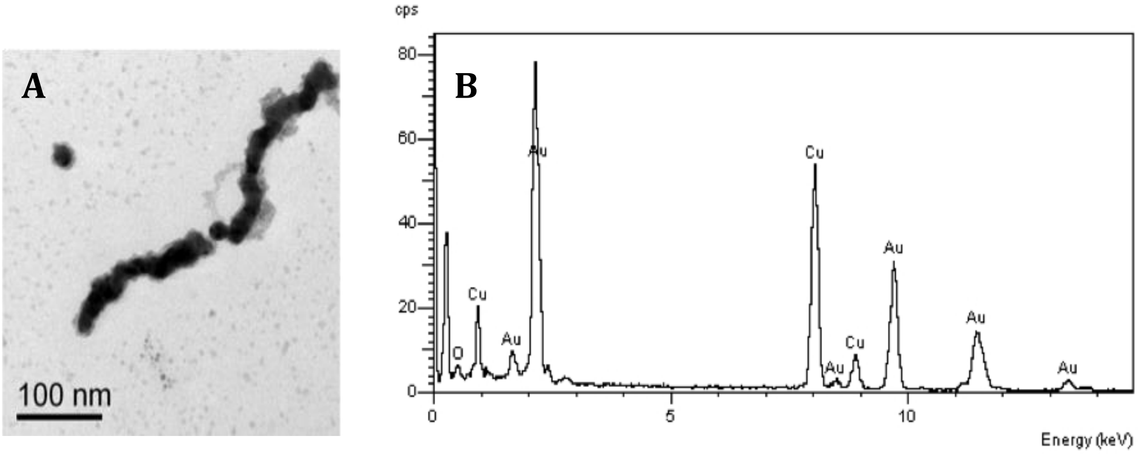

Fig 4.12. **EDX spectrum of an annealed M13G phage-based gold nanowire (A)** Area of the gold nanowire selected for EDX investigation, unstained. **(B)** EDX spectrum of the annealed M13G phage-based gold nanowire. Scale bar equals 100 nm.

The crystal structure of the gold in the annealed M13G phage-based gold nanowire was then examined using SAED. The area containing the nanowire used to get the diffraction pattern is shown in Figure 4.13 (**A**).

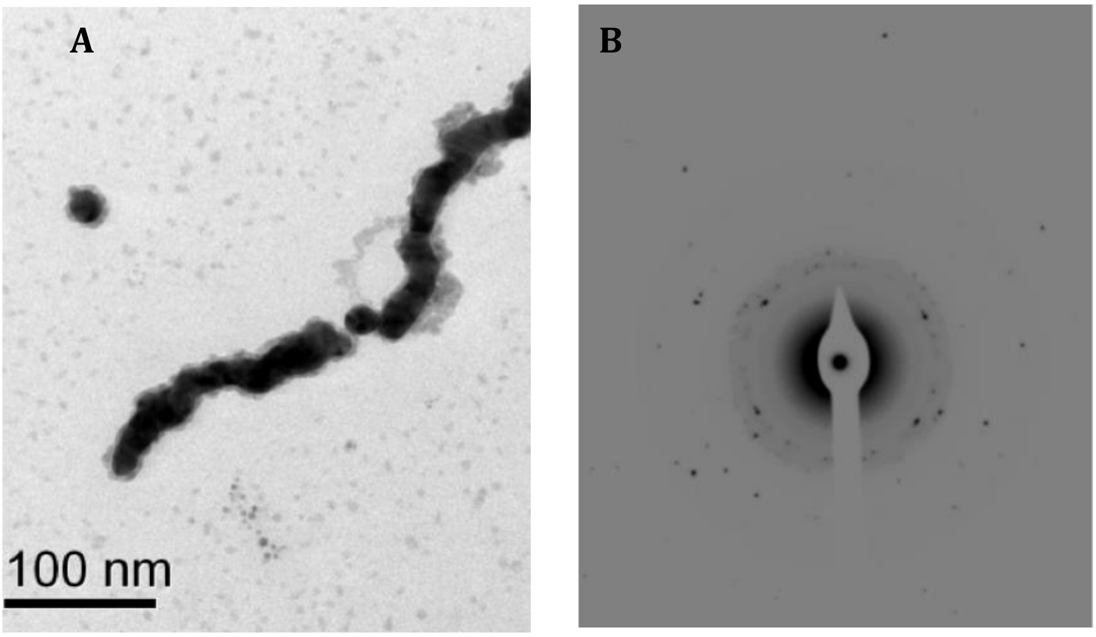

Fig 4.13. **SAED of the M13G phage-based gold nanowire annealed at 250ºC**. **(A)** Area selected for SAED investigation**. (B)** The diffraction pattern obtained from the annealed gold nanowire. Scale bar equals 100 nm.

From the diffraction pattern of the gold nanowire shown in Figure 4.13 (**B**), seven rings were identified. As discussed earlier in section 4.3, a simplified version of Bragg's equation was used to determine the interplanar spacing in the crystal lattice (*d*), which was calculated from the measured values of the radii of individual rings (*R*) of the diffraction pattern. Again *λl,* the camera constant for the equipment is 23 A°. The interplanar *d*-spacing calculated from the radius of the individual ring measured is shown in Table 4.2. These spacing values were then compared with the data for fcc gold and gold oxide, in the Joint Committee on Powder Diffraction Standards database (JCPDS), reference code 00-004-0784 and 00-043-1039. The gold crystals in the annealed M13G phage-based gold nanowire did not corresponded to the fcc crystal structure of the bulk gold found in the non-annealed nanowire. It was instead characteristic of the crystal structure of gold oxide as shown in Table 4.2, indicating that the gold nanowire had oxidized during thermal annealing.

Table 4.2 Comparison of lattice '*d*' spacing of the thermally annealed M13G phage-based gold nanowire with the Au_2O_3**.**

ANNEALED GOLD NANOWIRE			JCPDS FOR Au_2O_3	
Ring No.	**R (mm)**	**d (A^o)**	**Ring No.**	**d (A^o)**
1	8.5	2.706	4	2.756
2	9.2	2.500	7	2.538
3	9.9	2.312	8	2.433
4	11.5	2.000	11	2.034
5	15.1	1.523	26	1.507
6	16.5	1.394	30	1.396
7	18.9	1.214	46	1.217

4.3 Conclusions

The experiment described in this chapter confirmed the successful fabrication of gold nanowires on the scaffold of M13G bacteriophage, where an eight amino acid long gold binding peptide (Huang, 2005) was displayed on each copy of pVIII (see Chapter 3). Gold nanoparticles bind to this mutant phage creating a non-continuous GNP layer which was used to deposit more gold on these nanoparticles by the electroless gold deposition reaction. Two electroless gold deposition reaction were employed; one of using 6 mM $HAuCl_4$ as the source of trivalent gold ions and 5 mM NH_2OH as reducing agent, while the other used commercially available Goldenhance-EM kit.

The chemical composition and polycrystalline nature of the nanowires were confirmed using HRTEM, EDX and SAED analyses. The non-annealed nanowire had fcc crystal structure which is same as found in bulk gold. In order to improve the electrical and mechanical properties, the M13G phage-based gold nanowires were thermally annealed at different temperatures. The number gaps in the nanowire reduced as the GNPs fused at higher temperature. The best results were obtained for annealing temperature of 250°C. However, this optimal annealing temperature is dependent on the thickness of the nanowire. The nanowires were still polycrystalline post-annealing, however the EDX and SAED analyses showed that the gold nanowires had oxidized during annealing to gold oxide, even when the annealing was done under vacuum. This maybe because the diffusion pump only created a vacuum pressure of 10^{-3} mbar, which may still leave enough oxygen in the tube for oxidation of small numbers of nanowires on the TEM grid. Hence, in future a two-stage vacuum system employing a turbomolecular pump to create vacuum of up to 10^{-5} mbar can be used during annealing.

As the TEM gives a two-dimensional projection of the object at nanoscale, it is difficult to determine if the nanowires are continuous after GNPs fused post-annealing. This continuity of the nanowire can be validated by the electrical characterization of these nanowires. The electrical characterization of the M13G phage-based gold nanowires is discussed in Chapter 5.

Chapter 5

Electrical characterization of the gold nanowires

5.1 Introduction

5.1.1. Nanowires on a biological template

The current electronic devices are made using a top-down lithography-based fabrication method. For device fabrication, lithography-based technique exposes a silicon wafer to UV through a pre-patterned ‘mask’, followed by chemical etching of the exposed surface. After coating the wafer with a new layer, the process is repeated until the desired device architecture is attained. Self-assembly is an alternative fabrication route, which has not yet been adopted by the industry as the preferred method for commercial production. The self-assembly route strives to assemble the device from its basic components via the principle of molecular recognition. The nanowires will be one of the many essential components of such a self-assembled electronic device fabricated from the bottom-up.

Fabrication of a wide range of metallic and semiconducting nanowires using biological templates have been reported (Cung, 2013; Nam, 2006). The chemistry to make the nanowires using an organic template is often done in an aqueous solution. The one-pot chemistry to synthesize the nanowires is simple, but the background of free nanoparticles and residual chemical reactants in the solution, leftover from the nanowire synthesis, can act as contaminants during the device fabrication. These contaminants will be deposited along with the nanowires when nanowires in solution are deposited on the surface.

In the current scheme of things, the nanowires made from the biological template need to be deposited on a substrate for device fabrication and further electrical characterization.

A clean SiO_2 surface is the preferred choice for such device fabrication. A favorable electrostatic charge interaction between the nanowires and the silicon surface is needed to get a considerable number of nanowires on the surface. The silica substrate can be chemically modified to change its surface charge density and thus affect the interaction between the nanowires and the silica substrate (Marie, 2007).

Filamentous biological structures such as bacteriophage particles tend to form aggregates in solution depending on particle concentration, ionic strength and pH of the solution (Sidhu, 2007). The nanowires in solution, fabricated using filamentous organic scaffolds were also found to form irreversible aggregates over time. Hence, it is desirable to find optimal conditions for device fabrication via self-assembly whereby the formation of such aggregates can be precisely controlled.

5.1.2 Electrical characterization of nanowires

The nanowires on an organic template fabricated after reduction of metal ions are polycrystalline in nature and likely have rough surfaces (Kondo, 2017). Electrical transport study of these nanowires showed that their electrical resistivity is almost always higher than the bulk metal (Huang, 2005). Grain boundary reflections, surface scattering and tunneling of the charge carriers across the grain boundaries are likely reasons for this increase in resistivity (Peng, 2008). However, changes at the molecular level brought about by the annealing of the nanowires at high temperatures were found to improve their electrical properties (Wang, 2017).

Many techniques can be used for the measurement of the electrical transport properties of the nanowires. The probes of the Multi-Probe Scanning Tunneling Microscope (MPSTM) can be arranged on the nanowire such that either two or four probes are in direct contact with the nanowire (Wnek, 2012). Further, the probes can be attached to an electrical system, which can be used to apply a specific electrical potential across the nanowire and then measure the resultant flow of current in the nanowire.

Alternatively, electrodes can be patterned on top of a nanowire at either ends using Electron Beam Lithography (EBL) such that these contact electrodes are further connected to bigger patterned electrodes (Bayrak, 2018). The electrodes of such a device can thus be easily connected to an electrical system used for measuring the electrical transport property of the nanowire. The stage supporting the nanowire device can be cooled using liquid helium or liquid nitrogen to measure the electrical property of the nanowire at very low temperatures. The electrical characterization of the nanowires at low temperatures can be useful in gaining more information about the electrical transport mechanism of the nanowire.

5.1.3 Aims of the work described within this Chapter

The aims were as follows:

1. The primary objective of the study was to investigate the electrical property of the gold nanowire made using the M13 bacteriophage scaffold, before and after the annealing of the nanowires at high temperatures.

2. To investigate various methods for the removal of residual chemicals and free gold nanoparticles in the background, leftover from the synthesis of the gold nanowire.

3. To investigate the deposition of the gold nanowire on various modified and unmodified silica-based surfaces.

4. One of the objectives of this project was to investigate the electric transport properties of the nanowire at very low temperatures (less than 10 K).

5.2. Results and Discussion

During the fabrication of the gold nanowires using electroless gold deposition, while gold was deposited on the GNPs bound to pVIII of the M13 bacteriophage, it also added gold to the 'free' unbound GNPs. Thus, the unbound nanoparticles also grew in size as the electroless deposition reaction progressed. Thus, a background of unbound gold nanoparticles was observed on a substrate along with the M13 phage-templated gold nanowires (see Chapter 4, Figure 4.3). The size of the unbound GNPs depended on the method of nanowire synthesis, reaction time, the size of gold nanoparticles used, and the concentration of the gold ions used in the deposition reaction. Longer reaction times lead to larger nanoparticles. For a reaction time of about 20 minutes of gold deposition using the GoldEnhance^{TM} kit (Nanoprobes, NY, USA), the size of the background nanoparticles was similar to one obtained using electroless deposition of gold using $HAuCl_4$ and hydroxylamine. However, for reaction times > 30 minutes, the GoldEnhance^{TM} protocol produced a larger background of unbound nanoparticles than the reduction using hydroxylamine (see Chapter 4, section 4.2.1). This background is undesirable for both the device fabrication and for a reliable study of the electrical transport properties of the gold nanowires.

5.2.1 Reduction of the background of unbound nanoparticles

Two strategies were employed to reduce the number of unbound nanoparticles in the final gold nanowire suspension. In the first approach, the free nanoparticles were to be removed from the nanowire suspension before further gold was deposited using various protocols of gold deposition. This way, the majority of the unbound nanoparticles left in the solution could be attributed to the non-specific seeding and growth of nanoparticles during the electroless gold deposition reaction. In the second, the unbound gold nanoparticles were removed after the completion of the gold deposition reaction.

The nanowire suspension was passed through a 0.1 micron filter membrane (Millipore, MA, USA). As the size of the unbound gold nanoparticles was less than 100 nm, it was expected that the unbound gold nanoparticles would pass through the membrane leaving behind the larger nanowires. However, the membrane retained the nanowires as was evident from the formation of a thin red film on the membrane. Further, when the flow of water through the membrane was reversed, the resultant suspension exhibited very few nanowires when observed under TEM. It can be concluded that the nanowires bind strongly to the membrane. Similar results were obtained with both 0.2 micron and 0.4 micron filter membranes. The method did get rid of the background nanoparticles; however, the nanowires bound too strongly to the membrane to be recovered via flow reversal. However, this technique can still be useful in concentrating the nanowires in a solution onto a film.

Commercially available high molecular weight cut-off (50 - 100 kDa) dialysis membranes have pore sizes in the range of 5 - 15 nm. The pore size of the membrane is comparable to the size of the unbound nanoparticles before the initiation of the electroless gold deposition reaction. As soon as the electroless deposition reaction was initiated, the reaction mixture was placed in the dialysis tubing. Dialysis membranes of molecular weight cut-off (MWCO) 3 kDa, 50 kDa and 100 kDa were used. There was no significant reduction of the background nanoparticles for 3 kDa membrane (Figure 5.1 **B**) which was same as the background before dialysis (Figure 5.1 **A**). However, the number of free nanoparticles reduced significantly in the case of 50 kDa and 100 kDa dialysis membranes (Figure 5.1 **C** and **D**).

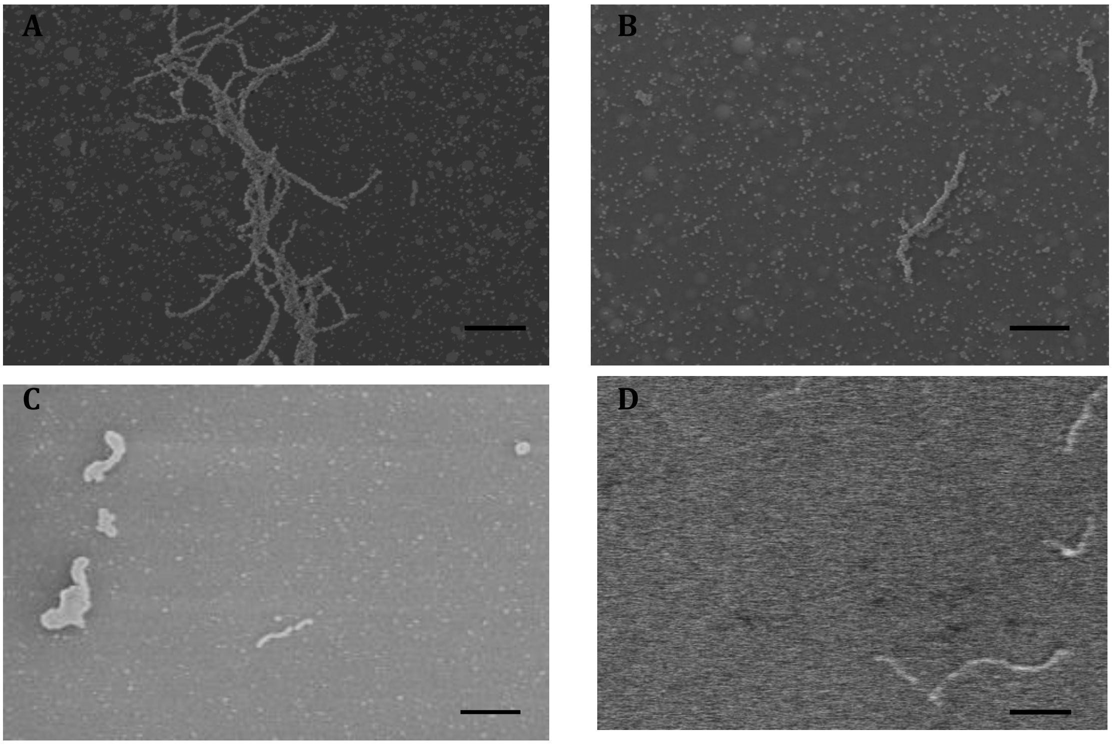

Figure 5.1. SEM image of the M13G phage-based gold nanowires suspension: **(A)** before dialysis and **(B)** after dialysis using 3 kDa MWCO membrane, **(C)** after dialysis using 50 kDa MWCO membrane, **(D)** after dialysis using 100 kDa MWCO membrane. Scale bar equals 500 nm.

The volume of the reaction mixture in the dialysis tubing increased as the dialysis progressed causing some dilution of the nanowire suspension. Formation of large aggregates of the gold nanowires was also reduced as very few of them were observed post-dialysis. The color of the dialysis membrane turned red, which indicated that either p-GNP complexes or GNPs bound to the dialysis membrane. Thus, dialysis of the nanowire reaction suspension was found to reduce the unbound gold nanoparticles in the background.

5.2.2 Deposition of Goldenhanced nanowires on a silicon substrate

The characterization of the gold nanowires synthesized using the GoldEnhance^{TM} kit (Nanoprobes, USA) was done on a formvar-supported TEM grids as described in the Chapter 4. For further electrical characterization, however, these nanowires must be deposited on a clean silicon dioxide (SiO_2) surface to form useful electronic devices. A drop of the dialyzed Goldenhanced nanowire suspension was deposited on a carbon-coated formvar-supported TEM grid and also on a piranha cleansed SiO_2 surface. After 30 seconds, the excess solution on the TEM grid was dried using blotting paper. Compressed argon gas was used to blow away the excess nanowire suspension after 30 seconds and subsequently dried the SiO_2 substrate. Nanowires deposited on the formavar supported TEM grid were easily seen under the TEM (Figure 5.2 **A**). However, very few nanowires were viewed under the SEM, when the nanowire suspension was deposited on the SiO_2 substrate (Figure 5.2 **B**). The observed ‘non-stickiness’ of the Goldenhanced M13 nanowire on a freshly cleaned SiO_2 surface was probably due to an unfavourable electrostatic charge interaction.

To counter this unfavorable charge interaction it was proposed to dry a drop of the nanowire suspension on the SiO_2 surface. The droplet was not blown off the surface using a jet of argon gas as is usually done for sample deposition. When a droplet of the nanowire suspension dialyzed for 15 minutes against water was air-dried in this manner, the majority of the surface had vast deposits of residual salt (Figure 5.2 **C**). No nanowires or their aggregates were seen in this ‘junk’ of residual salt deposit. Upon increasing the dialysis time to two hours with three changes of buffer (de-ionized water) pockets of nanowire aggregates were seen on the SiO_2 surface (Figure 5.2 **D**).

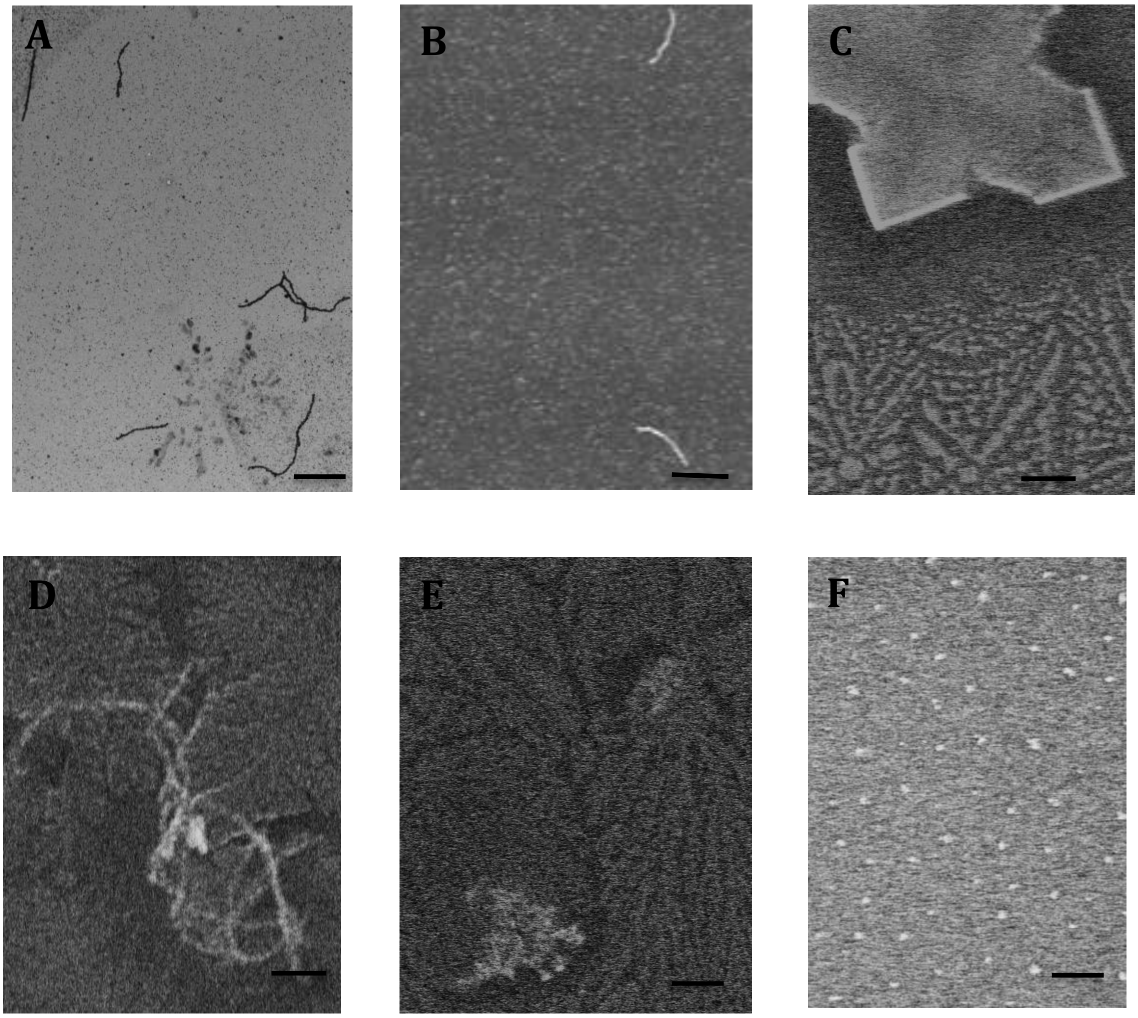

Figure 5.2. (A) TEM image of the dialyzed phage-based gold nanowires. **(B)** SEM image of the gold nanowires on a SiO_2 surface. SEM image obtained, when nanowires were deposited on a SiO_2 surface by blowing off a droplet of a nanowire suspension after **(C)** after 15 minutes dialysis, **(D)** after 2 hours dialysis. SEM image of: **(E)** plain de-ionized water dried on SiO_2 surface, **(F)** Untreated SiO_2 surface as a negative control. Scale bar equals 500 nm.

The residual salt deposit was significantly less than with the nanowire suspension after 15 minutes of dialysis, but it was still not reliable for device fabrication using EBL. The source of the residual salt deposit (Figure 5.2 **C** and **D**) was likely to be the residual chemicals in the nanowire suspension, which were not completely removed after dialysis.

However, when a drop of the de-ionized water alone was air-dried under the same conditions, some junk mass was also observed under SEM (Figure 5.2 **E**). An SEM image of a freshly prepared Piranha cleansed SiO_2 surface shows that the junk was present in the solution or surprisingly de-ionized water and not on silica surface (Figure 5.2 **F**). The residual salt was still visible when commercially available de-ionized water or distilled water was air-dried.

Hence, it was proposed to use an alternative silicon-based surface to find favorable charge interactions between the nanowires and the surface. Silicon nitride (SiN) wafers which reportedly have been used for device fabrication, were selected for this purpose. A Piranha cleansed SiN wafer was used for the nanowire deposition studies. Goldenhanced M13 nanowires dialyzed in de-ionized water was deposited on cleaned SiN and SiO_2 surfaces, whereby the excess nanowire solution was blown off. Nanowires were seen on a SiO_2 surface (Figure 5.3 **A**). A SiN surface was found to be too saturated with the accumulated charge from the electron beam of the SEM, to see any nanoscale features (Figure 5.3 **B**). No such charge accumulation was observed for the SiO_2 surface. Application of double-sided copper tapes or carbon cement on the SiN wafer, to dissipate the charge, was not successful. When the dialyzed Goldenhanced nanowire suspension was deposited on a 100nm thick SiN membrane TEM grid (SPI supplies, West Chester, USA) many nanowires were seen under the TEM (Figure 5.3 **C**). However, the SiN TEM grid was not a suitable surface for device fabrication.

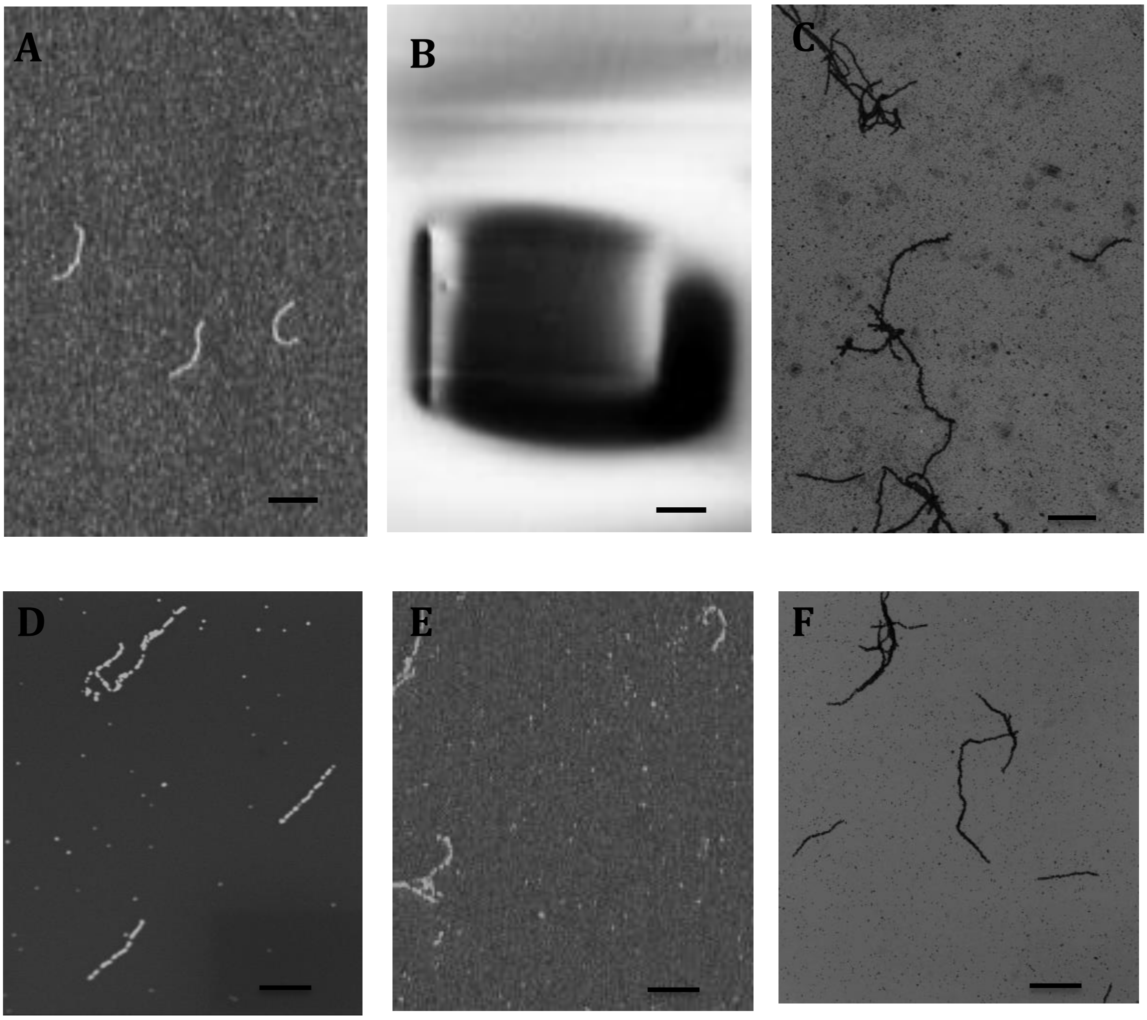

Figure 5.3: The M13G phage-based gold nanowires used here were dialyzed for 2 hours and deposited on: **(A)** SiO_2 surface **(B)** SiN wafer surface. TEM image of dialyzed M13G phage-based gold nanowires on **(C)** SiN TEM grid. SEM image of of M13G phage-based gold nanowires after deposition on: **(D)** amine modified SiO_2 surface, **(E)** thiol modified SiO_2 surface. TEM image of dialyzed M13G phage-based gold nanowires on **(F)** a carbon coated formvar supported TEM grid. The excess solution was blown off using compressed argon gas in all the cases. Scale bar equals 500 nm.

The difference in surface charge of the SiO_2 wafer and the SiN TEM grid could account for the difference in the number of nanowires deposited on each surface. Hence, it was proposed to modify the SiO_2 surface to get a favorable charge interaction. Bourgoin, *et* *al.*, (2006) reported selective deposition of carbon nanotubes on a SiO_2 surface using an amine-terminated monolayer. A similar approach was utilized to deposit Goldenhanced M13 nanowires on a SiO_2 surface. 3-aminopropyl trimethoxysilane (APTS) attaches to the freshly cleansed SiO_2 surface which is OH-terminated and forms a monolayer exposing the amine group on the outside. A 4% solution of APTS in isopropyl alcohol was used to make such a monolayer on a SiO_2 surface. However, again only a few gold nanowires were seen under SEM (Figure 5.3 **D**) when compared to nanowires deposited on the carbon coated TEM grid (Figure 5.3 **F**). Similarly, nanowire suspension was deposited on a thiol terminated SiO_2 surface made using a 4% solution of 3-mercaptopropyl trimethoxy silane (MPTS) in isopropyl alcohol. Again only a few gold nanowires were seen under SEM (Figure 5.3 **F**).

Although, Goldenhanced nanowires were deposited on the SiO_2 and SiN wafer surfaces, the number of nanowires on the surface was considerably less when the same suspension was deposited on a plasma treated carbon-coated formvar supported TEM grid or a SiN TEM grid. The few nanowires on the silicon surface could still be used for device fabrication using EBL for electrical characterization, it would be desirable to find conditions whereby the number of nanowires deposited on the surface could be improved. Next, it was proposed to see if the nanowires made using alternative techniques displayed any favorable charge interaction with the silicon-based surfaces. Hence, gold nanowires synthesized from electroless reduction of gold ions using hydroxylamine was used.

5.2.3 Deposition of hydroxylamine electroless deposited gold nanowires

The electroless deposited nanowire using hydroxylamine was dialyzed in de-ionized water for 2 hours. It was then deposited on a Piranha cleansed SiO_2 surface and left to incubate on the surface for 5 minutes. The nanowires solution droplet on the surface was then blown off the SiO_2 surface using an argon gas jet. M13G phage-based gold nanowires were found to have near even distribution over the surface (Figure 5.4), which is in sharp contrast with the Goldenhanced nanowire (see Section 5.2.2).

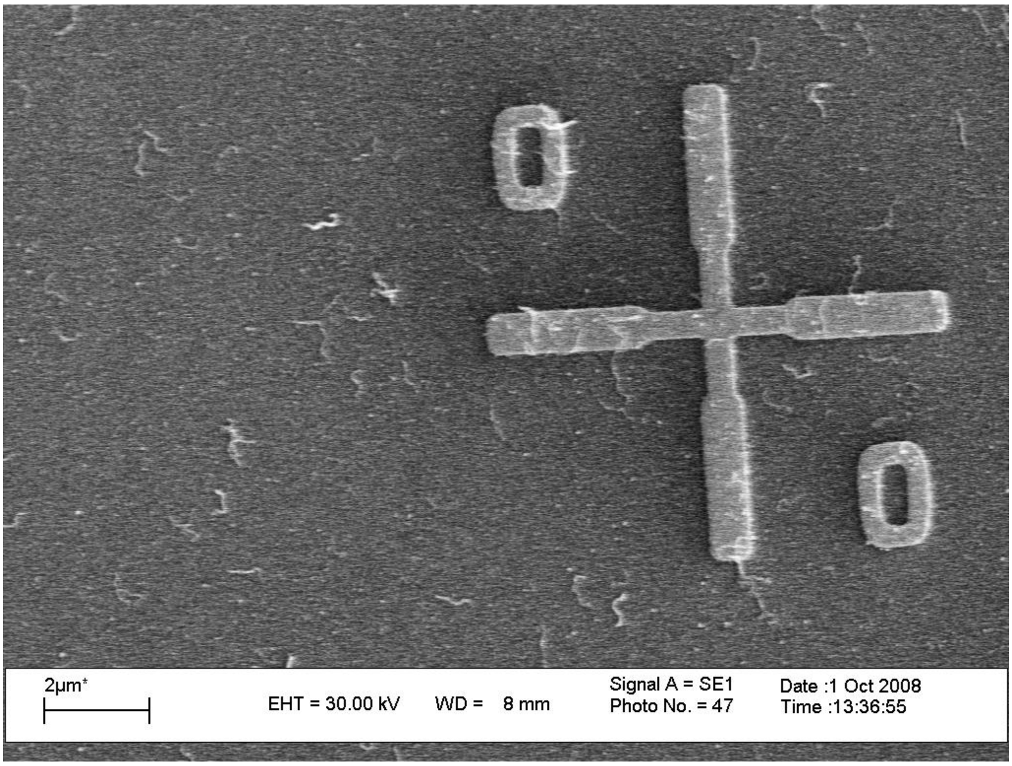

Figure 5.4: SEM image of the electroless deposited M13G phage-based gold nanowires (after 2 hours of dialysis in de-ionized water using a 100 kDa membrane) deposited on a Piranha cleansed SiO_2 surface.

This indicates that the charge on a hydroxylamine reduced nanowire is different from the Goldenhanced nanowire.

5.2.4 Electrical characterization of the M13 nanowire.

5.2.4.1 Conductivity measurement using the MPSTM

It is important to know the electrical characteristics of nanowires in order to design any useful nanoelectronic devices. In order to pass a current through a single gold nanowire in a controlled manner, probes must be connected to the two ends of the nanowire. To measure the conductivity of the M13G phage-based gold nanowire, a drop of the gold nanowire suspension was placed on a silicon nitride (SiN) TEM grid (Agar Scientific, Essex, U.K.). The TEM grid was then placed in the grid sample holder of the 4-probe STM (Omicron Nanotechnology GmbH, Taunusstein, Germany) and the holder was subsequently placed inside the STM. The chamber was then sealed, and the rotary pump was turned on. When the chamber pressure reached 10^{-3} psi, the turbo pump was switched on. Again, when a vacuum pressure of 10^{-6} psi was achieved, the ion pump was switched on. Once the chamber pressure was 10^{-7} psi, the field emission gun for the electron beam was turned on.

The SEM was then used to view the features on the grid. The UHV Nanoprobe stage was then moved with an external XY manipulator to get the probes to touch the nanowires at the desired location. Current was passed through the probes by applying electric potential between the two probes in contact in order to measure the gold nanowire electrical characteristics. Only two probes of the 4-probe STM were used to measure the electrical characteristics of the non-annealed M13G phage-based gold nanowire. It was because the nanowire displayed non-linear length dependent electrical conductivity characteristics (Figure 5.5 **A**).

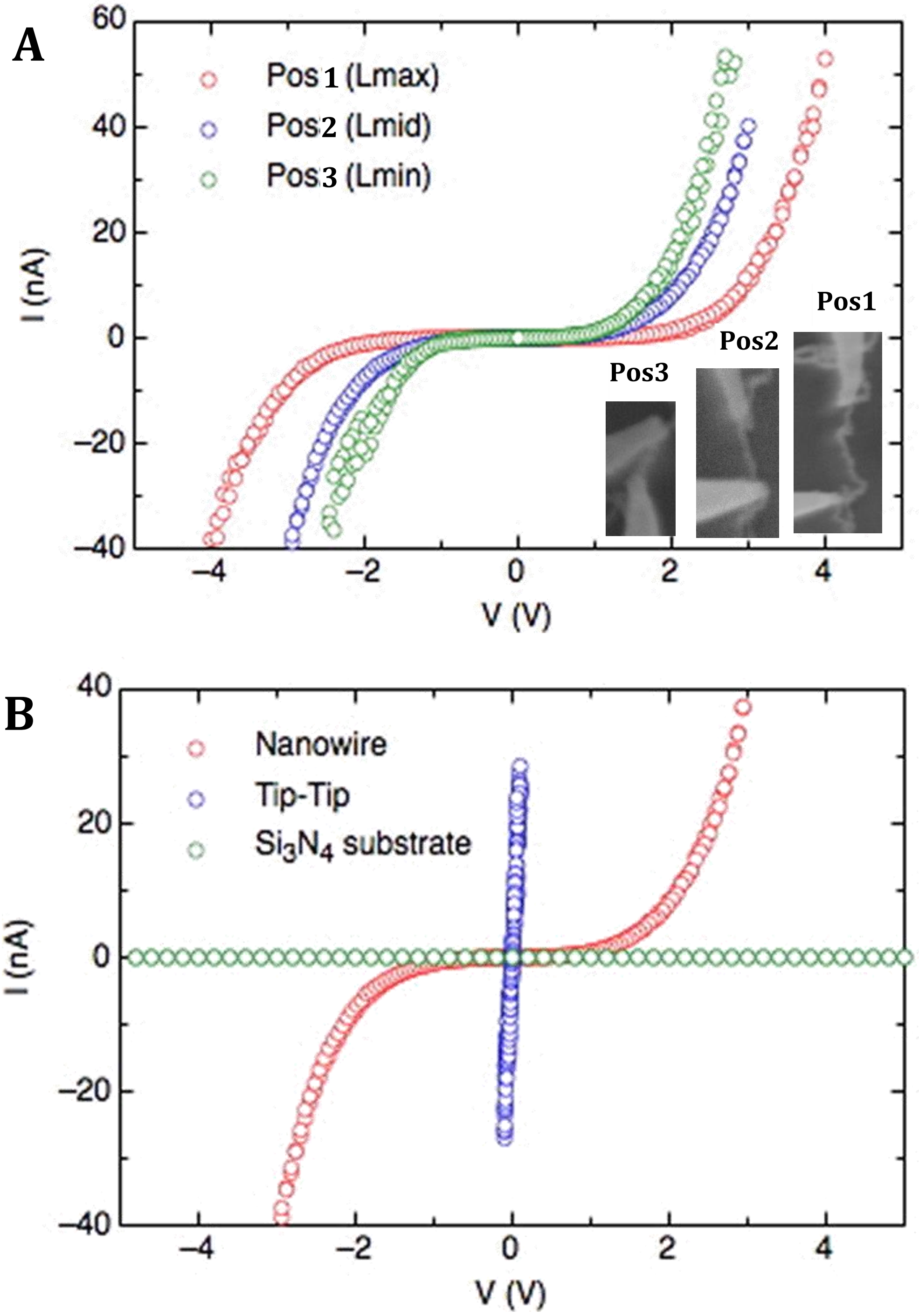

Figure 5.5. (A) Length dependent non-linear conductivity characteristics of the non-annealed M13 phage-based gold nanowires. Inset shows the SEM image of a gold nanowire attached to the two probes of the MPSTM. The distance between the two tips was maximum for 'Pos1' and minimum for 'Pos3'. **(B)** Controls showing the current-voltage (I-V) characteristics of the tip-to-tip interaction and of the Si_3N_4 substrate.

The non-linear and length dependent electrical characteristics of the nanowires indicated tunnelling of electrons through the gaps between GNPs on the M13G phage surface as the dominant conducting mechanism in the nanowire. Higher voltage requirements to detect any current when the probes were placed further apart, as in the case of 'Pos1' and 'Pos2' (Figure 5.5 **A**), further supported the theory of tunneling being the dominant conducting mechanism through the nanowire. For the control measurement, when the two tips of the MPSTM were in direct contact with each other, a low resistance ohmic contact between the probe was evident from the slope of the IV curve (Figure 5.5 **B**). When the two probes were placed on the insulating SiN surface, to measure any current flowing through the SiN substrate, no electrical conduction was observed as was expected (Figure 5.5 **B**).

However, in order to confirm the exact mechanism of conduction and find the accurate value of the nanowire resistance, measurements needed to be done at cryogenic temperatures. Hence, liquid helium was used to cool down the stage of the four-probe STM, on which the nanowire sample deposited on a SiN TEM grid was placed. But the MPSTM probes were at room temperature, as the existing set-up of the MPSTM had no provision for cooling the probes to be used for the nanowire characterization. Hence, upon contacting the nanowire with the MPSTM probes, the vast temperature differential between the two led to an instant contraction of the probes, leading to the loss of contact between the probes and the nanowires. In cases when the probe was able to make contact with the nanowire, a sharp rise in the temperature of the sample was observed when the probe made contact with the nanowires. This meant that the sub-zero temperature measurement of the nanowires was not possible with the existing MPSTM set up. Hence, a different approach for electrical characterization at cryogenic temperatures was explored.

5.2.4.2. Patterning of contacts onto the gold nanowires using EBL

EBL can be used to make contact with the nanowires and the resultant device can then be placed in a cryogenic chamber connected to external circuit. for low-temperature conductivity measurement. All EBL steps and subsequent conductivity measurement were done with the assistance of Dr Steve Johnson (School of Electronic and Electrical 'Engineering, University of Leeds). A regular 10 x 10 array of alignment marks (Figure 5.6 **A**) was made on a 2 x 2 cm SiO_2 substrate using a Raith 50 EBL machine (Raith, Dortmund, Germany). M13G phage-based gold nanowires were deposited on this patterned SiO_2 substrate and then annealed under vacuum for 1 hour at 250^oC. The position of the nanowires relative to the alignment marks was recorded using the SEM. After a 300 nm thick layer of PMMA was spin coated onto the silica substrate, the nanowires were not visible under SEM, however the electron dense gold alignment marks were still visible under SEM.

Thus, the alignment marks were used to locate the nanowire and pattern the desired electrical circuit to make contacts with the nanowires. The resist mask containing the alignment marks as well as the circuit pattern was aligned to the substrate using the three-point alignment shown in Figure 5.6 (**B**). Alignment marks away from the one where target nanowires are located were used for the alignment purpose. This approach was followed to prevent the exposure of PMMA to the electron beam in the targeted regions for patterning. The electron beam was then used to scan the pattern designed for connecting the nanowire to electrodes (Figure 5.6 **C**). The SiO_2 layer was then incubated in a 3:1 mixture of methyl isobutyl ketone for 70 seconds to dissolve the exposed PMMA regions. Then a 150 nm layer of gold was evaporated onto the surface using an electron beam evaporator. Finally, the SiO_2 substrate was 'developed' in a 100% (v/v) acetone overnight to lift off remaining PMMA. The resulting circuit was connected to the nanowire (Figure 5.6 **D**).

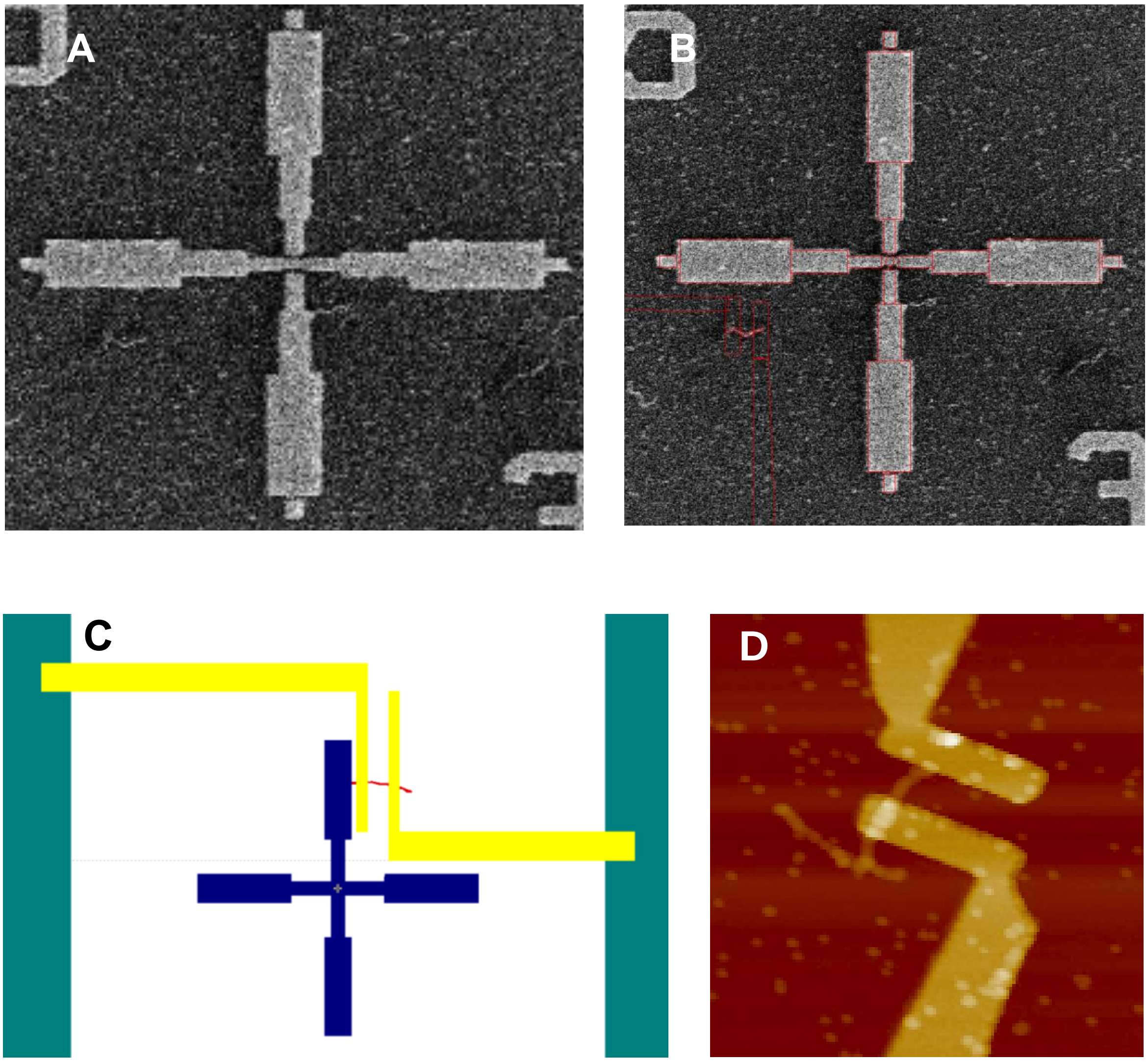

Figure 5.6: **The steps in nanowire contacts fabrication using EBL**. **(A)** SEM image of the annealed M13 phage-based gold nanowires on SiO_2 substrate, pre-patterned with gold electrodes. **(B)** The alignment of the resist mask (as red outline) with the substrate using the pre-patterned alignment marks (cross) on the substrate. The alignment marks are numbered for ease in identification during patterning and imaging. **(C)** A schematic showing the features fabricated using EBL for making contact with the nanowires. **(D)** An AFM image of the nanowire connected to the gold electrodes, patterned using EBL.

The successful patterning of contact electrodes using EBL depended on the machine alignment and its response to the software guiding the patterning process. Issues with such software and hardware synchronization mismatch in the EBL set-up resulted in failure of making contact with many nanowires using patterned electrodes. The conductivity measurement was done using the probes of a MPSTM to make contacts with the electrodes patterned on gold nanowires.

5.2.4.3. Electrical characterization of the gold nanowires

As described above, EBL was used to pattern contact electrodes on the non-annealed gold nanowires, deposited on a plasma-cleansed SiO_2 surface with alignment marks. Conductivity measurement were done using the two probes of the MPSTM. The gold nanowires displayed no electrical conduction when electrical potential was in the range of millivolts (Figure 5.7). However, when the absolute electrical potential was increased (up to 2V), the nanowire started conducting non-linearly but had high electrical resistance. Also, many nanowires displayed hysteresis in their I-V characteristics (Figure 5.7 **A**). The thicker nanowires had no apparent discontinuity when observed under SEM (Figure 5.7 **A**, inset on the right) and were expected to exhibit linear ohmic conducting behavior. However, the nanowires showed similar electrical conduction behavior, irrespective of their diameter. Although, the resistance of the thicker nanowires was less in general. The resistance of the non-annealed nanowires ranged from 10 MΩ – 1 GΩ. The sample size was 8. Unlike 4-probe STM, a length dependent conductivity measurement cannot be done on the same nanowire using EBL, in order to identify the mechanism behind the non-linear conduction behaviour. The annealed gold nanowires were expected to exhibit ohmic conduction as the nanowires were continuous when viewed under electron microscope and also had fewer grain boundaries after annealing.

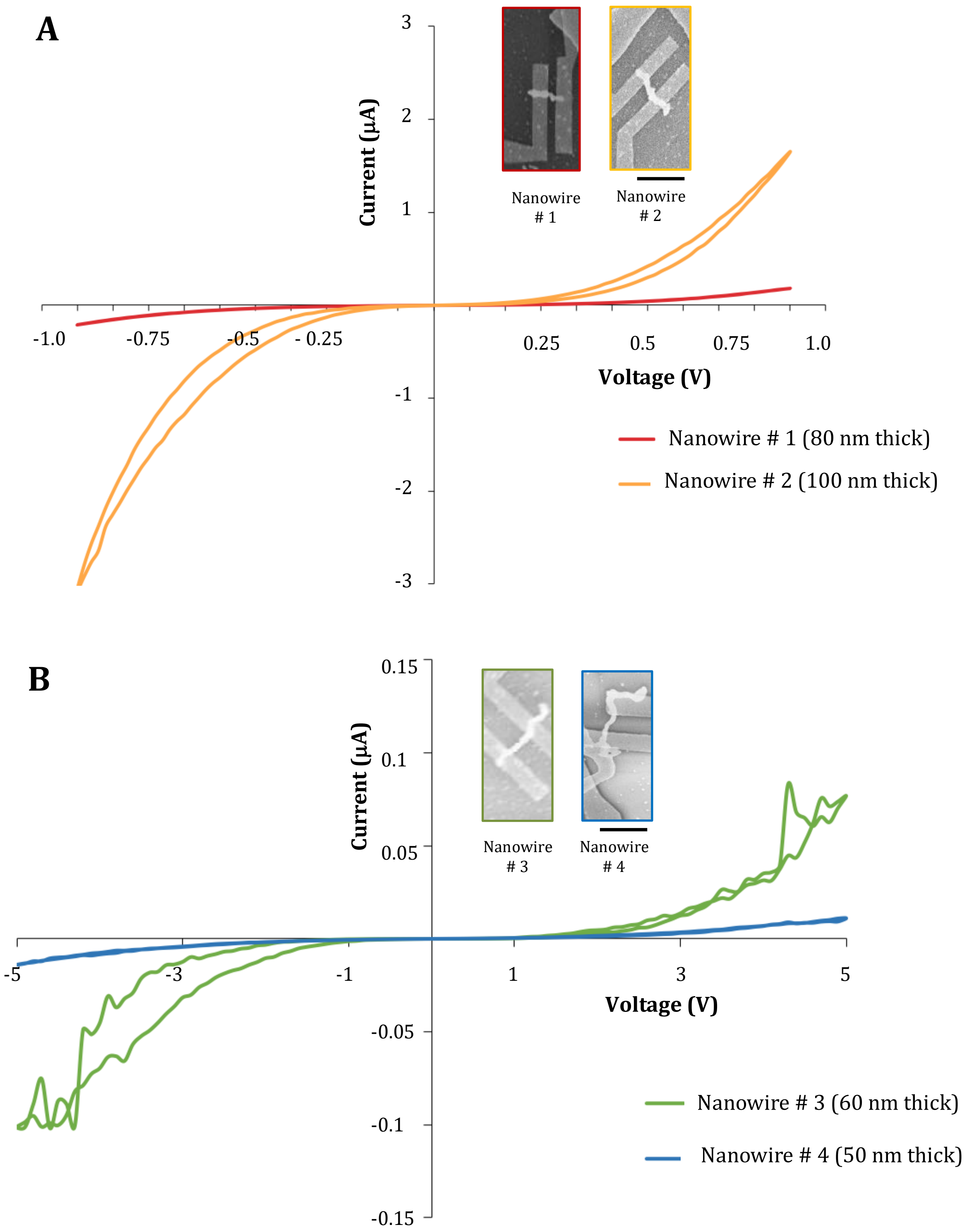

Figure 5.7. Conductivity measurement of M13 phage-based gold nanowires using EBL. Conductivity plot of the: **(A)** non-annealed gold nanowires, **(B)** annealed gold nanowires. Insets show the SEM image of the nanowire, patterned with contact electrodes, for which measurement was done. Scale bar equals 500 nm.

EBL was used to pattern contact electrodes on the annealed gold nanowires, deposited on a plasma cleansed SiO_2 surface with alignment marks. However, contrary to expectation, the nanowires displayed a non-linear conduction behaviour similar to the non-annealed nanowires (Figure 5.7 **B**). Again, nanowires with no apparent gaps, when observed under SEM or TEM, exhibited very high resistance to electrical conduction. This suggested that there might be other factors affecting the conductivity measurements.

Figure 5.8 shows the control electrical measurements. When current was passed through the two probes of MPSTM in contact with each other linear conduction was observed with very low resistance as expected. Similarly, when the two probes were placed on the same patterned electrode ohmic conduction with low resistance was observed. Finally when the two probes were placed on the SiO_2 surface no conduction was observed as expected. These control measurements only confirmed that there was no insulating layer on the tip. It did not confirm if the EBL process or the nanowire deposition was adding any insulating layer on the nanowire.

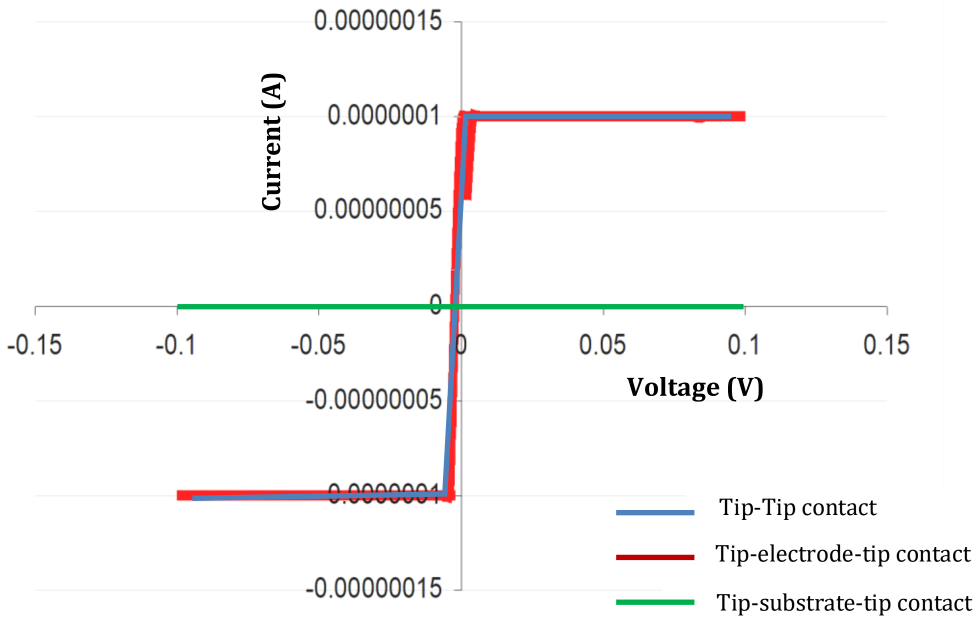

Figure 5.8: A plot of the conductivity measurement for gold nanowires control.

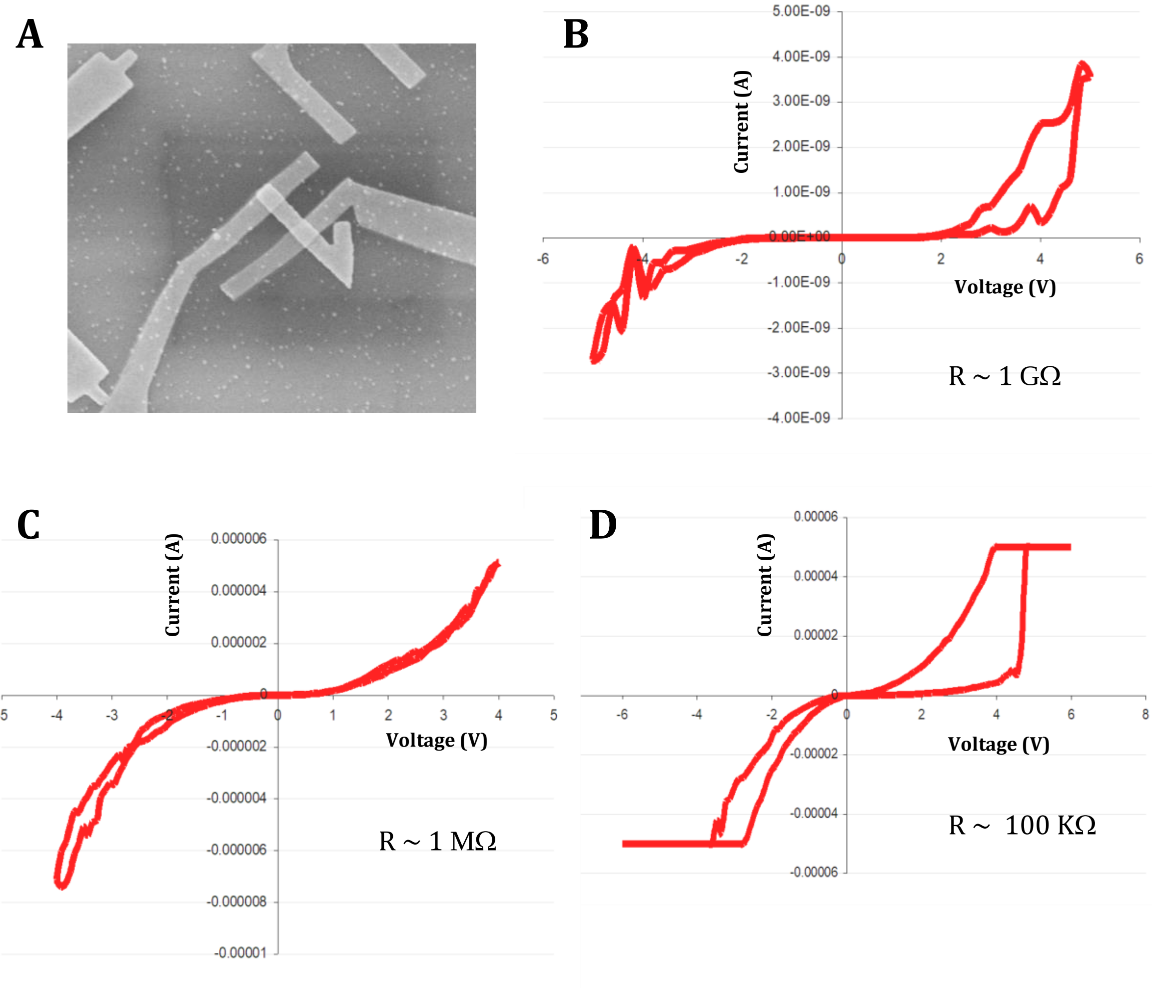

Figure 5.9. Conductivity measurement of a gold alignment mark patterned using EBL (A) SEM image of the alignment mark used for conductivity measurement using MPSTM. The electrical conductivity plot of the alignment mark: **(B)** before voltage sweeps were applied, **(C)** after 2nd set of voltage sweep, **(D)** after 3rd set of voltage sweep.

The gold nanowires were deposited again on a plasma cleansed SiO_2 surface with alignment marks and the nanowires were annealed at 250°C in vacuum. EBL was used to pattern contact electrodes on the annealed gold nanowires as well as on a prefabricated alignment mark (Figure 5.9 **A**). Surprisingly, a non-linear I-V characteristic with a very high resistance was observed for the case of conduction between a gold alignment mark

(Figure 5.9 **B**). This suggested the presence of a resistive layer on the surface of the patterned structures, which was likely formed during the patterning of the contact electrodes on the nanowire using EBL or during nanowire deposition on plasma cleansed SiO_2 surface with alignment marks. This resistive layer had a very high resistance of the order of 1 GΩ. However, this resistance of the alignment mark decreased after several voltage sweeps with incremental increase in applied potential after every sweep. The apparent resistance of the gold alignment mark decreased from about 1 GΩ ((Figure 5.9 **B**), to 1000 kΩ (Figure 5.9 **C**) to ultimately about 100 kΩ (Figure 5.9 **D**) after several sets of such applied voltage sweeps. Thus, the resistive layer could be burnt off by passing a high current through it.

This resistive layer would explain the high resistance and non-linear conductive behavior of the gold nanowires. A schematic showing the likely location and origin of this resistive layer is shown in Figure 5.10 (**C**). The control conducting experiment explained in Figure 5.8 does not rule out EBL as the source. This is because when the MPSTM probes come in contact with the gold electrodes surface for electrical measurement, the resistive layer can get scraped off the surface in the process. Hence, the resistive layer was likely introduced either during the EBL process or during the nanowire deposition. However, more study needs to be done to identify its origin.

Burning this resistive layer is likely to give more accurate prediction about the gold nanowire electrical properties. As expected, the resistance of the annealed gold nanowires decreased after several voltage sweeps with incremental increase in applied voltage after each sweep. The initial resistance of the gold nanowire was 1 GΩ (Figure 5.10 **A**), which reduced to 1 MΩ (Figure 5.10 **B**). Near the compliance of the current measuring device, the resistive layer was successfully burnt, and the nanowire exhibited linear I-V characteristic (Figure 5.10 **D**). The resistance of the nanowire was 807 Ω.

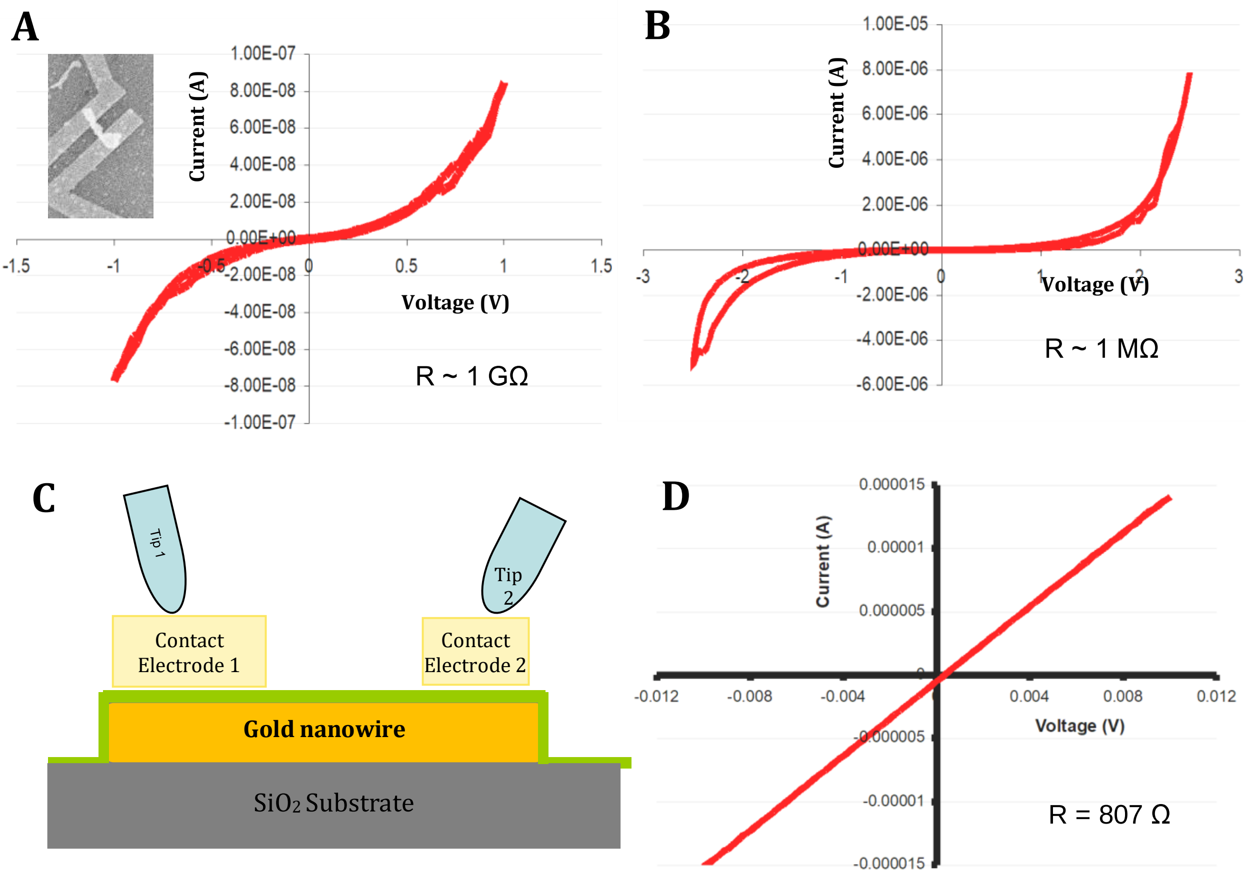

Figure 5.10. The conducting behavior of the annealed gold nanowire while the resistive layer was burnt off by applying several sets of voltage sweeps across it. The I-V characteristics of the annealed gold nanowire: **(A)** before voltage sweeps were applied, **(B)** after 2nd set of voltage sweep, **(D)** after 3rd set of voltage sweep. **(C)** shows a schematic explaining the possible region of the resistive layer, which is indicative of its origin. The resistive layer is shown in green.

The average resistance of the annealed M13 phage-based gold nanowire was about 709 Ω. The resistivity of the gold nanowire was found to be about 5.76 x 10^{-6} Ωm, which is two orders of magnitude higher than bulk gold resistivity of 2.04 x 10^{-8} Ωm (Peng, 2008).

5.3 Conclusions

The work in this chapter describes the investigation of the electrical characteristics of the gold nanowires made using the M13 bacteriophage scaffold. The residual chemical from the synthesis of the gold nanowire during the electroless gold deposition reaction formed a layer of contaminants on both the SiO_2 and SiN surfaces. The contaminants' layer was successfully removed by dialyzing nanowire suspension. Nanowires were found to be evenly distributed on a silica surface with minimal background of free GNPs.

The electrical property of the nanowires was measured for both the non-annealed and annealed M13 phage-based gold nanowires. However, a resistive layer was observed which is likely to exist between the nanowire and the contact electrodes patterned using EBL. Although this layer was not visible under the SEM, it attributed a large resistance, which ranged from 100 MΩ - 1 GΩ. As it was likely introduced during EBL process or while depositing gold nanowires on the plasma cleansed SiO_2 surface. Hence, it affected the conducting behavior of even the bulk gold electrodes. The resistive layer could be burnt on passing current through it by applying several voltage sweeps, with incremental increase in applied voltage after each sweep. The consequent measurement of the M13 phage-based nanowire resistance gave a value of approximately 709 Ω. The source of this resistive layer needs to be further investigated in order to make any useful and reliable electrical devices from the phage-based gold nanowires.

In future, an efficient method for removal of residual chemicals from the nanowires synthesis should be explored. The residual chemicals though small in quantity can be a source of contamination on the device surface, which can manifest itself as a resistive layer during device functioning.

Chapter 6

MS2 phage encapsulated nanoparticle

6.1. Introduction

Viruses are one of the smallest self-replicating units found in nature and have a simple design, whereby a protein shell protects its genetic material. The nucleic acid molecule inside the protein shell not only stores the design data, but often also has a role in the assembly of the virus from its constituent coat proteins. The assembly of a virus is often initiated by specific interactions between some portions of the encoding nucleic acid and the virus coat protein subunits (Perlmutter, 2015; Stockley, 2005; Stockley, 2016). The electrostatic interactions between the coat protein subunits and the negatively charged phosphate backbone of the nucleic acid help stabilise the capsid and sometimes initiate the virus particle assembly independent of the nucleic acid sequence (Zhao, 1995). The role of the small nucleic acid sequences and the electrostatic charge in initiating the virus assembly can be exploited to load various cargos such as foreign nucleic acids, proteins, nanoparticles etc. inside the capsid (Chen, 2006).

6.1.1. Phage capsid or protein shell encapsulated nanoparticle

Douglas and Young first reported the entrapment of a nanoparticle inside a cowpea chlorotic mottle virus (CCMV). They utilized the pores on the surface of the virion, which can be reversibly expanded under a pH change, for nucleation and growth of the polyoxometalate crystals in the virus cavity (Douglas, 1998). The virus capsid was intact throughout the process in this case. However, the range of materials, which can be encapsulated, is limited by the stability of the capsid under various chemical conditions and reagents needed for such a mineralization event.

Dragnea *et. al.* (2003) reported the encapsulation of nanoparticles inside a Bromo Mosaic Virus (BMV) capsid. However, the assembly was not initiated by the nucleic acid and protein interaction, but by the electrostatic interaction between the negatively charged citrate coat on the gold nanoparticle (GNP) surface and the positively charged surface of the inner cavity of the virus coat protein shell. However, the yield of the reaction was low, (~1%) in this case. This low yield was attributed to the hydrophobic interactions between the protein and the citrate coated metal core, which was likely to adversely affect the precursor required for the assembly. The yield of GNP encapsulation dramatically increased to 95%, when carboxylate-terminated thiolalkylated tetraethylene glycol (TEG) labelled GNPs were used. TEG is hydrophilic and imparts a negative charge to the GNPs (Chen, 2006). Similarly, HS-PEG-COOH-coated quantum dots and DNA coated quantum dots were used by the Dragnea group to encapsulate the quantum dot inside the BMV capsid (Dixit, 2006). The electrostatic charge interactions between the protein domains and the nanoparticle surface can act as a trigger to assemble the virus capsid around it (Yang *et. al.* 2012). They thus encapsulated a GNP inside a designed protein shell. However, the protein shell was found to have collapsed on to the nanoparticle surface in most of the cases and a uniform intact shell was not observed which is common in the case of the nucleic acid-triggered assembly of shell encapsulated nanoparticle.

Loo *et al.* (2006, 2007) reported the encapsulation of gold and cobalt nanoparticles inside the red clover necrotic mosaic virus (RCNMV) capsid. However, in this case, GNPs were bound to an RNA molecule whose sequence was known to initiate the assembly of the capsid. This RNA molecule initiated the capsid assembly and the nanoparticle bound to it was encapsulated as well. Yang and Burkhard (2012) reported the encapsulation of GNPs coated with a citrate, PEG, carboxyl and an amine functionalised polymer layer inside a self-assembling protein shell. However, in this case, the electrostatic interaction between the gold nanoparticle and the protein was not crucial for the encapsulation of GNPs (Yang, 2012). Ashley (2011) encapsulated quantum dots and other cargoes by attaching them to the TR stem loop of MS2 bacteriophage.

The inner cavity of the virus can also be modified to encapsulate cargo inside. Sainsbury (2011) modified S protein of CPMV to load cobalt inside the capsid. Wen (2012) loaded fluorophores and PEG molecules by targeting cysteine in the inner cavity of CPMV. Czapar and Steinmetz (2017) and Gulati (2018) describe the delivery of therapeutic cargoes by modifying the inner and outer surfaces of various plant viruses. The applications of such virus encapsulated nanoparticles (VENs) have been explored for the purpose of bioimaging, drug delivery and cell targeting (Wu, 2005; Cheng, 2012). The work done in this thesis, explores the use of such VENs for the fabrication of structures, which can act as a component for a molecular transistor.

6.1.2 *In-vitro* assembly of a MS2 bacteriophage capsid

MS2 coat proteins exist as coat protein dimers in solution. The coat protein dimers in the absence of RNA is symmetrical in solution as C/C dimer. The MS2 genomic RNA encodes a set of capsid assembly instructions via multiple packaging signals which act as allosteric triggers. Binding of the C/C dimer to TR, and other related stem-loops, triggers a conformational change to the A/B dimer (Stockley, 2016; Stockley, 2007). The capsid assembly is initiated *in-vitro* when the 19-nucleotide long RNA stem loop, translational repressor operator (TR), binds to the coat protein dimers. This assembly mechanism has been utilised for loading various cargoes such as nucleic acid (Wu, 2005), proteins (Glasgow, 2012) etc. inside the MS2 phage capsid. It should however be noted that the TR RNA stem loop is not compulsory for the capsid assembly. Capsid assembly has been reported in the presence of other RNA stem loops and even without any RNA at high concentrations of coat protein dimers (Stockley, 2007; Glasgow, 2012).

Both the interior and the exterior surface of the MS2 phage capsid was modified to simultaneously attach a cargo to it by Kovacs *et. al.* (2007). Electrostatic charge interaction between the GNP surface and the MS2 coat protein domains was used to encapsulate the nanoparticles inside the MS2 phage capsid by Capehart *et. al.* (2013). RNA stem loop triggered encapsulation of the quantum dots inside the MS2 phage capsid was also reported (Ashley, 2011). These two strategies of nanoparticle encapsulation inside the MS2 phage capsid were then used to deliver diverse therapeutic and imaging agents to the human hepatocellular carcinoma (HCC).

The structure of the MS2 phage capsid has been studied well at a high resolution. At the threefold and fivefold axis of the MS2 phage capsid, there are 32 pores with a diameter of 1.8 nm (Valegard, 1990). These pores can be used for the modification of the interior cavity of the MS2 phage capsid. The inner cavity is about 20 nm in diameter (Toropova, 2008; Valegard, 1990).

6.1.3. Higher order biological super structures

Biological subunits such as proteins, nucleic acids, lipids etc. self-assemble using molecular recognition to form higher order super-structures in nature such as chromatins, large proteins etc. Nanoparticles conjugated to biomolecules have been designed to self-assemble with other biological subunits in order to form higher order super-structures, which can be used for different nanotechnology applications (Nam, 2006). Self-assembly of engineered biomolecules or subunits into higher order structures is the basis of the design of simple electronic structures such as a single electron transistor. Electronic properties can be then be imparted to the biomolecular template.

6.1.4. Aims of the work described in this chapter

The aims were as follows:

1. The primary objective was to investigate if a GNP or a quantum dot is encapsulated inside the MS2 phage capsid using the assembly initiator TR RNA stem loop bound to the nanoparticle.

2. To investigate the encapsulation efficiency of the different sizes and types of nanoparticles inside the MS2 phage capsid.

3. To investigate if the nanoparticle inside the virus-like particle can be subjected to chemistry using the pores on the surface of the MS2 phage capsid.

4. One of the final objectives of the research was to fabricate a molecular transistor-like structure using phage-based nanostructures. M13GB phage programmed to bind to biotin was to be tested for binding against biotin-labelled MS2 virus-like particles to form higher order phage-based structures.

6.2. Results and Discussion

6.2.1. Encapsulation of gold nanoparticles in the MS2 phage capsid

A schematic for the encapsulation of nanoparticles inside the MS2 phage capsid is shown in Figure 6.1.

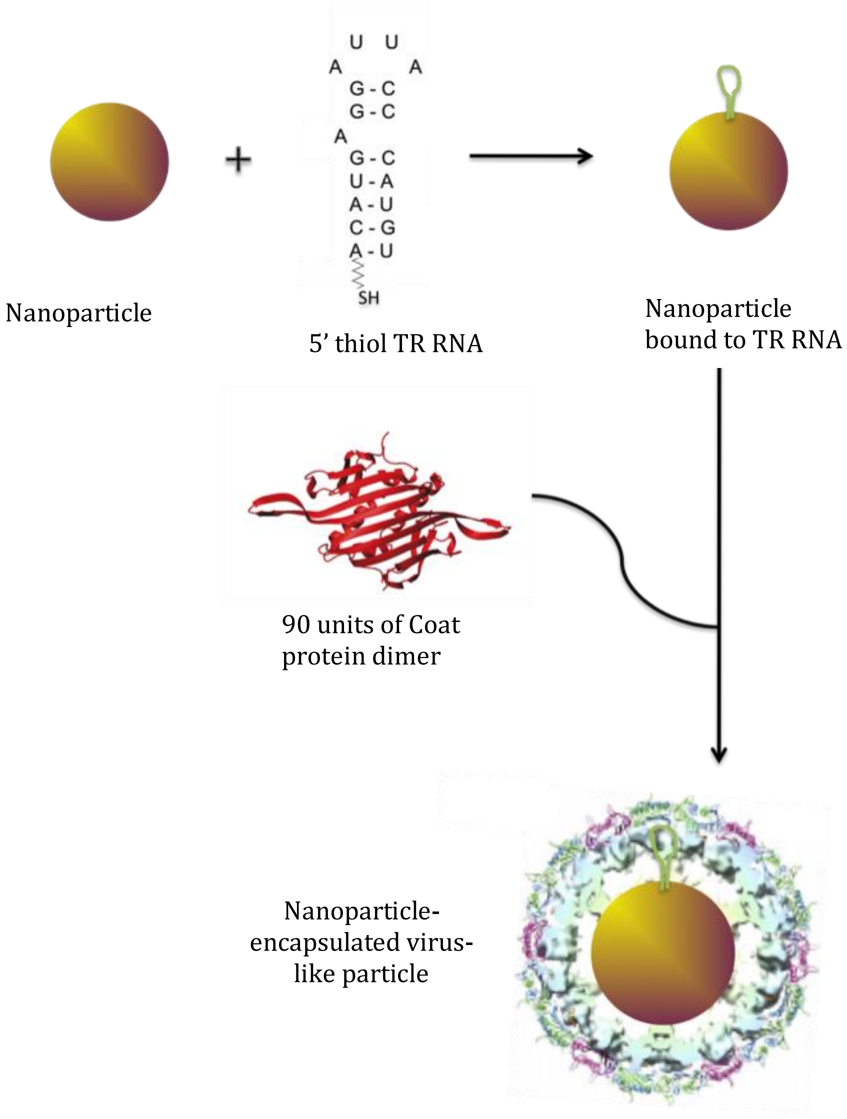

Figure 6.1. Schematic showing the mechanism of assembly of nanoparticles encapsulation in a MS2 virus-like particle. A GNP (or a quantum dot) is attached to a 19-nucleotide long TR RNA stem loop containing a thiol group at the 5' end. The nanoparticle bound to the TR RNA is mixed with MS2 phage coat protein dimers in an assembly buffer to get MS2 phage encapsulated nanoparticles. (adapted from Toropova, 2008)

The initiation of the MS2 phage capsid assembly upon the binding of a specific RNA sequence to the coat protein dimers can be exploited for the encapsulation of a nanoparticle inside the capsid. Such an RNA molecule bound to a nanoparticle should promote the assembly of the MS2 phage capsid around the nanoparticle, provided the nanoparticle can fit inside the inner cavity of the capsid. The TR RNA molecule as an assembly initiator has been successfully used to load different kinds of cargo such as siRNA, DNA, protein molecules etc. inside the MS2 phage capsid (Wu, 2005; Glasgow 2012).

Andrew Roche at the University of Leeds kindly provided the MS2 bacteriophage capsids in 80% ammonium sulfate solution. 6 mL of this solution was spun down and dialysed overnight in a 40 mM ammonium acetate buffer. The concentration of the dialysed MS2 phage capsids was about 400 µM. Intact MS2 phage capsids were seen using TEM. MS2 phage capsids were dissociated to get the coat protein dimers (CP2), which were further purified using size exclusion chromatography for use in a reassembly reaction (see sections 2.2.28.1 and 2.2.28.2).

A 19-nucleotide long thiol functionalised TR RNA stem loop of the MS2 bacteriophage was synthesised and further purified using HPLC. The mass of the RNA molecule was verified using mass spectroscopy and polyacrylamide gel electrophoresis as shown in Appendix D. The thiol group was attached to the 5’ end of the RNA using a six-carbon linker molecule. The assembly reaction set up to encapsulate the 5 nm GNPs bound to TR RNA inside the MS2 phage capsid (see sections 2.2.28.4). The samples from the assembly reaction were viewed under a TEM (Figure 6.2).

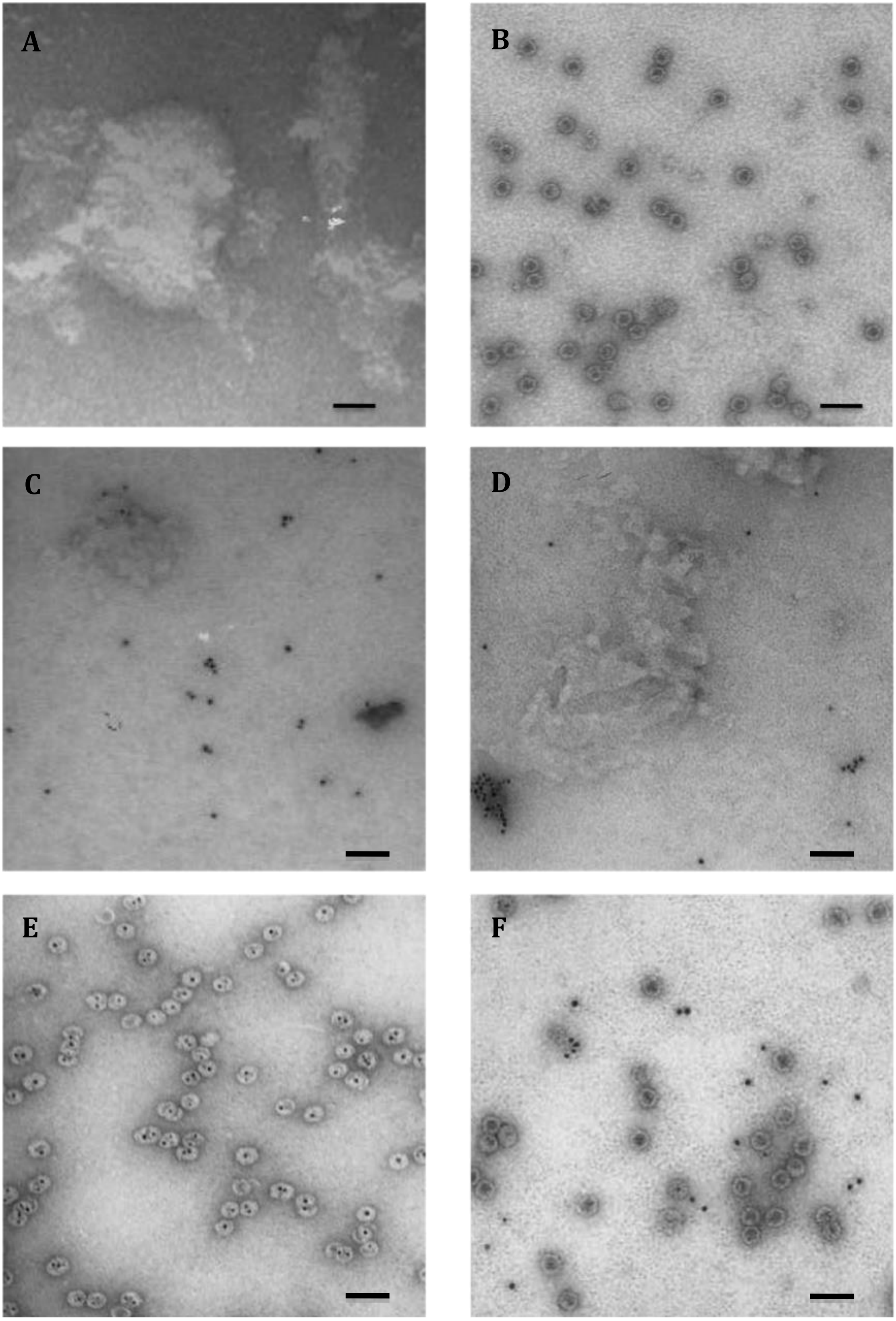

Figure 6.2. TEM image of MS2 phage coat proteins mixed with: **(A)** reassembly buffer, **(B)** TR RNA, **(C)** citrate coated GNPs, **(D)** phosphine coated GNPs, **(E)** 5 nm GNPs bound to TR RNA, **(F)** 5nm GNPs and TR RNA not bound to each other. The sample was stained with 2% (w/v) uranyl acetate. Scale bar in micrographs equal 50 nm.

MS2 phage capsids were not seen in the assembly reaction containing only the CP2 without the TR RNA to act as the assembly initiator (Figure 6.2 **A**). As expected, the CP2 assembled in the presence of the 5’ thiol TR RNA, to form empty capsids (Figure 6.2 **B**). No VENs were seen when the coat protein dimers were mixed with the citrate and phosphine stabilized GNPs (Figure 6.2 **C** and **D** respectively**)**. However, MS2 phage encapsulated gold nanoparticles (MS2-PEGNPs) were seen in the assembly reaction mix containing CP2 and TR RNA bound to the GNPs (Figure 6.2 **E**). It was observed that the MS2-PEGNPs encapsulated between one to three 5 nm GNPs. When the CP2 was mixed with the TR RNA and GNPs not bound to any RNA molecule, empty capsids along with free GNPs were seen (Figure 6.2 **F**).

The TEM images are 2-D projections of the sample density. It cannot differentiate between an encapsulated GNP and a capsid placed on top of a GNP in an orientation such that the line joining the centre of the capsid to the centre of the GNP is parallel to the incident electron beam. After capsid assembly in the presence of TR RNA bound to the GNP, most of MS2-PEGNPs formed had orientation of GNP and MS2 virus like particle (VLP) as described above (Figure 6.2 **E**). The same was not true when CP2 was mixed with GNPs not bound to any RNA molecule (Figure 6.2 **F**). This clearly shows that the GNPs were encapsulated inside the capsid when the phage assembled in the presence of TR RNA bound to GNP. The assembly reaction produced four different VLP populations: empty capsid, MS2-PEGNP with 1, 2 and 3 GNPs inside it (Figure 6.3 **A**). The individual MS2-PEGNP shown in Figure 6.3 (**A**) were selected from wide-field TEM images as shown in Figure 6.2 (**E**).

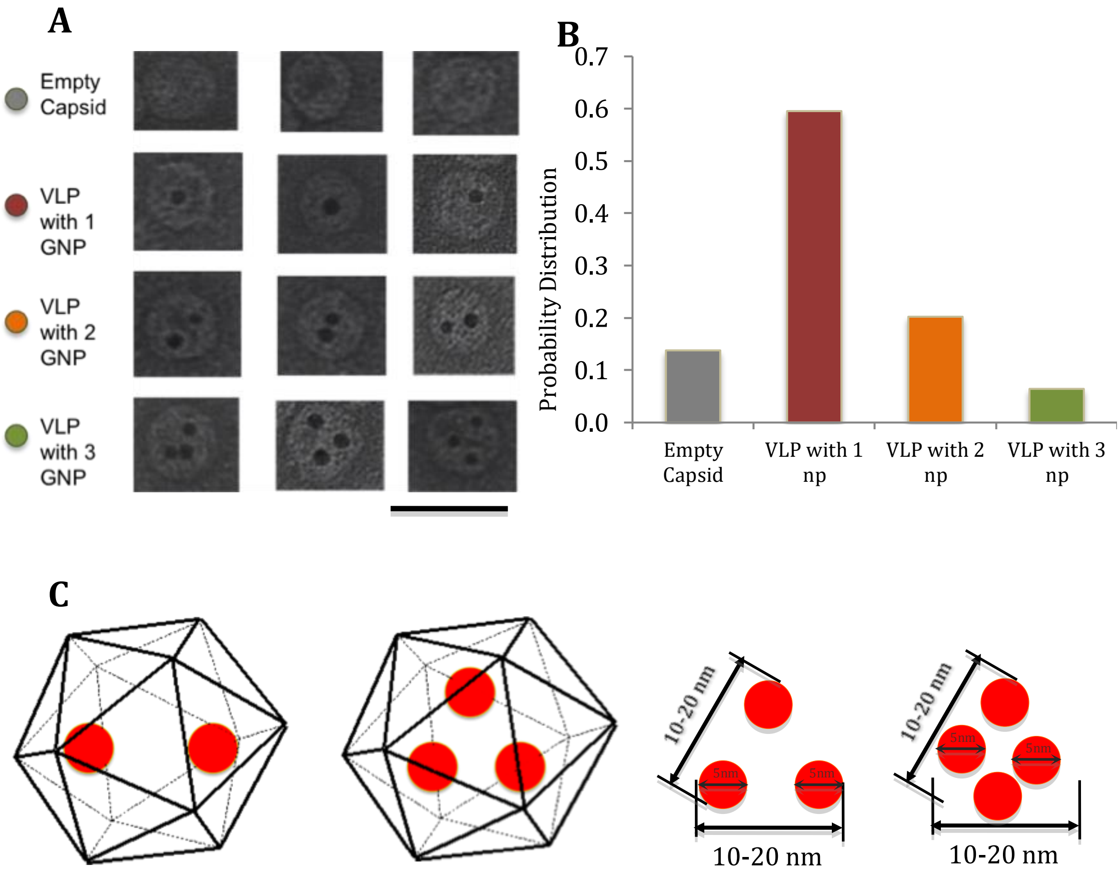

Figure 6.3. **(A)** TEM images of different MS2-PEGNPs formed during the encapsulation of 5 nm GNPs, viz. empty capsids and VLPs encapsulating 1, 2 and 3 GNPs. The sample was stained with 2% (w/v) uranyl acetate. Scale bar equals 50 nm. **(B)** Graph showing the probability distribution of the four different MS2-PEGNPs populations after the assembly reaction. **(C)** Schematic showing a possible explanation of the encapsulation of up to four 5 nm GNPs inside a MS2 phage capsid.

The probability distribution of MS2-PEGNPs encapsulating one or more 5 nm GNPs is shown in Figure 6.3 (**B**). The total sample size was 567. Most of the MS2-PEGNPs had only one nanoparticle inside them, while MS2-PEGNPs with three GNPs inside them were the least probable. There was no apparent difference in the size of the MS2-PEGNPs encapsulating one, two or three 5 nm GNPs. The average size of the MS2-PEGNP was close to the wild-type MS2 phage capsid at 28.3 nm ± 3 nm.

As the inner cavity of the wild-type MS2 virus capsid is about 20 nm, it is possible for up to four 5 nm GNPs to be encapsulated inside a VLP (Figure 6.3 **C**). However, only one MS2-PEGNP with four 5 nm GNP inside it was observed. Also, no MS2-PEGNP with more than four GNPs inside was observed. This supports the argument that the MS2-PEGNP has a T=3 structure, like the wild-type MS2 phage capsid.

The assembly of a VEN due to non-specific electrostatic charge interactions between the coat protein and the nanoparticle surface has also been reported (Dragnea, 2003; Chen, 2006). However, no MS2-PEGNP was found when the MS2 coat protein was mixed with citrate and phosphine stabilized GNPs in an assembly buffer (Figures 2.2 **C** and **D**). Daniel *et. al.* (2010) reported hydrophobic interactions between the GNP and the coat protein of the virus. Any effect of such an interaction on the assembly of the MS2-PEGNP was not observed. The MS2-PEGNPs were found to be stable up to 55^{o}C.

6.2.2. Encapsulation of GNPs bigger than 5 nm

A similar strategy was used to encapsulate bigger GNPs inside the MS2 phage capsid. Citrate coated GNPs with diameters 10 nm, 15 nm and 20 nm were sourced from Ted Pella Inc. (California, USA). These GNPs were coated with phosphine (see section 2.2.26) and subsequently functionalized with 5’-thiol TR RNA. An assembly reaction with the MS2 coat protein dimers was set up for each GNP as described earlier. A GNP was found to be encapsulated inside the MS2 phage capsid for all the different sized GNPs, when observed under the TEM (Figures 6.4 **A, B, C** and **D**).

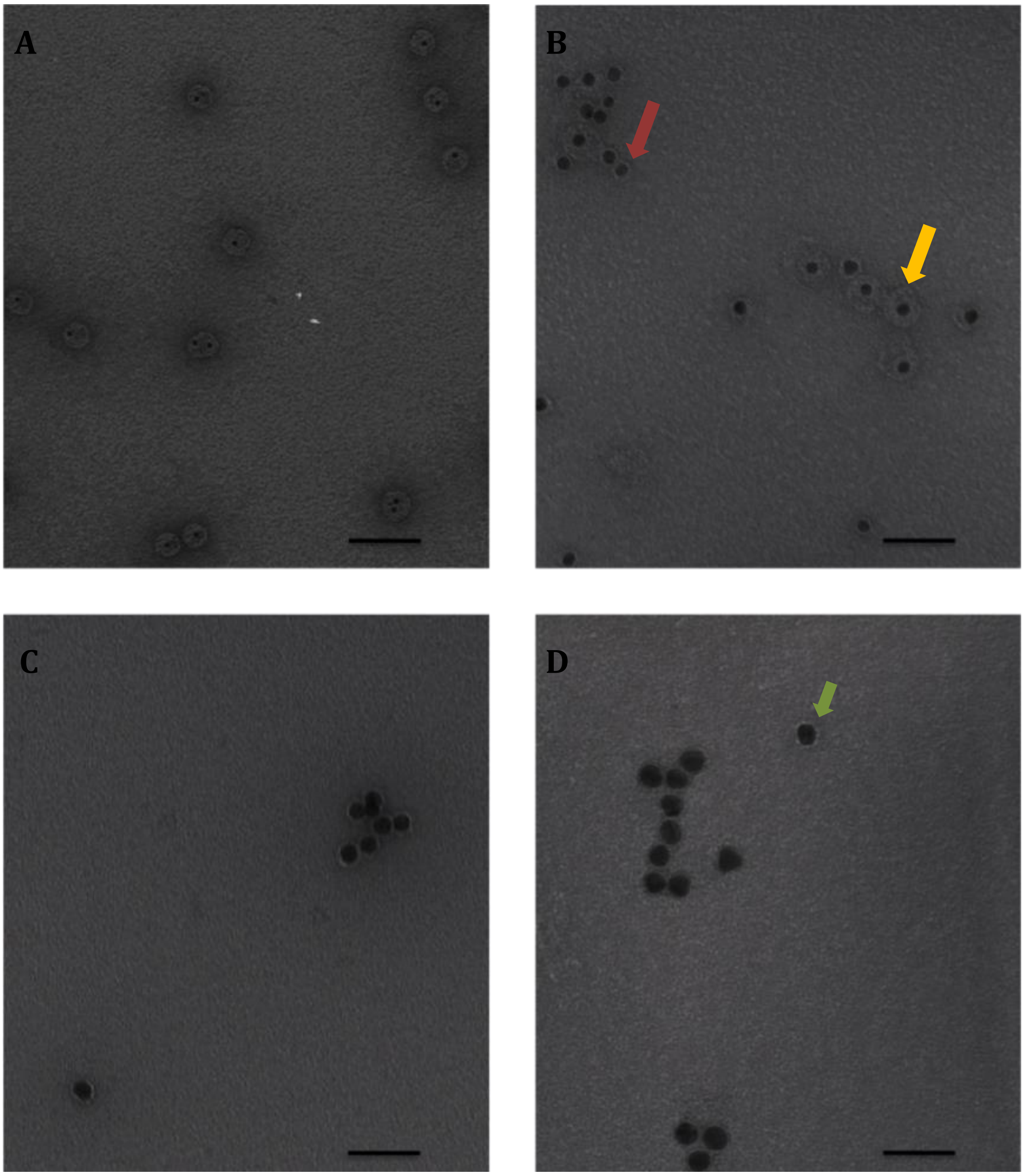

Figure 6.4. **TEM images of MS2-PEGNPs encapsulating**: **(A)** 5 nm GNPs, **(B)** a 10 nm GNP, **(C)** a 15 nm GNP, **(D)** a 20 nm GNP (green arrow points to a MS2-PEGNP). The sample was stained with 2% (w/v) uranyl acetate. Scale bar in micrographs equal 60 nm.

However, unlike the MS2-PEGNP with a 5 nm GNP inside (Figure 6.4 **A**), the size of the MS2-PEGNPs were different from the WT MS2 bacteriophage capsid. In the case of 10 nm GNPs, two different types of MS2-PEGNPs were observed (Figure 6.5 **B**). While one of them was similar in shape and size to the WT MS2 phage capsid (pointed by the orange arrow in the Figure 6.4 **B**), the other was distinctly smaller (pointed by the red arrow in the Figure 6.4 **B**). The number of small MS2-PEGNPs was greater than their bigger counterpart. Although, it was difficult to estimate the thickness of the capsid protein shell from the TEM image, the smaller MS2-PEGNP encapsulating a 10 nm GNP showed a non-uniform thickness of the protein shell of different VLPs. Since the inner capsid diameter of the MS2 phage capsid is about 20 nm, it is theoretically possible for two 10 nm GNPs to encapsulate inside a single capsid. However, no such MS2-PEGNPs were seen. This may be because of the steric hindrance encountered by the coat proteins during the assembly around a large GNP. As expected, encapsulation of more than one GNP in the case of 15 nm and 20 nm GNP was not observed (Figure 6.4 **C** and **D**). The size of the MS2-PEGNPs incorporating 15 nm and 20 nm GNPs was smaller than the WT MS2 phage capsid.

The probability distribution of the empty capsid and the two different MS2-PEGNPs encapsulating 10 nm GNP is shown in Figure 6.5 (**B**). The sample size was 291. The small MS2-PEGNP is more than three times likelier than the bigger VLP. Very few empty capsids were observed. For the 10 nm GNP, plotting the size of different MS2-PEGNPs against their distribution, gave two peaks at 18 nm and 28 nm (Figure 5.8 **D**). This indicated that two different mechanisms were working in the MS2-PEGNPs formation. In the case of smaller MS2-PEGNPs, the protein shell likely collapsed on the GNP surface because of the electrostatic charge interaction between the GNP and the coat protein shell, as reported by Yang and Burkhand (2012) while fabricating synthetic VLPs. Such electrostatic charge interactions were weak in case of the 5 nm GNP because of their smaller surface area. This is the likely reason why no such small MS2-PEGNP was observed during the encapsulation of 5 nm GNPs.

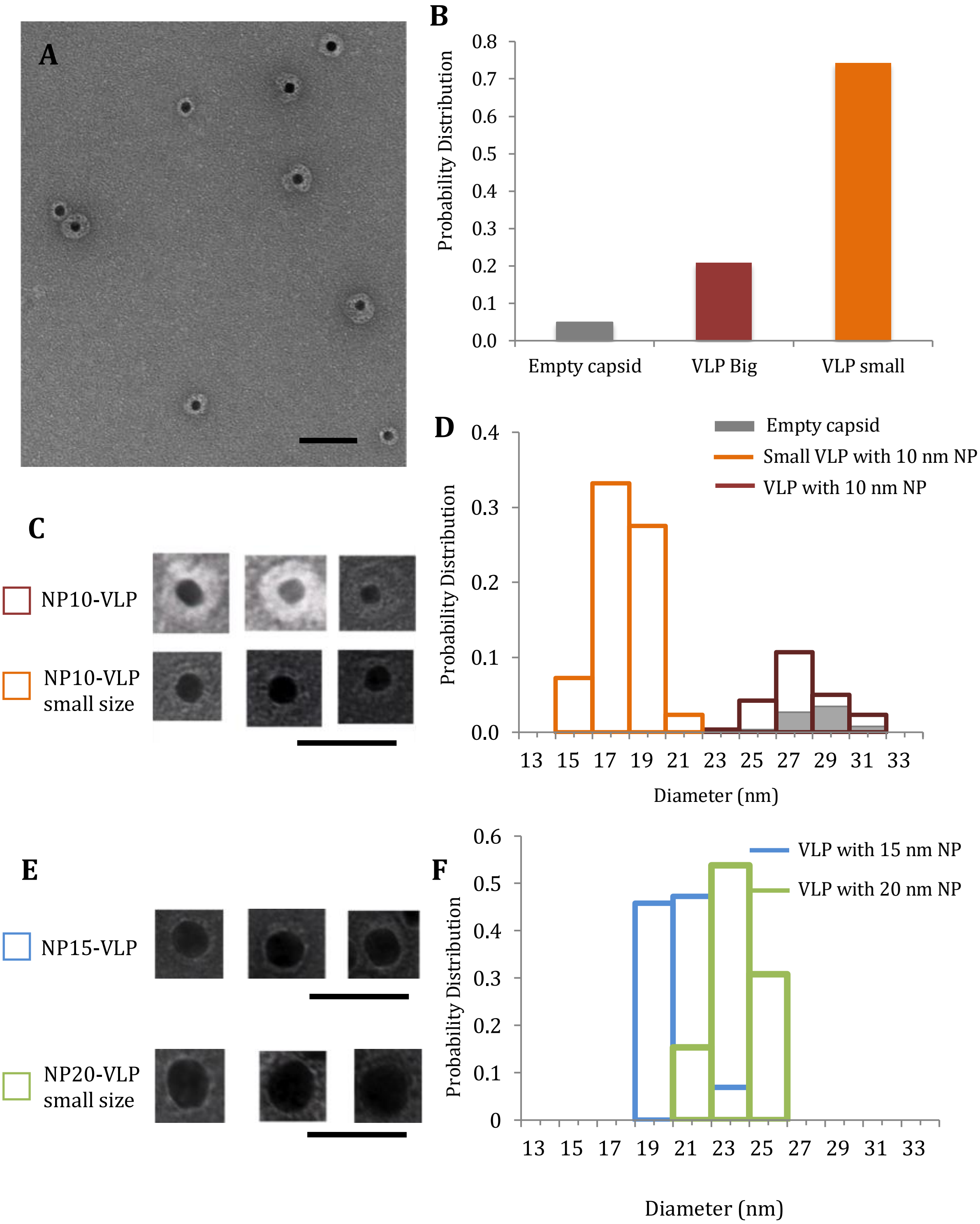

Figure 6.5. **(A)** shows the TEM image of MS2-PEGNPs encapsulating a 10 nm GNP and their **(B)** probability distribution during the encapsulation. **(C)** shows the TEM images of two different kinds of MS2-PEGNPs formed during encapsulation of a 10 nm GNP and their **(D)** size and probability distributions. **(E)** shows the TEM images of MS2-PEGNPs incorporating a 15 nm GNP and a 20 nm GNP and their **(F)** size and probability distributions. Scale bar equals 50 nm.

The size and the probability distribution of the MS2-PEGNPs incorporating a 15 nm GNP and a 20 nm GNP is shown in Figure 6.5 (**F**). The sample size was 118 and 47 respectively. The TEM images of the corresponding MS2-PEGNPs is shown in Figure 6.5 (**E**). The average size of the MS2-PEGNPs encapsulating a 15 nm GNP was 21.6 nm, while the average size of the MS2-PEGNPs incorporating a 20 nm GNP was 25 nm. Both the MS2-PEGNP were smaller than the wild-type MS2 phage capsid. Again, this may be because of the collapsing of the protein shell on to the GNP surface because of the electrostatic charge interaction between the GNP surface and the coat protein shell. Most of the MS2-PEGNPs encapsulating a 20 nm GNP had a non-uniform thickness of protein shell around the GNP. In many cases, there was no protein shell around some regions of the encapsulated GNP, suggesting incomplete capsid formation. The small size of the MS2-PEGNPs encapsulating a 15 nm GNP when compared to the wild-type capsid also suggests that the MS2-PEGNP structure may be different from the T=3 wild-type capsid. All the MS2-PEGNPs were stable at 4^{o}C for up to 12 weeks and did not aggregate much over time, as was observed with the M13G phage mixed with GNPs.

6.2.3 Encapsulation of quantum dots in the MS2 phage capsid

Streptavidin labelled CdTe quantum dots (QD) with emission maximum at 565 nm were obtained from Invitrogen (Paisley, UK). They were mixed with 5’-biotin TR RNA, obtained from Dharmacon, (Lafayette, USA) in a ratio of 1:1. This TR RNA bound to streptavidin-labelled QD was added to CP2 for capsid assembly reaction (see section 2.2.28.3 and 2.2.28.4). MS2 phage encapsulated CdTe QD were observed, though they were few in numbers (Figure 6.6 **A**).

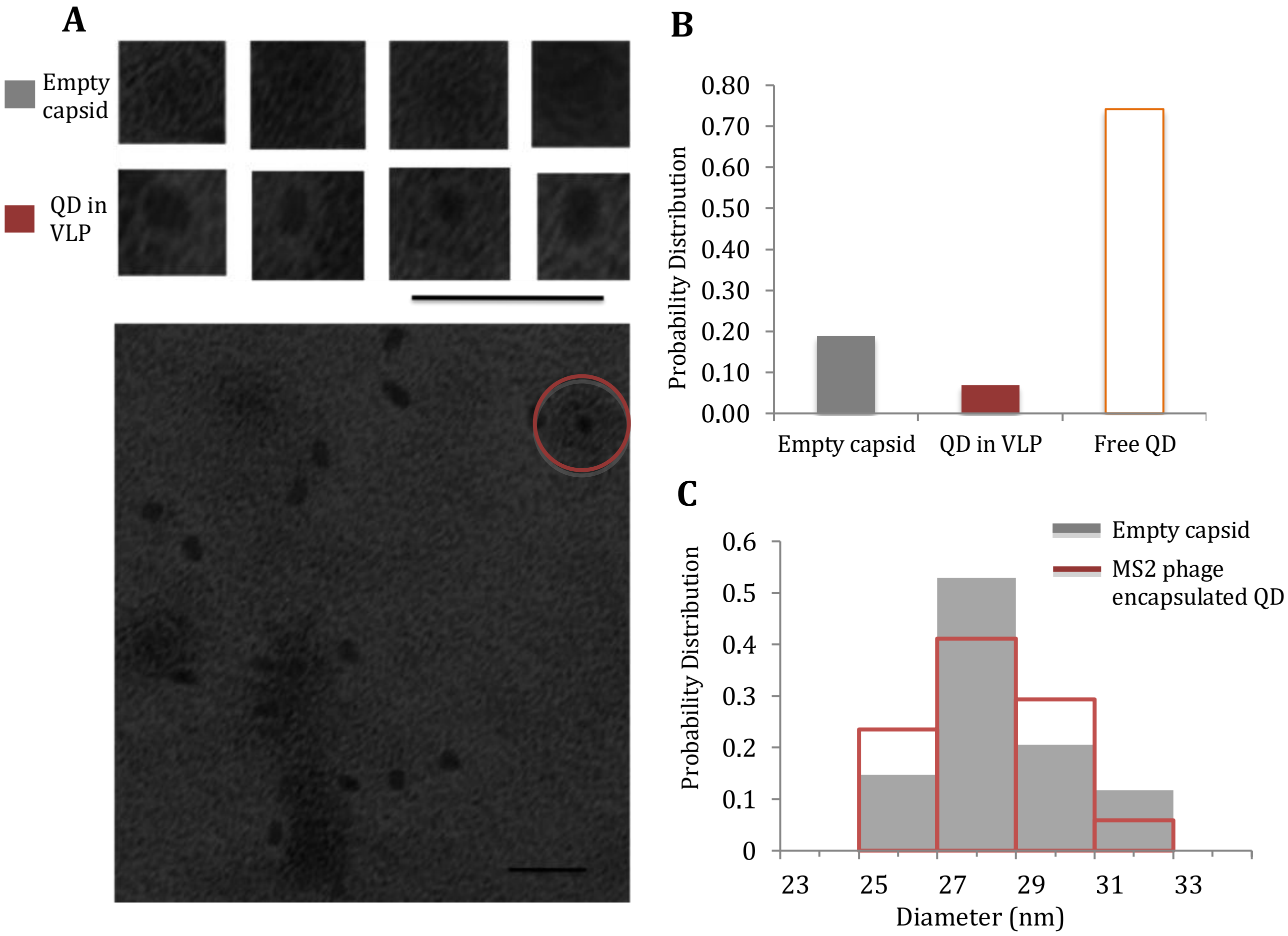

Figure 6.6. **(A)** shows the TEM images of the empty capsid and the MS2 phage encapsulating quantum dot. The individual TEM images were selected (indicated by the red circle) from the wide-field TEM image. The sample was stained with 2% (w/v) uranyl acetate. Scale bars equal 60 nm. **(B)** shows the Probability distribution and **(C)** shows the size distribution of the VLPs formed during the encapsulation of the quantum dot in a MS2 phage capsid.

Most of the VLP formed were empty capsids as shown in the probability distribution plot in Figure 6.6 (**B**). The sample size was 305. The size of the MS2 phage encapsulated quantum dot was about 28 nm, which was close to the empty capsids formed during the assembly (Figure 6.6 **C**).

Although, the actual semiconductor core of the quantum dot is about 5 nm wide, a ZnS shell and a polymer shell encapsulate it to give it stability. Further, streptavidin molecules are attached to this polymer shell using a linker molecule. This effectively increases the size of the quantum dot to 15 - 20 nm, as has been reported in the product manual. The large size of the quantum dot is the likely reason for this low encapsulation efficiency of about 7 % as shown in the graph in Figure 6.7.

The yield of the GNPs encapsulation also dropped with the increase in the GNP diameter. The encapsulation efficiency of 15 nm and 20 nm GNPs was about 11 % and 6 % respectively, whereas that of 5 nm and 10 nm GNPs was 76 % and 74 % respectively. No encapsulation of 30 nm GNP in the MS2 phage capsid was observed. The decrease in yield can be attributed to the size of nanoparticles approaching the inner cavity diameter of the MS2 phage capsid. It should be noted that the encapsulation of nanoparticles slightly bigger than the inner cavity of capsid has been reported (Yang, 2012; Goicochea 2007). But in these cases, the capsid was assembled by non-specific electrostatic charge interactions between the coat protein and the nanoparticle surface, unlike the assembly of the MS2 phage capsid.

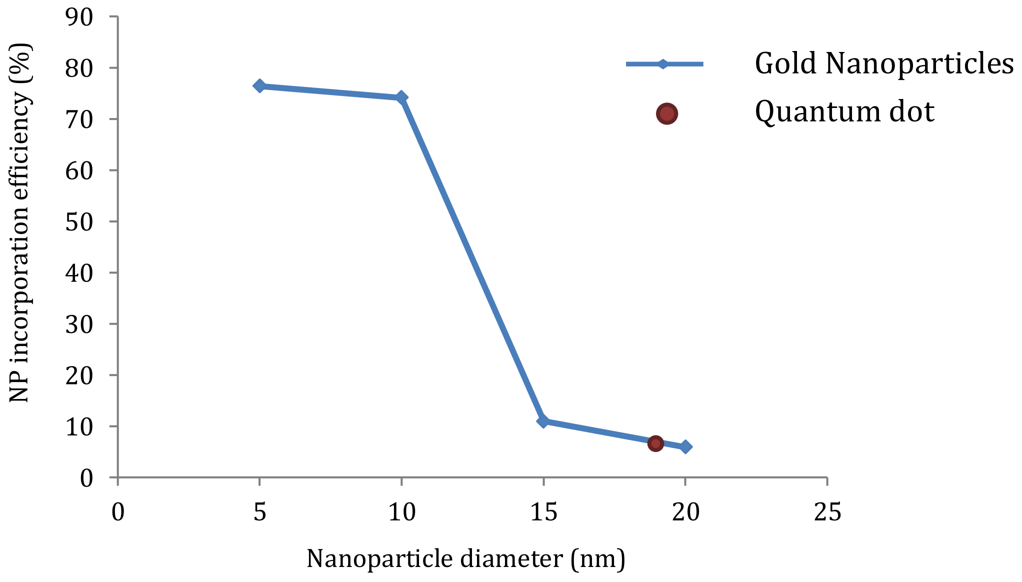

Figure 6.7. Graph showing the incorporation efficiency of nanoparticles (GNPs and QDs) inside a MS2 phage capsid against their size.

When the assembly reaction mix containing the MS2 phage encapsulated QD, free QDs and empty capsids was loaded on a 50% sucrose density gradient, no separate bands for the MS2 phage encapsulated QDs and free QDs were seen. Although, a distinct band containing empty capsids and the unused coat protein was seen. As the encapsulation efficiency of the quantum dot into the MS2 phage capsid was very low, it was important to isolate the MS2 phage encapsulated QDs from the free QDs in order to characterise the VLPs.

Attempts to purify the MS2 phage encapsulated QDs using gel electrophoresis or size exclusion chromatography also did not result in a distinct band for MS2 phage encapsulating QD (data not shown here).

6.2.4 Deposition of gold on the nanoparticle inside the MS2-PEGNPs

The wild-type MS2 phage capsid has pores at the three-fold and five-fold axis. These pores have been used to perform chemistry on the inner cavity of the MS2 phage capsid (Kovacs, 2007). Since the shape and size of the MS2-PEGNPs encapsulating a 5 nm and 10 nm GNPs is similar to the wild-type MS2 phage capsid, it is likely that their structure is the same as the T=3 capsid of the wild-type MS2 phage capsid. If so, MS2-PEGNPs would have pores on their surface like the wild-type capsid.

In order to determine the presence of pores on the MS2-PEGNP capsid, they were subjected to electroless gold deposition reaction. The Goldenhance^{TM} LM kit (Nanoprobes Inc., NY, USA) was used for this purpose. It was found that the gold inside the MS2-PEGNPs grew bigger after 5 minutes of the Goldenhance reaction (Figure 6.8).

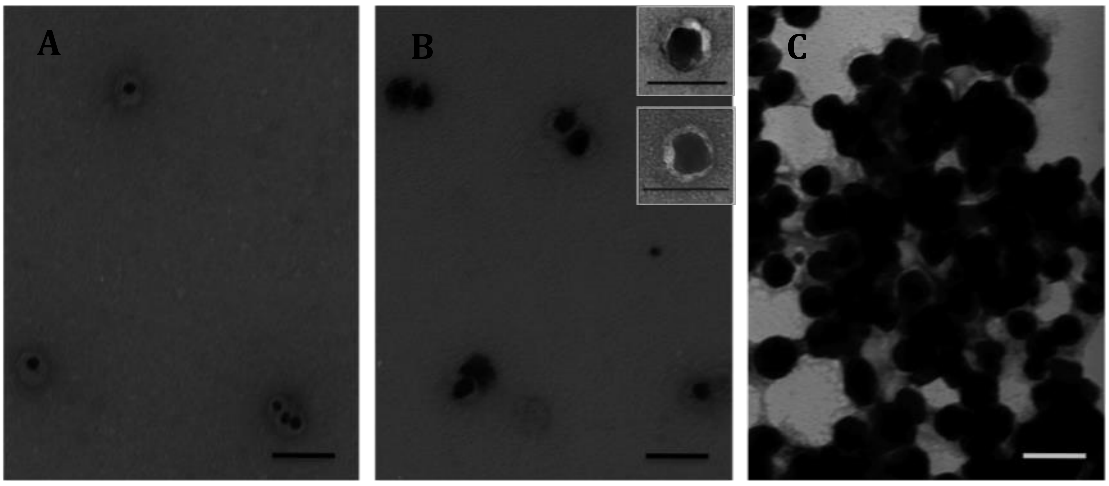

Figure 6.8. **TEM image of Goldenhance^{TM} reaction on MS2-PEGNPs with 5 nm GNP inside it.** The volume of the solution A of Goldenhance^{TM} LM kit used: **(A)** 1 μL, **(B)** 2 μL, (inset showing the enhanced nanoparticles) **(C)** 3 μL. The sample was stained with 2% (w/v) uranyl acetate. Scale bar equals 50 nm.

This suggested that there are pores on the surface of the MS2-PEGNPs and the pores are accessible to perform further chemistry on the inner cavity of the VLP or on the encapsulated nanoparticle. The size of the encapsulated GNP grew with the increase in the amount of the Goldenhance^{TM} solution used, (Figure 6.8 **A**, **B** and **C**). The size of the GNPs also increased in each of the above cases with time. Mostly the GNPs outgrew the capsids over time bursting it open, followed by the aggregation of the MS2-PEGNPs (Figure 6.8 **C**). Since the chemical identity of the solutions provided in the Goldenhance^{TM} kit was unknown due its propriety nature, a different approach of electroless gold deposition (Slot, 1985) was used to achieve better control of the gold deposition process. In the first step, the concentration of the gold ions in the electroless gold deposition reaction was varied while keeping the reaction time constant at 30 minutes (Figure 6.9). 5 mM $HAuCl_4$ was used as the source of Au^{3+} ions and 50 mM $NaBH_4$ was used as the reducing agent.

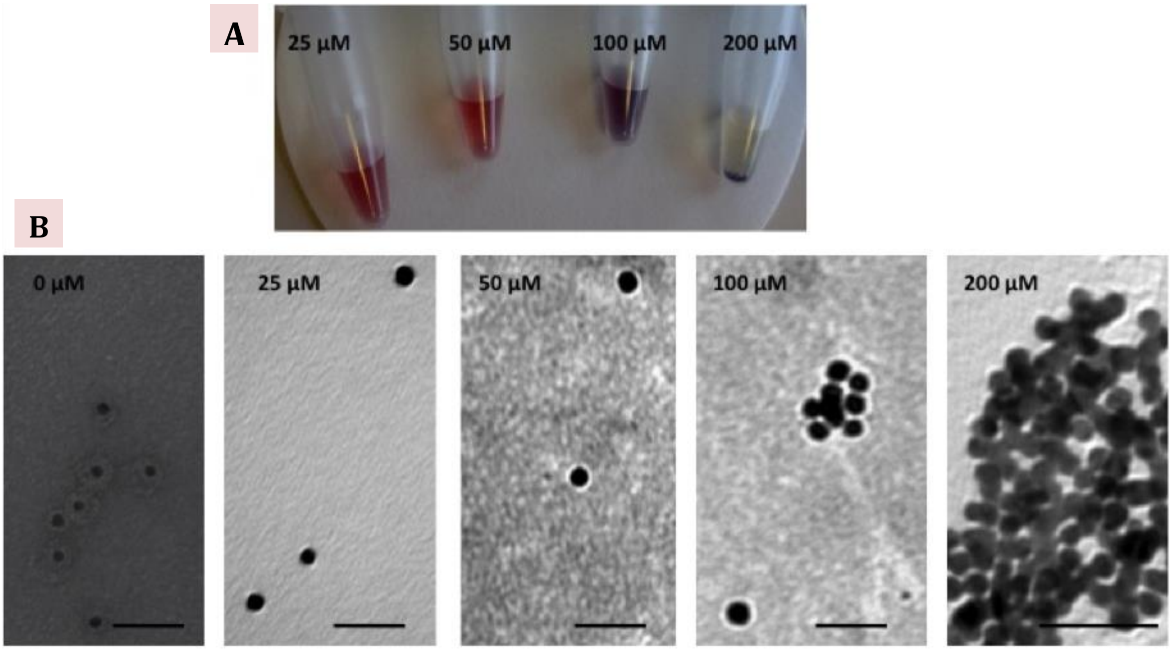

Figure 6.9. **(A)** MS2-PEGNPs solution encapsulating a 10 nm GNP after electroless gold deposition at varying concentration of gold ions. **(B)** TEM images of the MS2-PEGNPs after the gold deposition using different concentration of gold ions. The samples were stained with 2% (w/v) uranyl acetate. Scale bar in micrographs equal 50 nm.

The MS2-PEGNPs produced aggregates with the increasing concentration of chloroauric acid ($HAuCl_4$) (Figure 6.9 **A**). The aggregation of the VLPs was irreversible. Also, the size of the encapsulated nanoparticle did not show any appreciable increase, when the $HAuCl_4$ concentration was increased above 50 µM (Figure 6.9 **B**). Hence in the next step, the concentration of gold ions was fixed at 50 µM and the size of the encapsulated GNP was monitored over the course of the gold deposition reaction. The size of the encapsulated GNP for different reaction times of the gold deposition reaction using 50 µM $HAuCl_4$ is shown in Figure 6.10. No GNP was formed inside the empty capsid throughout the reaction (Figure 6.10 **B**).

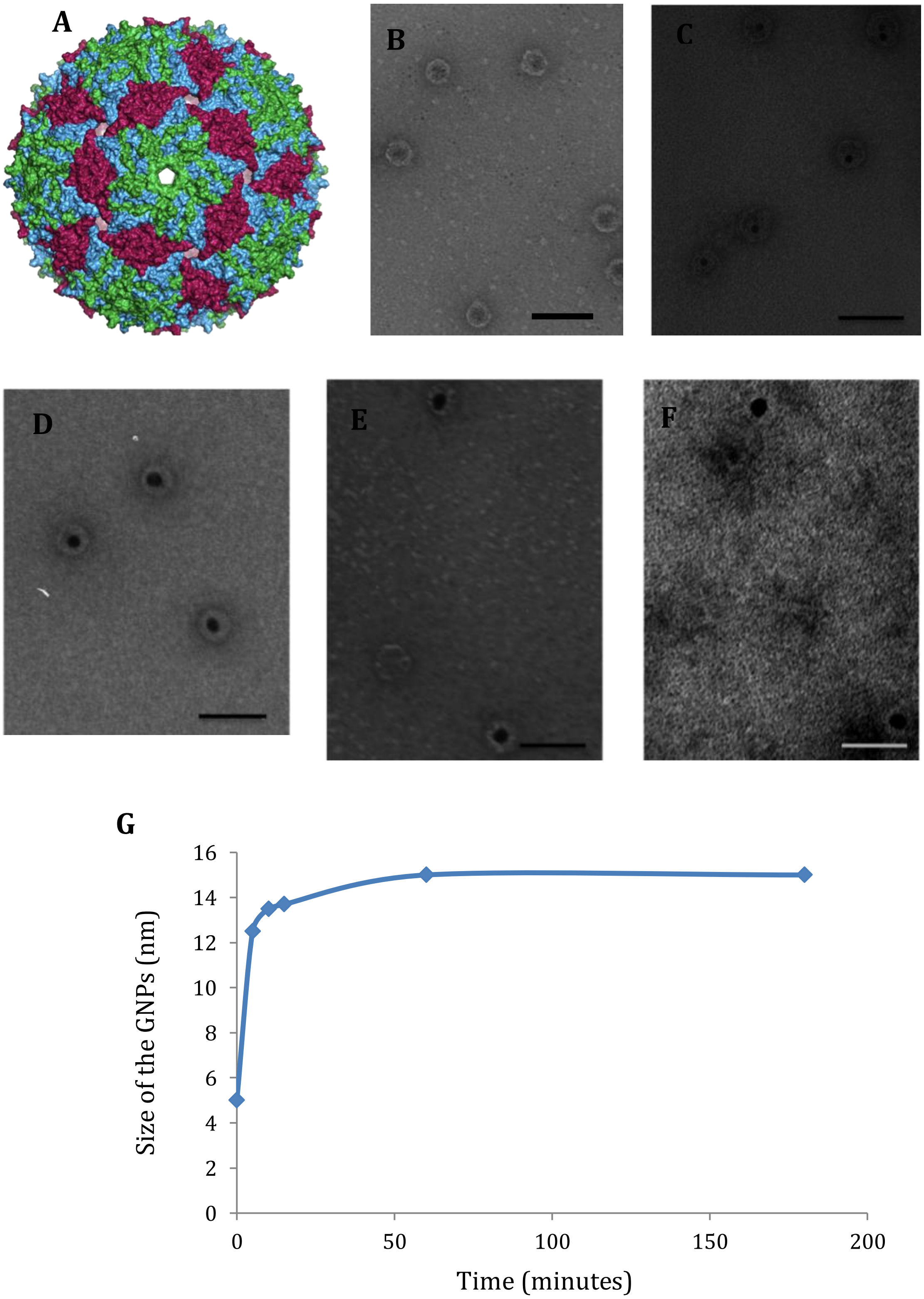

Figure 6.10. **(A)** Schematic showing the pores on the surface of the MS2 phage capsid (taken from Stockley, 2007). TEM image of the VLPs after electroless gold deposition reaction on MS2-PEGNPs **(B)** for an empty capsid, **(C)** at the start of the reaction, **(D)** after 5 minutes, **(E)** after 10 minutes and **(F)** after 3 hours. Scale bars equal 60 nm. **(G)** Graph showing the size of the GNPs against time for the gold deposition reaction.

Initially, the size of the GNPs increased rapidly for up to 10 minutes, but then levelled off. This is evident from Figure 6.10 (**E**) and (**F**) showing the size of the encapsulated nanoparticle after the reaction time of 10 minutes and 3 hours respectively. A plot of the size of the encapsulated GNPs over the course of the reaction is shown in Figure 6.10 **G**. The MS2-PEGNPs when viewed under TEM after overnight incubation showed aggregates of enhanced nanoparticles inside the MS2-PEGNPs, similar to those shown earlier in Figure 6.9 (**B**). Although, no visible precipitate was observed unlike at higher concentration of gold (Figure 6.9 **A**). It seems that the phosphine or citrate coating over the GNPs is disrupted after gold is electroless deposited over the nanoparticle. The GNPs become unstable without such a coating. Further, the electrostatic charge interactions between the coat protein shell and nanoparticles disrupts the VLPs exposing the GNP inside to other unstable nanoparticles and thus forming aggregates. This mechanism needs further investigation.

6.2.5 Higher order structures using virus-like particles

One of the main objectives of this research was the fabrication of a molecular transistor-like structure from virus-based nanostructures using self-assembly. Icosahederal MS2 and filamentous M13 bacteriophage were selected for the purpose. Hence a dual functional phage M13GB was created with biotin-binding motif displayed on the minor coat protein, pIII and gold-binding motif on major coat protein, pVIII (See Chapter 3). Many M13GB phage particles should bind to a biotin-labelled MS2-PEGNP to create higher order structures (See Figure 1.15 in Chapter 1). The M13GB phage can then be coated with gold to form gold nanowire electrodes of the molecular transistor-like structure.

Biotin was bound to the primary amine of the exposed lysine residue on the surface of the MS2 phage capsid using the NHS-LC Biotin reagent from Sigma-Aldrich (St. Louis, U.S.A.). The labelling of the wild-type MS2 phage capsid with biotin was successful, which is evident from the denaturing polyacrylamide gel and the western blot shown in Figure 6.11 (**A**) and (**B**) respectively.

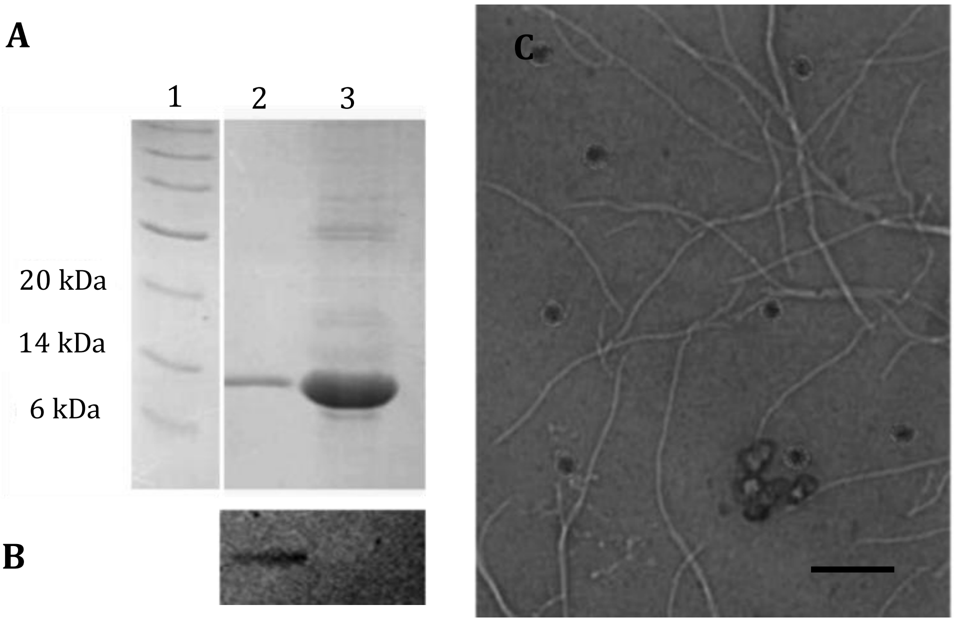

Figure 6.11. **(A)** Denaturing polyacrylamide gel electrophoresis of biotin-labelled MS2 phage capsid. **(B)** Western blot of the biotin-labelled MS2 phage capsid. **(C)** TEM image of the biotin-labelled MS2 phage capsid mixed with the M13GB phage. The sample was stained with 2% (w/v) uranyl acetate. Scale bar equals 100 nm.

Lane 1 was loaded with a protein ladder. Biotin-labelled MS2 phage capsid was loaded in lane 2, while the wild-type MS2 phage capsid in lane 3. The gel stained with the Coomassie reagent shows the coat protein bands in both the lanes. The gel in Figure 6.11 (**B**) was incubated with the cy3 labelled anti-biotin antibody and then scanned with a 488 nm laser. The biotin-labelled protein band was clearly visible in lane 2, but no band was observed for the non-labelled wild-type MS2 phage capsid in lane 3. Further, when the biotin-labelled MS2 phage capsid was mixed with streptavidin labelled magnetic beads, the MS2 phage capsids bound to the bead as was observed under TEM (data not shown).

3 equivalents of the M13GB phage was mixed with 1 equivalent of the biotin-labelled MS2 phage capsid and viewed under TEM (Figure 6.11 **C**). However, M13GB phage did not bind to the biotin-labelled MS2 VLP to form any higher order structures. It may be because the biotin-binding motif used in this experiment was identified using a pVIII phagemid library. It has been reported that when a pVIII-derived motif is transferred to pIII for display, it may not be as effective (Clackson, 2004; Sidhu, 2001). The other reason for no observed binding between biotin-labelled MS2 VLP and M13GB can be because the low binding affinity of the selected biotin-binding motif towards biotin. Saggio (1993) reported the IC_{50} of the biotin-binding motif used in this experiment to be 50 μM. This value indicates that the biotin-binding peptide used does not have strong binding affinity to biotin. The peptide motifs with IC_{50} value of about 50 nM or lower would have higher chance of working in self-assembly based nanotechnology applications (Peters, 2006). Hence, it seems that although the binding affinity of the biotin-binding peptide in the M13GB phage was enough to bind to biotin molecules in solution (see Chapter 3), it was not enough to bind and hold on to a large biotin-labelled MS2 VLP.

6.3. Conclusions

Gold nanoparticles of different sizes were successfully encapsulated inside the MS2 phage capsid using the assembly initiator TR RNA molecule bound to the GNP. The encapsulation efficiency of the MS2-PEGNPs decreased with the increase in the size of the nanoparticle. Expectedly, GNP encapsulation was not observed for nanoparticles bigger than the size of the inner cavity of the MS2 phage capsid. Also, for bigger nanoparticles, the VLPs formed were not similar in shape and size to the T=3 capsid formed by the wild-type MS2. It may be because the protein shell collapsed on to the surface of the nanoparticle due to the electrostatic charge interaction between the nanoparticle surface and viral capsid protein shell. Similarly, streptavidin labelled CdTe quantum dots were encapsulated inside the MS2 phage capsid, but even their encapsulation efficiency was low due to their overall large size.

Gold was deposited on the GNP inside the MS2-PEGNPs using the pores on the surface of the VLPs. These pores could be used to perform further chemistry on the encapsulated nanoparticle, which can be useful in the fabrication of electronic devices using this hybrid MS2-PEGNP.

Finally, it was shown that the biotin-binding M13GB phage, which binds to free biotin molecules in solution, did not bind to the biotin-labelled MS2 phage capsid. This may be because, the biotin-binding motif selected using the pVIII library may lose some of its binding affinity when displayed on the pIII protein of the M13 bacteriophage. The absence of any M13GB phage bound to biotin functionalised MS2 phage capsid could also be attributed to the low binding affinity of the biotin-binding motif and the larger weight of the M13GB and MS2 phage.

Chapter 7

Nanomanipulation of virus-templated nanostructures

7.1 Introduction

7.1.1 Bottom-up assembly by nanomanipulation

Inorganic nanostructures using biological templates have been assembled into simple electronic devices such as the lithium ion battery electrode (Nam, 2006), sodium ion battery cathode (Moradi, 2015) and photovoltaic cells (Dang, 2011) using the principles of molecular recognition and self-assembly. This was achieved by programming the biological template to display the design motifs on its surface using genetic engineering, chemical modification etc. The process of fabricating such electronic devices on tailored biological nanostructures for self-assembly requires a lot of time and effort during the design phase. An alternative method of assembling a prototype nanodevice from its components would be highly desirable, if it eliminates some of these steps involved in the engineering of the biological nanostructures. The design cycle time for the device fabrication can be reduced significantly in that case. Assembly of nanostructures into useful devices using such a method would require the ability to visualize these nanostructures before they can be handled and manipulated with some degree of precision and control. Imprinting and lithographic techniques like Electron Beam Lithography (EBL) are used to make nanostructures but have not been used for precise handling and manipulation of the nanostructures.

Developing such technologies, to control and manipulate the nanostructures, is at the heart of the nanotechnology research. Richard Feynman envisioned the manufacturing at the nanoscale and also discussed the challenges associated with such technologies in his famous lecture ‘There's plenty of room at the bottom’ (Feynman, 1960). Many techniques to image nanoscale objects are well established. Some of these techniques use Transmission Electron Microscope (TEM), Scanning Electron Microscope (SEM) and Scanning Tunnelling Microscope (STM). However, attempts to modify these devices to incorporate them with the ability to handle and move objects at the nanoscale to make a complex assembly have met with limited success. Some techniques of handling objects in SEM have been developed, but they are not yet suitable for device fabrication by nanomanipulation of the nanostructures (Mazerolle, 2005; Ru, 2012; Suga, 2009; Woo, 2012). Although, TEM has a superior resolution when compared to SEM, the sample space is very narrow and thus limiting the possibility for *in-situ* TEM nanomanipulation in practice. Scanning Tunnelling Microscope (STM) has been used to move atoms and molecules around in a set pattern. Recent advances in this field have combined the fast imaging of SEM with the atomic resolution of STM along with the flexibility of multiple scanning probes to provide a useful tool to make rapid prototypes of nanodevices (Qin *et al.,* 2012). Atomic Force Microscope (AFM) is a powerful tool for imaging nanoscale objects. However, the imaging frame rate is usually slower compared to the SEM.

7.1.2 Atomic Force Microscope

The Atomic Force Microscope (AFM) is a scanning probe microscope, which uses a tip placed at the end of a cantilever to probe the sample surface. A laser beam is directed onto the cantilever near the tip. The force acting on the AFM tip causes the cantilever to bend. This deflection of the cantilever is detected by measuring the position of a reflected laser beam on a photo detector system. The movement and position of the tip and the stage is maintained by piezoelectric elements and is capable of sub-angstrom level resolution in normal and lateral directions (Jalili, 2004). A feedback control is employed to control the cantilever vibration and hence the distance between the tip and the surface. The AFM cantilever can measure forces in the range of a few pico-Newtons to several micro-Newtons in both the normal and lateral directions. This movement of the cantilever is used to create a three-dimensional map of the surface at nanoscale. Contact mode and tapping mode are the two major modes of imaging in the AFM (Figure 7.1).

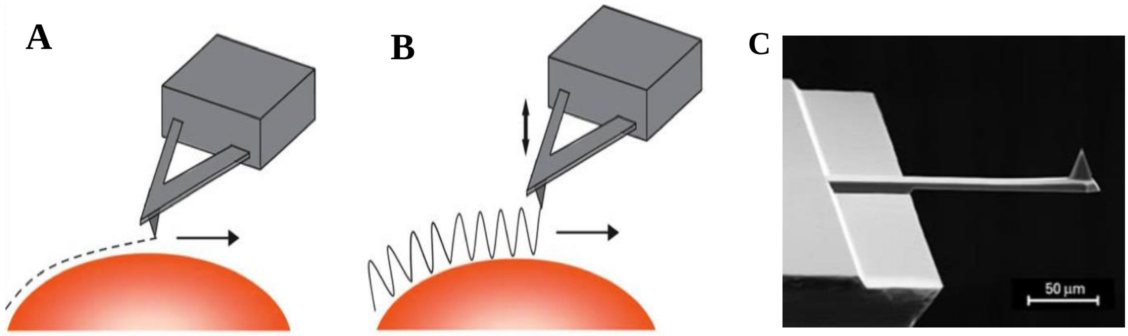

Fig 7.1. AFM imaging using a cantilever tip in **(A)** Contact mode and **(B)** Tapping mode. (C) SEM image of an AFM cantilever tip (taken from the Schaefer product catalogue).

In contact mode (Figure 7.1 **A**), the tip scans the sample in close contact with the surface, whereby a repulsive force acts on the tip of the probe. This force is the result of the AFM cantilever being pushed against the sample surface with a piezoelectric positioning element and has a mean value of approximately 10^{-9} N (Jalili, 2004). An SEM image of the AFM cantilever is shown in Figure 7.1 (**C**). The deflection of the cantilever is sensed and compared with a desired value of the deflection in a DC feedback amplifier. If the measured deflection is different from the set value, the feedback amplifier applies a voltage to the piezo to raise or lower the sample relative to the cantilever to restore the desired value of deflection. The voltage that the feedback amplifier applies to the piezo is a measure of the height of the features on the sample surface. It is displayed as a function of the lateral position of the sample. However, high lateral forces act between the cantilever tip and surface in the contact mode and can damage the both the tip and the sample.

To solve this, another imaging mode is used, where the tip touches the surface only for a short duration at regular frequency, hence referred to as Tapping Mode (Figure 7.1 **B**). As the piezo excites the cantilever substrate, it causes it to oscillate vertically at its resonant frequency. The reflected laser beam thus generates a sinusoidal “detector signal" using the photodiode array. As the probe approaches the sample surface, the amplitude decreases. A feedback control system is used to move the tip up or down to maintain a constant oscillation amplitude according to user-defined amplitude setpoint. Thus, a high-resolution three-dimensional image of the sample surface topography is produced.

7.1.3. Manipulation of nanostructures using an AFM tip

The AFM tip can also be used for manipulation of the objects at the nanoscale. The probes of an AFM can also be used for the nanomanipulation of the nanostructures or even atoms (Custance, 2009). Gold nanoparticles and nanorods were moved using an AFM tip by Requicha (2001). 5 - 15 nm metallic and semiconductor nanoparticles were manipulated by Kim (2011). They also devised a method to detach the nanoparticle from the AFM tip which often bind to the tip because of electrostatic interactions and modify the effective tip shape. Although, AFM had been used to manipulate nanoparticles, it is difficult to manipulate inorganic or soft one-dimensional (1D) materials, as the samples are easily distorted or often broken due to the adhesive and friction forces at the sample-substrate interface. Kim (2013) manipulated ZnO nanowire on a silica substrate to observe both rolling and sliding motions depending on the nanowire–silica frictional interaction. However, the nanowires had low aspect ratio and thus lower resultant adhesive/frictional forces acting on the nanowire. Hou (2015) devised a method to estimate static friction force acting on the nanowire while trying to move Al_2O_3

nanowires on a silica substrate. However, this estimation was limited for short nanowires only. Yang (2013) moved flexible carbon nanotubes on a substrate but again the movement was limited to a narrow range of bending angles, exceeding which resulted in mechanical failure.

The nanomanipulation of the phage-based metallic and semiconducting nanostructures can be used to make electronic nanodevices in a relatively short period of time when compared to traditional methods of electronic device fabrication such as lithography or EBL. The AFM tip, however, cannot image and manipulate concurrently, hence all, but the simplest tasks require a laborious cycle of imaging followed by blind manipulation. Virtual Reality (VR) technology is used to build an interactive, three-dimensional virtual topographical map of the sample surface. When combined with the haptic devices the AFM tip can be used for nanomanipulation.

7.1.4. Virtual haptic AFM

Michael Measures (Department of Physics, University of Leeds) developed such a telerobotic AFM set-up, whereby the motion of the AFM tip could be controlled in real time using a haptic device (Figure 7.2 **A** and **B**). The setup for nanomanipulation was constructed around the Nanoman AFM system developed by Veeco (Veeco Instruments, Plainview, New York), which incorporated a closed-loop head for greatly improved positional linearity in the XY plane, ideal for nanomanipulation tasks. The VR interface was a clone of the Virtual Workbench which crucially enables the simultaneous location of the haptic device with the floating VR surface. The NanoManipulator combined the elements of VR, haptic feedback and computer simulation to deliver an intuitive user interface for the AFM. This scaled representation of the interaction forces between the tip and the sample enabled one to manipulate the nanostructures. It uses an AFM to gather the data describing the 3D shape of the sample within the microscope, and then uses a computer-generated virtual world to allow the user to see and feel the sample surface.

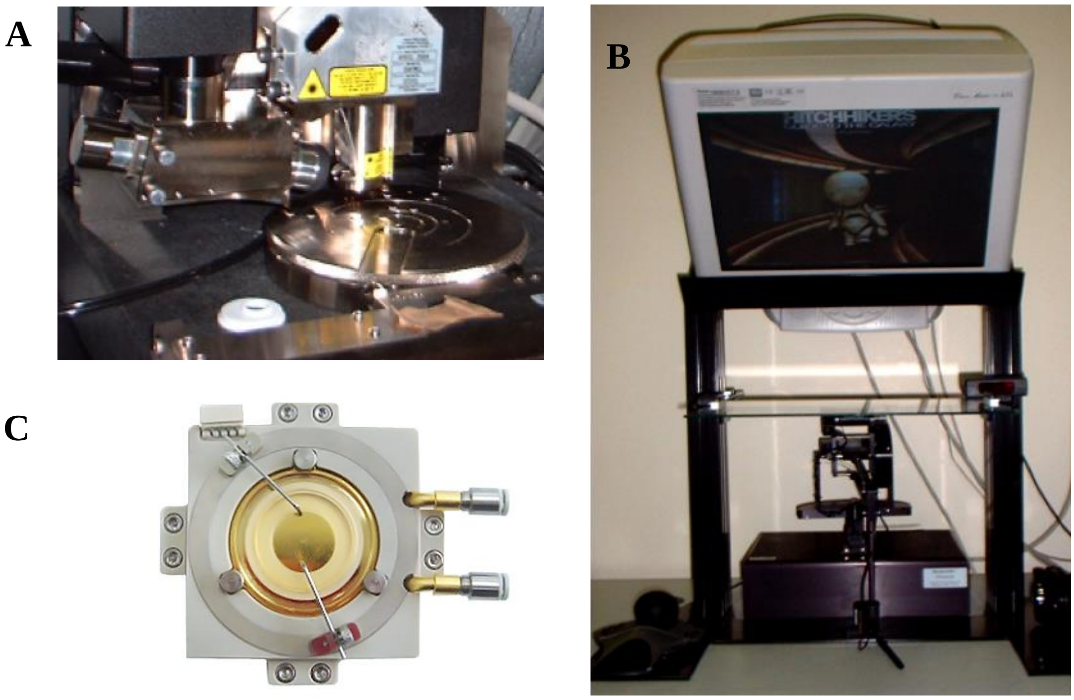

Fig 7.2. **The virtual haptic atomic force microscope**. **(A)** Sample and tip holder of the AFM used. **(B)** The haptic interface with the virtual reality set-up for visualisation. **(C)** A fluid cell for imaging samples submerged in a liquid (taken from Park Systems product catalogue).

In the direct tip control mode, the user can take control of the AFM tip and feel in real-time a scaled representation of the interaction forces being experienced between the tip and the sample. In effect, the user's eyes and hands are projected into the nanoworld and with the use of a tele-operated AFM tip, the user can manipulate nanoscale objects in real-time. To solve the issue of being unable to image and manipulate concurrently, computer simulation is utilised. The simulation code runs across a standard TCP/IP network.

The biological templates mostly have hydrated natural environment. The fluid cell (Figure 7.2 **C**) provides the ability to image and subsequently manipulate the biological structures on a substrate, while they are submerged in a fluid (Li, 2003). However, leakage is a common problem along with more fundamental problems such as damage of the hydrated and vulnerable biological samples during nanomanipulation.

7.1.5. Aims of the work described within this chapter

The aims were as follows:

1. The primary objective was to investigate if the M13g phage-based gold nanowires and MS2-PEGNPs can be manipulated using an AFM tip.
2. To investigate the effect of the ‘soft’ and ‘hard’ AFM tip on the manipulation of phage-based inorganic nanostructures.
3. To investigate the effect of the substrate type outcome of the manipulation using an AFM tip.

7.2. Results and Discussion

7.2.1. Nanomanipulation of filamentous organic and inorganic structures

All AFM imaging was done in tapping mode using the Veeco Dimension 3100 AFM. The location of the tip in the virtual world was offset by approximately 50 nm when compared with a real-time scan during the sample imaging. This meant that the tip force felt in the virtual world did not correspond to the same location in the real world. Hence, during the manipulation of the nanowire, an adjustment was made so that a point in the virtual world corresponded to the intended point in real world. Relative humidity and the ambient temperature seemed to affect this offset, as the offset was almost eliminated after the AFM scan was done under vacuum in a more controlled condition.

7.2.1.1. Manipulation of the M13 bacteriophage

The ability to manipulate electronically useful virus templates on a surface could be useful for making rapid prototypes of electronic devices. This approach gives freedom to perform chemistry on the template before or after manipulation. Hence, the nanomanipulation of the M13 bacteriophage was explored on different substrates using an AFM tip (Figure 7.3). The tip amplitude was adjusted so that the tip tapped as lightly as possible on the phage. A fresh mica surface was cleaved and cleaned with water. The mica surface was then treated with 10 mM $NiCl_2$ solution to positively charge the mica surface, in order to hold the phage onto the surface. The M13 phage can be seen in an AFM scan in Figure 7.3 (**A**). The manipulation of the nanowire was done in contact mode using an AFM cantilever tip. On manipulation of the virus using the haptic controlled AFM tip, the virus was dissected by the AFM tip (Figure 7.3 **C**).

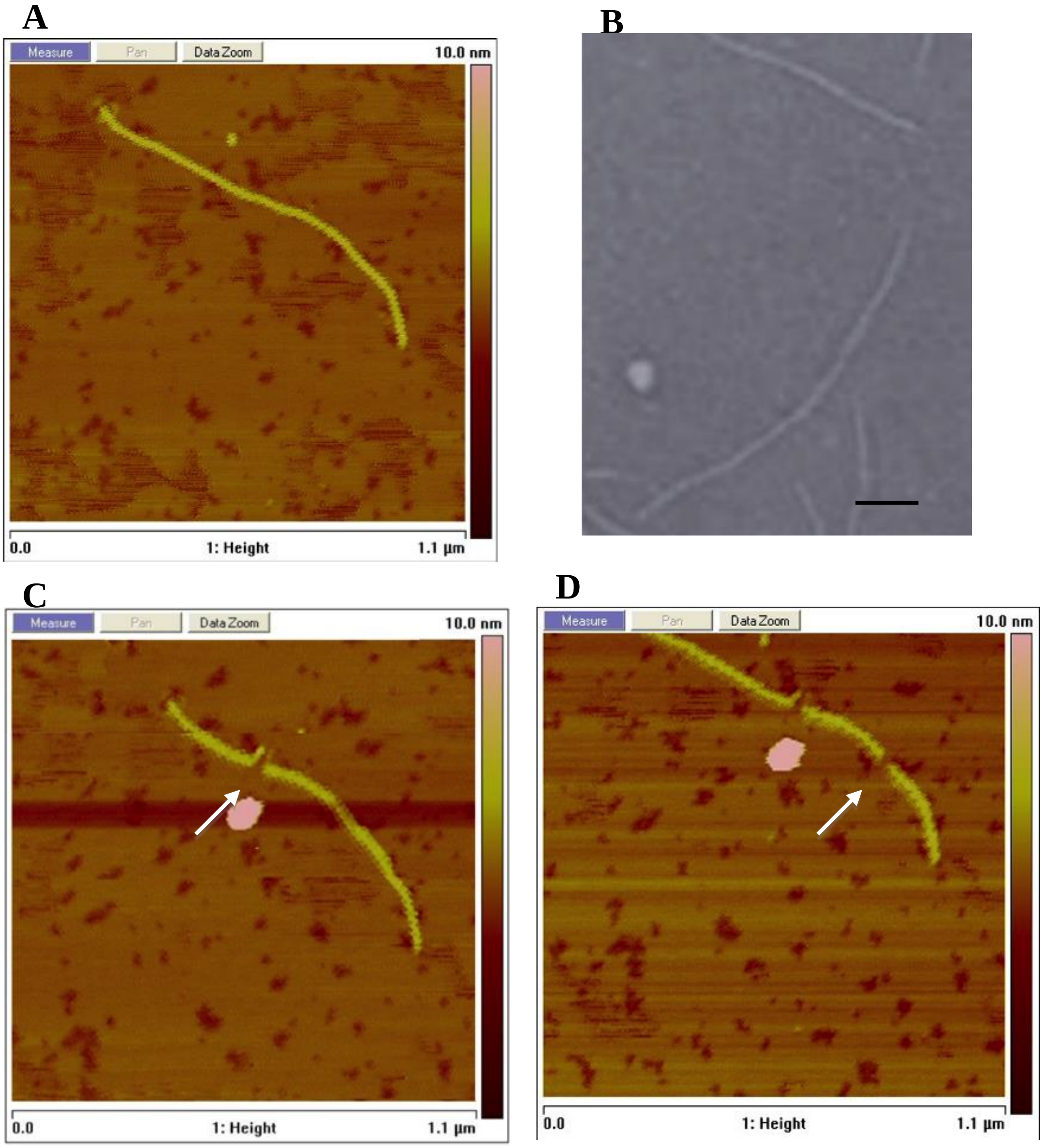

Figure 7.3. **Manipulation of the M13 bacteriophage using an AFM tip**. **(A)** The M13 phage on a mica substrate. **(B)** A TEM image of the M13 phage sample. Scale bar equals 100 nm **(C)** The mechanical failure of the M13 phage at the point of the tip-phage interaction as shown by the arrow. **(D)** A second mechanical failure of the same phage at another point of the tip-phage interaction as shown by the arrow.

This suggested that the adhesive and frictional forces acting at the M13 phage-mica interface were greater than the yield stress of the M13 phage before any translation occurred. Falvo *et. al.* (1997) reported the manipulation of the smaller Tobacco Mosaic

Virus (TMV) fragments using an AFM tip after the larger fragments were similarly dissected. However, the M13 phage was dissected again after trying to manipulate the smaller fragment of the M13 phage made after the first manipulation attempt (Figure 7.3 **D**). This maybe because the M13 bacteriophage is not a rigid structure as is the TMV and likely has lower yield stress than TMV particles.

In order to reduce the surface charge density and thus reduce the adhesive force at the M13 phage-mica interface, the mica surface was not treated with $NiCl_2$ solution. However, the phage particle experienced mechanical failure again on manipulation with an AFM tip. In order to reduce the adhesive forces between the phage particle and the substrate, the substrate was covered in deionised water and the nanomanipulation was done by submerging the AFM tip in this fluid. However, the manipulation of the M13 phage particle submerged in water still resulted in the mechanical failure of the phage particles. Addition of 10 µL of 0.05% Tween 20 to the fluid cell, to affect the adhesive forces at the phage-mica interface, also did not yield in successful phage manipulation. Different substrates were used to reduce the adhesive forces between the nanowire and the substrate.

Falvo et. al. (1997) reported that the adhesive forces at virus-mica interface was very high. Hence silica was selected as the substrate of choice for any nanomanipulation as they are further useful in device fabrication using EBL. A silica substrate cleansed by Piranha solution was used for phage nanomanipulation, but this also resulted in the dissection of the phage particles. A silica substrate was chemically modified to coat it with a self-assembled thiol and amine monolayer. However, the phage particle was dissected again during nanomanipulation in both the cases.

7.2.1.2. Manipulation of the M13G phage-based gold nanowire

The M13G phage-based gold nanowires made by electroless deposition of gold ions on p-GNP complexes were used for manipulation using an AFM tip. Such nanomanipulation of the nanowire could also help understand nanowire's physical properties. A SiO_2 surface was cleaned with freshly made Piranha solution and dried using a jet of nitrogen gas. The M13G phage-based gold nanowire solution was deposited on it and the drop dried again using a jet of nitrogen gas. An AFM scan of the sample is shown in Figure 7.4 (**A**).

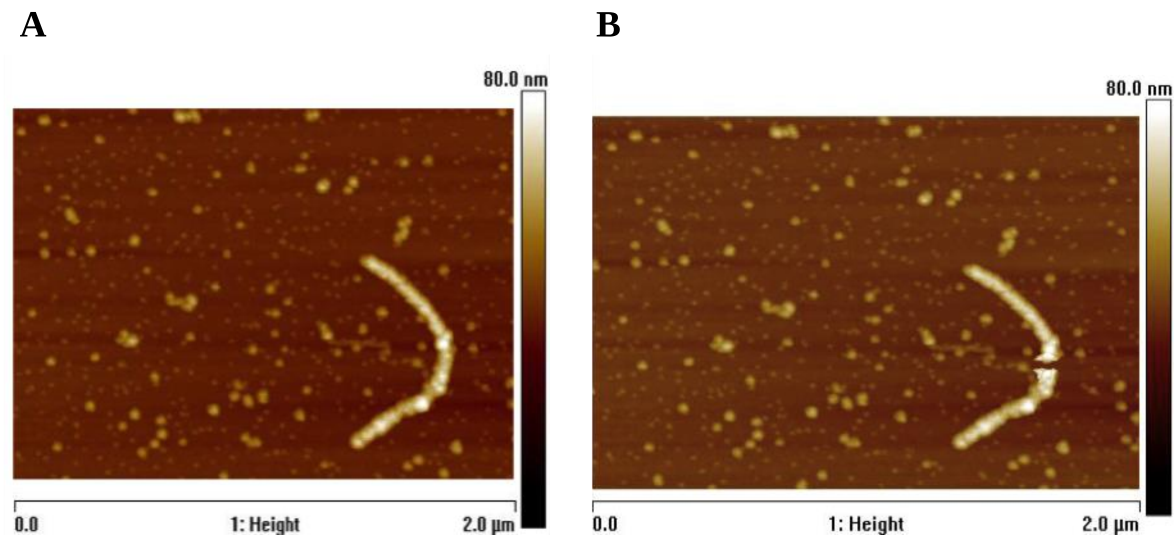

Fig 7.4. AFM image of a non-annealed M13 phage-based gold nanowire **(A)** before manipulation and **(B)** after manipulation with an AFM tip.

On manipulation of the nanowire using an AFM tip, the mechanical failure of the nanowire was observed (Figure 7.4 **B**). A similar dissection of the nanowires occurred while moving the wire in contact mode without the VR interface. The nanowires were about 45 nm in diameter. The yield stress of the non-annealed M13G phage-based gold nanowire was less than the adhesive/frictional forces at the nanowire-silica interface. The mechanical property of the M13G phage-based gold nanowire can be improved by increasing the thickness of the nanowire. Hence longer duration of gold deposition reaction should likely improve the strength of the nanowire. Thermal annealing of the nanowire under vacuum can improve the mechanical property of the nanowire as GNPs on the nanowire surface fuse together (see Chapter 4). The M13 phage-based gold nanowire on a silica substrate was annealed at 250^{o}C (Figure 7.5 **A**).

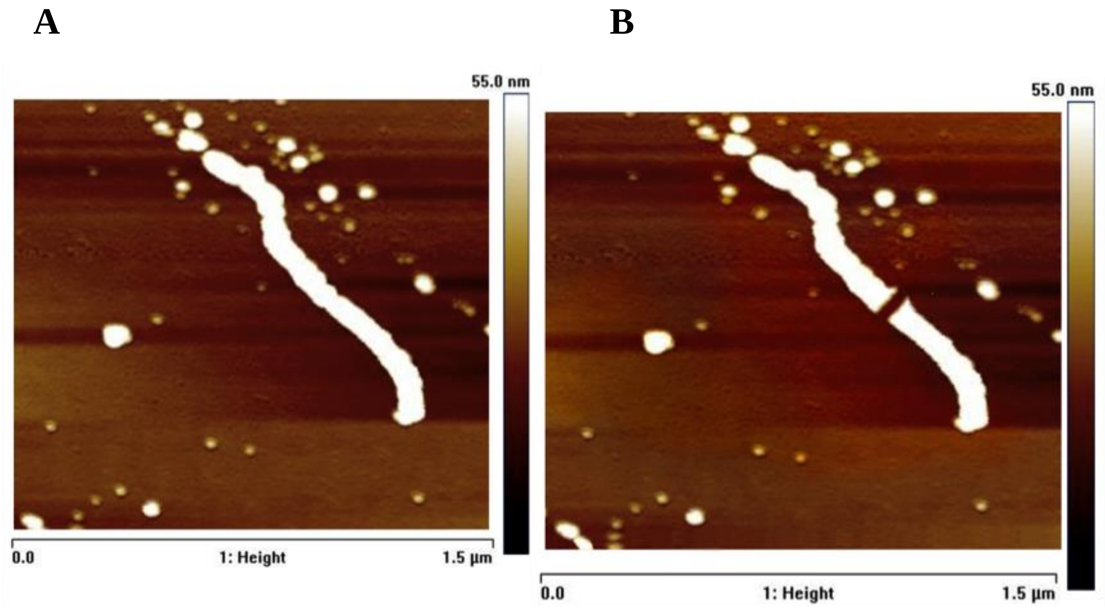

Fig 7.5. AFM image of the annealed M13 phage-based gold nanowire **(A)** before manipulation and **(B)** after manipulation with an AFM tip.

However, the annealed nanowire also experienced mechanical failure during nanomanipulation (Figure 7.5 **B**). The nanowires were about 55 nm in diameter. This suggested that increasing the thickness of the nanowire and thermal annealing did not result in a significant increase in the mechanical strength of the nanowire so as to overcome the adhesive/frictional forces.

The AFM tip used for manipulation can also be a crucial factor in manipulation. To rule out the effect of the AFM tip on the results of the nanomanipulation of the M13G phage-based gold nanowires, different tips were used.

7.2.1.3. Manipulation of the gold nanowire using different AFM tips

As different robotic tools and 'hands' are employed in factories and assembly shops for handling different materials and carrying out various manipulation jobs, the characteristics of the AFM tip can be crucial for nanomanipulation. However, unlike the variety of shapes and designs of the robotic hands, the AFM tip has limited options of basic shape. Change in the stiffness of the cantilever, tip radii and tip material/coating are some of the modifications done to the AFM tip for specialized purposes.

The tip used in nanomanipulation attempts above was rather 'hard' with a spring constant of 40 N/m and frequency of 300 kHz. The stiff cantilever of the 'hard' tip could play a role during nanomanipulation. To test the effect of the cantilever stiffness on the manipulation of the gold nanowire, a 'softer' tip with a spring constant of 2 - 4 N/m and frequency of 70 kHz was used to manipulate an M13 phage-based gold nanowire annealed at 250^{o}C. However, the nanowires were dissected by this 'soft' tip as well (Figure 7.6).

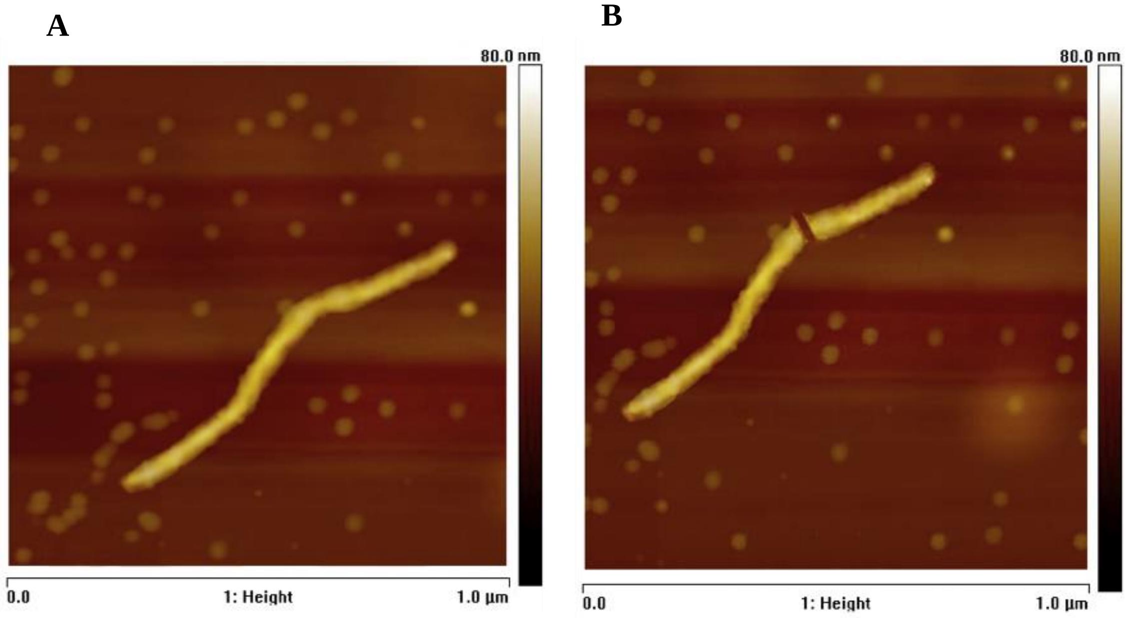

Fig 7.6. AFM image of an annealed M13 phage-based gold nanowire using a 'soft' AFM tip **(A)** before manipulation and **(B)** after manipulation.

7.2.1.4. Manipulation of a gold nanowire on silica substrate submerged in water

The adhesive/friction forces at the substrate-sample interface are the major obstacle in the nanomanipulation of soft or inorganic nanostructures. The hydration of the sample affects the resultant adhesive forces and can affect the outcome of the manipulation (Kweon, 2015). Hence, M13 phage-based gold nanowire annealed at 250°C was manipulated in a 'fluid cell' whereby the AFM tip was submerged in water (Figure 7.7).

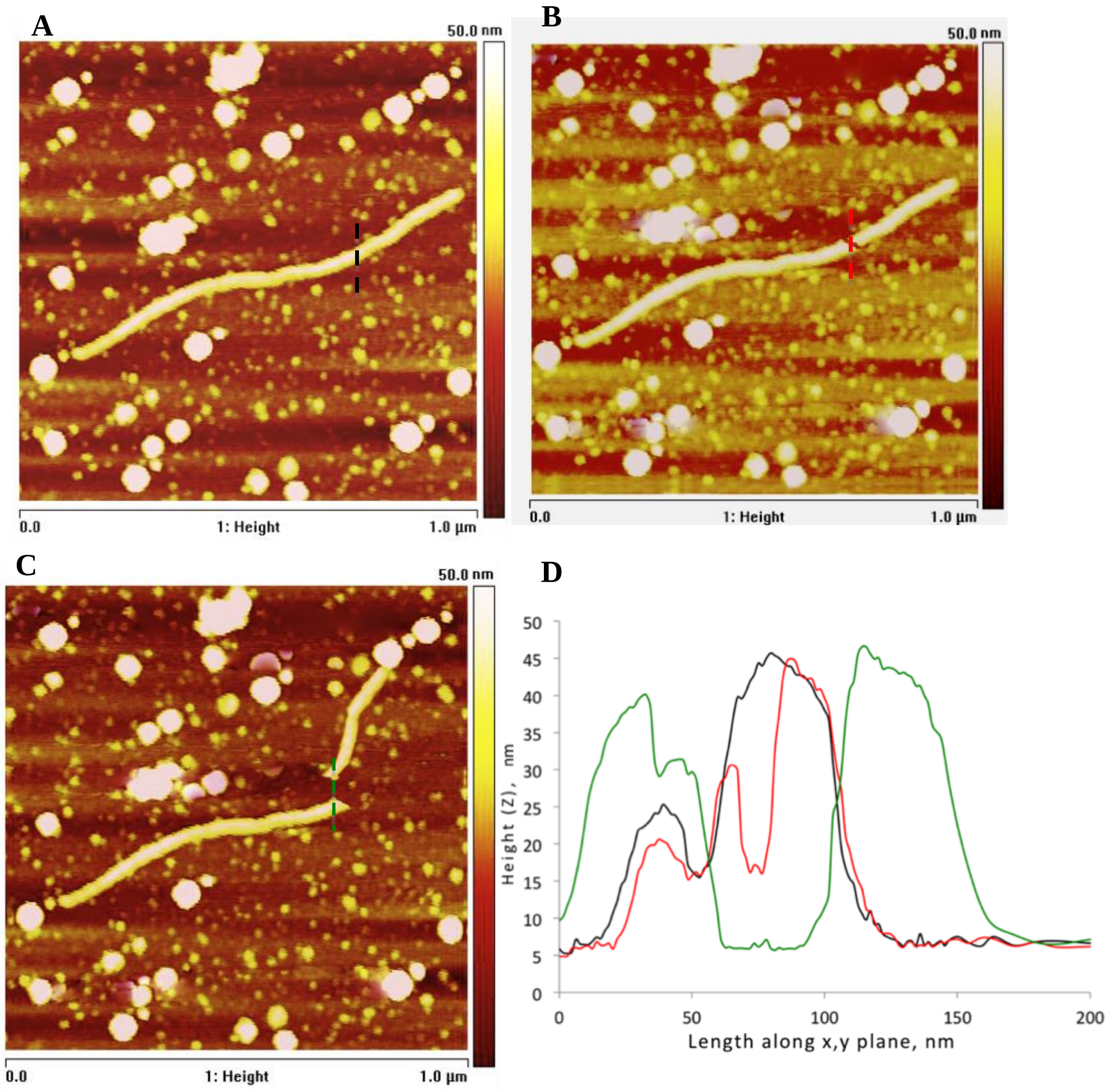

Fig 7.7. AFM image of the M13G phage-based gold nanowire **(A)** before manipulation and **(B)** after manipulation with an AFM tip. **(C)** AFM scan of after manipulation of the smaller fragments left after dissection in the first manipulation attempt. **(D)** Height profile of the nanowire before and after two manipulations.

The gold nanowire was imaged in contact mode (Figure 7.7 **A)**. The nanowire was dissected by the AFM tip during manipulation (Figure 7.7 **B**). However, the resultant short fragment of the cut nanowire (approximately 200 nm long) moved upon manipulation with an AFM tip without further cutting the nanowire into small pieces (Figure 7.7 **C**). The nanowire fragment showed both translational movement as well as the bending of the nanowire as can be seen in height profile of the nanowire fragments at the site where nanomanipulation was attempted. However, the nanowire fragment underwent irreversible deformation where it came in contact with the AFM tip as can be seen in the non-uniform thickness of the nanowire in that region (Figure 7.7 **C**).

This suggested that the ‘adhesive’ forces at the substrate-sample interface are dependent on the length of the nanowire in contact with the substrate. This explains why long fragments of the nanowires were dissected during manipulation by the AFM tip. The adhesive/friction forces at the substrate-sample interface at nanoscale is affected by the hydration of the sample.

7.2.2. Manipulation of GNPs and sphere-like VLPs

A nanoelectronic device is likely to be made of components, which have different dimensions, shape and size. The molecular transistor, fabrication of which is the ultimate objective of this research, has nanoparticles or hybrid nanoparticle structures as essential components (see section 1.10 in Chapter 1). Hence, the nanomanipulation of GNPs and MS2-PEGNPs was done on a silica surface.

7.2.2.1. Manipulation of GNPs on a silica surface.

GNPs are dense and hard, unlike the protein-nucleic acid shells of the virus-like particles. Hence, they are likely to keep their structural integrity intact during manipulation by the AFM tip. 10 nm GNPs from Ted Pella (NY, USA) were deposited on a silica surface. The nanoparticles were imaged in tapping mode and three GNPs were selected for manipulation (Figure 7.8 **A**). The GNP labelled ‘2’ was moved and the area was re-imaged in the tapping mode (Figure 7.8 **B**). The GNP moved without any apparent loss of their structural integrity as viewed under the AFM. Although, it took multiple attempt to move the GNP at the desired location. An offset was observed between the real-world and virtual-world AFM scan which became problematic while moving smaller GNPs.

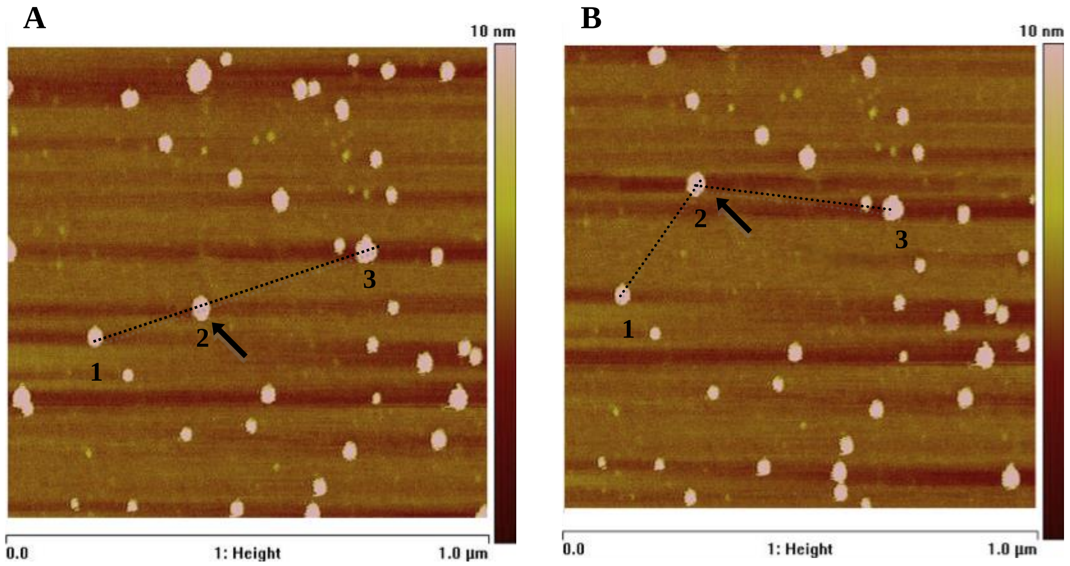

Fig 7.8. **Manipulation of 10 nm GNPs using an AFM tip on a SiO_2 surface. (A)** A 10 nm GNP (labelled 2) before manipulation. GNPs labelled 1, 2 and 3 lie on a straight line. **(B)** GNP labelled ‘2’ after manipulation. The GNPs 1, 2 and 3 do not lie on a straight line anymore after GNP labelled ‘2’ was moved from its original position.

7.2.2.2. Manipulation of MS2 phage particle

Although metallic nanoparticles could be nanomanipulated without damaging the nanoparticles, the organic M13 phage particles were cut by the AFM tip while trying to move the phage particle on a silica surface. The strong adhesive/friction forces at the phage-substrate interface can be attributed to large surface area in contact with the substrate, because of its length. Hence only shorter nanowire fragments could be moved on a substrate. However, a MS2 phage particle has a relatively smaller area in contact with the substrate and is likely to retain its structural integrity during manipulation using an AFM tip.

The MS2 phage particles in a PBS buffer were deposited on a silica surface and imaged using an AFM in tapping mode (Figures 7.9 **B** and **C**). A TEM image of the MS2 phage sample from the batch is shown in Figure 7.9 (**A**). The majority of the phage particles were damaged either partially or completely when manipulated using an AFM tip (Figures 7.9 **F** and **G**). However, some of the VLPs could be moved around without showing any signs of structural damage (Figures 7.9 **C** and **D**). The phage particle on the middle right was moved to the left, which is evident from the height profile along a line crossing the three contiguous phage particles (Figure 7.9 **E**). The appearance of a peak in the red plot indicates the capsid was successfully moved from its location. Such a successful manipulation was not common and most such attempts compromised the structural integrity of the phage particles. In some cases (Figure 7.9 **G**) the virus particle on the right side of the image was completely destroyed during the manipulation which was confirmed by the height profile of the same virus before and after the manipulation (Figure 7.9 **H**).

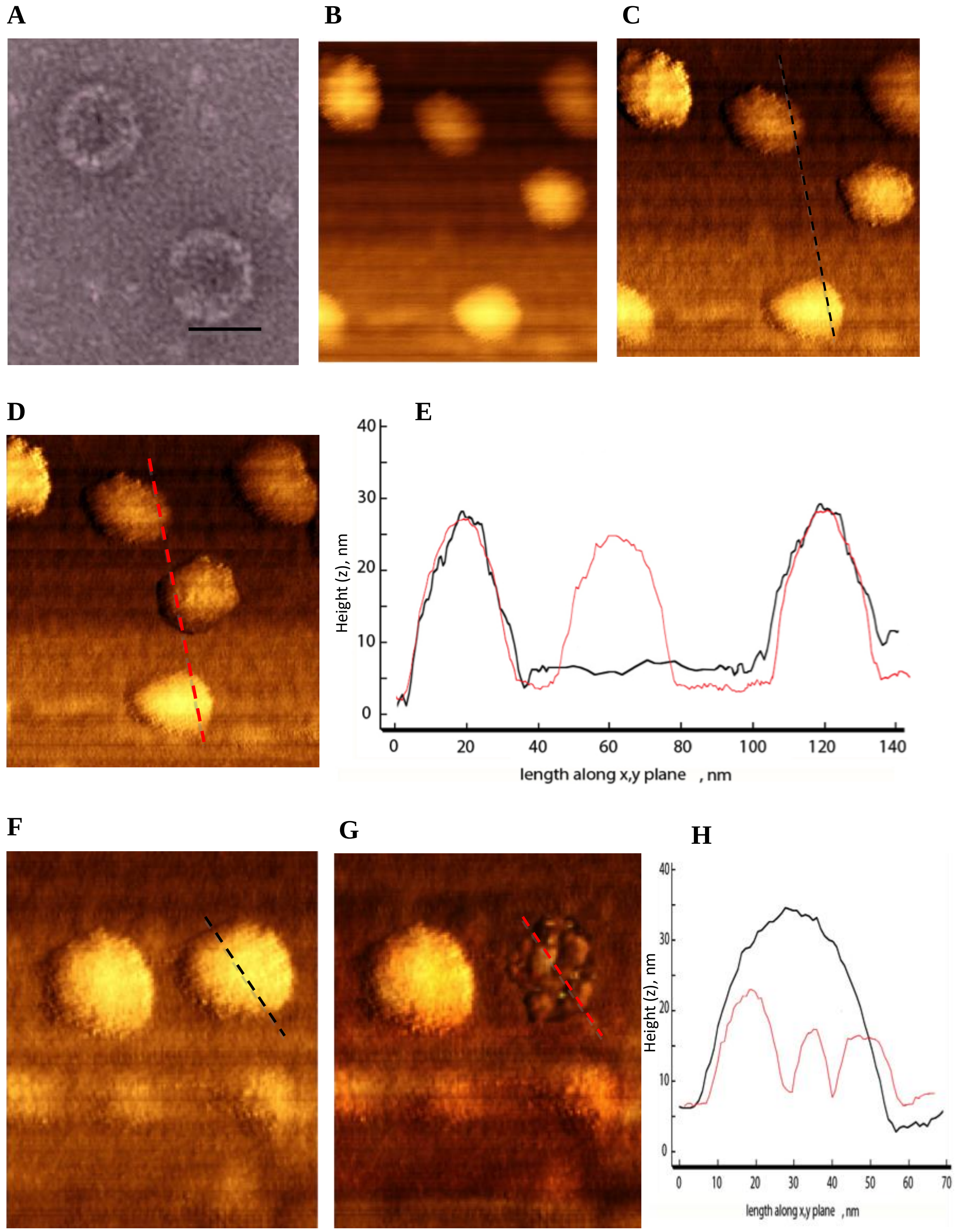

Fig 7.9. **Manipulation of the MS2 bacteriophage capsid on a silica substrate**. **(A)** A TEM image of the MS2 phage sample. Scale bar equals 25nm. **(B)** An AFM scan of the MS2 phage capsid before manipulation. **(C)** Derived image of the MS2 capsid. **(D)** MS2 phage capsid in **C** after manipulation. **(E)** The height profile of the MS2 phage capsid before and after the manipulation. An AFM image of another MS2 capsid: **(F)** before nanomanipulation and **(G)** showing the disintegration of the phage capsid from **F** after manipulation. **(H)** Height profile of the phage capsid from **F** before and after manipulation.

7.2.2.3. Manipulation of MS2-PEGNP complex

The MS2-PEGNPs with a 5 nm GNP inside it was deposited on the silica surface and imaged using an AFM in tapping mode (Figure 7.10 **A**). The inset shows the TEM image of the MS2-PEGNPs of the same batch.

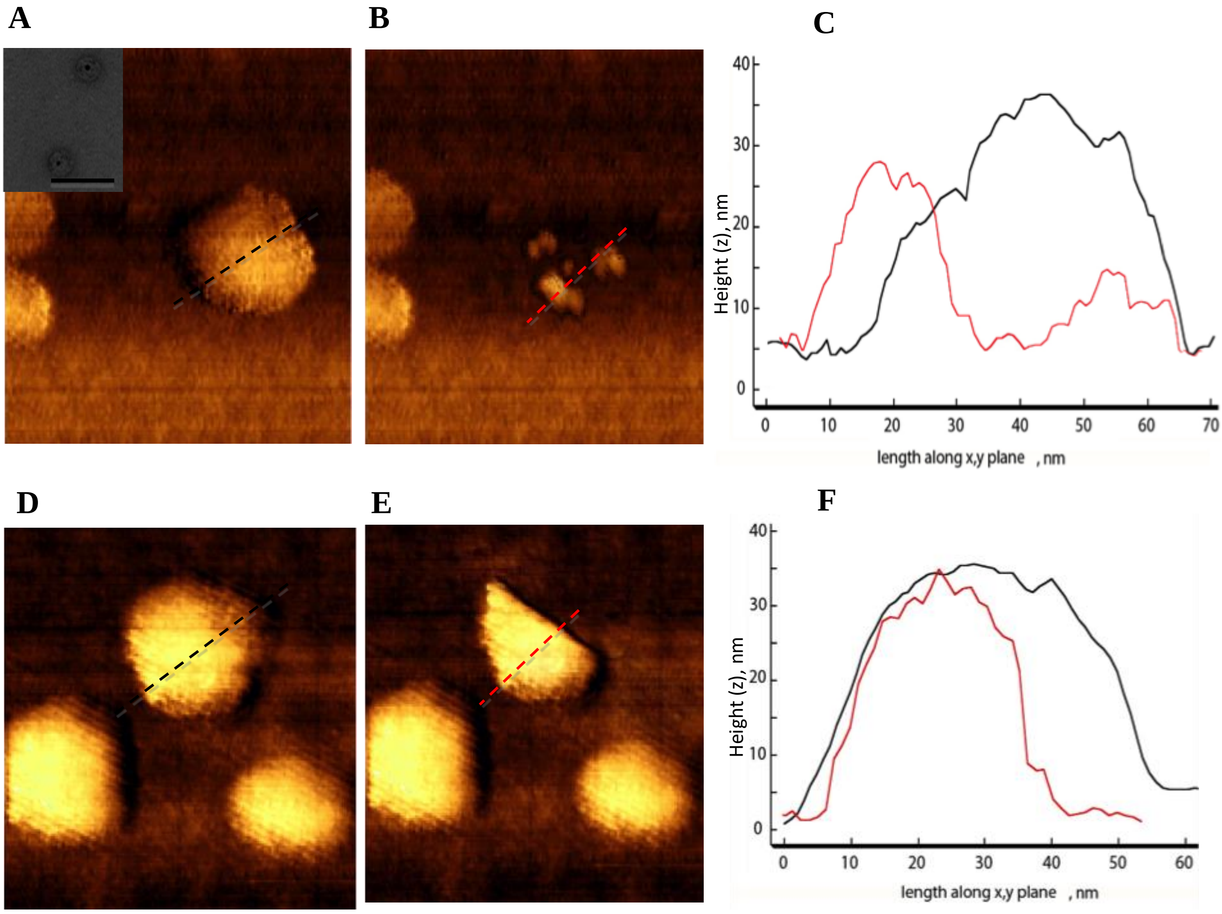

Fig 7.10. **Manipulation of the MS2-PEGNPs on a silica substrate.** An AFM image of the: **(A)** MS2-PEGNP. (Inset- TEM image of the MS2-PEGNP sample. Scale bar equals 100 nm), **(B)** disintegrated MS2-PEGNP after manipulation. **(C)** shows the height profile of the MS2-PEGNP from **A** before and after manipulation. An AFM image of: **(D)** another MS2-PEGNP, **(E)** MS2-PEGNP from **D** after manipulation **(F)** shows the height profile of the MS2-PEGNP from **D** before and after manipulation.

When the MS2-PEGNP on the right side of the Figure 1.10 (**A**) was moved using the AFM tip, the particle was completely damaged (Figure 7.10 **B**), which is evident from the height profile of the particle before and after the manipulation attempt (Figure 7.10 **C**). Figures 7.10 (**D**) and (**E**) show the partial damage done to a MS2-PEGNP before and after manipulation. The AFM tip sliced though the protein shell of the MS2-PEGNP. This was evident form the height profile of the MS2-PEGNP before and after manipulation (Figure 7.10 **F**). Successful nanomanipulation of the MS2-PEGNP was not observed unlike the case of the manipulation of the MS2 phage particles. The MS2-PEGNPs were also damaged during nanomanipulation when submerged in water in a fluid cell. This suggests that the MS2-PEGNPs have poor mechanical properties when compared to the wild-type MS2 phage capsids, possibly because of some structural difference.

7.3. Conclusions

The AFM tip was used to manipulate the phage particles and phage-based nanostructures using a virtual haptic. The metallic gold nanoparticles retained their structural integrity during nanomanipulation because of their hard and dense interior. However, the M13 phage particles and the phage-based gold nanowires lost their structural integrity during nanomanipulation on mica as well as a variety of other surfaces. This maybe because the resultant adhesive/frictional forces at the phage-substrate interface was greater than the yield stress of the phage particles or the nanowire.

Although, smaller fragments of annealed M13G phage-based gold nanowires could be manipulated on a silica surface when the nanowire was submerged in water. This was likely because the hydration of the nanowires affected the resultant adhesive forces at the phage-substrate interface.

While the majority of the wild-type MS2 phage capsids were damaged during nanomanipulation, some of the MS2 phage particles could be successfully manipulated using an AFM tip. This suggests that the resultant adhesive/frictional forces at the MS2 phage-substrate interface is less than in case of M13 phage. This could be attributed to the low surface area of the MS2 phage capsid in contact with the silica surface, compared to its mass. MS2-PEGNPs were damaged during manipulation with an AFM tip. This suggests that the MS2-PEGNPs have poor mechanical properties compared to wild-type MS2 phage capsids, possibly because of structural difference between the two particles.

Chapter 8

General Conclusions and Future Works

The ultimate aim of the work described in this thesis was to fabricate a self-assembling molecular transistor using the M13 and MS2 bacteriophages as a template. Although, this objective was not fully achieved, many landmarks associated with this project were and significant progress was made towards the final goal.

8.1. Conclusions from Chapter 3

Organic substrates like the M13 bacteriophage have no useful electrical properties, which can be used for electronic device fabrication. However, the M13 phage was genetically modified to express the gold binding peptide found by Huang, *et. al.* (2005) on the N-terminus of the major coat protein, pVIII of the M13KE bacteriophage. The mutant phage, M13G was shown to bind to citrate-stabilized GNPs bigger than 5 nm. However, M13G phage did not bind to 1.4 nm GNPs or 2 nm GNPs. As the peptide was selected against a bulk gold surface with fcc crystal structure, the M13G phage only showed binding affinity to GNPs with fcc crystal structure. As more gold was deposited on the 2 nm GNPs in solution, they bound to M13G phage, possibly because of change in their crystal structure as they grew in size which resembled fcc crystal structure.

In order to form a self-assembling molecular transistor, the minor coat protein of the M13 bacteriophage can be genetically modified to impart molecular recognition properties to identify and bind to other components of the molecular transistor. Hence, the minor coat protein, pIII of the M13G phage was genetically modified to express a 21 amino acid long biotin-binding motif, found by Saggio *et al.* (1993), on the N-terminus of the pIII protein. This dual functional phage, M13GB was shown to bind to both the gold and the biotin. The titre of this mutant phage (3 x 10^{11} pfu/mL) was, however, less than the wild-type and the gold binding mutant phage (3 x 10^{12} pfu/mL).

8.2 Conclusions from Chapter 4

The work described in Chapter 4 dealt with the fabrication of gold nanowires from the gold binding M13G phage. The gold nanowires were successfully made by electroless depositing gold ions on the gold nanoparticle-phage complex (p-GNP). However, upon close examination of the gold nanowire under the HRTEM, it was found that the nanowires were discontinuous along their length. They were also found to be polycrystalline in nature. The discontinuity in the nanowire could be substantially overcome by depositing more gold ions on the nanowire, but that resulted in nanowire thickness exceeding 100 nm. These polycrystalline and discontinuous nanowires would adversely affect the desirable linear electrical characteristics of the nanowires needed for the fabrication of the molecular transistor.

Hence, the M13G phage-based gold nanowires were annealed at high temperatures under vacuum and their physical and chemical properties were measured before and after annealing. The annealing of the nanowires did not eliminate the discontinuity in the nanowire completely, but it did reduce such discontinuities as were visible through the TEM. Although, the annealing process did not affect the polycrystallinity of the gold nanowires, it was found that the chemical nature of the gold nanowire has changed, as corroborated by the SAED measurements. The nanowires were found to oxidise to gold oxide during the thermal annealing process. This occurred even when annealing was done in vacuum at a pressure of 10^{-3} mbar. It seems that this level of vacuum pressure still left enough oxygen molecules in the annealing tube to oxidize the small numbers of nanowires on the TEM grid. Hence, in future a two-stage vacuum pump system, using a turbomolecular pump in the second stage could be used, in order to create a vacuum of up to 10^{-5} mbar during the annealing of the gold nanowires.

8.3 Conclusions from Chapter 5

The work described in this chapter measured the electrical characteristics of the M13G phage-based gold nanowires before and after annealing of the nanowire. But before that could be done, it was necessary to the remove unreacted residual chemicals from the gold nanowire synthesis. Such contaminants, visible under the electron microscope, were successfully removed and the gold nanowires were deposited on clean SiO_2 and SiN surfaces.

The electrical properties of the nanowires were measured before and after annealing. A resistive layer was found enveloping the nanowire and the electrode patterned on the surface of the SiO_2 chip. Although, this layer was not visible under the SEM, it attributed a large resistance to the nanowires or even bulk gold electrodes, of the order of 100 MΩ - 1 GΩ. This resistive layer could often be burned after passing multiple repetitions of high current sweeps through it. The resistance of the nanowires then dropped to the expected value of ~700 Ω, which is closer to the values reported for gold nanowires by other research groups. In future the source of this resistive layer needs to be investigated in order to make any reliable electronic device using these nanowires.

One of the objectives of this project was to investigate the electrical transport properties of the nanowire at very low temperatures (less than 10 K). However, it could not be achieved because of the inherent design fault of the 4-probe SPM (Omicron) used. The contact-probes of the 4-probe SPM could not be cooled to the liquid helium temperature and thus were at room temperature. Only the cryostat holding the nanowire sample could reach the temperature of liquid helium. Hence, upon contacting the nanowire with the SPM probes, the vast temperature differential between the two led to an instant contraction of the probe leading to loss of contact. Thus, the contact between the probe and the nanowire could not be achieved to take electrical measurements at low temperatures.

8.4 Conclusions from Chapter 6

A simple molecular transistor needs more than one component to work. If the M13 phage-based gold nanowires can act as the source, gate and drain of the nanowire, then a nanoparticle encapsulated in a protein shell can act as the island needed for the construction of the molecular transistor. Therefore, the work described in this chapter investigated the encapsulation of a GNP or a QD inside the MS2 capsid using the assembly initiator TR RNA stem loop. GNPs of different sizes were encapsulated inside the MS2 bacteriophage capsid to form hybrid VLPs. However, the encapsulation efficiency dropped drastically as the size of the nanoparticles approached the MS2 inner capsid diameter of about 20 nm. The size of such MS2-PEGNPs also varied with the size of the nanoparticle encapsulated inside it. CdTe QD was also encapsulated inside MS2 capsid, but again the encapsulation efficiency was low.

The wild-type MS2 phage capsid has pores at the threefold and fivefold axis. To ascertain if the MS2-PEGNPs also had such pores, gold deposition chemistry was done on the MS2-PEGNPs. It was found that the size of the GNPs inside the MS2 capsid could be modified indicating the presence of such pores on the MS2-PEGNPs surface.

The ultimate objective of the research in this thesis was to fabricate a molecular transistor via self-assembly, using the phage-templated nanostructures. The biotin and gold-binding mutant phage, M13GB was tested for its binding affinity to biotin-functionalized MS2 phage capsids. But no binding was observed between the M13GB bacteriophage and the MS2 VLPs. As the biotin-binding motif was selected using a pVIII display library, it may may lose some of its binding affinity when displayed on the pIII protein of the M13 bacteriophage. This could be one of the reasons for no observed binding between. The biotin-binding peptide had an IC_{50} value of about 50 μM. This indicates that the binding affinity of the biotin-binding motif was sufficient for binding small biotin tagged molecules but not enough to bind and hold onto large phage capsids Naik *et al.* (2004) suggested a PCR based biopanning method for selecting strong ligand binder from a phage display library. In future, a strong biotin-binding peptide can be selected using this phage display technique such that the IC_{50} value of the peptide if at least 50 nM or lower, which is indicator of a strong binder.

8.5 Conclusions from Chapter 7

Self-assembly has been used for the fabrication of the nanostructures and devices in the earlier chapters. However, an alternative method of fabricating a nanoelectronic device would be to manipulate the individual components on a substrate and thus get them to the desired location on the substrate. Such a method would be slow for large scale device fabrication, but it would be faster to make prototype devices using this method than the self-assembly based device fabrication. The work described in this chapter investigated the fabrication of such a device using the AFM tip controlled by a virtual haptic. However, it was found that the M13 phage-based gold nanowires lost their structural integrity during such manipulation by an AFM tip. This maybe because the resultant adhesive/frictional forces at the phage-substrate interface was greater than the yield stress of the nanowire-based nanowires. However, the hydration of the annealed nanowires affected the resultant adhesive forces at the nanowire-substrate interface in way that the smaller nanowire fragments on a silica surface could be manipulated using an AFM tip.

Some of the wild-type MS2 phage capsids could be moved using an AFM tip unlike the MS2-PEGNPs. This suggests that the MS2-PEGNPs have poor mechanical properties compared to wild- type MS2 phage capsids, possibly because of structural difference between the two particles. In future, slightly hydrophobic graphite can be used as the substrate for nanomanipulation, as they have been shown to have lower adhesive-frictional forces at the sample-substrate interface than mica or silica surface (Leite *et. al.*, 2012). In future, a novel nanomanipulation technique designed by Liu *et. al.* (2017) can be used, whereby a group of short parallel pushing vectors (PPVs) is applied on the nanowire along its longitudinal direction.

8.6 Closing remarks

Although, the final aim of the fabrication of a self-assembling molecular transistor was not realised within this study, significant progress was made towards achieving this goal. Specifically, gold nanowires were successfully made using the M13 bacteriophage scaffold and their electrical and physical properties were characterised. Gold nanoparticles and quantum dots were encapsulated inside the MS2 phage capsid. It was shown that both the inner and the outer surface of such hybrid VLPs could be chemically modified. An alternate method of molecular transistor fabrication by nanomanipulation using a haptic controlled AFM tip was investigated and useful deductions about the physical strength of the bacteriophage templated nanostructures were made. The major aspect that is lacking is the self-assembly of different bacteriophage based nanostructures into a structure resembling a molecular transistor. If this can be accomplished in the future then other features can be employed to characterize such a transistor device.

References

- **Ali, H.O. and Christie, I.R.,** 1984. A review of electroless gold deposition processes. *Gold bulletin*, **17**(4), pp.118-127.

- **Aljabali, A.A., Barclay, J.E., Cespedes, O., Rashid, A., Staniland, S.S., Lomonossoff, G.P. and Evans, D.J.,** 2011. Charge modified Cowpea mosaic virus particles for templated mineralization. *Advanced Functional Materials*, **21**(21), pp.4137-4142.

- **Aljabali, A.A., Barclay, J.E., Lomonossoff, G.P. and Evans, D.J.**, 2010. Virus templated metallic nanoparticles. *Nanoscale*, **2**(12), pp.2596-2600.

- **Aljabali, A.A., Lomonossoff, G.P. and Evans, D.J.**, 2011. CPMV-polyelectrolyte-templated gold nanoparticles. *Biomacromolecules*, **12**(7), pp.2723-2728.

- **Aljabali, A.A., Sainsbury, F., Lomonossoff, G.P. and Evans, D.J.,** 2010. Cowpea mosaic virus unmodified empty viruslike particles loaded with metal and metal oxide. *Small*, **6**(7), pp.818-821.

- **Aljabali, A.A., Shah, S.N., Evans-Gowing, R., Lomonossoff, G.P. and Evans, D.J.,** 2011. Chemically-coupled-peptide-promoted virus nanoparticle templated mineralization. *Integrative Biology*, **3**(2), pp.119-125.

- **Altissimo, M.,** 2010. E-beam lithography for micronanofabrication. *Biomicrofluidics*, **4**(2), p.026503

- **Asensio, M.A., Morella, N.M., Jakobson, C.M., Hartman, E.C., Glasgow, J.E., Sankaran, B., Zwart, P.H. and Tullman-Ercek, D.,** 2016. A selection for assembly reveals that a single amino acid mutant of the bacteriophage MS2 coat protein forms a smaller virus-like particle. *Nano Letters*, **16**(9), pp.5944-5950

- **Ashley, C.E., Carnes, E.C., Phillips, G.K., Durfee, P.N., Buley, M.D., Lino, C.A., Padilla, D.P., Phillips, B., Carter, M.B., Willman, C.L. and Brinker, C.J.,**

2011. Cell-specific delivery of diverse cargos by bacteriophage MS2 virus-like particles. *ACS Nano*, **5**(7), pp.5729-5745

- **Awramik, S.M.,** 1992. The history and significance of stromatolites. In *Early Organic Evolution* (pp. 435-449). Springer, Berlin, Heidelberg

- **Bassindale, A.R., Codina-Barrios, A., Frascione, N. and Taylor, P.G.,** 2007. An improved phage display methodology for inorganic nanoparticle fabrication. *Chemical Communications*, **28**, pp.2956-2958

- **Bastús, N.G., Comenge, J. and Puntes, V.**, 2011. Kinetically controlled seeded growth synthesis of citrate-stabilized gold nanoparticles of up to 200 nm: size focusing versus Ostwald ripening. *Langmuir*, **27**(17), pp.11098-11105.

- **Bayrak, T., Jagtap, N. and Erbe, A.,** 2018. Review of the Electrical Characterization of Metallic Nanowires on DNA Templates. *InternationalJjournal of Molecular Sciences*, **19**(10), p.3019.

- **Beck, E., Sommer, R., Auerswald, E.A., Kurz, C., Zink, B., Osterburg, G., Schaller, H., Sugimoto, K., Sugisaki, H., Okamoto, T. and Takanami, M.,** 1978. Nucleotide sequence of bacteriophage fd DNA. *Nucleic Acids Research*, **5**(12), pp.4495-4504.

- **Blaik, R.A., Lan, E., Huang, Y. and Dunn, B**., 2016. Gold-coated M13 bacteriophage as a template for glucose oxidase biofuel cells with direct electron transfer. *ACS Nano*, **10**(1), pp.324-332.

- **Blum, P., Holzschu, D., Kwan, H.S., Riggs, D. and Artz, S.,** 1989. Gene replacement and retrieval with recombinant M13mp bacteriophages. *Journal of Bacteriology*, **171**(1), pp.538-546

- **Bourgoin, J.P., Borghetti, J., Chenevier, P., Derycke, V., Filoramo, A., Goux, L., Goffman, M.F., Lyonnais, S., Nguyen, K., Robert, G. and Streiff, S.,** 2006, December. Directed assembly for carbon nanotube device fabrication. In 2006 *International Electron Devices Meeting* (pp. 1-4). IEEE.

- **Braun, E., Eichen, Y., Sivan, U. and Ben-Yoseph, G.,** 1998. DNA-templated assembly and electrode attachment of a conducting silver wire. *Nature*, **391**(6669), p.775

- **Bromley, K.M., Patil, A.J., Perriman, A.W., Stubbs, G. and Mann, S.,** 2008. Preparation of high quality nanowires by tobacco mosaic virus templating of gold nanoparticles. *Journal of Materials Chemistry*, **18**(40), pp.4796-4801.

- **Brown, S.,** 1997. Metal-recognition by repeating polypeptides. *Nature Biotechnology*, **15**(3), p.269

- **Brown, S., Sarikaya, M. and Johnson, E.,** 2000. A genetic analysis of crystal growth1. *Journal of Molecular Biology*, **299**(3), pp.725-735

- **Blakemore, R**., 1975. Magnetotactic bacteria. *Science*, **190**(4212), pp.377-379

- **Capehart, S.L., Coyle, M.P., Glasgow, J.E. and Francis, M.B.,** 2013. Controlled integration of gold nanoparticles and organic fluorophores using synthetically modified MS2 viral capsids. *Journal of the American Chemical Society*, **135**(8), pp.3011-3016.

- **Cárcamo, J., Ravera, M.W., Brissette, R., Dedova, O., Beasley, J.R., Alam-Moghé, A., Wan, C., Blume, A. and Mandecki, W**., 1998. Unexpected frameshifts from gene to expressed protein in a phage-displayed peptide library. *Proceedings of the National Academy of Sciences*, **95**(19), pp.11146-11151

- **Carlsson, S.B., Junno, T., Montelius, L. and Samuelson, L.,** 1999. Mechanical tuning of tunnel gaps for the assembly of single-electron transistors. *Applied Physics Letters*, **75**(10), pp.1461-1463

- **Champness, P.E.,** *2001*. Electron diffraction in the transmission electron microscope. BIOS Scietific Publishers Ltd, Oxford.

- **Chatellier, J., Hartley, O., Griffiths, A.D., Fersht, A.R., Winter, G. and Riechmann, L.,** 1999. Interdomain interactions within the gene 3 protein of filamentous phage. *FEBS Letters*, **463**(3), pp.371-374

- **Chen, C., Daniel, M.C., Quinkert, Z.T., De, M., Stein, B., Bowman, V.D., Chipman, P.R., Rotello, V.M., Kao, C.C. and Dragnea, B.,** 2006. Nanoparticle-templated assembly of viral protein cages. *Nano Letters*, **6**(4), pp.611-615

- **Chen, L., Bazylinski, D.A. and Lower, B.H.,** 2010. Bacteria that synthesize nano-sized compasses to navigate using earth's geomagnetic field. *Nature Education Knowledge*, **3**(10), p.30

- **Chen, P.Y., Lin, A.Y.M., Lin, Y.S., Seki, Y., Stokes, A.G., Peyras, J., Olevsky, E.A., Meyers, M.A. and McKittrick, J.,** 2008. Structure and mechanical properties of selected biological materials. *Journal of the Mechanical Behavior of Biomedical Materials*, **1**(3), pp.208-226

- **Cheng, F., Tsvetkova, I.B., Khuong, Y.L., Moore, A.W., Arnold, R.J., Goicochea, N.L., Dragnea, B. and Mukhopadhyay, S.,** 2012. The packaging of different cargo into enveloped viral nanoparticles. *Molecular Pharmaceutics*, **10**(1), pp.51-58.

- **Chung, W.J., Lee, D.Y. and Yoo, S.Y.,** 2014. Chemical modulation of M13 bacteriophage and its functional opportunities for nanomedicine. *International Journal of Nanomedicine*, **9**, p.5825

- **Clackson, T. and Lowman, H.B.**, 2004. *Phage Display: a Practical Approach*. Oxford University Press, USA

- **Culver, J.N., Brown, A.D., Zang, F., Gnerlich, M., Gerasopoulos, K. and Ghodssi, R.,** 2015. Plant virus directed fabrication of nanoscale materials and devices. *Virology*, **479**, pp.200-212

- **Cung, K., Han, B.J., Nguyen, T.D., Mao, S., Yeh, Y.W., Xu, S., Naik, R.R., Poirier, G., Yao, N., Purohit, P.K. and McAlpine, M.C.,** 2013. Biotemplated synthesis of PZT nanowires. *Nano Letters*, **13**(12), pp.6197-6202

- **Custance, O., Perez, R. and Morita, S.,** 2009. Atomic force microscopy as a tool for atom manipulation. *Nature Nanotechnology*, **4**(12), p.803.

- **Czapar, A.E. and Steinmetz, N.F.,** 2017. Plant viruses and bacteriophages for drug delivery in medicine and biotechnology. *Current Opinion in Chemical Biology*, **38**, pp.108-116.

- **Dai, X., Li, Z., Lai, M., Shu, S., Du, Y., Zhou, Z.H. and Sun, R.,** 2017. In situ structures of the genome and genome-delivery apparatus in a single-stranded RNA virus. *Nature*, **541**(7635), p.112

- **Danev, R., Kanamaru, S., Marko, M. and Nagayama, K.,** 2010. Zernike phase contrast cryo-electron tomography. *Journal of Structural Biology*, **171**(2), pp.174-181

- **Dang, X., Yi, H., Ham, M.H., Qi, J., Yun, D.S., Ladewski, R., Strano, M.S., Hammond, P.T. and Belcher, A.M.,** 2011. Virus-templated self-assembled single-walled carbon nanotubes for highly efficient electron collection in photovoltaic devices. *Nature Nanotechnology*, **6**(6), p.377

- **Daniel, M.C. and Astruc, D.,** 2004. Gold nanoparticles: assembly, supramolecular chemistry, quantum-size-related properties, and applications toward biology, catalysis, and nanotechnology. *Chemical Reviews*, **104**(1), pp.293-346

- **Daniel, M.C., Tsvetkova, I.B., Quinkert, Z.T., Murali, A., De, M., Rotello, V.M., Kao, C.C. and Dragnea, B.,** 2010. Role of surface charge density in nanoparticle-templated assembly of bromovirus protein cages. *ACS Nano*, **4**(7), pp.3853-3860.

- **Danscher, G.,** 1981. Histochemical demonstration of heavy metals. *Histochemistry*, **71**(1), pp.1-16.

- **Day, L. A. and Wiseman, R. L**. (1978). A comparison of DNA packaging in the virions of fd, Xf, and Pfl. In *The Single-Stranded DNA Phages*, (ed. D. T. Denhardt, Dressler, D., and Ray, D.S.), pp. 605-625. Cold Spring Harbor, N.Y.: Cold Spring Harbor Laboratory.

- **Deng, L.W., Malik, P. and Perham, R.N**., 1999. Interaction of the globular domains of pIII Protein of filamentous bacteriophage fd with the F-Pilus of Escherichia coli. *Virology*, **253**(2), pp.271-277

- **Deng, L.W. and Perham, R.N.,** 2002. Delineating the site of interaction on the pIII protein of filamentous bacteriophage fd with the F-pilus of Escherichia coli. *Journal of Molecular Biology*, **319**(3), pp.603-614

- **Dettke, M., Stein, L., Schering AG.,** U.K. Pat 2, 081-309A, 1981

- **de Wildt, R.M., Tomlinson, I.M., Ong, J.L. and Holliger, P.,** 2002. Isolation of receptor–ligand pairs by capture of long-lived multivalent interaction complexes. *Proceedings of the National Academy of Sciences*, **99**(13), pp.8530-8535

- **Dixit, S.K., Goicochea, N.L., Daniel, M.C., Murali, A., Bronstein, L., De, M., Stein, B., Rotello, V.M., Kao, C.C. and Dragnea, B.,** 2006. Quantum dot encapsulation in viral capsids. *Nano Letters*, **6**(9), pp.1993-1999.

- **Dogic, Z. and Fraden, S.,** 2006. Ordered phases of filamentous viruses. *Current Opinion in Colloid & Interface Science*, **11**(1), pp.47-55

- **Dorval Courchesne, N.M., Klug, M.T., Huang, K.J., Weidman, M.C., Cantú, V.J., Chen, P.Y., Kooi, S.E., Yun, D.S., Tisdale, W.A., Fang, N.X. and Belcher, A.M.,** 2015. Constructing multifunctional virus-templated nanoporous composites for thin film solar cells: contributions of morphology and optics to photocurrent generation. *The Journal of Physical Chemistry C*, **119**(25), pp.13987-14000

- **Dotto, G.P., Horiuchi, K. and Zinder, N.D.,** 1984. The functional origin of bacteriophage f1 DNA replication: Its signals and domains. *Journal of molecular biology*, **172**(4), pp.507-521

- **Dotto, G.P., and Zinder, N.D.,** 1983. The morphogenetic signal of bacteriophage f1. *Virology*, **130** (1)**,** pp.252-256

- **Douglas, T. and Young, M.,** 1998. Host–guest encapsulation of materials by assembled virus protein cages. *Nature*, **393**(6681), p.152.

- **Dragnea, B., Chen, C., Kwak, E.S., Stein, B. and Kao, C.C.,** 2003. Gold nanoparticles as spectroscopic enhancers for in vitro studies on single viruses. *Journal of the American Chemical Society*, **125**(21), pp.6374-6375.

- **Edwardson, T.G., Mori, T. and Hilvert, D.,** 2018. Rational Engineering of a Designed Protein Cage for siRNA Delivery. *Journal of the American Chemical Society*, **140**(33), pp.10439-10442

- **Eteshola, E., Brillson, L.J. and Lee, S.C.,** 2005. Selection and characteristics of peptides that bind thermally grown silicon dioxide films. *Biomolecular Engineering*, **22**(5-6), pp.201-204.

- **Falvo, M.R., Washburn, S., Superfine, R., Finch, M., Brooks Jr, F.P., Chi, V. and Taylor 2nd, R.M.,** 1997. Manipulation of individual viruses: friction and mechanical properties. *Biophysical Journal*, **72**(3), pp.1396-1403.

- **Feynman, R. P**.,1960. There’s Plenty of room at the bottom, *Engineering and Science*, **23**, 22-36.

- **Fiers, W., Contreras, R., Duerinck, F., Haegeman, G., Iserentant, D., Merregaert, J., Jou, W.M., Molemans, F., Raeymaekers, A., Van den Berghe, A. and Volckaert, G.,** 1976. Complete nucleotide sequence of bacteriophage MS2 RNA: primary and secondary structure of the replicase gene. *Nature*, **260**(5551), p.500

- **Fischer-Bühner, J.,** 2005. Hardening of low-alloyed gold. *Gold Bulletin*, **38**(3), pp.120-131.

- **Flynn, C.E., Lee, S.W., Peelle, B.R. and Belcher, A.M.,** 2003. Viruses as vehicles for growth, organization and assembly of materials1. *Acta Materialia*, **51**(19), pp.5867-5880

- **Gao, C., Mao, S., Lo, C.H.L., Wirsching, P., Lerner, R.A. and Janda, K.D.,** 1999. Making artificial antibodies: a format for phage display of combinatorial heterodimeric arrays. *Proceedings of the National Academy of Sciences*, **96**(11), pp.6025-6030

- **Gelderblom, H.R.,** 1996. Structure and classification of viruses. In Medical Microbiology. 4th edition. University of Texas Medical Branch at Galveston.

- **Glasgow, J.E., Capehart, S.L., Francis, M.B. and Tullman-Ercek, D.,** 2012. Osmolyte-mediated encapsulation of proteins inside MS2 viral capsids. *ACS Nano*, **6**(10), pp.8658-8664.

- **Goede, K., Busch, P. and Grundmann, M.,** 2004. Binding specificity of a peptide on semiconductor surfaces. *Nano Letters*, **4**(11), pp.2115-2120

- **Goicochea, N.L., De, M., Rotello, V.M., Mukhopadhyay, S. and Dragnea, B.,** 2007. Core-like particles of an enveloped animal virus can self-assemble efficiently on artificial templates. *Nano Letters*, **7**(8), pp.2281-2290.

- **Gray, C.W.,** 1989. Three-dimensional structure of complexes of single-stranded DNA-binding proteins with DNA: IKe and fd gene 5 proteins form left-handed helices with single-stranded DNA. *Journal of Molecular Biology*, **208**(1), pp.57-64

- **Green, T.A.,** 2007. Gold electrodeposition for microelectronic, optoelectronic and microsystem applications. *Gold Bulletin*, *40*(2), pp.105-114

- **Grieco, S.H.H., Lee, S., Dunbar, W.S., MacGillivray, R.T. and Curtis, S.B.,** 2009. Maximizing filamentous phage yield during computer-controlled fermentation. *Bioprocess and Biosystems Engineering*, **32**(6), pp.773-779

- **Gulati, N.M., Stewart, P.L. and Steinmetz, N.F.,** 2018. Bioinspired shielding strategies for nanoparticle drug delivery applications. *Molecular Pharmaceutics*, **15**(8), pp.2900-2909.

- **Hansen, T.W., DeLaRiva, A.T., Challa, S.R. and Datye, A.K.,** 2013. Sintering of catalytic nanoparticles: particle migration or Ostwald ripening?. *Accounts of Chemical Research*, **46**(8), pp.1720-1730.

- **Hartman, E.C., Jakobson, C.M., Favor, A.H., Lobba, M.J., Álvarez-Benedicto, E., Francis, M.B. and Tullman-Ercek, D.,** 2018. Quantitative characterization of all single amino acid variants of a viral capsid-based drug delivery vehicle. *Nature Communications*, **9**(1), p.1385

- **Hayakawa, R., Chikyow, T. and Wakayama, Y.,** 2017. Vertical resonant tunneling transistors with molecular quantum dots for large-scale integration. *Nanoscale*, **9**(31), pp.11297-11302.

- **Hayat, M.A.,** 1989. Colloidal gold: principles, methods, and applications. Elsevier.

- **Her, S., Jaffray, D.A. and Allen, C.,** 2017. Gold nanoparticles for applications in cancer radiotherapy: Mechanisms and recent advancements. *Advanced Drug Delivery Reviews*, **109**, pp.84-101.

- **Hofschneider, P. H.,** 1963. Untersuchungen uber 'kleine' *E.coli* K-12 Bacteriophagen M12, M13, und M20. *Zeitschriftfur Natuiforschung* C, **18**, pp.203-205

- **Holliger, P., Riechmann, L. and Williams, R.L.,** 1999. Crystal structure of the two N-terminal domains of g3p from filamentous phage fd at 1.9 Å: evidence for conformational lability1. *Journal of Molecular Biology*, **288**(4), pp.649-657

- **Homberger, M. and Simon, U.,** 2010. On the application potential of gold nanoparticles in nanoelectronics and biomedicine. *Philosophical Transactions of the Royal Society A: Mathematical, Physical and Engineering Sciences*, **368**(1915), pp.1405-1453

- **Horn, W.T., Tars, K., Grahn, E., Helgstrand, C., Baron, A.J., Lago, H., Adams, C.J., Peabody, D.S., Phillips, S.E., Stonehouse, N.J. and Liljas, L.,** 2006. Structural basis of RNA binding discrimination between bacteriophages Qβ and MS2. *Structure*, **14**(3), pp.487-495

- **Horne, R.W. and Wildy, P.,** 1979. An historical account of the development and applications of the negative staining technique to the electron microscopy of viruses. *Journal of Microscopy*, **117**(1), pp.103-122

- **Hou, L., Wang, S. and Huang, H.,** 2015. A simple criterion for determining the static friction force between nanowires and flat substrates using the most-bent-state method. *Nanotechnology*, **26**(16), p.165702.

- **Huang, J.X., Bishop-Hurley, S.L. and Cooper, M.A.,** 2012. Development of anti-infectives using phage display: biological agents against bacteria, viruses, and parasites. *Antimicrobial Agents and Chemotherapy*, **56**(9), pp.4569-4582

- **Huang, Y., Chiang, C.Y., Lee, S.K., Gao, Y., Hu, E.L., Yoreo, J.D. and Belcher, A.M.,** 2005. Programmable assembly of nanoarchitectures using genetically engineered viruses. *Nano Letters*, **5**(7), pp.1429-1434

- **Hufton, S.E., Moerkerk, P.T., Meulemans, E.V., de Bruïne, A., Arends, J.W. and Hoogenboom, H.R.,** 1999. Phage display of cDNA repertoires: the pVI display system and its applications for the selection of immunogenic ligands. *Journal of Immunological Methods*, **231**(1-2), pp.39-51

- **Iannolo, G., Minenkova, O., Petruzzelli, R. and Cesareni, G.,** 1995. Modifying filamentous phage capsid: limits in the size of the major capsid protein. *Journal of Molecular Biology*, **248**(4), pp.835-844

- **Ilyichev, A.A., Minenkova, O.O., Kishchenko, G.P., Tat'kov, S.I., Karpishev, N.N., Eroshkin, A.M., Ofitzerov, V.I., Akimenko, Z.A., Petrenko, V.A. and Sandakhchiev, L.S.,** 1992. Inserting foreign peptides into the major coat protein of bacteriophage M13. *FEBS letters*, **301**(3), pp.322-324

- **Jaafar, M., Aljabali, A.A.A., Berlanga, I., Mas-Ballesté, R., Saxena, P., Warren, S., Lomonossoff, G.P., Evans, D.J. and De Pablo, P.J.,** 2014. Structural insights into magnetic clusters grown inside virus capsids. *ACS Applied Materials & Interfaces*, **6**(23), pp.20936-20942.

- **Jalili, N. and Laxminarayana, K.,** 2004. A review of atomic force microscopy imaging systems: application to molecular metrology and biological sciences. *Mechatronics*, **14**(8), pp.907-945.

- **Kang, A.S., Barbas, C.F., Janda, K.D., Benkovic, S.J. and Lerner, R.A.,** 1991. Linkage of recognition and replication functions by assembling combinatorial antibody Fab libraries along phage surfaces. *Proceedings of the National Academy of Sciences*, **88**(10), pp.4363-4366

- **Kastelein, R.A., Remaut, E., Fiers, W. and Van Duin, J.,** 1982. Lysis gene expression of RNA phage MS2 depends on a frameshift during translation of the overlapping coat protein gene. *Nature*, **295(**5844), p.35

- **Kehoe, J.W. and Kay, B.K.,** 2005. Filamentous phage display in the new millennium. *Chemical Reviews*, **105**(11), pp.4056-4072

- **Khalil, A.S., Ferrer, J.M., Brau, R.R., Kottmann, S.T., Noren, C.J., Lang, M.J. and Belcher, A.M.,** 2007. Single M13 bacteriophage tethering and stretching. *Proceedings of the National Academy of Sciences*, **104**(12), pp.4892-4897

- **Khan, H.N., Hounshell, D.A. and Fuchs, E.R.,** 2018. Science and research policy at the end of Moore's law. *Nature Electronics*, **1**(1), pp.14-21

- **Kilby, J. S.** 1964. *Miniaturized Electronic Circuits.* U.S. Patent 3,138,743

- **Kilby, J. S.** 1966. *Method of Making Miniaturized Electronic Circuits.* U.S. Patent 3,261,081

- **Kim, H.J., Kang, K.H. and Kim, D.E.,** 2013. Sliding and rolling frictional behavior of a single ZnO nanowire during manipulation with an AFM. *Nanoscale*, **5**(13), pp.6081-6087.

- **Kim, J., Lin, C.Y., Xing, W., Mecartney, M.L., Potma, E.O. and Penner, R.M.,** 2013. Laser annealing of nanocrystalline gold nanowires. *ACS Applied Materials & Interfaces*, **5**(15), pp.6808-6814.

- **Kim, S., Shafiei, F., Ratchford, D. and Li, X.,** 2011. Controlled AFM manipulation of small nanoparticles and assembly of hybrid nanostructures. *Nanotechnology*, **22**(11), p.115301.

- **Kondo, J., Tada, Y., Dairaku, T., Hattori, Y., Saneyoshi, H., Ono, A. and Tanaka, Y.,** 2017. A metallo-DNA nanowire with uninterrupted one-dimensional silver array. *Nature hemistry*, **9**(10), p.956.

- **Kweon, H., Yiacoumi, S. and Tsouris, C.,** 2015. The role of electrostatic charge in the adhesion of spherical particles onto planar surfaces in atmospheric systems. *Colloids and Surfaces A: Physicochemical and Engineering Aspects*, **481**, pp.583-590.

- **Klug, A.,** 1999. The tobacco mosaic virus particle: structure and assembly. *Philosophical Transactions of the Royal Society of London B: Biological Sciences*, **354**(1383), pp.531-535

- **Knott, C.G.,** 1911. Quote from undated letter from Maxwell to Tait. *Life and Scientific Work of Peter Guthrie Tait. Cambridge University Press*, 215

- **Koning, R.I., Gomez-Blanco, J., Akopjana, I., Vargas, J., Kazaks, A., Tars, K., Carazo, J.M. and Koster, A.J.,** 2016. Asymmetric cryo-EM reconstruction of phage MS2 reveals genome structure in situ. *Nature Communications***, *7*,** p.12524

- **Koudelka, K.J., Pitek, A.S., Manchester, M. and Steinmetz, N.F.,** 2015. Virus-based nanoparticles as versatile nanomachines. *Annual Review of Virology*, **2**, pp.379-401

- **Kouwenhoven, L.,** 1997. Single-molecule transistors. *Science*, **275**(5308), pp.1896-1897

- **Kovacs, E.W., Hooker, J.M., Romanini, D.W., Holder, P.G., Berry, K.E. and Francis, M.B.,** 2007. Dual-surface-modified bacteriophage MS2 as an ideal scaffold for a viral capsid-based drug delivery system. *Bioconjugate Chemistry,* **18**(4), pp.1140-1147.

- **Krebber, A., Bornhauser, S., Burmester, J., Honegger, A., Willuda, J., Bosshard, H.R. and Plückthun, A.,** 1997. Reliable cloning of functional antibody variable domains from hybridomas and spleen cell repertoires employing a reengineered phage display system. *Journal of Immunological Methods,* **201**(1), pp.35-55

- **Kremser, A. and Rasched, I.,** 1994. The adsorption protein of filamentous phage fd: assignment of its disulfide bridges and identification of the domain incorporated in the coat. *Biochemistry*, **33**(46), pp.13954-13958

- **Knez, K., Noppe, W., Geukens, N., Janssen, K.P., Spasic, D., Heyligen, J., Vriens, K., Thevissen, K., Cammue, B.P., Petrenko, V. and Ulens, C.,** 2013. Affinity comparison of p3 and p8 peptide displaying bacteriophages using surface plasmon resonance. *Analytical Chemistry*, **85**(21), pp.10075-10082

- **Lagrange, M., Langley, D.P., Giusti, G., Jiménez, C., Bréchet, Y. and Bellet, D.,** 2015. Optimization of silver nanowire-based transparent electrodes: effects of density, size and thermal annealing. *Nanoscale*, **7**(41), pp.17410-17423.

- **Langley, D.P., Lagrange, M., Giusti, G., Jiménez, C., Bréchet, Y., Nguyen, N.D. and Bellet, D.,** 2014. Metallic nanowire networks: effects of thermal annealing on electrical resistance. *Nanoscale,* **6**(22), pp.13535-13543.

- **Lee, J.Y., Lee, J.G., Lee, S.H., Seo, M., Piao, L., Bae, J.H., Lim, S.Y., Park, Y.J. and Chung, T.D.,** 2013. Hydrogen-atom-mediated electrochemistry. *Nature Communications*, *4*, p.2766

- **Lee, J.Y., Shin, S.J., Lee, J.G., Yun, J., Oh, M.A. and Chung, T.D.,** 2017. Direct Electrodeposition of Thin Metal Films on Functionalized Dielectric Layer and Hydrogen Gas Sensor. *Journal of The Electrochemical Society*, *164*(2), pp.D1-D5

- **Lee, S.Y., Royston, E., Culver, J.N. and Harris, M.T.,** 2005. Improved metal cluster deposition on a genetically engineered tobacco mosaic virus template. *Nanotechnology*, **16**(7), p.S435

- **Lee, Y.J., Yi, H., Kim, W.J., Kang, K., Yun, D.S., Strano, M.S., Ceder, G. and Belcher, A.M.,** 2009. Fabricating genetically engineered high-power lithium-ion batteries using multiple virus genes. *Science*, **324**(5930), pp.1051-1055

- **Leite, F.L., Bueno, C.C., Da Róz, A.L., Ziemath, E.C. and Oliveira, O.N**., 2012. Theoretical models for surface forces and adhesion and their measurement using atomic force microscopy. *International Journal of Molecular Sciences*, **13**(10), pp.12773-12856.

- **Li, G., Xi, N., Yu, M., Salem, F., Wang, D.H. and Li, J.,** 2003, August. Manipulating nano scale biological specimen in liquid. In 2003 Third IEEE Conference on Nanotechnology, 2003. *IEEE-NANO* 2003. (Vol. 1, pp. 68-71). IEEE.

- **Likharev, K.K.,** 1999. Single-electron devices and their applications. *Proceedings of the IEEE*, **87**(4), pp.606-632

- **Linderoth, N.A., Simon, M.N. and Russel, M.,** 1997. The filamentous phage pIV multimer visualized by scanning transmission electron microscopy. *Science*, **278**(5343), pp.1635-1638

- **Liu, H.Z., Wu, S., Zhang, J.M., Bai, H.T., Jin, F., Pang, H. and Hu, X.D.,** 2017. Strategies for the AFM-based manipulation of silver nanowires on a flat surface. *Nanotechnology*, **28**(36), p.365301.

- **Liu, Y., Mao, J., Zhou, B., Wei, W. and Gong, S.,** 2010. Peptide aptamers against titanium-based implants identified through phage display. *Journal of Materials Science: Materials in Medicine*, **21**(4), pp.1103-1107

- **Lomonossoff, G.P. and Evans, D.J.,** 2011. Applications of plant viruses in bionanotechnology. In *Plant Viral Vectors* (pp. 61-87). Springer, Berlin, Heidelberg

- **Loo, L., Guenther, R.H., Basnayake, V.R., Lommel, S.A. and Franzen, S.,** 2006. Controlled encapsidation of gold nanoparticles by a viral protein shell. *Journal of the American Chemical Society*, **128**(14), pp.4502-4503.

- **Loo, L., Guenther, R.H., Lommel, S.A. and Franzen, S.,** 2007. Encapsidation of nanoparticles by red clover necrotic mosaic virus. *Journal of the American Chemical Society*, **129**(36), pp.11111-11117.

- **Løset, G.Å., Bogen, B. and Sandlie, I.,** 2011. Expanding the versatility of phage display I: efficient display of peptide-tags on protein VII of the filamentous phage. *PloS one*, *6*(2), p.e14702

- **Lubkowski, J., Hennecke, F., Plückthun, A. and Wlodawer, A.,** 1998. The structural basis of phage display elucidated by the crystal structure of the N-terminal domains of g3p. *Nature Structural and Molecular Biology*, **5**(2), p.140

- **Lu, Y., Berry, S.M. and Pfister, T.D.,** 2001. Engineering novel metalloproteins: design of metal-binding sites into native protein scaffolds. *Chemical reviews*, **101**(10), pp.3047-3080

- **Lu, Y. and Valentine, J.S.,** 1997. Engineering metal-binding sites in proteins. *Current Opinion in Structural Biology*, **7**(4), pp.495-500

- **Malik, P. and Perham, R.N.,** 1996. New vectors for peptide display on the surface of filamentous bacteriophage. *Gene*, **171**(1), pp.49-51

- **Malik, P. and Perham, R.N.,** 1997. Simultaneous display of different peptides on the surface of filamentous bacteriophage. *Nucleic Acids Research*, **25**(4), pp.915-916

- **Mani, S., Saif, T. and Han, J.H.,** 2006. Effect of annealing on the conductivity of electroless deposited Ni nanowires and films. *IEEE Transactions on Nanotechnology*, **5**(2), pp.138-141.

- **Manohar, S., Mantz, A.R., Bancroft, K.E., Hui, C.Y., Jagota, A. and Vezenov, D.V.,** 2008. Peeling single-stranded DNA from graphite surface to determine oligonucleotide binding energy by force spectroscopy. *Nano Letters*, *8*(12), pp.4365-4372

- **Mao, C., Solis, D.J., Reiss, B.D., Kottmann, S.T., Sweeney, R.Y., Hayhurst, A., Georgiou, G., Iverson, B. and Belcher, A.M**., 2004. Virus-based toolkit for the directed synthesis of magnetic and semiconducting nanowires. *Science*, **303**(5655), pp.213-217

- **Marciano, D.K., Russel, M. and Simon, S.M.,** 2001. Assembling filamentous phage occlude pIV channels. *Proceedings of the National Academy of Sciences*, **98**(16), pp.9359-9364

- **Marie, R., Dahlin, A.B., Tegenfeldt, J.O. and Höök, F.,** 2007. Generic surface modification strategy for sensing applications based on Au/SiO2 nanostructures. *Biointerphases*, **2(**1), pp.49-55.

- **Marvin, D.A., Hale, R.D., Nave, C. and Citterich, M.H.,** 1994. Molecular models and structural comparisons of native and mutant class I filamentous bacteriophages: Ff (fd, f1, M13), If1 and IKe. *Journal of Molecular Biology*, **235**(1), pp.260-286

- **Marvin, D. A., and Hoffmann-Berling, H.**, 1963. Physical and chemical properties of two new small bacteriophage. *Nature*, **197**, pp. 517-518

- **Mastico, R.A., Talbot, S.J. and Stockley, P.G.,** 1993. Multiple presentation of foreign peptides on the surface of an RNA-free spherical bacteriophage capsid. *Journal of General Virology*, **74**(4), pp.541-548

- **Matsuura, K.,** 2018. Synthetic approaches to construct viral capsid-like spherical nanomaterials. *Chemical Communications*, **54**, 8944—8959

- **Mazerolle, S., Breguet, J.M., Steinecker, A., Agnus, J., Perez, R. and Michler, J.,** 2005. Nanomanipulation in a scanning electron microscope. *Journal of materials processing technology*, **167**(2-3), pp.371-382.

- **McBride, D.G. and Vlasak, G.P.,** 1971. Sodium borohydride ($NaBH_4$) initiation of electroless plating. *Journal of The Electrochemical Society*, **118**(12), pp.2055-2058.

- **McDonnell, P.A., Shon, K., Kim, Y. and Opella, S.,** 1993. fd Coat protein structure in membrane environments. *Journal of Molecular Biology*, **233**(3), pp.447-463

- **McCafferty, J., Griffiths, A.D., Winter, G. and Chiswell, D.J.,** 1990. Phage antibodies: filamentous phage displaying antibody variable domains. *Nature*, **348**(6301), p.552

- **McMillan, R.A., Paavola, C.D., Howard, J., Chan, S.L., Zaluzec, N.J. and Trent, J.D.,** 2002. Ordered nanoparticle arrays formed on engineered chaperonin protein templates. *Nature Materials*, **1**(4), p.247

- **Messing, J.,** 1991. Cloning in M13 phage or how to use biology at its best. *Gene*, **100**, pp.3-12

- **Mirza, M.M., Schupp, F.J., Mol, J.A., MacLaren, D.A., Briggs, G.A.D. and Paul, D.J.,** 2017. One dimensional transport in silicon nanowire junction-less field effect transistors. *Scientific Reports*, **7**(1), p.3004

- **Moon, J.S., Kim, W.G., Kim, C., Park, G.T., Heo, J., Yoo, S.Y. and Oh, J.W.,** 2015. M13 bacteriophage-based self-assembly structures and their functional capabilities. *Mini-reviews in Organic Chemistry*, **12**(3), pp.271-281

- **Moore, G. E**., 1965, Cramming more components onto integrated circuits. *Electronics* **38**, pp.114-116

- **Moradi, M., Li, Z., Qi, J., Xing, W., Xiang, K., Chiang, Y.M. and Belcher, A.M.,** 2015. Improving the capacity of sodium ion battery using a virus-templated nanostructured composite cathode. *Nano Letters*, **15**(5), pp.2917-2921.

- **Mottet, C., Tréglia, G. and Legrand, B.,** 1997. New magic numbers in metallic clusters: an unexpected metal dependence. *Surface science*, **383**(1), pp.L719-L727

- **Murphy, F.A., Gibbs, E.P.J., Horzinek, M.C. and Studdert, M.J.,** 1999. *Veterinary Virology*. Elsevier, p.631

- **Naik, R.R., Jones, S.E., Murray, C.J., McAuliffe, J.C., Vaia, R.A. and Stone, M.O.,** 2004. Peptide templates for nanoparticle synthesis derived from polymerase chain reaction-driven phage display. *Advanced Functional Materials*, **14**(1), pp.25-30

- **Nam, K.T., Kim, D.W., Yoo, P.J., Chiang, C.Y., Meethong, N., Hammond, P.T., Chiang, Y.M. and Belcher, A.M.,** 2006. Virus-enabled synthesis and assembly of nanowires for lithium ion battery electrodes. *Science*, **312**(5775), pp.885-888

- **Nam, K.T., Peelle, B.R., Lee, S.W. and Belcher, A.M.,** 2004. Genetically driven assembly of nanorings based on the M13 virus. *Nano Letters*, **4**(1), pp.23-27

- **Narayanan, T.S. and Seshadri, S.K.,** 2004. Formation and characterization of borohydride reduced electroless nickel deposits. *Journal of Alloys and Compounds*, **365**(1-2), pp.197-205.

- **Nguyen, T.H., Easter, N., Gutierrez, L., Huyett, L., Defnet, E., Mylon, S.E., Ferri, J.K. and Viet, N.A.,** 2011. The RNA core weakly influences the interactions of the bacteriophage MS2 at key environmental interfaces. *Soft Matter*, **7**(21), pp.10449-10456

- **Noble, J.E., De Santis, E., Ravi, J., Lamarre, B., Castelletto, V., Mantell, J., Ray, S. and Ryadnov, M.G.,** 2016. A de novo virus-like topology for synthetic virions. *Journal of the American Chemical Society*, **138**(37), pp.12202-12210

- **Noyce, Robert N.** 1961. *Semiconductor Device-and-Lead Structure*, U. S. Patent 2981877

- **Nuraje, N., Dang, X., Qi, J., Allen, M.A., Lei, Y. and Belcher, A.M.,** 2012. Biotemplated synthesis of perovskite nanomaterials for solar energy conversion. *Advanced Materials*, **24**(21), pp.2885-2889

- **Oh, D., Qi, J., Han, B., Zhang, G., Carney, T.J., Ohmura, J., Zhang, Y., Shao-Horn, Y. and Belcher, A.M.,** 2014. M13 virus-directed synthesis of nanostructured metal oxides for lithium–oxygen batteries. *Nano Letters*, **14**(8), pp.4837-4845

- **Park, S.H., Barish, R., Li, H., Reif, J.H., Finkelstein, G., Yan, H. and LaBean, T.H.,** 2005. Three-helix bundle DNA tiles self-assemble into 2D lattice or 1D templates for silver nanowires. *Nano Letters*, **5**(4), pp.693-696

- **Parameswaran, K.N.,** 1990. A facile synthesis of biotin N-hydroxysuccinimide ester. *Organic Preparations and Procedures International*, **22**(1), pp.119-121

- **Peng, Y., Cullis, T. and Inkson, B.,** 2008. Accurate electrical testing of individual gold nanowires by in situ scanning electron microscope nanomanipulators. *Applied Physics Letters*, **93**(18), p.183112.

- **Perlmutter, J.D. and Hagan, M.F.,** 2015. Mechanisms of virus assembly. *Annual Review of Physical Chemistry*, **66**, pp.217-239.

- **Peters, B., Bui, H.H., Frankild, S., Nielsen, M., Lundegaard, C., Kostem, E., Basch, D., Lamberth, K., Harndahl, M., Fleri, W. and Wilson, S.S.,** 2006. A community resource benchmarking predictions of peptide binding to MHC-I molecules. *PLoS Computational Biology*, **2**(6), p.e65.

- **Petrenko, V.A., Smith, G.P., Gong, X. and Quinn, T.,** 1996. A library of organic landscapes on filamentous phage. *Protein Engineering, Design and Selection*, **9**(9), pp.797-801

- **Ploss, M., Facey, S.J., Bruhn, C., Zemel, L., Hofmann, K., Stark, R.W., Albert, B. and Hauer, B.,** 2014. Selection of peptides binding to metallic borides by screening M13 phage display libraries. *BMC Biotechnology*, *14*(1), p.12

- **Porath, D., Goldstein, Y., Grayevsky, A. and Millo, O.,** 1994. Scanning tunneling microscopy studies of annealing of gold films. *Surface Science*, 321(1-2), pp.81-88.

- **Postma, H.W.C., Teepen, T., Yao, Z., Grifoni, M. and Dekker, C.,** 2001. Carbon nanotube single-electron transistors at room temperature. *Science*, **293**(5527), pp.76-79

- **Qin, S., Kim, T.H., Wang, Z. and Li, A.P.,** 2012. Nanomanipulation and nanofabrication with multi-probe scanning tunneling microscope: From individual atoms to nanowires. *Review of Scientific Instruments*, **83**(6), p.063704.

- **Rakonjac, J., Bennett, N.J., Spagnuolo, J., Gagic D., and Russel M.,** 2011, Filamentous Bacteriophage: Biology, Phage Display and Nanotechnology Applications, *Curr. Issues Mol. Biol.*, **13**, pp51-76

- **Rakonjac, J., Feng, J.N. and Model, P.,** 1999. Filamentous phage are released from the bacterial membrane by a two-step mechanism involving a short C-terminal fragment of pIII1. *Journal of Molecular Biology*, **289**(5), pp.1253-1265

- **Rakonjac, J. and Model, P.,** 1998. Roles of pIII in filamentous phage assembly1. *Journal of Molecular Biology*, **282**(1), pp.25-41

- **Ramakrishnan, V.,** 2002. Ribosome structure and the mechanism of translation. *Cell*, **108**(4), pp.557-572

- **Rapoza, M.P. and Webster, R.E.,** 1995. The products of gene I and the overlapping in-frame gene XI are required for filamentous phage assembly. *Journal of Molecular Biology*, **248**(3), pp.627-638

- **Rasched, I.H.A.B. and Oberer, E.,** 1986. Ff coliphages: structural and functional relationships. *Microbiological Reviews*, **50**(4), p.401

- **Requicha, A.A.G., Meltzer, S., Arce, F.T., Makaliwe, J.H., Sikén, H., Hsieh, S., Lewis, D., Koel, B.E. and Thompson, M.E.,** 2001, October. Manipulation of nanoscale components with the AFM: principles and applications. *In Proceedings of the 2001 1st IEEE Conference on Nanotechnology*. IEEE-NANO 2001 (Cat. No. 01EX516) (pp. 81-86). IEEE.

- **Riechmann, L. and Holliger, P.,** 1997. The C-terminal domain of TolA is the coreceptor for filamentous phage infection of E. coli. *Cell,* **90**(2), pp.351-360

- **Robinson, D.H. and Sullivan, C.W.,** 1987. How do diatoms make silicon biominerals?. *Trends in Biochemical Sciences*, ***12***, pp.151-154

- **Rohrmann, G.F. and Krueger, R.G.,** 1970. The self-assembly of RNA free protein subunits from bacteriophage MS-2. *Biochemical and Biophysical* Research *Communications*, **38**(3), pp.406-413

- **Rolfsson, Ó., Middleton, S., Manfield, I.W., White, S.J., Fan, B., Vaughan, R., Ranson, N.A., Dykeman, E., Twarock, R., Ford, J. and Kao, C.C.,** 2016. Direct evidence for packaging signal-mediated assembly of bacteriophage MS2. *Journal of Molecular Biology*, **428**(2), pp.431-448

- **Rosant, C., Avalle, B., Larcher, D., Dupont, L., Friboulet, A. and Tarascon, J.M.,** 2012. Biosynthesis of Co_3O_4 electrode materials by peptide and phage engineering: comprehension and future. *Energy & Environmental Science*, **5**(12), pp.9936-9943

- **Roth, T.A., Weiss, G.A., Eigenbrot, C. and Sidhu, S.S.,** 2002. A minimized M13 coat protein defines the requirements for assembly into the bacteriophage particle. *Journal of molecular biology*, ***322***(2), pp.357-367

- **Ru, C. and To, S.,** 2012. Contact detection for nanomanipulation in a scanning electron microscope. *Ultramicroscopy*, **118**, pp.61-66.

- **Russel, M.,** 1991. Filamentous phage assembly. *Molecular Microbiology*, **5**(7), pp.1607-1613

- **Saggio, I. and Laufer, R.,** 1993. Biotin binders selected from a random peptide library expressed on phage. *Biochemical Journal*, **293**(3), pp.613-616

- **Sainsbury, F., Saunders, K., Aljabali, A.A., Evans, D.J. and Lomonossoff, G.P.,** 2011. Peptide-controlled access to the interior surface of empty virus nanoparticles. *Chembiochem*, **12**(16), pp.2435-2440.

- **Salivar, W.O., Henry, T.J. and Pratt, D.,** 1967. Purification and properties of diploid particles of coliphage M13. *Virology*, **32**(1), pp.41-51

- **Salstrom, J.S. and Pratt, D.,** 1971. Role of coliphage M13 gene 5 in single-stranded DNA production. *Journal of Molecular Biology*, **61**(3), pp.489-501

- **Sanghvi, A.B., Miller, K.P.H., Belcher, A.M. and Schmidt, C.E.,** 2005. Biomaterials functionalization using a novel peptide that selectively binds to a conducting polymer. *Nature Materials*, **4**(6), p.496

- **Sarikaya, M., Tamerler, C., Schwartz, D.T. and Baneyx, F.,** 2004. Materials assembly and formation using engineered polypeptides. *Annu. Rev. Mater. Res.*, **34**, pp.373-408

- **Sarikaya, M., Tamerler, C., Jen, A.K.Y., Schulten, K. and Baneyx, F.,** 2003. Molecular biomimetics: nanotechnology through biology. *Nature Materials*, **2**(9), p.577

- **Sasaki, E., Böhringer, D., van de Waterbeemd, M., Leibundgut, M., Zschoche, R., Heck, A.J., Ban, N. and Hilvert, D.,** 2017. Structure and assembly of scalable porous protein cages. *Nature Communications*, **8**, p.14663

- **Schaller, H., Voss, H. and Gucker, S.,** 1969. Structure of the DNA of bacteriophage fd: II. Isolation and characterization of a DNA fraction with double strand-like properties. *Journal of Molecular Biology*, **44**(3), pp.445-458

- **Scheibel, T., Parthasarathy, R., Sawicki, G., Lin, X.M., Jaeger, H. and Lindquist, S.L**., 2003. Conducting nanowires built by controlled self-assembly of amyloid fibers and selective metal deposition. *Proceedings of the National Academy of Sciences*, **100**(8), pp.4527-4532

- **Schliwa, M. and Woehlke, G.,** 2003. Molecular motors. *Nature*, **422**(6933), pp.759-766

- **Serwer, P**., 1977. Flattening and shrinkage of bacteriophage T7 after preparation for electron microscopy by negative staining. *Journal of Ultrastructure Research*, **58**(3), pp.235-243

- **Shah, S.N., Steinmetz, N.F., Aljabali, A.A., Lomonossoff, G.P. and Evans, D.J.,** 2009. Environmentally benign synthesis of virus-templated, monodisperse, iron-platinum nanoparticles. *Dalton Transactions*, (**40**), pp.8479-8480.

- **Shenton, W., Douglas, T., Young, M., Stubbs, G. and Mann, S.,** 1999. Inorganic–organic nanotube composites from template mineralization of tobacco mosaic virus. *Advanced Materials*, **11**(3), pp.253-256

- **Sidhu, S.S.,** 2001. Engineering M13 for phage display. *Biomolecular Engineering*, **18**(2), pp.57-63

- **Sidhu, S.S., Feld, B.K. and Weiss, G.A**., 2007. M13 bacteriophage coat proteins engineered for improved phage display. *In Protein Engineering Protocols* (pp. 205-219). Humana Press.

- **Sigel, A., Sigel, H. and Sigel, R.K.** eds., 2008. *Biomineralization: From Nature to Application* (**Vol. 12**). John Wiley & Sons

- **Slot, J.W. and Geuze, H.J.,** 1985. A new method of preparing gold probes for multiple-labeling cytochemistry. *European Journal of Cell Biology*, **38**(1), pp.87-93.

- **Smeal, S.W., Schmitt, M.A., Pereira, R.R., Prasad, A. and Fisk, J.D.,** 2017. Simulation of the M13 life cycle I: Assembly of a genetically structured deterministic chemical kinetic simulation. *Virology*, **500**, pp.259-274

- **Smith, G.P.,** 1985. Filamentous fusion phage: novel expression vectors that display cloned antigens on the virion surface. *Science*, **228**(4705), pp.1315-1317

- **Smith, G.P. and Petrenko, V.A.,** 1997. Phage display. *Chemical Reviews*, **97**(2), pp.391-410

- **Speck, J., Arndt, K.M. and Müller, K.M.,** 2011. Efficient phage display of intracellularly folded proteins mediated by the TAT pathway. *Protein Engineering, Design & Selection*, **24**(6), pp.473-484

- **Steinmetz, N.F., Shah, S.N., Barclay, J.E., Rallapalli, G., Lomonossoff, G.P. and Evans, D.J.,** 2009. Virus-templated silica nanoparticles. *Small*, **5**(7), pp.813-816.

- **Stengele, I., Bross, P., Garces, X., Giray, J. and Rasched, I.,** 1990. Dissection of functional domains in phage fd adsorption protein: discrimination between attachment and penetration sites. *Journal of Molecular Biology*, **212**(1), pp.143-149

- **Stockley, P.G., Ashcroft, A.E., Francese, S., Thompson, G.S., Ranson, N.A., Smith, A.M., Homans, S.W. and Stonehouse, N.J.,** 2005. Dissecting the fine details of assembly of a T= 3 phage capsid. *Journal of Theoretical Medicine*, **6**(2), pp.119-125.

- **Stockley, P.G., Rolfsson, O., Thompson, G.S., Basnak, G., Francese, S., Stonehouse, N.J., Homans, S.W. and Ashcroft, A.E**., 2007. A simple, RNA-mediated allosteric switch controls the pathway to formation of a T= 3 viral capsid. *Journal of Molecular Biology*, **369**(2), pp.541-552

- **Stockley, P.G., Stonehouse, N.J., Murry, J.B., Goodman, S.T., Talbot, S.J., Adams, C.J., Lilijas, L. and Valegå, K.,** 1995. Probing sequence-specific RNA recognition by the bacteriophage MS2 coat protien. *Nucleic Acids Research*, **23**(13), pp.2512-2518

- **Stockley, P.G., White, S.J., Dykeman, E., Manfield, I., Rolfsson, O., Patel, N., Bingham, R., Barker, A., Wroblewski, E., Chandler-Bostock, R. and Weiß, E.U.,** 2016. Bacteriophage MS2 genomic RNA encodes an assembly instruction manual for its capsid. *Bacteriophage*, **6**(1), p.e1157666

- **Suga, H., Naitoh, Y., Tanaka, M., Horikawa, M., Kobori, H. and Shimizu, T**., 2009. Nanomanipulation of single nanoparticle using a carbon nanotube probe in a scanning electron microscope. *Applied Physics Express*, **2**(5), p.055004.

- **Takizawa, T. and Robinson, J.M.,** 1994. Use of 1.4-nm immunogold particles for immunocytochemistry on ultra-thin cryosections. *Journal of Histochemistry & Cytochemistry*, **42**(12), pp.1615-1623.

- **Tamerler, C., Oren, E.E., Duman, M., Venkatasubramanian, E. and Sarikaya, M.,** 2006. Adsorption kinetics of an engineered gold binding peptide by surface plasmon resonance spectroscopy and a quartz crystal microbalance. *Langmuir*, **22**(18), pp.7712-7718

- **Toropova, K., Basnak, G., Twarock, R., Stockley, P.G. and Ranson, N.A.,** 2008. The three-dimensional structure of genomic RNA in bacteriophage MS2: implications for assembly. *Journal of Molecular Biology*, **375**(3), pp.824-836

- **Terasaka, N., Azuma, Y. and Hilvert, D.,** 2018. Laboratory evolution of virus-like nucleocapsids from nonviral protein cages. *Proceedings of the National Academy of Sciences*, **115**(21), pp.5432-5437

- **Thota, V. and C Perry, C**., 2017. A review on recent patents and applications of inorganic material binding peptides. *Recent Patents on Nanotechnology*, **11**(3), pp.168-180

- **Toropova, K., Basnak, G., Twarock, R., Stockley, P.G. and Ranson, N.A.,** 2008. The three-dimensional structure of genomic RNA in bacteriophage MS2: implications for assembly. *Journal of Molecular Biology*, **375**(3), pp.824-836

- **Tseng, A.A., Notargiacomo, A. and Chen, T.P.,** 2005. Nanofabrication by scanning probe microscope lithography: A review. *Journal of Vacuum Science & Technology B: Microelectronics and Nanometer Structures Processing, Measurement, and Phenomena*, **23**(3), pp.877-894

- **Tseng, A.A., Chen, K., Chen, C.D. and Ma, K.J.,** 2003. Electron beam lithography in nanoscale fabrication: recent development. *IEEE Transactions on Electronics Packaging Manufacturing*, **26**(2), pp.141-149

- **Twarock, R., Leonov, G. and Stockley, P.G.,** 2018. Hamiltonian path analysis of viral genomes. *Nature communications*, **9**(1), p.2021

- **Umetsu, M., Mizuta, M., Tsumoto, K., Ohara, S., Takami, S., Watanabe, H., Kumagai, I. and Adschiri, T.,** 2005. Bioassisted room-temperature immobilization and mineralization of zinc oxide—The structural ordering of ZnO nanoparticles into a flower-type morphology. *Advanced Materials*, **17**(21), pp.2571-2575

- **Valegård, K., Murray, J.B., Stockley, P.G., Stonehouse, N.J. and Liljas, L.,** 1994. Crystal structure of an RNA bacteriophage coat protein–operator complex. *Nature*, **371**(6498), p.623

- **van Duin, J. and Tsareva, N.,** 2006. Single-stranded RNA phages Chapter 15. *The Bacteriophages, 2nd edn. Oxford University Press, Oxford*, pp.175-196

- **Van Wezenbeek, P. and Schoenmakers, J.G.G.,** 1979. Nucleotide sequence of the genes III. VI and I of bacteriophage M13. *Nucleic Acids Research*, **6**(8), pp.2799-2818

- **van Wezenbeek, P.M., Hulsebos, T.J. and Schoenmakers, J.G.,** 1980. Nucleotide sequence of the filamentous bacteriophage M13 DNA genome: comparison with phage fd. *Gene*, **11**(1), pp.129-148

- **Vodnik, M., Zager, U., Strukelj, B. and Lunder, M.,** 2011. Phage display: selecting straws instead of a needle from a haystack. *Molecules*, *16*(1), pp.790-817

- **Vrielink, J., Heins, M.S., Setroikromo, R., Szegezdi, E., Mullally, M.M., Samali, A. and Quax, W.J.,** 2010. Synthetic constrained peptide selectively binds and antagonizes death receptor 5. *The FEBS Journal*, **277**(7), pp.1653-1665

- **Wang, L. and Nilsen-Hamilton, M.,** 2013. Biomineralization proteins: from vertebrates to bacteria. *Frontiers in Biology*, **8**(2), pp.234-246

- **Wang, S., Shan, Z. and Huang, H.,** 2017. The mechanical properties of nanowires. *Advanced Science*, **4**(4), p.1600332.

- **Wang, Q., Chen, Y.F., Long, S.B., Niu, J.B., Wang, C.S., Jia, R., Chen, B.Q., Liu, M. and Ye, T.C.,** 2007. Fabrication and characterization of single electron transistor on SOI. *Microelectronic Engineering*, **84**(5-8), pp.1647-1651

- **Wang, Q., Kaltgrad, E., Lin, T., Johnson, J.E. and Finn, M.G.,** 2002. Natural supramolecular building blocks: wild-type cowpea mosaic virus. *Chemistry & Biology*, **9**(7), pp.805-811

- **Wang, Q., Lin, T., Tang, L., Johnson, JE and Finn, MG,** 2002. Icosahedral virus particles as addressable nanoscale building blocks. *Angewandte Chemie*, **114** (3), pp.477-480

- **Wang, W. and Malcolm, B.A.,** 1999. Two-stage PCR protocol allowing introduction of multiple mutations, deletions and insertions using QuikChangeTM site-directed mutagenesis. *Biotechniques*, **26**(4), pp.680-682

- **Wang, Y.A., Yu, X., Overman, S., Tsuboi, M., Thomas Jr, G.J. and Egelman, E.H.,** 2006. The structure of a filamentous bacteriophage. *Journal of Molecular Biology*, **361**(2), pp.209-215

- **Webster, R.E.,** 1991. The tol gene products and the import of macromolecules into Escherichia coli. *Molecular Microbiology*, **5**(5), pp.1005-1011

- **Webster, R.E., Grant, R.A., and Hamilton, L.A.,** 1981. Orientation of the DNA in the filamentous bacteriophage f1. *J Mol Biol***, 152**, pp**.**357-374

- **Weis, J.,** 2005. Single-electron devices. In *CFN Lectures on Functional Nanostructures Vol.* ***1*** (pp. 87-121). Springer, Berlin, Heidelberg

- **Weiss, G.A. and Sidhu, S.S.,** 2000. Design and evolution of artificial M13 coat proteins1. *Journal of Molecular Biology*, **300**(1), pp.213-219

- **Wen, A.M., Shukla, S., Saxena, P., Aljabali, A.A., Yildiz, I., Dey, S., Mealy, J.E., Yang, A.C., Evans, D.J., Lomonossoff, G.P. and Steinmetz, N.F.,** 2012. Interior engineering of a viral nanoparticle and its tumor homing properties. *Biomacromolecules*, **13**(12), pp.3990-4001.

- **Whaley, S.R., English, D.S., Hu, E.L., Barbara, P.F. and Belcher, A.M.,** 2000. Selection of peptides with semiconductor binding specificity for directed nanocrystal assembly. *Nature*, **405**(6787), p.665

- **Whitesides, G.M. and Grzybowski, B.**, 2002. Self-assembly at all scales. *Science*, **295**(5564), pp.2418-2421

- **Wilkinson, P.,** 1986. Understanding gold plating. *Gold Bulletin*, *19*(3), pp.75-81

- **Wnęk, M., Górzny, M.Ł., Ward, M.B., Wälti, C., Davies, A.G., Brydson, R., Evans, S.D. and Stockley, P.G.,** 2012. Fabrication and characterization of gold nano-wires templated on virus-like arrays of tobacco mosaic virus coat proteins. *Nanotechnology*, **24**(2), p.025605

- **Woo, P., Mekuz, I. and Chen, B**., 2012, May. Nanomanipulation system for scanning electron microscope. In Scanning Microscopies 2012: Advanced Microscopy Technologies for Defense, Homeland Security, Forensic, Life, Environmental, and Industrial Sciences (Vol. **8378**, p. 83780O). *International Society for Optics and Photonics.*

- **Wu, B., Heidelberg, A. and Boland, J.J.,** 2005. Mechanical properties of ultrahigh-strength gold nanowires. *Nature Materials*, **4**(7), p.525.

- **Wu, C.H., Liu, I.J., Lu, R.M. and Wu, H.C.,** 2016. Advancement and applications of peptide phage display technology in biomedical science. *Journal of Biomedical Science*, *23*(1), p.8

- **Wu, H.N., Kastelic, K.A. and Uhlenbeck, O.C.,** 1988. A comparison of two phage coat protein-RNA interactions. *Nucleic Acids Research*, **16**(11), pp.5055-5066

- **Wu, M., Sherwin, T., Brown, W.L. and Stockley, P.G.,** 2005. Delivery of antisense oligonucleotides to leukemia cells by RNA bacteriophage capsids. *Nanomedicine: Nanotechnology, Biology and Medicine*, **1**(1), pp.67-76

- **Xue, X.Y., Feng, P., Wang, C., Chen, Y.J., Wang, Y.G. and Wang, T.H.,** 2006. Electrical transport through individual nanowires with transverse grain boundaries. *Applied Physics Letters*, **89**(2), p.022115.

- **Yan, H., Park, S.H., Finkelstein, G., Reif, J.H. and LaBean, T.H.,** 2003. DNA-templated self-assembly of protein arrays and highly conductive nanowires. *Science*, **301**(5641), pp.1882-1884

- **Yang, S.C. and Qian, X.,** 2013. Controlled manipulation of flexible carbon nanotubes through shape-dependent pushing by atomic force microscopy. *Langmuir*, **29**(37), pp.11793-11801.

- **Yang, Y. and Burkhard, P**., 2012. Encapsulation of gold nanoparticles into self-assembling protein nanoparticles. *Journal of Nanobiotechnology*, **10**(1), p.42.

- **Zhang, G., Wei, S. and Belcher, A.M.,** 2018. Biotemplated zinc sulfide Nanofibers as anode materials for sodium-ion batteries. *ACS Applied Nano Materials*, **1**(10), pp.5631-5639

- **Zhang, X., Pang, Z., Liu, H. and Zhai, T.,** 2011. Achieving continuous sub-100-nm plasmonic nanowires as long as centimeters. *Journal of Nanomedicine & Nanotechnology*, **6**(2), p.1.

- **Zhang, X., Sun, B., Friend, R.H., Guo, H., Nau, D. and Giessen, H.,** 2006. Metallic photonic crystals based on solution-processible gold nanoparticles. *Nano Letters*, **6**(4), pp.651-655.

- **Zhao, X., Fox, J.M., Olson, N.H., Baker, T.S. and Young, M.J.,** 1995. In vitro assembly of cowpea chlorotic mottle virus from coat protein expressed in Escherichia coli and in vitro-transcribed viral cDNA. *Virology*, **207**(2), pp.486-494.

- **Zygiel, E.M., Noren, K.A., Adamkiewicz, M.A., Aprile, R.J., Bowditch, H.K., Carroll, C.L., Cerezo, M.A.S., Dagher, A.M., Hebert, C.R., Hebert, L.E. and Mahame, G.M.,** 2017. Various mutations compensate for a deleterious lacZα insert in the replication enhancer of M13 bacteriophage. *PloS one*, **12**(4), p.e0176421

Appendix A

1.0 PCR primers and sequence gold-binding phage, M13G

1.1 Forward primer: Gold mut-1 DNA sequence

5’- GTTCCGATGCTGTCTTTCGCTGCAGTATCTGGTTCTTCTCCGGAC -3’

1.2 Reverse Primer: Gold mut-1 DNA sequence

5’- GGCCGCTTTTGCGGGATCCGAGTCCGGAGAAGAACCAG-3’

1.3 Goldoligo2-S DNA sequence

5’GTTCCGATGCTGTCTTTCGCTGCAGTATCTGGTTCTTCTCCGGACTCGGATCCCGCAAAAGCGGCC -3’

1.4 Goldoligo2-AS DNA sequence

5’GGCCGCTTTTGCGGGATCCGAGTCCGGAGAAGAACCAGATACTGCAGCGAAAGACAGCATCGGAAC-3’

1.5 Peptide sequence of pVIII in M13KE

M K K S L V L K A S V A V A T L V P M L S F A A E G D D P A K A A F N S L Q A S A T E Y I G Y A W A M V V V I V G A T I G I K L F K K F T S K A S Stop

1.6 Peptide sequence of pVIII in M13G

Met K K S L V L K A S V A V A T L V P Met L S F A A V S G S S P D S D P A K A A F N S L Q A S A T E Y I G Y A W A Met V V V I V G A T I G I K L F K K F T S K A S Stop

1.7 Gene VIII sequence in M13KE

ATGAAAAAGTCTTTAGTCCTCAAAGCCTCTGTAGCCGTTGCTACCCTCGTTCCGATGCTGTCTTTCGCTGCTGAGGGTGACGATCCCGCAAAAGCGGCCTTTAACTCCCTGCAAGCCTCAGCGACCGAATATATCGGTTATGCGTGGGCGATGGTTGTTGTCATTGTCGGCGCAACTATCGGTATCAAGCTGTTTAAGAAATTCACCTCGAAAGCAAGCTGA

1.8 Gene VIII sequence in M13G

ATGAAAAAGTCTTTAGTCCTCAAAGCCTCTGTAGCCGTTGCTACCCTCGTTCCGATGCTGTCTTTCGCTGCAGTATCTGGTTCTTCTCCGGACTCGGATCCCGCAAAAGCGGCCTTTAACTCCCTGCAAGCCTCAGCGACCGAATATATCGGTTATGCGTGGGCGATGGTTGTTGTCATTGTCGGCGCAACTATCGGTATCAAGCTGTTTAAGAAATTCACCTCGAAAGCAAGCTGA

Appendix B

1.0 Analytical ultracentrifugation run of 5 nm GNPs with M13G phage

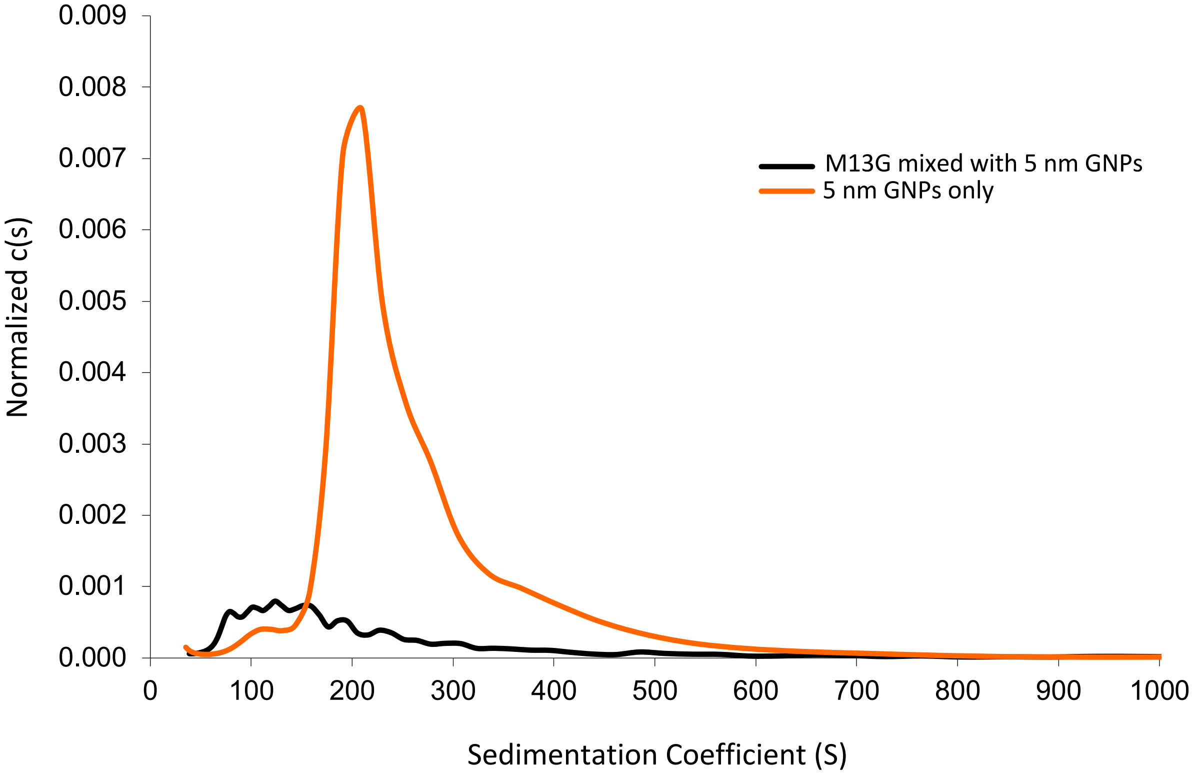

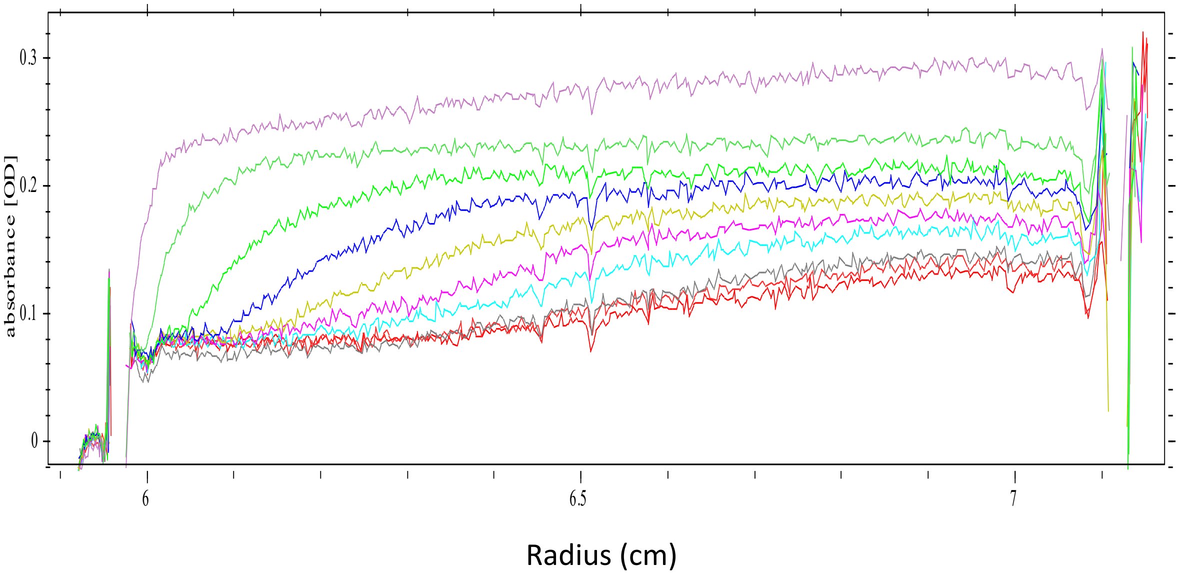

2. 0 Analytical ultracentrifugation run of 2 nm GNPs with M13G phage

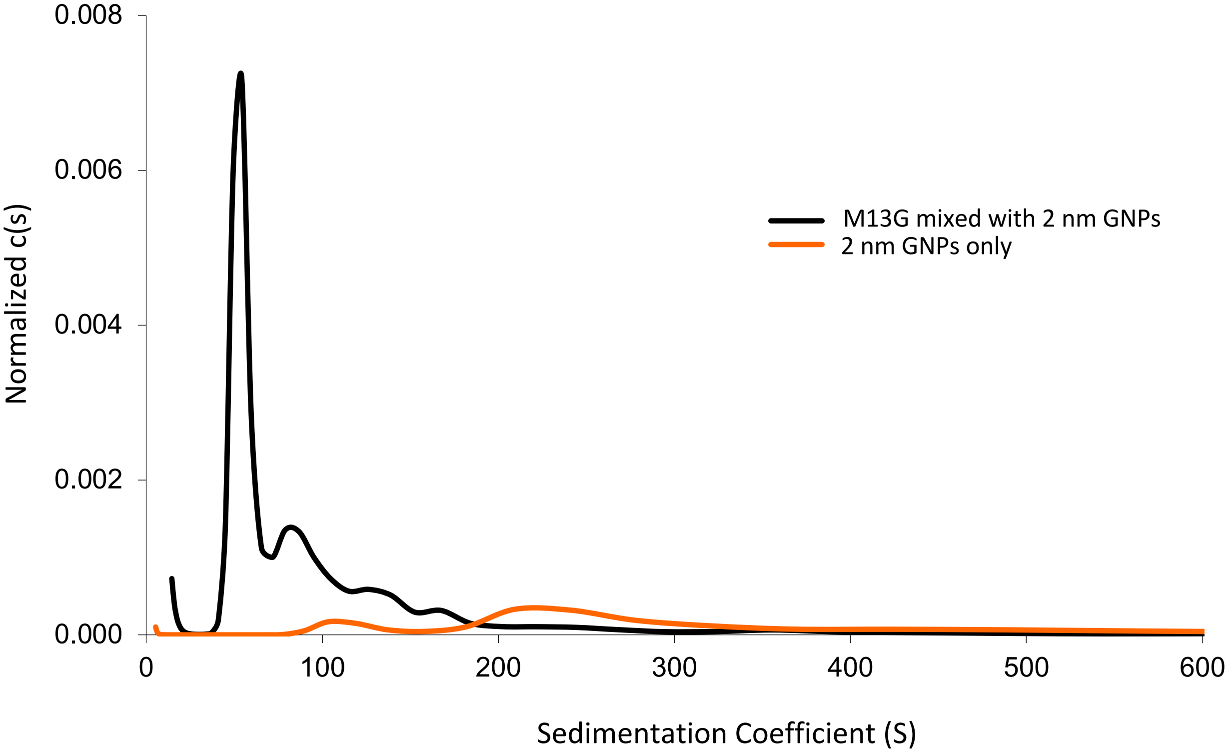

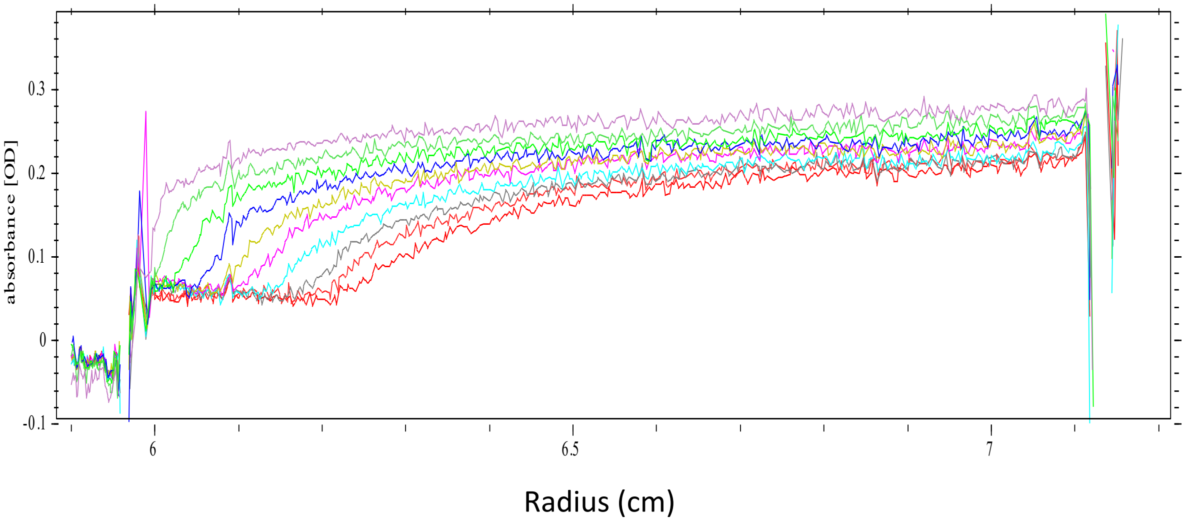

Appendix C

1.0 PCR primers and sequences for Biotin-binding insert preparation

1.1 Biotin-For-Template DNA sequence

5` - GCT GAA GGT GAA TTC TGC TCT TGG GCT CCG CCG TTC AAA GCT TCT TGC G

1.2 Biotin-For-1 DNA sequence

CTAT G GTA CCT TTC TAT TCT CAC TCT GCT GAA GGT GAA TTC TGC TC

1.3 Biotin-Rev-2 DNA sequence

CTAT C GGC CGA TTT AGC CGG GTC ACC GCA AGA AGC TTT GAA CGG

1.4 Gene III Sequence DNA sequence

GTG AAAAAATTAT TATTCGCAAT

1601 TCCTTTAGTG GTACCTTTCT ATTCTCACTC GGCCGAAACT GTTGAAAGTT

1651 GTTTAGCAAA ATCCCATACA GAAAATTCAT TTACTAACGT CTGGAAAGAC

1701 GACAAAACTT TAGATCGTTA CGCTAACTAT GAGGGCTGTC TGTGGAATGC

1751 TACAGGCGTT GTAGTTTGTA CTGGTGACGA AACTCAGTGT TACGGTACAT

1801 GGGTTCCTAT TGGGCTTGCT ATCCCTGAAA ATGAGGGTGG TGGCTCTGAG

1851 GGTGGCGGTT CTGAGGGTGG CGGTTCTGAG GGTGGCGGTA CTAAACCTCC

1901 TGAGTACGGT GATACACCTA TTCCGGGCTA TACTTATATC AACCCTCTCG

1951 ACGGCACTTA TCCGCCTGGT ACTGAGCAAA ACCCCGCTAA TCCTAATCCT

2001 TCTCTTGAGG AGTCTCAGCC TCTTAATACT TTCATGTTTC AGAATAATAG

2051 GTTCCGAAAT AGGCAGGGGG CATTAACTGT TTATACGGGC ACTGTTACTC

2101 AAGGCACTGA CCCCGTTAAA ACTTATTACC AGTACACTCC TGTATCATCA

2151 AAAGCCATGT ATGACGCTTA CTGGAACGGT AAATTCAGAG ACTGCGCTTT

2201 CCATTCTGGC TTTAATGAGG ATTTATTTGT TTGTGAATAT CAAGGCCAAT

2251 CGTCTGACCT GCCTCAACCT CCTGTCAATG CTGGCGGCGG CTCTGGTGGT

2301 GGTTCTGGTG GCGGCTCTGA GGGTGGTGGC TCTGAGGGTG GCGGTTCTGA

2351 GGGTGGCGGC TCTGAGGGAG GCGGTTCCGG TGGTGGCTCT GGTTCCGGTG

2401 ATTTTGATTA TGAAAAGATG GCAAACGCTA ATAAGGGGGC TATGACCGAA

2451 AATGCCGATG AAAACGCGCT ACAGTCTGAC GCTAAAGGCA AACTTGATTC

2501 TGTCGCTACT GATTACGGTG CTGCTATCGA TGGTTTCATT GGTGACGTTT

2551 CCGGCCTTGC TAATGGTAAT GGTGCTACTG GTGATTTTGC TGGCTCTAAT

2601 TCCCAAATGG CTCAAGTCGG TGACGGTGAT AATTCACCTT TAATGAATAA

2651 TTTCCGTCAA TATTTACCTT CCCTCCCTCA ATCGGTTGAA TGTCGCCCTT

2701 TTGTCTTTGG CGCTGGTAAA CCATATGAAT TTTCTATTGA TTGTGACAAA

2751 ATAAACTTAT TCCGTGGTGT CTTTGCGTTT CTTTTATATG TTGCCACCTT

2801 TATGTATGTA TTTTCTACGT TTGCTAACAT ACTGCGTAAT AAGGAGTCTT

2851 AA

1.5 pIII peptide sequence

V K K L L F A I P L V V P F Y S H S A E T V E S C L A K S H T E N S F T N V W K D
D K T L D R Y A N Y E G C L W N A T G V V V C T G D E T Q C Y G T W V P I G L
A I P E N E G G G S E G G G S E G G G S E G G G T K P P E Y G D T P I P G Y T Y I
N P L D G T Y P P G T E Q N P A N P N P S L E E S Q P L N T F Met F Q N N R F R N
R Q G A L T V Y T G T V T Q G T D P V K T Y Y Q Y T P V S S K A Met Y D A Y W
N G K F R D C A F H S G F N E D L F V C E Y Q G Q S S D L P Q P P V N A G G G S
G G G S G G G S E G G G S E G G G S E G G G S E G G G S G G G S G S G D F D Y E
K Met A N A N K G A Met T E N A D E N A L Q S D A K G K L D S V A T D Y G A A
I D G F I G D V S G L A N G N G A T G D F A G S N S Q Met A Q V G D G D N S P L
Met N N F R Q Y L P S L P Q S V E C R P F V F G A G K P Y E F S I D C D K I N L F R
G V F A F L L Y V A T F Met Y V F S T F A N I L R N K E S Stop

1.6 Biotin-binding peptide Gene III Sequence

TCCTTTAGT GGTACCTTTC

TATTCTCACT CTGCTGAAGG TGAATTCTGC TCTTGGGCTC CGCCGTTCAA

AGCTTCTTGC GGTGACCCGGC TAAATCGGCC GAAACTGTTGA AAGTT

GTTTAGCAAA ATCCCATACA GAAAATTCAT TTACTAACGT CTGGAAAGAC

GACAAAACTT TAGATCGTTA CGCTAACTAT GAGGGCTGTC TGTGGAATGC

TACAGGCGTT GTAGTTTGTA CTGGTGACGA AACTCAGTGT TACGGTACAT

GGGTTCCTAT TGGGCTTGCT ATCCCTGAAA ATGAGGGTGG TGGCTCTGAG

GGTGGCGGTT CTGAGGGTGG CGGTTCTGAG GGTGGCGGTA CTAAACCTCC

TGAGTACGGT GATACACCTA TTCCGGGCTA TACTTATATC AACCCTCTCG

ACGGCACTTA TCCGCCTGGT ACTGAGCAAA ACCCCGCTAA TCCTAATCCT

TCTCTTGAGG AGTCTCAGCC TCTTAATACT TTCATGTTTC AGAATAATAG

GTTCCGAAAT AGGCAGGGGG CATTAACTGT TTATACGGGC ACTGTTACTC

AAGGCACTGA CCCCGTTAAA ACTTATTACC AGTACACTCC TGTATCATCA

AAAGCCATGT ATGACGCTTA CTGGAACGGT AAATTCAGAG ACTGCGCTTT

CCATTCTGGC TTTAATGAGG ATTTATTTGT TTGTGAATAT CAAGGCCAAT

CGTCTGACCT GCCTCAACCT CCTGTCAATG CTGGCGGCGG CTCTGGTGGT

GGTTCTGGTG GCGGCTCTGA GGGTGGTGGC TCTGAGGGTG GCGGTTCTGA

GGGTGGCGGC TCTGAGGGAG GCGGTTCCGG TGGTGGCTCT GGTTCCGGTG

ATTTTGATTA TGAAAAGATG GCAAACGCTA ATAAGGGGGC TATGACCGAA

AATGCCGATG AAAACGCGCT ACAGTCTGAC GCTAAAGGCA AACTTGATTC

TGTCGCTACT GATTACGGTG CTGCTATCGA TGGTTTCATT GGTGACGTTT

CCGGCCTTGC TAATGGTAAT GGTGCTACTG GTGATTTTGC TGGCTCTAAT

TCCCAAATGG CTCAAGTCGG TGACGGTGAT AATTCACCTT TAATGAATAA

TTTCCGTCAA TATTTACCTT CCCTCCCTCA ATCGGTTGAA TGTCGCCCTT

TTGTCTTTGG CGCTGGTAAA CCATATGAAT TTTCTATTGA TTGTGACAAA

ATAAACTTAT TCCGTGGTGT CTTTGCGTTT CTTTTATATG TTGCCACCTT

TATGTATGTA TTTTCTACGT TTGCTAACAT ACTGCGTAAT AAGGAGTCTT

AA

Appendix D

1. 0 Mass Spectroscopy of 5’ thiol TR RNA

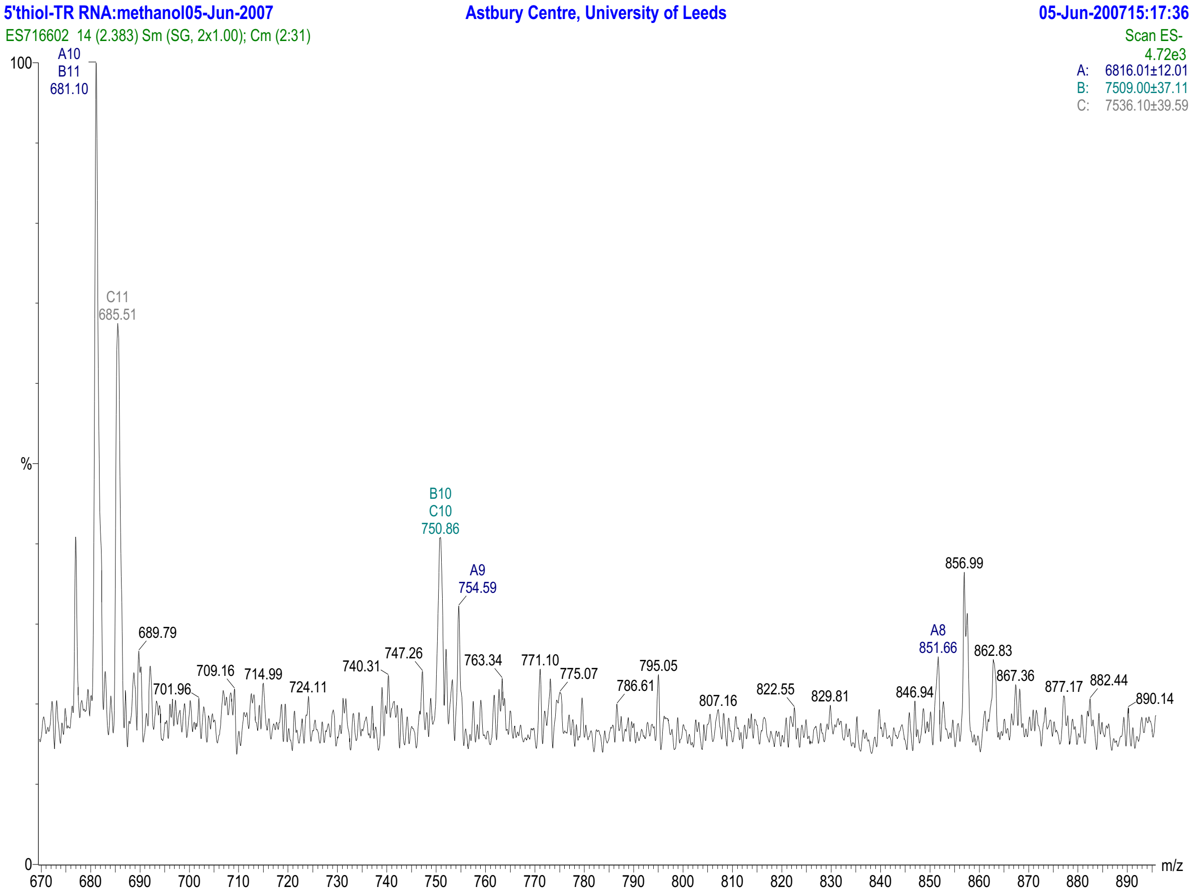

2.0 Polyacrylamide gel electrophoresis of 5’ thiol TR RNA

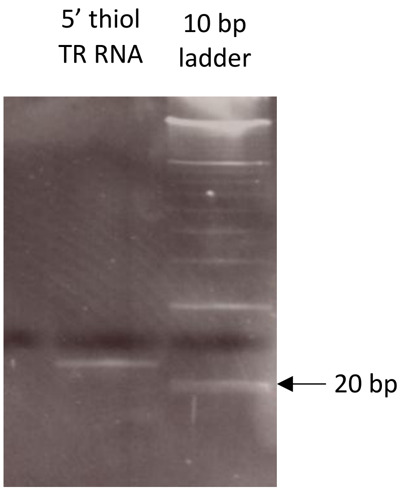

3.0 Analytical HPLC run of 5’ thiol TR RNA

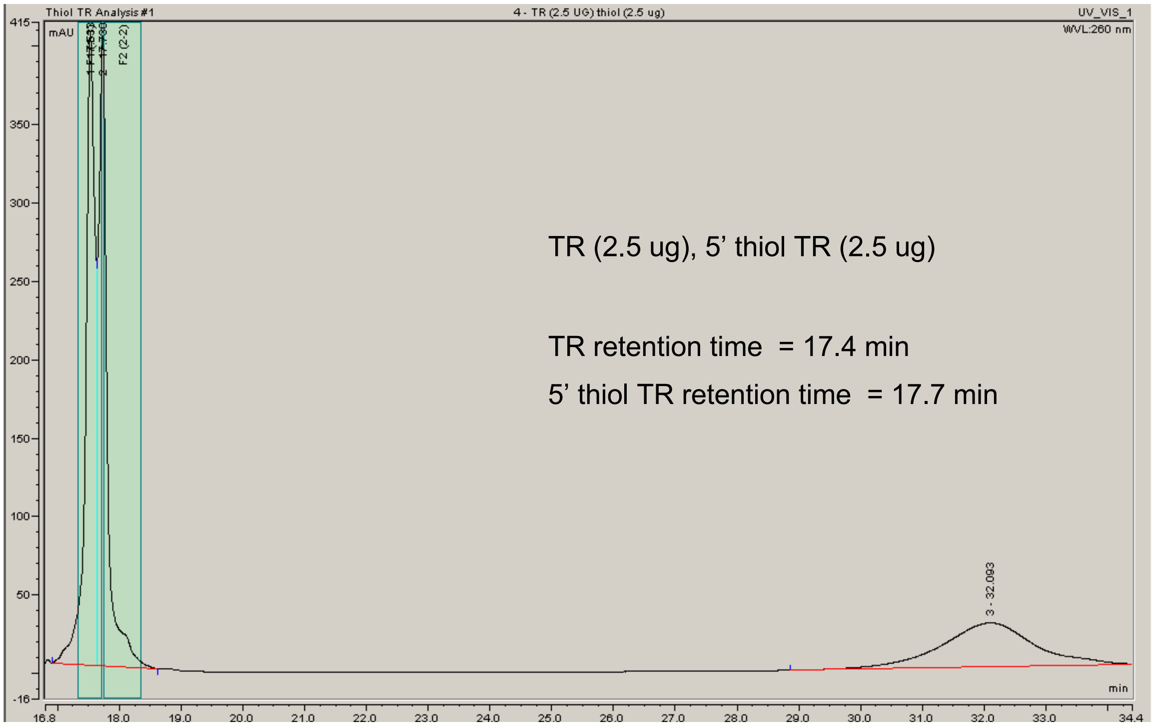

TR (2.5 ug), 5’ thiol TR (2.5 ug)

TR retention time = 17.4 min

5’ thiol TR retention time = 17.7 min

4.0 Analytical HPLC run of 5’ thiol TR RNA in 250 mM DTT

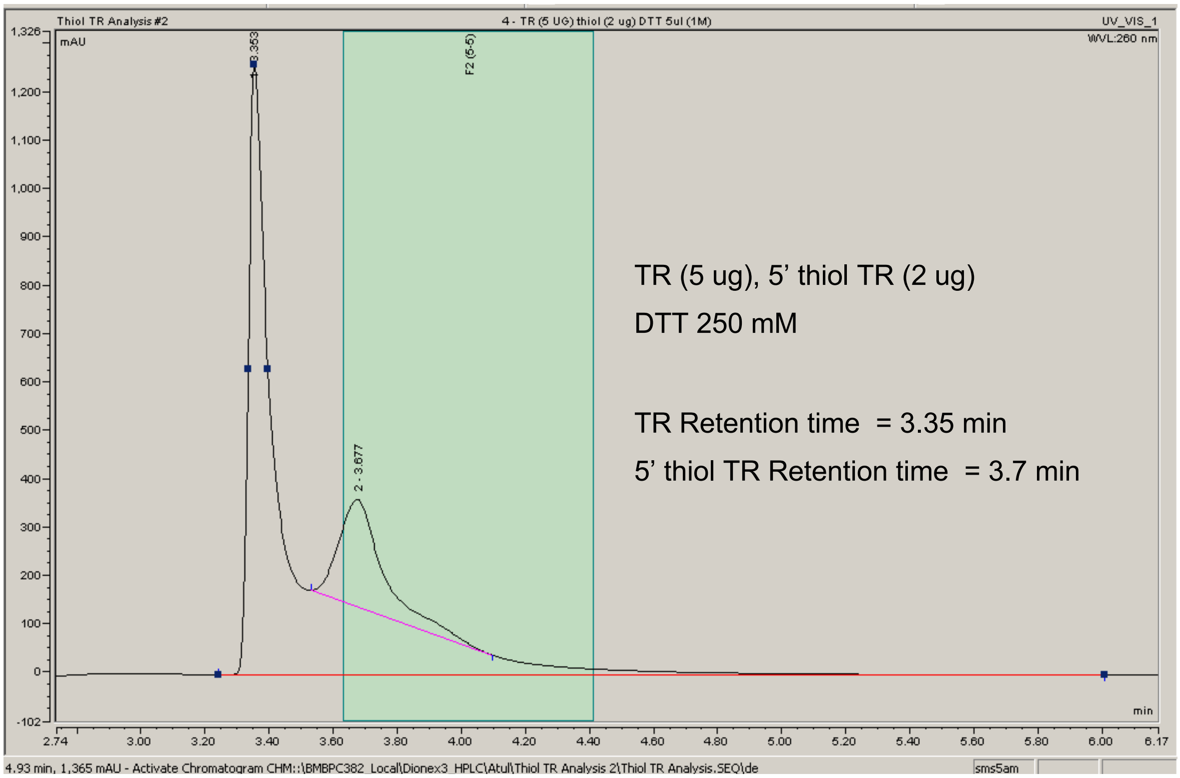

TR (5 ug), 5’ thiol TR (2 ug)

DTT 250 mM

TR Retention time = 3.35 min

5’ thiol TR Retention time = 3.7 min

4.93 min, 1,365 mAU - Activate Chromatogram CHM::\BMBPC382_Local\Dionex3_HPLC\Atul\Thiol TR Analysis 2\Thiol TR Analysis.SEQ\de